Pressure-Induced Structural and Electronic Effects in Solids

Thesis submitted by

Jason Crain

For the Degree of
Doctor of Philosophy

Department of Physics
The University of Edinburgh

February 1993

TABLE OF CONTENTS

§7.1 Introduction

§7.3 III-V Semiconductors in complex tetrahedral structures

§7.4 Future work

Appendicies

Declaration

In those cases where the research described in this thesis was performed in collaboration with others, acknowledgement is given in the following section and in appropriate references to resulting publications throughout the main text. In all other cases, this thesis represents the unaided work of the author.

Signed,

Jason Crain

Acknowledgements

First and foremost, it is a pleasure to thank my thesis supervisor, Dr. Peter Hatton who encouraged and supported me in all aspects of this work.

I also wish to gratefully acknowledge the following people for their generous help and support:

Dr. Graeme Ackland for his interest, keen insight, instruction and assistance in performing the computations described in chapters 6 and 7.

Dr. Mike Payne, Dr. Victor Milman, and Prof. Volker Heine at Cambridge University for very helpful discussions on the theoretical and computational background to the pseudopotential total energy method.

Dr. J.S. Lin for the generation of the *ab initio* pseudopotentials used throughout Chapters 6 and 7.

Dr. Guang-Yu Guo and Dr. Walter Temerman of the Daresbury Laboratory Theory and Computation Group for their help in performing the calculations described in Chapter 5 as well as their instruction on the theory and implimentation of relativistic APW and KKR calculations.

Mr. Stewart Clark for lattice dynamics calculations used in Chapter 7.

Prof. H. Kawamura and Dr. Y. Akehama at the Himeji Institute of Technology for their expert assistance and continued friendship during a very successful first visit to their laboratory in Japan.

Dr. Bob Cernik and Mr. A.M.T. Bell, for help, in the early days of my research in Edinburgh and Daresbury, with powder diffraction analysis packages.

Dr.Graham Bushnell-Wye also at Daresbury Laboratory, for assitance during the nervous moments in performing the experiments on Cyclohexane at low temperature at Daresbury.

Mr. Brendan Ried and Mr. John Maclean, who did their final year projects with me on some of the *ab initio* calculations described in Chapter 7. Also much appreciated were their helpful comments on parts of Chapter 2.

Mr. Hugh Vass for his expert technical assistance with the Raman scattering experiments described in Chapter 1.

Dr. Wilson Poon for his help on the Cyclohexane experiments and analysis.

Dr. Nigel Wilding for working with me (despite snowstorms) on the diffraction experiments at ILL and Daresbury described in Chapter 1.

Dr. Ross Piltz for help on countless occasions and in particular for help in the detailed analysis of powder diffraction data for the work in Chapter 6, critical reading of Chapter 3 (and the acknowledgements) and for introducing me to the joys of Thailandi red curries.

Mrs. Eleanor McKirdy for her endless patience and support.

Ms. Louise Grant for her kindness and capacity to adapt to the lifestyle of a physicist. Also thanks to her parents Cameron and Kerstin for a month of Sunday dinners.

Abstract

A series of detailed experimental and computational studies on aspects of pressure-induced structural phase transitions in solids is described. The emphasis is on the nature of such transitions in tetrahedral semiconductors. It is found that the materials investigated exhibit previously unreported and very complex behaviour which is related to the structural transition. New high-pressure diffraction evidence suggests that the crystallographic structures of several III-V semiconductors are not in agreement with those suggested either by prior experimentation or total energy calculation. The high-pressure structures determined in this work are generally of lower symmetry than previously believed and in at least one case of much greater complexity. It is also argued that phase-transition-induced defects are created at the transition in many of these materials and that the transition may be sensitive to either the concentration or mobility of such defects. The development and implementation of a simple new x-ray detection method has allowed for the observation of these subtle processes for the first time. To a certain degree, these novel aspects of previously well-studied transitions are now amenable to theoretical and computational treatment through the advances made in modern computer technology and parallel algorithms. As a result, new *ab-initio* local density functional investigations of structural stability and possible transition routes in one of these materials has been performed and the results are in good agreement with observation. Also the issue of defects has been treated by Car-Parrinello-type pseudopotential calculations on defect energetics. It is found, among other things that the defect formation energies are relatively low and that structural relaxation under the influence of Hellmann-Feynman forces is necessary in order to obtain accurate values of such energies. The remainder of the thesis is devoted to an exploration of pressure-induced metastable forms of group IV and III-V semiconductors. These studies unite and compare results from image plate experiments, *ab initio* pseudopotential calculations as well as empirical calculations using pair potentials and are applied in an attempt to make speculations as to the relative structural stability of these phases at finite temperature.

CHAPTER 1

HIGH-PRESSURE STRUCTURAL STUDIES ON THE MOLECULAR CRYSTAL CYCLOHEXANE : A "SIMPLE" PROBLEM IN ENERGY MINIMISATION

§1.1 Introduction and background

The primary contribution to "bonding" in a simple molecular crystal occurs via the fluctuations in dipole moments which give rise to the Van der Waals attraction. The simplest molecular crystals are the solid forms of noble gases which have completely filled electronic shells in the atomic state. This situation is only very weakly disturbed in the solid and from the point of view of electronic band structure, molecular crystals are extreme examples of materials for which the tight-binding model is an appropriate description of electron states. As all electrons in such a solid are part of the core there is little attention paid to the concept of valence or conduction bands though they have been calculated and lie high above the top of the filled core states. Despite their electrically neutral character, the origin of the attraction between noble gas atoms or of molecules has a well-defined electrostatic nature as well as a rigourous quantum-mechanical origin. The quantum-mechanical origin of the Van der Waals interaction arises simply from consideration of two isolated rare gas atoms and their two Hamiltonians, H_1 and H_2. The Hamiltonian for the two-atom system is then H_1+H_2+U where U is the Coulombic interaction between all pairs of charged particles associated with different atoms. In many cases the interaction energy is sufficiently small so that U can be taken as a perturbation. To second order in a perturbation expansion for the interaction energy the leading non-vanishing term is negative and falls off as the inverse-sixth power of the separation between the nuclei. In the opposite limit of small nuclear separations, repulsive forces must dominate the interaction. The competition between the repulsive and attractive influences determines the equilibrium separation for the atoms. In the simplest of descriptions this situation can be well-modeled by isotropic pairwise additive interactions [1] which include the Lennard-Jones potential $\Phi^{LJ}(R)$

$$\Phi^{LJ}(R) = [(\frac{B}{R^{-n}}) - (\frac{A}{R^6})] \quad (n=8,9...,14) \qquad (1.1.1)$$

and the Buckingham potential $\Phi^B(R)$

$$\Phi^B(R) = [\ Be^{(-CR)} - (\frac{-A}{R^6})\ ] \tag{1.1.2}$$

which will be used in a subsequent treatment of cyclohexane. A term which explicitly describes the Coulomb energy is not included in these analytic forms but this does not imply that the electrostatic energy is completely neglected in this model. There is no *a priori* physical interpretation assigned to any of the fitting parameters which appear in the potentials and the electrostatic energy will be at least partially reflected when the potential is fitted to various properties of the material. The inclusion of a Coulombic term to the potential explicitly not only results in an increase in the number of empirical parameters but also requires evaluation of the very slowly convergent Madelung terms which undermine the attractive simplicity of the calculation.

In addition to simple energy considerations, several general principles have been identified which appear to determine, to a large extent, trends in structures more complex than rare gas solids such as organic molecular crystals [2]. In conjunction with a rigid molecule approximation and the assumption of pairwise additive molecular interactions these rules have been used successfully to model structures of a variety of organic compounds. In general, however, the role of molecular distortions in structure adoption is not negligible as has been evidenced by such compounds as cyclopentane and succinonitrile [3,4]. For these and many other systems, structure adoption is determined by a compromise between the configuration which minimizes the intramolecular strain and intermolecular energy. Other factors that govern structure adoption in solids include dynamic disorder, sample history and isotopic substitution.

C_6H_{12} has long been recognized as an important prototypical molecular crystal and has attracted a great deal of experimental attention over the past decade [5]. Its attractiveness stems principally from the fact that although comprised of a simple molecule (Figure 1.1), the cyclohexane molecular crystal displays wide pressure- and temperature-induced polymorphic variety over experimentally accessible conditions. It has, therefore been subjected to a large number of experimental probes including differential thermal analysis (DTA), neutron and x-ray diffraction and Raman and infrared spectroscopy. It will be useful to review the results of experimental effort prior to describing the motivation for the research discussed in the following sections.

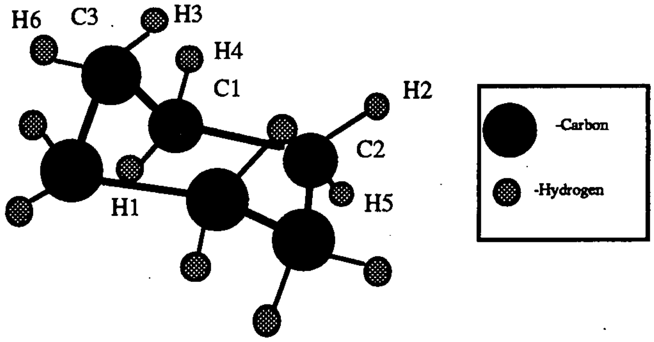

Figure 1.1. Cyclohexane molecule in its undistorted "chair" configuration. The molecular symmetry is that of the D_{3d} point group.

At ambient pressure and approximately 280 K, the cyclohexane molecular crystal undergoes a liquid-solid transition to a cubic plastic crystal (Phase I) with a lattice parameter of 8.61 Å. Early NMR studies revealed that this phase is characterized by a large degree of dynamic molecular disorder in which the molecules undergo rapid reorientations on the lattice sites [6]. Upon slow further cooling to 186.1 K at ambient pressure, a solid-solid transition to a monoclinic structure (Phase II) is observed which is found to be stable to the lowest attainable temperatures. The formation of Phase II, however, is dependent upon the cooling rate and is only observed for relatively slow quenches. Diffraction studies have determined that phase II has lattice parameters a = 11.23 Å, b = 6.44 Å, c = 8.20 Å and the monoclinic angle β =108.83° and the spacegroup was found to be C2/c [7]. Faster quenches introduce a new temperature-induced metastable phase (Phase M) [8]. Efforts to determine the structure of this phase will be described in a subsequent section. Spectroscopic investigations led to the conclusions that Phase M is a plastic-crystal glass [9,10] which loses the rotational, reorientational freedom characteristic of the liquid phase but possesses a well-defined face-centred-cubic (FCC) lattice.

Several phases of cyclohexane can be synthesized exclusively by the application of hydrostatic pressure and these were first identified using Differential Thermal Analysis (DTA) up to 3 kbar [11]. A similar technique has also been applied to cyclohexane in an effort to determine transition entropies at pressure-induced phase transitions [12]. Upon increasing pressure from ambient to 0.25 kbar at room temperature a transition is observed between Phase I and another solid form of cyclohexane denoted as Phase III. The structure of this high pressure form was determined by high-resolution neutron powder diffraction [13]. It was found to be orthorhombic with spacegroup Pmnn and lattice constants a = 6.587 Å, b = 7.844 Å and c = 5.463 Å.

The effect of isotopic substitution of deuterium for hydrogen was also studied. In addition to identifying all of the corresponding phases (I,II and III) in the deuterated material a new pressure-induced phase (Phase IV) was discovered which had not been previously observed in the hydrogenated material. As a result, mixtures of C_6H_{12} and C_6D_{12} were studied and it was found that the(I,II,III) triple point shifted to lower pressures with increasing C_6H_{12} concentration while the III-IV boundary moved to higher pressures.

In addition to the DTA studies summarized above, a great deal of high-pressure, ambient temperature Raman and infrared spectroscopic studies have been performed on cyclohexane and its deuterated analogue [14]. Two pressure-induced transitions were reported in both C_6H_{12} and C_6D_{12} at pressures of 5.1 kbar and 9.6 kbar for the hydrogenated material and 5.3 kbar and 7.4 kbar for the deuterated compound. The highest pressure phase obtained in both of these compounds was found to be of C_{2h} symmetry, the same as Phase II, which led to the conclusion that further pressure increase in Phase IV induces a transition to the stable low-temperature phase II. The work described in this thesis was motivated by the need to fill several substantial gaps in the present understanding of pressure-induced polymorphism in the simple molecular crystal cyclohexane. The issues to be addressed were as follows:

1) Does Phase IV exist in C_6H_{12} or does deuteration induce a completely new phase?

2) What is the structure of Phase IV and its relation to other conformations?

3) Does further pressure increase in Phase IV lead to transformation to Phase II as previously suggested?

4) What is the nature, structure and relation of Phase M to the low temperature Phase II?

The following studies have included neutron (ILL - Grenoble) and x-ray diffraction (Daresbury Lab. Synchrotron Source), Raman spectroscopy

(Edinburgh) and energy minimisation calculations. The extensive light scattering experiments were performed in order to address questions 1 and 3 which relate to the phase diagrams and their topologies. The remaining structural issues (questions 2 and 4) were simultaneously resolved through conclusions drawn from the diffraction experiments and minimum energy considerations.

§1.2 High pressure phenomenology of cyclohexane

1.2.1 Experimental

Raman spectra were obtained using the 514.5 nm line of an Ar laser operating at a power setting of approximately 300 mw and scattered light was collected with a scanning Coderg T-800 triple-grating spectrometer. A standard diamond anvil cell (DAC) was used to apply pressure to the sample. Pressure was determined using the ruby fluorescence method. For pressure calibration the ruby fluorescence patterns were referenced to an internal neon bulb line for improved accuracy. Nickel gaskets were chosen as this material allows for pressure increase in finer increments than many other gasket materials.

For the low temperature measurements, samples were sealed in glass capillaries while for the high-pressure experiments spectra were collected in backscattering geometry as shown in Figure 1.3.

Count times were generally 5 seconds/(data point) and scans were made over the range 700 to 1250 cm^{-1} for C_6D_{12} and the corresponding range (750 to 1500 cm^{-1}) in C_6H_{12}.

1.2.2 Results and discussion

a) Symmetry considerations

An isolated cyclohexane molecule exhibits D_{3d} point group symmetry and 48 normal vibrational modes which span the representation

$$\Gamma^{D_{3d}}_{vib} = 6A_{1g} + 2A_{2g} + 8E_g + 3A_{1u} + 5A_{2u} + 8E_u$$

where only the A_{1g} and E_g modes are Raman active. The assignments of the vibrations are given in Table 1. For the low temperature phase II a similar number of vibrational modes is expected as for the isolated molecule.

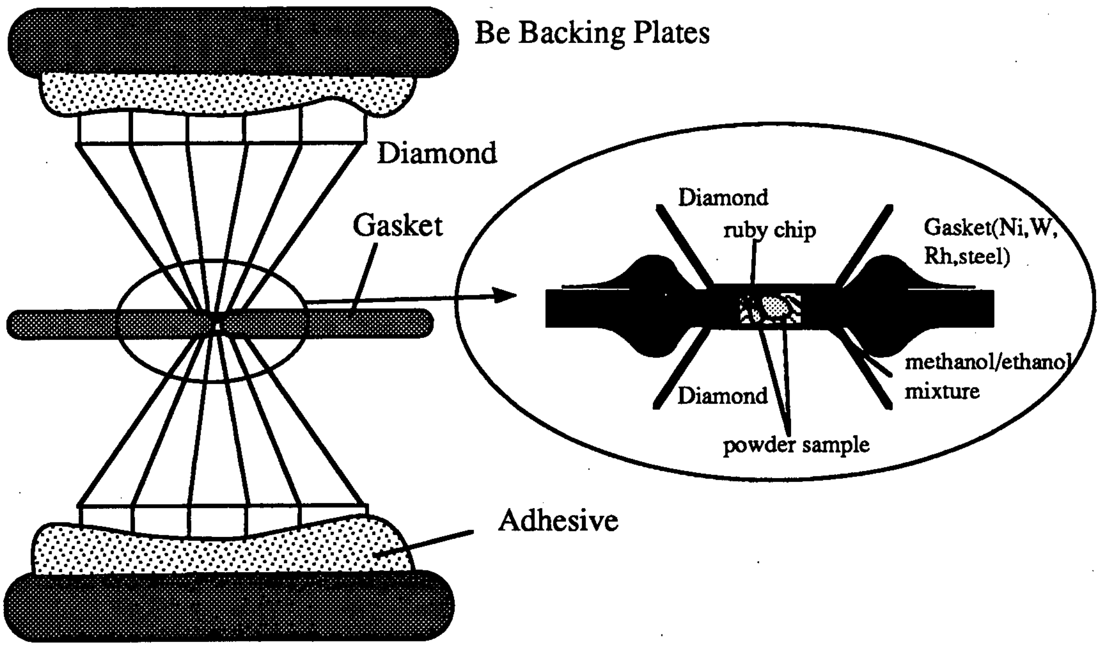

Figure 1.2 General experimental situation for high-pressure studies using a standard Diamond Anvil Cell (DAC) and metal gasket.

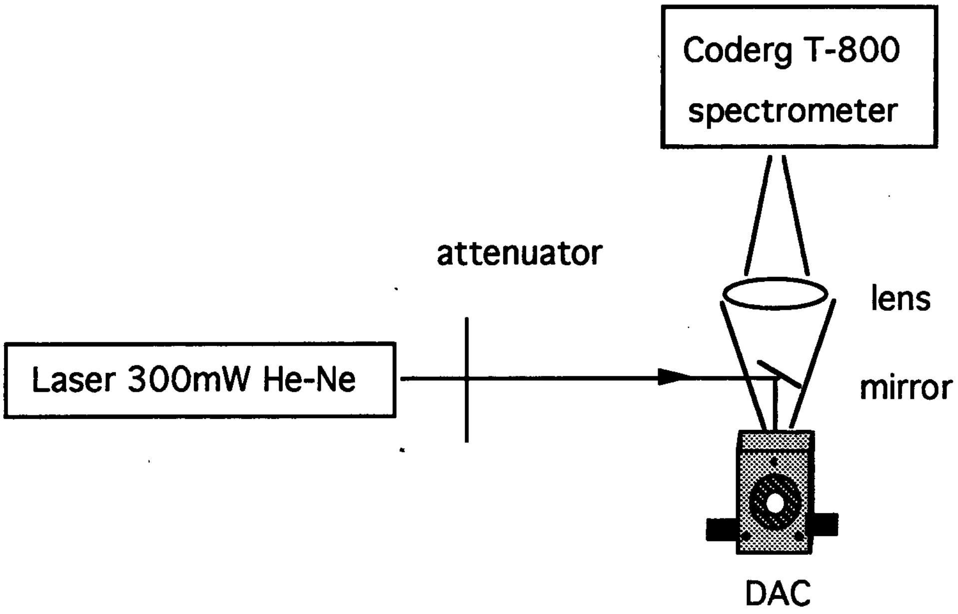

Figure 1.3 Schematic diagram of the experimental arrangement for high pressure Raman spectroscopy in backscattering geometry.

They span the representation

$$\Gamma_{vib}^{C_{2h}} = 12A_g + 12B_g + 12A_u + 12B_{2u}$$

For the high pressure phase III:

$$\Gamma_{vib}^{D_{2h}} = 6A_{1g} + 6B_{1g} + 6B_{2g} + 6B_{3g} + 6A_u + 6B_{1u} + 6B_{2u} + 6B_{3u}$$

The above group theory considerations suggest that the spectra in all three solid phases of cyclohexane will show a general similarity. However the Raman scattering spectra will be sensitive to distortions of the molecular geometry.

Table 1.1 Raman mode assignments of cyclohexane C_6H_{12} and C_6D_{12}. These assignments are taken from reference [15].

Symmetry	No.	Frequency (cm^{-1})		Assignment
		H_{12}	D_{12}	
A_{1g}	ν_1	2937	2152	CH_2 (D_2) anti. stretch
	ν_2	2852	2082	CH_2 (D_2) sym. stretch
	ν_3	1465	1117	CH_2 (D_2) scissors
	ν_4	1157	1012	CH_2 (D_2) rock
	ν_5	802	723	CC stretch
	ν_6	383	297	CCC deform. + CC torsion
E_g	ν_{17}	2930	2198	CH_2 (D_2)anti. stretch
	ν_{18}	2897	2105	CH_2 (D_2) sym. stretch
	ν_{19}	1444	1072	CH_2 (D_2) scissors
	ν_{20}	1346	1212	CH_2 (D_2) wag
	ν_{21}	1266	938	CH_2 (D_2) twist
	ν_{22}	1029	795	CC stretch
	ν_{23}	784	637	CH_2 (D_2) rock
	ν_{24}	426	373	CCC deform. + CC torsion

b) Deuterated cyclohexane

All of the Raman spectra were collected with 0.5 cm^{-1} resolution. Figures 1.4(a) and 1.4(b) show the spectra obtained in each of the high pressure solid phases and in the stable low temperature phase II. Upon increase of pressure from the liquid phase, the first solid phase induced was found at 2.7 kbar and was assigned to the plastic phase I. The large

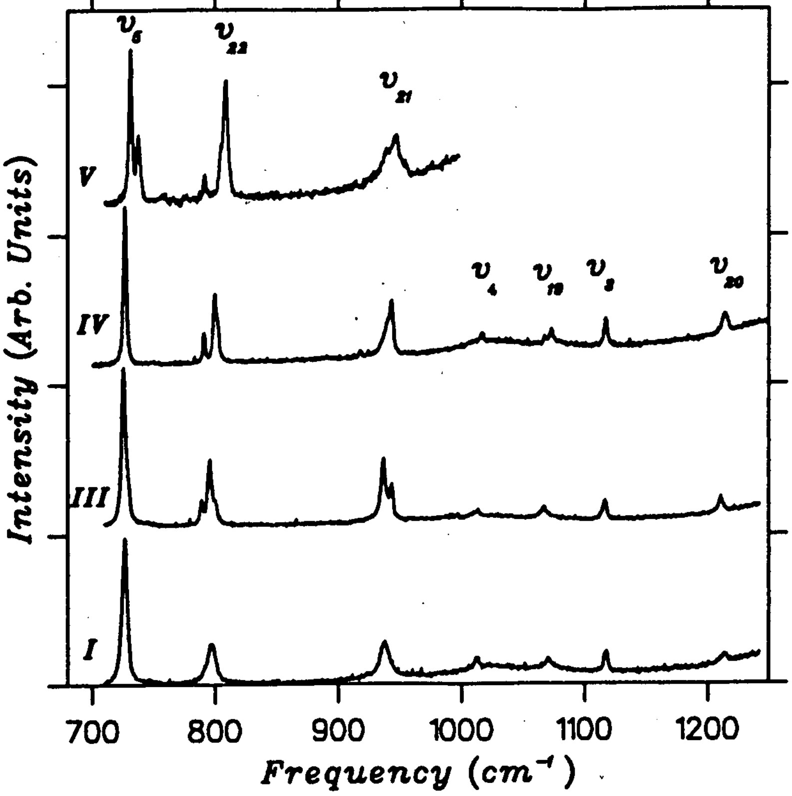

Figure 1.4(a) The Raman spectra collected in each of the pressure-induced solid phases of cyclohexane: Phases I, III, IV and V.

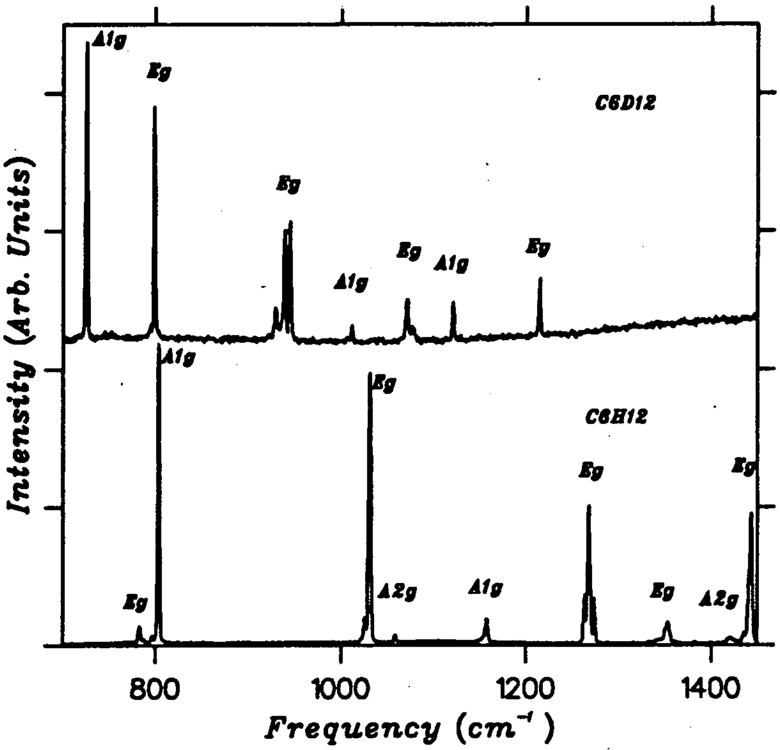

Figure 1.4(b) The Raman spectra collected in the equilibrium low-temperature Phase II. For comparison, and later reference, the corresponding Phase II in C_6H_{12} is also shown.

peak widths are consistent with the large degree of rotational dynamic disorder present in this phase.

The next pressure-induced phase transition was observed to occur at approximately 6.5 kbar and was characterized by a narrowing of the mode lineshape which indicated that the dynamic disorder in Phase I has been frozen out. The are also many splittings of the peaks in this phase relative to Phase I suggesting that it is of lower symmetry.

Upon further pressure increase, a very subtle transition occurs at approximately 7.5 kbar. At this pressure, a splitting of the ν_{20} mode at 1070 cm^{-1} is observed. The minimal effect of this phase transition on the Raman spectrum is evidence that it is not accompanied by appreciable molecular distortion. The observation of this phase transition at 7.5 kbar is consistent with the observation of a transition at 7.4 kbar by Haines and Gilson [16] who attributed their finding to a III-II transition. The known III-IV boundary at low temperature extrapolates linearly to a pressure of roughly 7 kbar at room temperature. In the present Raman study, the spectrum observed above 7 kbar is distinct from that collected in Phase II at low temperature. As a result of these findings we attribute the phase transition above 7 kbar to a III-IV transition (Figure 1.5). The similarity of spectra collected in these two phases suggests that very little molecular distortion occurs at the transition. Further increase pressure from Phase IV does not bring about a transition to Phase II as an extrapolation of the existing phase diagram would suggest. Instead a gradual splitting of the A_{1g} skeletal breathing mode is observed to develop at 17 kbar. There is also a strong pressure dependence of the relative intensities of this doublet and the splitting between them as shown in Figure 1.6. We attribute these observations to a transition from Phase IV to a previously unreported Phase V.

c) Hydrogenated cyclohexane

All spectra were collected with 2 cm^{-1} resolution. As was found for the deuterated compound, pressure increase from ambient on this material induces three solid-solid phase transitions. Figure 1.7 shows the Raman spectra collected in each of the pressure-induced phases.

The proposed hypothesis is that the observed sequence is the same as that observed for the deuterated material and there is substantial evidence

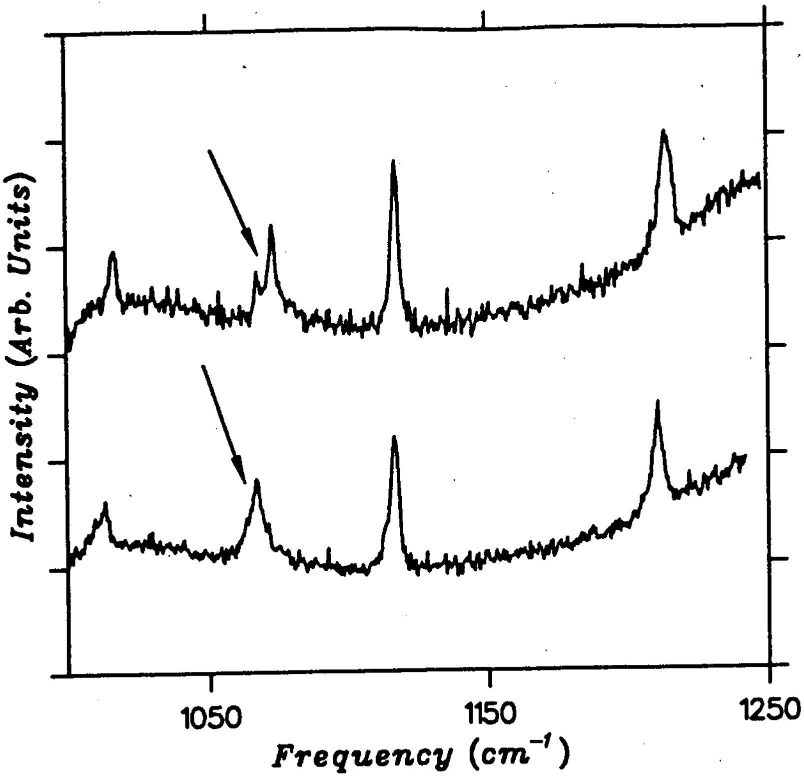

Figure 1.5 Detail of the spectroscopic evidence for a Phase III to Phase IV transition in C_6D_{12}.

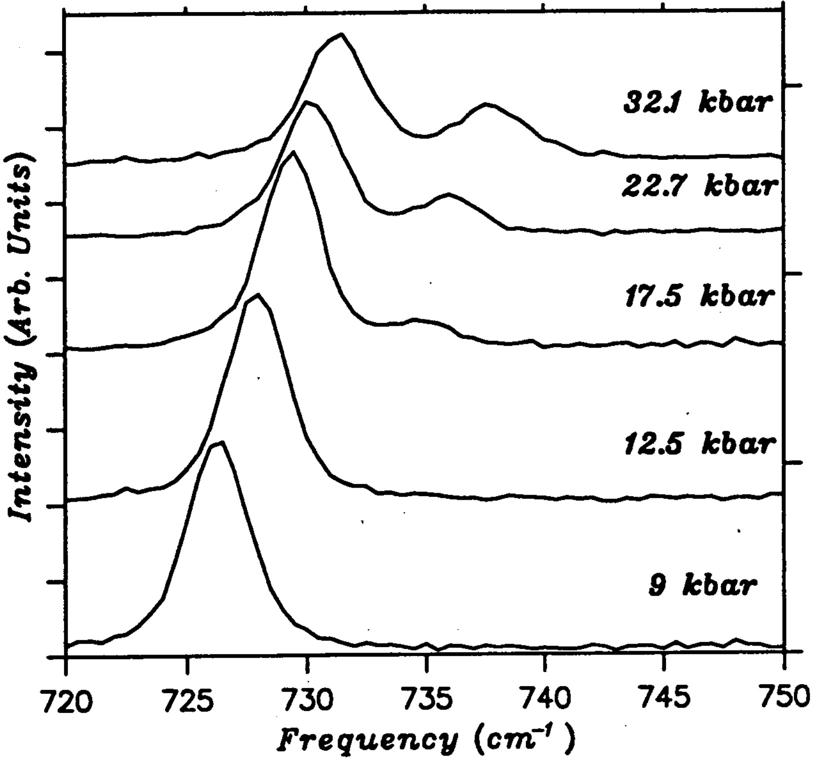

Figure 1.6 Detail of the pressure dependence of the skeletal breathing mode in C_6D_{12} illustrating the pronounced splitting . This behaviour has been attributed to a pressure-induced transition to a previously unreported phase (Phase V).

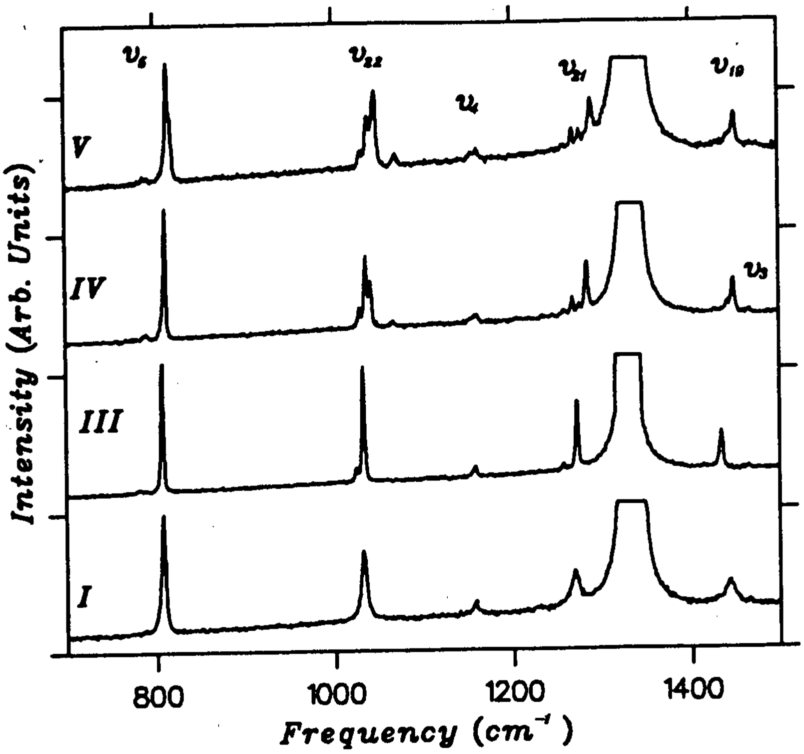

Figure 1.7 Raman spectra collected in each of the pressure induced phase of C_6H_{12} showing a marked similarity of phase-transitions sequences to that observed or C_6D_{12} prompting the conclusion that phase diagram topology is not affected by deuteration. The Raman spectrum collected in Phase II is shown in Figure 1.4 (a).

for this in the case of phases IV and V. Between 14 and 22 kbar the spectra of C_6H_{12} is extremely similar to that collected in Phase IV on C_6H_{12}. Regarding 'Question 1', it appears that Phase IV exists in C_6H_{12} and that deuteration does not, in fact, introduce a new phase. At the highest pressure applied to C_6H_{12}, the symmetric breathing mode is again split and the relative intensities of the peaks in the spectrum suggests that a transition to Phase V also occurs in C_6H_{12}. The evidence for the existence of Phase III in C_6H_{12} is less obvious than it was in the case of deuterated material. The υ_{22} group of peaks at 800 cm^{-1} is seen to be a clear triplet in C_6D_{12}, the corresponding complex located at 1050 cm^{-1} appears only as a doublet in C_6D_{12}. Despite these slight differences, the available spectroscopic evidence

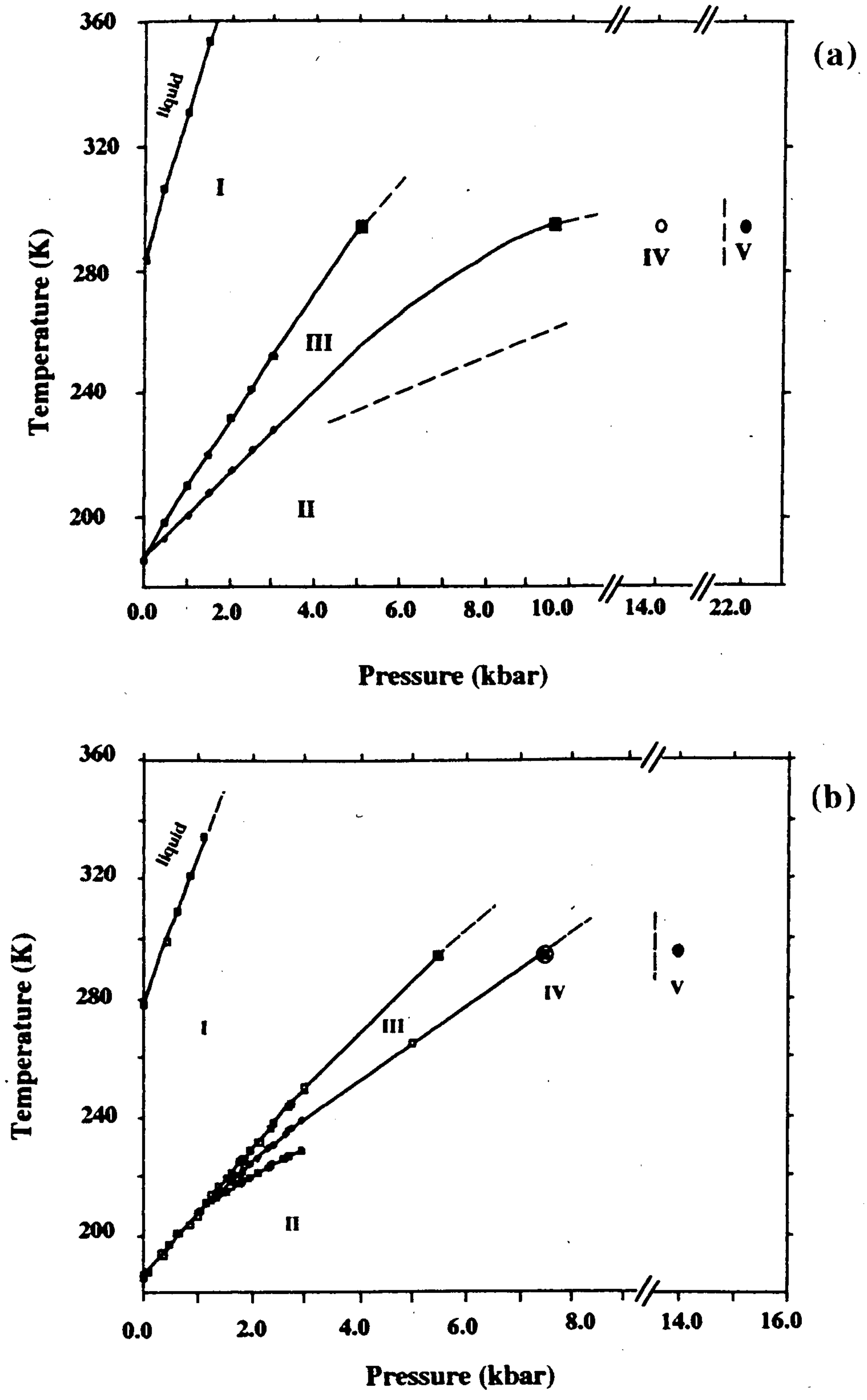

Figures 1.8 (a) and (b) Phase diagram of C_6H_{12}(a) and C_6D_{12}(b). All data below 3 kbar are due to DTA studies. Above 3 kbar, filled squares represent observations by Haines and Gilson. In Figure b, The open squares represent the points at which the work of Wilding, Crain, Hatton and Bushnell-Wye was performed. Open and filled circles represent the present work (Crain, Poon, Cairns-Smith and Hatton [17]). Dotted lines are to be interpreted as inferred phase boundaries.

is still consistent with the hypothesis that the pressure-induced phase transition sequence in both C_6D_{12} and C_6H_{12} are the same.

d) The metastable phase

Detailed studies of the equilibrium low temperature Phase II of C_6H_{12} have been performed by a variety of techniques and its structural and spectroscopic properties are well known. Quenching C_6H_{12} from either the liquid or Phase I, however produced a metastable phase, Phase M, which is distinct from the stable Phase II obtained by slower cooling. Phase M was discovered in 1966 by Renaud and Fourme [8]. Several models have been suggested to describe the nature of Phase M: the seemingly accepted proposal made in 1984 by Burns and Dacol [9], is that Phase M is similar to the FCC Phase I but without the reorientational degrees of freedom of the molecules. This was termed a plastic-crystal glass. Previous powder diffraction results obtained on Phase M appear to be inconsistent with an FCC lattice. In order to address some of the issues mentioned in "Question 4", a Raman scattering study has been performed on the metastable phase of C_6H_{12}.

Phase M was produced by rapid quenching from the liquid to 77 K. The Raman signature of the metastable phase is the complex band at 1270 cm^{-1} which is absent in Phase II.

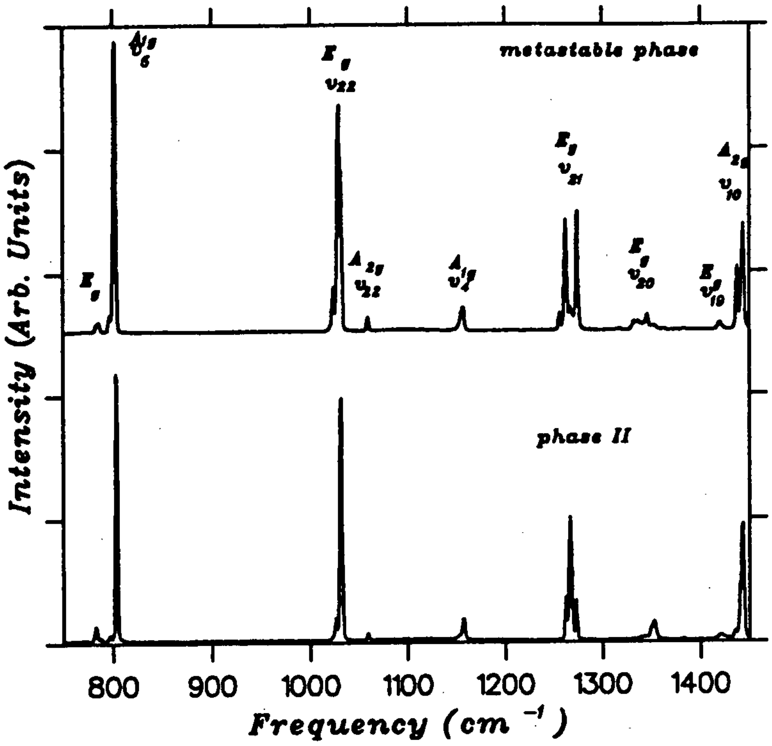

Figure 1.9 Raman spectrum collected in the metastable phase of C_6H_{12}. The phase was synthesized by rapidly cooling from Phase I to 77 K. The spectrum obtained in the stable low temperature form (Phase II) is shown for comparison.

It was found that the lines of the Phase M spectrum (Figure 1.9) are distinctly sharper than those of Phase I. This may be interpreted (within the context of a plastic-crystal glass model) as a substantial lengthening of the reorientation period compared to that of Phase I. It is also, however, consistent with an orientationally ordered structure. A preliminary study of the Phase M lattice modes was also made which revealed three well-defined lattice modes. The widths were comparable to those of the stable low-temperature form (Phase II). It seems unlikely that a phase having molecules which exist in many energetically equivalent orientations would exhibit such well-defined lattice modes. These spectroscopic results in no way lead to a definitive conclusion regarding the nature of Phase M however, the spectroscopic evidence is difficult to reconcile with a plastic-crystal glass interpretation and it is tempting to consider other possibilities.

One possibility is that Phase M is one of the three high-pressure forms. The orthorhombic Phase III is perhaps the most natural candidate because it has a triple point with Phases II and I at the relatively low pressure of 0.25 kbar. However, the spectroscopic evidence does not support this conjecture as the Raman patterns collected of Phases III and M are not similar and that Phase M is likely to be of lower symmetry than Phase III based on the number of observable modes. The spectroscopic data collected of Phase IV does show a significant similarity to that collected of Phase M and it also exhibits the same number of observable Raman modes. This result suggests that, of the high-pressure forms of cyclohexane, Phase IV is the most likely candidate to be the low-temperature metastable phase.

§1.3 Neutron diffraction studies of cyclohexane (C_6D_{12}) IV

1.3.1 The powder diffraction method and the Rietveld approach

In the powder diffraction method, the sample crystal is reduced to a very fine powder and placed in a beam of either x-rays or neutrons. Each particle of the powder is a small crystal which is oriented at random with respect to the incident beam. There is some probability that a given particle will be in the diffraction condition for a particular reflection. If there are sufficient numbers of particles then all lattice planes will be capable of reflection. This situation is equivalent to a single crystal rotated about all possible axes. If a given (hkl) plane in a single crystal is rotated about the incident beam axis the reflected beam will trace out the surface of a cone, the Debye-Scherrer cone. This rotation does not occur in practice in the powder diffraction method but in the limit of a large population of crystals having all possible orientations in the powder a certain fraction of them will lie in all possible rotation positions about the axis of the beam. The most accurate one-dimensional profile of the Debye-Scherrer cone would be an azimuthal integration around the rings but, in practice, a scanning detector is used which records the diffracted intensity at discrete intervals of scattering angle but only intercepts a small portion of the Debye-Sherrer cone. When the sample volume is large , as it is in the present case, the scanning detection method is a produces a diffraction profile which will allow for full structural determinations to be made. This is not the case when sample volumes are greatly reduced as they are in very high pressure experiments. This situation will be discussed more fully in Chapter 3.

In even a relatively simple powder diffraction pattern, considerable overlap may occur between peaks of nearby reflections. In such a situation, it is generally not straightforward to determine the integrated intensities of each of the independent contributing peaks. The most direct means of avoiding the need to determine individual reflection intensities is to employ a least-squares fit to the data using a calculated diffraction pattern which for a given functional form of the peakshape incorporates the overlap automatically. The peak position in the calculated profile depends only on the unit cell dimensions and the relative intensities are mainly governed by the structure factors determined by the relative atomic positions. These, among many other parameters, such as overall scale and zeropoint error, can then be used in a least-squares fit to the full diffraction profile. The original attempts at this strategy were reported by Rietveld [18,19].

In general, the value of the calculated profile at each point, $Y(n)$, in the simulated pattern (up to a scale factor) is given by

$$Y(n) = \sum_{p} \{ \sum_{k} |F(k)|^{2} f(\Theta(n,k)) \} + B(n) \qquad (1.3.1)$$

Where $F(k)$ is the structure factor of each reflection, $f(\Theta(n,k))$ is the peakshape function for each reflection and $B(n)$ is the calculated or input background at each point, n. The two sums are over the number of phases, p, in the profile and the number of reflections, k, contributing to each point n.

The quality of the fit to the data is quantified by several different 'agreement factors' defined as

$$R_I = \frac{\Sigma\{|Y_{obs} - Y_{calc}|\}}{\Sigma Y_{obs}} \qquad (1.3.2)$$

$$R_{wp}{}^2 = \frac{\Sigma\{w[Y_{obs} - Y_{calc}]^2\}}{\Sigma[wY_{obs}{}^2]} \qquad (1.3.3)$$

$$R_{exp}^2 = \frac{(N - P + C)}{\Sigma[wY_{obs}^2]} \qquad (1.3.4)$$

where N, P and C are the number of data points, refined parameters and the scale factor, respectively. Also, Y_{obs} = Y(total) - Background and w = 1/Y(total) + Background. The background was interpolated between user-input points which were determined visually.

1.3.2 Motivation

Although the conclusions drawn in the previous section have contributed to a reasonably simple picture of the phase diagram topology and nature of the metastable phase in both the hydrogenated and deuterated forms of cyclohexane up to 30 kbar there are still several outstanding issues still to be addressed. These are primarily structural issues and were referred to as questions 2 and 4 in Section 1.1. Since spectroscopic techniques can provide only limited structural information, a series of extensive neutron powder diffraction experiments have been performed in an attempt to determine the crystal structure of Phase IV and Phase M and their relation to the other high pressure phases. The stability field of Phase V lies outside the maximum attainable pressures for neutron studies.

1.3.3 Experimental

All data were collected at the Institut Laue-Langevin using the D2B high-resolution diffractometer and an incident wavelength of 1.5938 ± 0.0002 Å. A diffractometer stepsize of $\delta 2\Theta = 0.05°$ was used. A He gas pressure cell was used inside a cryostat allowing for a maximum pressure of approximately 5.5 kbar at 60 K. Controlled pressure application was performed using a calibrated pumping apparatus and an independent strain gauge both of which agreed to better than 0.1 kbar. The aluminium housing of the pressure cell causes contaminant diffraction peaks at 2Θ = 39.9°, 46.0°, 67.2° and 81.7°. As in the preceding light scattering experiments, a commercially available C_6D_{12} sample (99.5% purity - Aldrich Chemical Co.) was used.

Since the sample was initially in liquid form when introduced into the sample chamber (a 12 mm diameter vanadium cylinder) there was a strong possibility that very large crystals may form during solidification which would severely reduce powder quality. Silica wool was therefore also packed inside the sample chamber to help maintain powder homogeneity [20].

1.3.4 Experimental results

At a pressure of 5 kbar, the sample was cooled slowly to 250 K from room temperature. A diffraction pattern of the resulting phase was found to be consistent with the unit cell of Phase IV. With the pressure stable at 5 kbar the temperature was lowered slowly to 60 K. No evidence of conversion to Phase II was observed even after several hours. At a constant temperature of 60 K, pressure was gradually released in an attempt to identify any transition to Phase II. Unexpectedly, no such transition was observed and the high-pressure Phase IV persisted to ambient pressure and was only observed to convert to Phase II upon subsequent heating to over 150 K at ambient pressure. At each pressure the unit cell parameters of Phase IV were determined by inputting the Bragg reflection positions into the CELREF program of Fitch and Murray [21] The pressure dependence of the unit cell dimensions and monoclinic angle are shown in Figure 1.10. It is easily seen that the crystal is most compressible along the <010> direction.

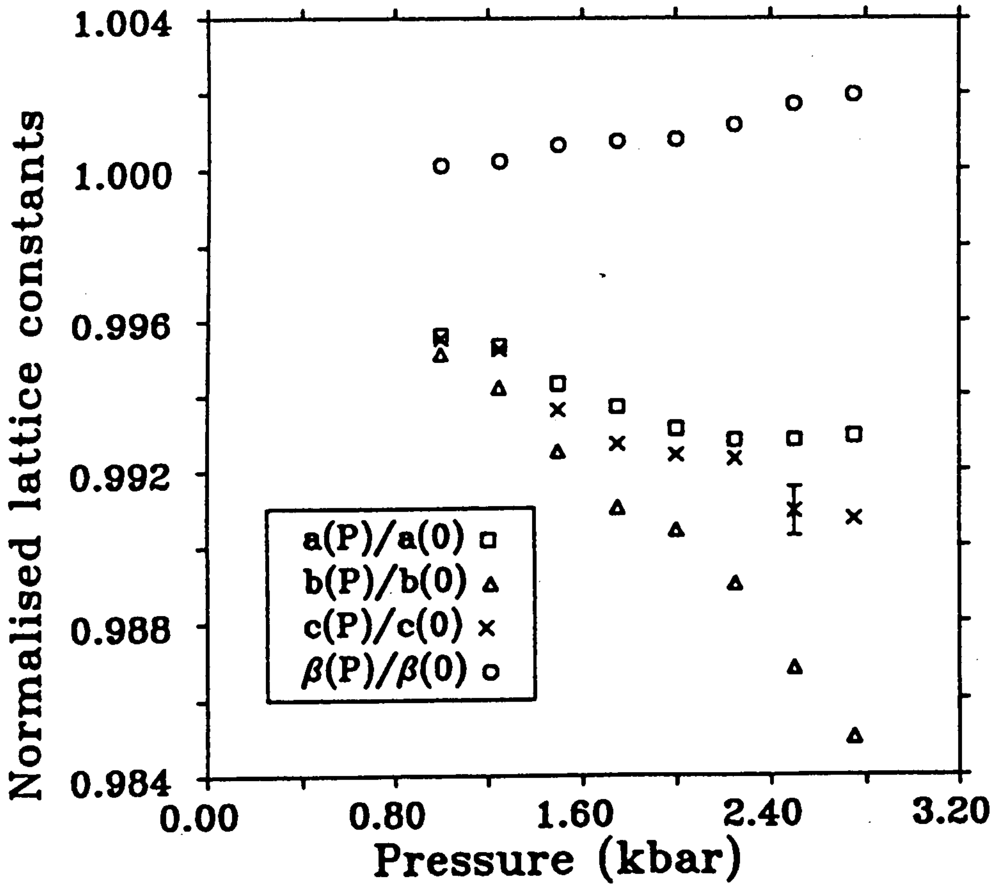

Figure 1.10 Pressure dependence of the structural parameters in Phase IV of C_6H_{12} as a function of pressure. The results were obtained by slowly releasing pressure from 5 kbar and were collected using high-resolution neutron diffraction on the D2B diffractometer at the ILL.

1.3.5 Energy minimisation

A cluster of approximately 100 atoms was used in an attempt to determine the most energetically favourable relative orientations of rigid cyclohexane molecules given the unit cell dimensions suggested by the neutron diffraction powder profile. The intermolecular potential used was of the Buckingham form (Equation 1.2) and the parameters were taken from those given by Williams [22] for C-C and C-H bonding [23]. All intramolecular strains were neglected in this calculation. The lattice energy was calculated as a function of rotation angle of the rigid cyclohexane molecule. Table 1.2 shows the calculated atomic positions obtained using this energy minimisation approach.

Table 1.2 Atomic positions (in fractional coordinates) as predicted by energy minimisation with respect to molecular orientation using a Buckingham pair-potential and the parameters reported by Williams [22].

atom	x	y	z
C1	0.206	-0.072	0.103
C2	0.171	0.022	-0.152
C3	-0.002	0.165	-0.152
D1	0.247	0.016	0.232
D2	0.130	-0.065	-0.281
D3	-0.038	-0.252	-0.024
D4	0.315	-0.161	0.104
D5	0.299	0.081	-0.183
D6	-0.024	0.224	-0.313

The unit cell dimensions, zeropoint offset and functional form for the peakshape were fitted using the ALLHKL package [24]. Then the constrained Rietveld (next section) refinement package EDINP [25] was used to determine the atomic positions in the phase IV structure as suggested by the neutron powder profile relative intensities. Positions of only half the atoms per molecule are given in Table 1.2 as the remaining half are related by an inversion through the origin. Strict constraints were applied to the C-C and C-D bond lengths and only the molecular orientation was allowed to vary.

1.3.6 Results for Phase IV

The fit to the neutron powder diffraction profile is shown in Figure 1.11. The pattern was collected at 250 K and 5 kbar. As is evident from the figure there is generally good agreement between the observed and calculated profiles suggesting that the proposed structural model is appropriate. The structural parameters deduced from the diffraction data (Table 1.3 and 1.4) and those arrived at through minimum energy considerations are also in reasonable accord. There are, however, some discrepencies between the observed and calculated diffraction intensities. A comparison of this pattern with one collected from a different sample

Table 1.3 Values of the instrumental parameters (u,v,w) and cell dimensions of C_6D_{12} Phase IV at 5 kbar and 250K. Estimated standard deviations of the last figure are shown in parentheses.

parameter	value
offset (°)	-0.338 (2)
u (°)^2	0.709 (1)
v (°)^2	-0.728 (8)
w(°)^2	0.324 (1)
a (Å)	6.529 (4)
b (Å)	7.601 (4)
c (Å)	5.461 (7)
β(°)	96.97 (1)
Volume (Å^3)	269.07 (4)

Table 1.4 Refined atomic positional coordinates in Phase IV at 5 kbar and 250 K based on a constrained molecular geometry. Estimated standard deviation in the three Euler angles ϕ ,Θ and ψ which determine the molecular orientation are 0.017 °, 0.016° and 0.018 ° respectively.

atom	x	y	z
C1	0.203	-0.068	0.102
C2	0.172	0.028	-0.147
C3	-0.002	0.163	-0.145
D1	0.242	0.025	0.248
D2	0.133	-0.065	-0.292
D3	-0.037	-0.257	0.001
D4	0.325	-0.163	0.101
D5	0.312	0.094	-0.176
D6	-0.024	0.231	-0.319

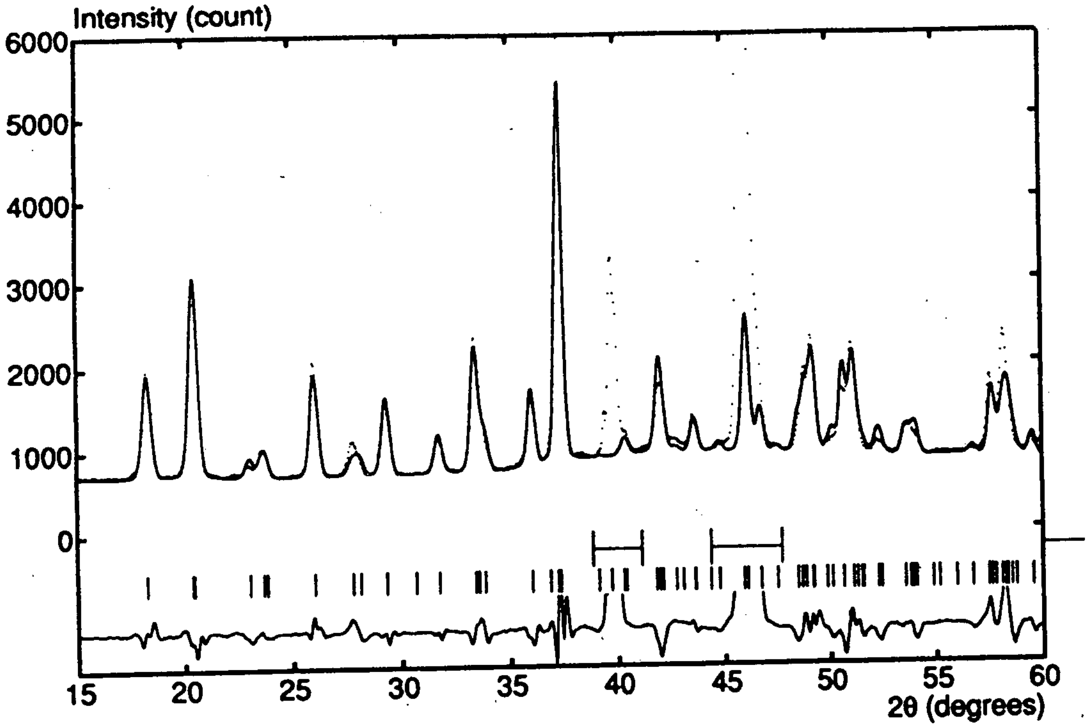

Figure 1.11 Least-squares fit to the neutron powder diffraction pattern of Phase IV-C_6H_{12} at 250 K and 5 kbar as collected on the D2-B powder diffractometer at the ILL.

under nearly identical conditions shows significantly different relative intensities of some of the powder diffraction peak intensities suggesting that inaccuracies due to powder averaging may play an important role.

§1.4 Synchrotron x-ray diffraction studies of the metastable phase in C_6H_{12} [26]: Phase IV revisited

1.4.1 Motivation

As stated in the previous sections, the majority of the existing evidence suggests that the model proposed for the full crystal structure of cyclohexane-IV is appropriate. Where discrepancies exist in the fit to the diffraction data, they are attributed to errors in the powder averaging and not to the structural model which is consistent with minimum energy considerations. In the section which follows, further support of the proposed structural model for this high-pressure phase is provided by an unexpected result from a synchrotron powder x-ray diffraction study of the metastable phase at low temperature and ambient pressure.

1.4.2 Advantages of a synchrotron source

Synchrotron radiation has many advantages over laboratory-based x-ray sources. These include far higher intensity and tunable wavelength. These advantages will be discussed in greater detail when x-ray diffraction experiments on samples held in high pressure cells are considered in the following chapters. These considerations are of particular relevance when studies of weakly scattering organic materials are concerned.

1.4.3 Experimental arrangement

The low temperature x-ray diffraction measurements were performed on the Powder Diffraction Station (9.1) of the Daresbury Synchrotron Radiation Source (SRS). An Oxford Instruments (CF1238) continuous flow cryostat with the capability for in-situ sample rotation during data collection was used to improve powder averaging. The sample was loaded in a nitrogen atmosphere to avoid condensation and ice formation on the capilliary. After the temperature had stabilized to 77 K +/- 1K, a powder pattern was collected using a 2-θ stepsize of 0.01°.

1.4.4 Results and Discussion: constrained refinement of multiple phases (Cyclohexane IV and II)

The powder profile of the quenched sample was collected at 77 K and examination of the peak positions indicated that the sample had undergone a transition to a mixture of a minority component of the low temperature Phase II and a dominant component of the high-pressure Phase IV. The d-spacings of this majority Phase IV component were, in fact, in good agreement with those reported by Renaud and Fourme in their original observation of the metastable phase. Based on this evidence it is concluded that the metastable phase of cyclohexane is, in fact, the high-pressure form - Phase IV.

Since mixed phases containing both Phase II and IV were formed upon cooling, in order for a reliable structural refinement of the diffraction pattern to be performed a two component Rietveld refinement was required. It is often helpful to restrict certain structural parameters to a fixed value or between fixed values. Refinements which incorporate such restrictions are called constrained refinements and there are two types. A "strict" constraint maintains a fixed relationship between structural parameters whereas a chemical constraint places a restriction on the structural parameters so that they remain within a specified range. This type of constraint has an associated user-supplied weight which determines the contribution of the constraint to the least-squares equations.

The standard Daresbury Laboratory Rietveld refinement package MPROF was used for the data analysis. Initial input parameters for the phase II atomic positions were taken from the work of Kahn et al (1973) and those for the Phase IV component were taken from the refined atomic positions yielded by the neutron diffraction results described in the previous section. Chemical constraints were applied to bond angles so as to favour 110° imposed by tetrahedral symmetry and C-C and H-C bond lengths were constrained to favour values of 1.53Å and 1.07Å, respectively. The results of this refinement are shown in figure 1.12. Resulting R-factors were $R_I = 7.88\%$, $R_{wp} = 18.84\%$ and $R_{exp} = 14.38$ and 43 parameters were used.

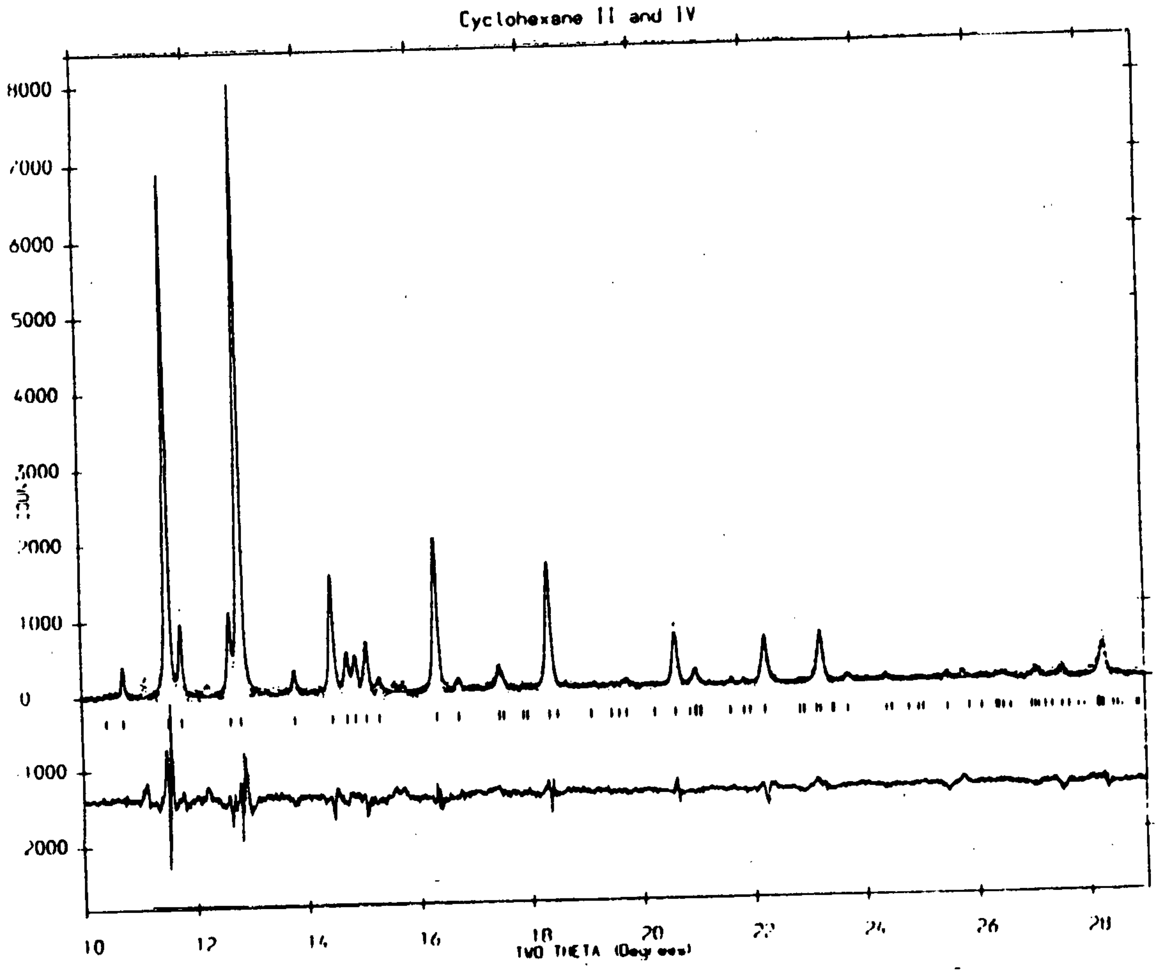

Figure 1.12 Two-component, chemically constrained Rietveld refinement of the powder diffraction profile of the metastable phase (primary) and Phase II (secondary) of C_6H_{12} at 77 K. The relative proportions of the two phases are 8:1 as deduced from the refinement scale factors. The improved fit to the x-ray diffraction pattern relative to that of the neutron results is attributed to the fact that the sample was rotated in the cryostat for the x-ray experiments to improve powder averaging statistics.

Table 1.5 Observed and calculated reflections from Phases II and IV. **-symbols indicate peaks due to ice on the capillary.

2Θ	2Θ cal	count	ph.	*hkl*	δ2Θ
10.729	10.734	2082	II	200	0.005
11.103	*****	1820			
11.534	11.529	7750	IV	110	-0.005
11.764	11.766	2500	II	-111	0.002
12.217	*****	1489			
12.641	12.640	2169	IV	-101	-0.001
12.828	12.831	8971	IV	011	0.003
13.798	13.792	1349	II	111	-0.006
14.467	14.466	2326	IV	101	-0.001
14.740	14.479	1489	IV	-111	-0.011
14.884	14.880	1506	II	002	-0.004
15.082	15.077	1451	IV	020	-0.005
15.291	15.302	1032	II	-202	0.011
16.326	16.328	2733	IV	111	0.002
16.734	16.726	779	II	-112	-0.008
17.447	17.456.	797	IV	120	0.009
18.345	18.350	2079	IV	021	0.005
20.614	20.612	1227	IV	-211	-0.002
20.981	20.984	541	II	220	0.003
21.610	21.598	414	II	400	-0.012
21.843	21.846	411	II	311	0.003
22.203	22.218	882	IV	012	0.015
23.216	23.213	953	IV	220	-0.003
23.691	23.694	367	II	-220	0.003
24.388	24.385	350	IV	130	-0.003
27.048	27.049	383	IV	131	0.001
27.532	27.531	374	IV	310	-0.001
28.256	28.269	850	IV	122	0.013

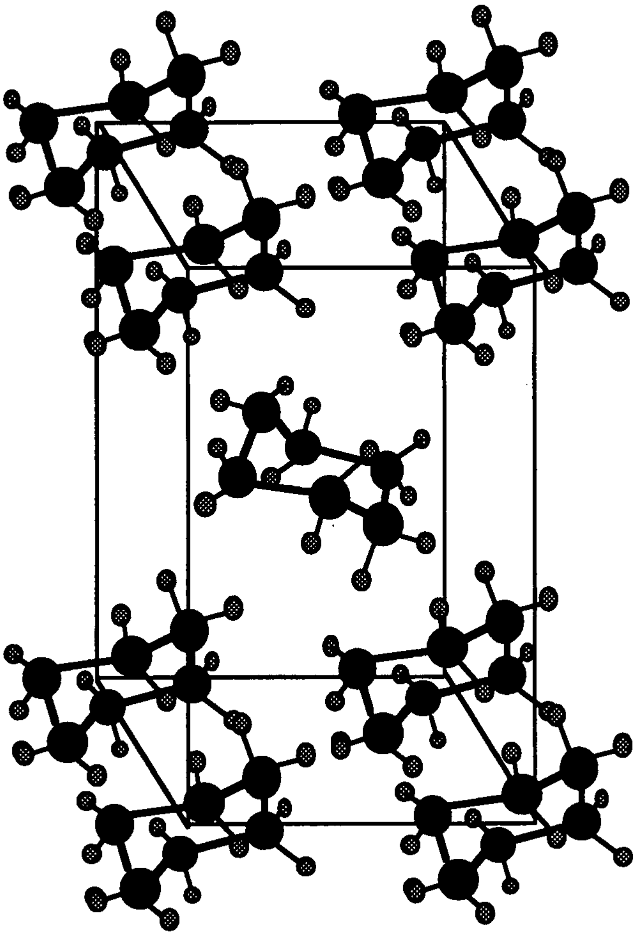

Figure 1.13 Representation of the crystal structure of Phase IV of cyclohexane - C_6H_{12} obtained from constrained Rietveld refinement of the neutron powder diffraction pattern at 5 kbar and 250 K at ILL.

Table 1.5 Atomic positional parameters for C_6H_{12} (Phases II and IV) as determined by constrained two-component Rietveld refinement of synchrotron powder x-ray diffraction data collected at 77 K and ambient pressure.

atom	phase	x	y	z
C1	IV	0.209(1)	-0.080(5)	0.066(4)
C2	IV	0.161(2)	0.032(2)	-0.164(3)
C3	IV	-0.018(2)	0.157(2)	-0.156(5)
H1	IV	0.266(8)	0.001(4)	0.214(5)
H2	IV	0.175(7)	-0.044(2)	-0.320(5)
H3	IV	0.003(8)	0.229(7)	0.009(6)
H4	IV	0.321(8)	-0.177(9)	0.038(8)
H5	IV	0.263(9)	0.142(6)	-0.153(6)
H6	IV	-0.031(8)	0.244(9)	-0.039(6)
C1	II	0.211(2)	0.461(3)	0.019(2)
C2	II	0.351(2)	0.400(4)	0.102(2)
C3	II	0.379(1)	0.221(5)	-0.014(3)
H1	II	0.195(6)	0.530(2)	0.893(7)
H2	II	0.142(6)	0.684(4)	0.190(8)
H3	II	0.391(8)	0.355(5)	0.349(5)
H4	II	0.413(4)	0.524(5)	0.078(8)
H5	II	0.317(6)	0.282(6)	0.774(6)
H6	II	0.488(4)	0.211(3)	0.020(9)

Table 1.7 Instrumental parameters for the two-component refinement of C_6H_{12}. The refinement was performed over the 2-Θ range of 10° to 35°. Estimated standard deviations are shown in parentheses.

parameter	value
offset (°)	-0.034 (2)
u (°)^2	-0.4166 (4)
v (°)^2	-0.2105 (2)
w (°)^2	-0.0128 (1)
Scale (IV)	0.234 (2)
Scale(II)	0.032 (1)

Table 1.8 unit cell dimensions for the C_6H_{12} as determined by constrained Rietveld refinement of Phases II and IV at 77 K and ambient pressure. Estimated standard deviations are shown in parentheses.

Parameter	Phase II	Phase IV
a (Å)	11.302(7)	6.637(8)
b (Å)	6.419(1)	7.635(2)
c (Å)	8.172(5)	5.585(6)
β (°)	108.78(7)	97.77(8)
volume (Å^3)	561.3	280.40

1.4.5 Remarks

A detailed study of pressure and temperature-induced polymorphism in the simple molecular crystal cyclohexane has been presented. Several experimental techniques have been used including light scattering, neutron and x-ray diffraction with substantial input to the analysis being drawn from the conclusions based on minimum energy considerations on molecular orientation.

Light scattering methods have revealed a clear sequence of three solid-solid pressure-induced structural phase transitions in both the deuterated and hydrogenated compounds suggesting that deuteration does not affect phase diagram topology but that the relative stability fields of the the phases in each compound are altered. A previously unreported pressure-induced phase, Phase V, was also discovered during the course of this work but detailed structural information has not been obtained because the pressure range required for its formation and stability exceeds that which is routinely obtainable using neutron diffraction techniques.

It is found that Phase IV of cyclohexane can exist at ambient pressure if it is quenched rapidly from the liquid. This high-pressure polymorph has also been identified as what had previously been referred to as the metastable phase of cyclohexane. Phase IV can also exist at ambient pressure by following another path in the phase diagram: it can first be induced at high-pressure and then cooled slowly and depressurised. Phase IV is then observed to persist down to ambient pressure with no reconversion to Phase II.

Several points regarding the nature of Phases II and IV can be inferred from the results of these studies. First, the kinetic pathway for conversion between these two phases must encounter a large energy barrier although the total energies of the two phases is apparently similar. This conclusion is motivated by the fact that conversion from IV to II requires input of thermal activation energy (if phase IV is formed at high pressure) but that upon quenching, Phases II and IV can coexist with almost identical molecular volumes. This type of consideration will be of importance in motivating much of the work in Chapters 5 and 6 when the nature of pressure-induced phase transitions in tetrahedral semiconductors is explored.

It is also possible to investigate the likely relationships between phases II and IV. A more detailed account of the relationship can be found in the work of Wilding, Crain, Hatton and Bushnell-Wye [27]. The proposed relationship is described in matrix form as

$$\begin{Bmatrix} x/a' \\ y/b' \\ x/c' \end{Bmatrix}_{\text{Phase II}} = \begin{Bmatrix} 3/4 \\ 3/4 \\ 0 \end{Bmatrix} + \begin{Bmatrix} 0 & -1/2 & -1/2 \\ -1 & 0 & 0 \\ 0 & 1/2 & -1/2 \end{Bmatrix} \begin{Bmatrix} x/a \\ y/b \\ x/c \end{Bmatrix}_{\text{Phase IV}}$$

In order to effect the IV-II transition, the angle α of phase IV must decrease substantially from 90° to approximately 77°. The corresponding β angle must decrease from 97.7° to 90°. As considerable molecular reorganisation is required, it is not surprising that a IV to II conversion was not observed at low temperature.

§1.5 Conclusions

In addition to serving as an introduction to spectroscopic and diffraction techniques at high-pressure the major results of the present chapter are summarized as follows. In regard to the spectroscopic results the pressure-induced Phase IV of cyclohexane exists in both C_6H_{12} and C_6D_{12}. Pressure increase on Phase IV does not bring about a transformation to the low temperature phase II was previously suggested but instead induces a new and previously unreported high-pressure phase - Phase V. In general the phase diagram topologies of C_6H_{12} and C_6D_{12} are found to be equivalent although the stability fields of each phase are slightly different. Regarding the results of the structural studies: the metastable phase of C_6H_{12} formed by quenching from the liquid or Phase I is found to be structurally equivalent to the high-pressure phase IV.

---

[1] A.J. Pertsin and A.I. Kitaigorodsky The Atom-Atom Potential Method Springer Verlag (Springer Series in Chemical Physics 43).

[2] A.I. Kitaigorodsky, *Physical Chemistry*, **29**, "Molecular Crystals and Molecules", Academic Press, New York (1973).

[3] D. Cavagnat, M.P.Roberts, R.M. Cavagnat and S. Vahedir-Banisaeid *J. Phys. Chem.* **95** (1991) 134.

[4] G.Dosseh, B. Fressigné, B. Rousseau N.B. Wilding and A.H. Fuchs. *J. Chem. Phys.* **87** (1990) 1821.

[5] A. Würflinger and G.M. Schneider *Ber. Bunsenges. Phys. Chem.* **77** (1973) 121: a review of calorimitry studies on molecular and plastic crystals at high pressure.

[6] E.R. Andrew and R.G. Eades *Proc. Roy. Soc.* **A216** (1953) 398.

[7] R. Kahn, R. Fourme, D. André and M. Renaud *Acta Cryst. B* **29** (1973) 131.

[8] M. Renaud and R. Fourme *J. Chim. Phys.* **62** (1966) 27.

[9] G. Burns and F.H. Dacol *Solid State Commun.* **51** (1984) 773.

[10] M. Ito *Spectrochem. Acta.* **21** (1965) 2063.

[11] L. Schulte and A. Würflinger *J. Chem. Thermodyn.* **19** (1987) 363.

[12] R. Sandrock and G.M. Schneider *Ber. Bunsenges Phys. Chem.* **87** (1975) 197.

[13] N.B. Wilding, P.D. Hatton and G.S. Pawley *Acta Cryst. B* **47** (1991) 797.

[14] L. Shulte and A. Würflinger *J. Chem. Thermodyn.* **19** (1987) 363.

[15] T. Shimanouchi, *Natnl. Stand. Ref. Data Serv.* **58** 1967.

[16] J. Haines and D.F.R. Gilson *J. Phys. Chem.* **93** (1989) 7920.

[17] J. Crain, W. C-K. Poon, A. Cairns-Smith and P. D. Hatton *J. Phys. Chem.* **96** (1992) 8168.

[18] H.M. Rietveld *J. Appl. Cryst.* **2** (1969) 65.

[19] H.M. Rietveld *Acta Cryst.* **20** (1966) 508.

[20] E. Baharie and G.S. Pawley *J. Appl. Cryst.* **10** (1977) 465.

[21] A.N. Fitch and A.D. Murray PDPL (Powder Diffraction Program Library): An integrated powder diffraction library. In preparation.

[22] D.E. Williams *J. Chem. Phys.* **47** (1967) 4680.

[23] No Buckingham potential parameters could be found in the literature which were appropriate for C-D bonds.

[24] G.S. Pawley *J. Appl. Cryst.* **14** (1981) 357.

[25] G.S. Pawley *J. Appl. Cryst.* **13** (1980) 630.

[26] This work was performed through and with the assistance of the Daresbury Laboratory Powder Diffraction Service.

[27] N.B. Wilding, J. Crain, P.D. Hatton and G. Bushnell-Wye *Acta Cryst. B* **48** 1993 (in press).

CHAPTER 2

DENSITY-FUNCTIONAL TOTAL ENERGY CALCULATIONS FOR PERIODIC SOLIDS: THEORETICAL PRELIMINARIES

§2.1 General formulation and the Hohenberg-Kohn theorem

Throughout this chapter an attempt will be made to review in detail only those aspects of the methodologies and theories which are of direct relevance to the calculations presented later. The discussion will be confined to density functional methods within the context of *ab initio* total energy calculations for solids although the fundamental tenets apply to a diverse range of topics in theoretical physics. For the solid state problem, the "density functional principle" states first, that the many-body groundstate is a *unique* functional of the groundstate charge density. And secondly, the groundstate charge density is that which minimizes the total energy functional. This proposal was put forward and proven in 1964 by Hohenberg, Kohn and Sham [1,2]. The standard simple proof that the groundstate energy is a unique functional of the charge density begins with the supposition that there exist two potentials which lead (via the Schrödinger equation) to different manybody wavefunctions which give rise to identical charge distributions. The requirement that the groundstate energy be a minimum leads to a contradiction that the charge densities arising from these states are identical. Formally, the proof proceeds as follows.

Define E and E' to be the eigenenergies of states $|S\rangle$ and $|S'\rangle$, respectively when operated on by the Hamiltonians H and H'. These Hamiltonians are assumed to differ only in their respective interaction terms V and V'. Then $E = \langle S|H|S\rangle$ and $E'=\langle S'|H'|S'\rangle$. According to the minimum principle for the groundstate energy of any Hamiltonian it follows that $E < \langle S'|H|S'\rangle$. This states simply that the energy obtained by evaluating the expectation value of H (for which E is the groundstate energy) in any state other than $|S\rangle$ must be larger than E. Since H and H' differ only in their interaction terms, it is possible to write $H = H' - V' + V$. This then leads to the statement that

$$E < \langle S'| H' - V' + V|S'\rangle = E' + \langle S'|V - V'|S'\rangle \qquad (2.1.1)$$

which gives

$$E < E' + \int \rho(\mathbf{r})[v(\mathbf{r}) - v'(\mathbf{r})]d\mathbf{r} \qquad (2.1.2)$$

This argument, however, can be applied with equal validity in the "primed" case which leads to

$$E' < E + \int \rho(\mathbf{r})[v'(\mathbf{r}) - v(\mathbf{r})]d\mathbf{r} \qquad (2.1.3)$$

There would be no contradictions in this formulation were it not for the initial assertion that the two charge densities which appear in the last two equations be identical. If they are identical then addition of equations (2.1.2) and (2.1.3) give an inconsistent inequality $E+E' < E'+E$ suggesting that the two charge densities must be different and that the Hamiltonian (and total groundstate energy) must be unique functionals of $\rho(\mathbf{r})$. The proof that the groundstate energy is a minimum at the correct $\rho(\mathbf{r})$ follows from the general quantum mechanical principle that the groundstate energy is a minimum for the correct wavefunction.

What is sought is not only a plausible and workable form for the energy functional but also the stationarity condition on the functional imposed by the Hohenberg-Kohn-Sham requirement of a unique charge density $\rho(\mathbf{r})$, which minimizes the energy functional. This will be treated in the next section.

2.2 The Kohn-Sham equations and the Local Density Approximation

For the purposes of actual calculations a number of drastic assumptions must be made in order to render this problem tractable. These include the adiabatic and pseudopotential approximations both of which will be discussed in later sections. Even within the framework of these assumptions, a formidable many-body problem remains. In this section an approach is outlined which reduces this to a more manageable single particle model. First, the terms in the energy functional F will be expressed as

$$F[\rho(\mathbf{r})] = T[\rho(\mathbf{r})] + \int d\mathbf{r}\, V(\mathbf{r})\rho(\mathbf{r}) + \int \frac{\rho(\mathbf{r})\rho(\mathbf{r}')}{|\mathbf{r} - \mathbf{r}'|} d\mathbf{r}d\mathbf{r}' + \tag{2.2.1}$$

$$E_{xc}[\rho(\mathbf{r})] + \sum_{I\,I'} \frac{Z_I Z_{I'}}{|\mathbf{R}_I - \mathbf{R}_{I'}|}$$

where $\rho(\mathbf{r})$ is an arbitrary charge density. This gives an explicit form for the functional which must be stationary with respect to variation of the ground state charge density. The terms in the functional represent the kinetic energy, the contribution from electron-ion interaction, the Hartree energy, many-body exchange and correlation and the Madelung (electrostatic) energy describing ion-ion interaction. A formal variation of the charge density can be performed which leads to

$$\int \delta\rho(\mathbf{r})\{\frac{\delta T[\rho(\mathbf{r})]}{\delta\rho(\mathbf{r})} + V(\mathbf{r}) + \int \frac{\rho(\mathbf{r}')}{|\mathbf{r} - \mathbf{r}'|} d\mathbf{r}' + \frac{E_{xc}[\rho(\mathbf{r})]}{\delta\rho(\mathbf{r})}\}d\mathbf{r} = 0 \tag{2.2.2}$$

which implies

$$\frac{\delta T[\rho(\mathbf{r})]}{\delta\rho(\mathbf{r})} + V(\mathbf{r}) + \int \frac{\rho(\mathbf{r}')}{|\mathbf{r} - \mathbf{r}'|} d\mathbf{r}' + \frac{E_{xc}[\rho(\mathbf{r})]}{\delta\rho(\mathbf{r})} = \mu \tag{2.2.3}$$

where μ is a constant Lagrange multiplier which constrains the number of particles to be constant and plays the role of the chemical potential. The form for the particle number constraint is

$$\int \delta\rho(\mathbf{r})\, d\mathbf{r} = 0 \tag{2.2.4}$$

Straightforward application of (2.2.3) is however not possible as there are still several *practical* difficulties with the present formulation. Firstly, one needs a method for self-consistent determination of $\rho(\mathbf{r})$ to minimize $F[\rho(\mathbf{r})]$. Also a means of calculating or a suitable approximation to the nonlocal $E_{xc}[\rho(\mathbf{r})]$ functional is required. In addition the kinetic energy functional is also undetermined. The difficulties with the kinetic energy functional can be substantially simplified if the problem is recast in terms of an assembly of non-interacting particles moving in an effective potential given by the sum of the last three terms on the LHS of (2.2.3). The wavefunctions, $\psi_i(\mathbf{r})$, of these non-interacting particles are introduced such that the charge density derived from them is given by

$$\sum_{i=1}^{N} |\psi_i(\mathbf{r})|^2 = \rho(\mathbf{r}) \tag{2.2.5}$$

The point is that density variation can now be carried out indirectly through variation of these single particle orbitals. The single particle kinetic energy operator then takes its usual form

$$T[\rho(\mathbf{r})] = \int \sum_{i=1}^{N} \psi^*{}_i(\mathbf{r})\,(-\nabla^2)\,\psi_i(\mathbf{r})\;d\mathbf{r} \tag{2.2.6}$$

and within this single-particle formalism the stationarity condition on $F[\rho(\mathbf{r})]$ yields the following equation which the groundstate eigenfunctions of the fictitious non-interacting particles must satisfy, namely,

$$(-\nabla^2 + V(\mathbf{r}) + \frac{1}{2}\int \frac{\rho(\mathbf{r}')}{|\mathbf{r} - \mathbf{r}'|}\,d\mathbf{r}' + \mu_{xc}[\rho(\mathbf{r})])\,|\psi_i^{K\text{-}S}(\mathbf{r})> = \varepsilon_i\,|\psi_i^{K\text{-}S}(\mathbf{r})> \tag{2.2.7}$$

which is traditionally known as the Kohn-Sham equation. $\mu_{xc}[\rho(\mathbf{r})]$ is the exchange-correlation potential defined by $\mu_{xc}[\rho(\mathbf{r})] = \delta E_{xc}[\rho(\mathbf{r})]/\delta\rho(\mathbf{r})$. Once the eigenvalue problem has been solved, $T[\rho(\mathbf{r})]$ can be evaluated as follows, if desired:

$$T[\rho(\mathbf{r})] = \sum_i <\psi_i^{K\text{-}S}(\mathbf{r})\,|\,\varepsilon_i - V_{ks}[\rho(\mathbf{r})]\,|\,\psi_i^{K\text{-}S}(\mathbf{r})> \tag{2.2.8}$$

$V_{ks}[\rho(\mathbf{r})]$ represents the Kohn-Sham potential including all the electron interaction effects.

The form for the exchange and correlation contribution is still yet to be specified and can be non-local even in the single-particle picture. However, for the remainder of the chapter a most crude but remarkably successful approximation will be made. That is, all the electron-electron interaction and self-avoiding behaviour will be approximated by a function which depends only on the local electronic charge density. This assumption constitutes the *Local Density Approximation* (LDA) and there exist several prescriptions for constructing the required local exchange-correlation energy density [3,4,5] which are based on parameterisations of the exchange-correlation energy of a homogeneous electron gas [6]. Justification of the assertion that a well-defined single particle potential (which includes the effects of exchange and correlation) actually exists has its origins in suitable generalisations of Thomas-Fermi theory of the many-body electron groundstate [7].

In summary, the Kohn-Sham proposal results in a set of *single particle* equations for the new variational parameters which are now the wavefunctions of non-interacting electrons as opposed to the charge density. The minimum of the energy functional with respect to variation of the wavefunctions corresponds (subject to an orthonormality constraint) to a point on the Born-Oppenheimer potential energy surface. The issue of the Adiabatic Approximation and how it is incorporated in calculations will be deferred to a future section in this chapter when density functional dynamics is introduced.

As the operator on the LHS of the Kohn-Sham equation contains terms such as the Hartree and exchange-correlation contributions which depend explicitly on the (local) charge density and therefore implicitly on the wavefunctions, the Kohn-Sham equations can only be solved self-consistently. In other words, the Kohn-Sham eigenstates must be determined such that the Hartree and exchange-correlation terms in the Hamiltonian are the same as those produced by the charge density generated by the eigenstates. In general, the solution to the Kohn-Sham equation requires a computationally expensive series of multiple matrix diagonalizations and updates to the Hamiltonian. As a result, pseudopotential methods are often impractical when used for large systems with matrix diagonalisation procedures. The computational cost of matrix diagonalisation scales as the third power of the number of plane waves in the basis set and the memory requirement for storage of the Hamiltonian matrix increases as the square of this number. The implication of this is that the system size treatable by conventional techniques [8] is severely limited by the computational costs and alternative approaches must be sought if calculations on large systems are required.

§2.3 The Car-Parrinello Lagrangian

In the approach advanced in 1985 by Car and Parrinello [9] the total energy functional is minimized with respect to variation of the expansion coefficients of the wavefunctions (which represent the electronic degrees of freedom) and the ionic positions. It will be shown that the Car-Parrinello approach leads to the prospect of simultaneously arriving at a self-consistent solution of the Kohn-Sham equation, while performing ionic and electronic relaxation. In this framework, the electronic and ionic degrees of freedom are treated simultaneously and appear as the arguments of the Car-Parrinello total energy functional as follows

$$F^{C\text{-}P}[\{\psi_i(\mathbf{r},t)\},\{\mathbf{R}_I(\mathbf{r},t)\}] =$$

$$\sum_i \int \psi^*{}_i(\mathbf{r},t)(-\nabla^2)\psi_i(\mathbf{r},t)\ d\mathbf{r} + \int d\mathbf{r}\ V(\mathbf{r})\rho(\mathbf{r}) + \int \frac{\rho(\mathbf{r})\rho(\mathbf{r}')}{|\mathbf{r} - \mathbf{r}'|}\, d\mathbf{r}d\mathbf{r}' \qquad (2.3.1)$$

$$+ \sum_{I\,I'} \frac{Z_I Z_{I'}}{|\mathbf{R}_I(\mathbf{r},t) - \mathbf{R}_{I'}(\mathbf{r},t)|} + E^{LDA}{}_{xc}[\rho(\mathbf{r})]$$

where a time dependence is introduced in anticipation of performing dynamics on wavefunctions and ionic positions. A Lagrangian which governs the dynamics of the $\{\psi_i(\mathbf{r},t)\}$ and $\{\mathbf{R}_I(\mathbf{r},t)\}$ is therefore introduced:

$$L[\{\psi_i(\mathbf{r},t)\},\{\mathbf{R}_I(\mathbf{r},t)\}] =$$

$$\frac{\mu}{2}\Sigma_i <\dot{\psi}_i(\mathbf{r},t)\dot{\psi}_i(\mathbf{r},t)> + \frac{1}{2}\Sigma_I M_I|\dot{\mathbf{R}}_I(\mathbf{r},t)|^2 - F^{C\text{-}P}[\{\psi_i(\mathbf{r},t)\}; \{\mathbf{R}_I(\mathbf{r},t)\}] \qquad (2.3.2)$$

where the dot stands for time differentiation and M_I for the ionic mass.

The parameter denoted by μ is to be interpreted as a fictitious electronic mass designed to govern the electron wavefunction response to the influence of the dynamics generated by the Lagrangian. The dynamics of the unit cell can also be modeled by explicitly incorporating further arguments in the Lagrangian which generate more equations of motion for the unit cell degrees of freedom.

As in the classical mechanics analogue, the equations of motion (for the electronic and ionic degrees of freedom in this case) are determined by a stationarity condition on the Lagrangian. In the general case this leads to the Euler-Lagrange equations

$$\frac{d}{dt}\frac{\partial L[\{\psi_i(\mathbf{r},t)\};\{\mathbf{R}_I\}]}{\partial\{\dot{\psi}_i(\mathbf{r},t)\}]} = \frac{\partial L[\{\psi_i(\mathbf{r},t)\};\{\mathbf{R}_I\}]}{\partial\psi_i(\mathbf{r},t)} \qquad (2.3.3a)$$

$$\frac{d}{dt}\frac{\partial L[\{\psi_i(\mathbf{r},t)\};\{\mathbf{R}_I\}]}{\partial\{\dot{\mathbf{R}}_I(\mathbf{r},t)\}]} = \frac{\partial L[\{\psi_i(\mathbf{r},t)\};\{\mathbf{R}_I\}]}{\partial\mathbf{R}_I(\mathbf{r},t)} \qquad (2.3.3b)$$

which, for the Lagrangian considered above give the required equations of motion for the electronic wavefunctions and ions $\psi_i(\mathbf{r},t)$ and $\mathbf{R}_I$.

$$\mu\ddot{\psi}_i(\mathbf{r},t) = \Sigma_j\,\Lambda_{ij}\,\psi_i(\mathbf{r},t) - \frac{\delta F^{C\text{-}P}[\,\{\psi_i(\mathbf{r},t)\};\{\mathbf{R}_I\}\,]}{\delta\psi^*{}_i(\mathbf{r},t)} \qquad (2.3.4a)$$

$$M_I\,\ddot{\mathbf{R}}_I(t) = -\,\nabla_{\mathbf{R}_I} F^{C\text{-}P}[\,\{\psi_i(\mathbf{r},t)\};\ \{\mathbf{R}_I\}] \qquad (2.3.4b)$$

Where $\nabla_{\mathbf{R}_I} = \partial/\partial\mathbf{R}_I$. The $\psi_i(\mathbf{r},t)$ are not entirely independent but are, instead subject to the holonomic orthonormality constraints

$$\int\psi_i^*(\mathbf{r},t)\psi_i(\mathbf{r},t)\,d\mathbf{r} = \delta_{ij} \qquad (2.3.5)$$

This constraint is indicated in the equations of motion by the terms containing the factor of Λ_{ij} which play the role of Lagrange multipliers.

Indirect methods of solution

There exist several procedures for arriving at the true ground state electronic configuration, i.e. that which coincides with the minimum of the Kohn-Sham functional. First a method based on integration of the equations of motion is described. Although this method is not the one which will be used in the actual calculations a discussion of it is included because it illustrates important potential problems. The kinetic energy contribution to the Car-Parrinello Lagrangian is a result of the "motion" of the expansion coefficients of the basis states and the potential energy contribution is the Kohn-Sham functional. Some initial electronic configuration and velocity must be assumed in order to integrate the electronic equations of motion. A common choice, and the one adopted here, is to assume that the coefficients of the plane wave expansions are random numbers and that their initial velocities are zero. The fact that this initial configuration is different from the Kohn-Sham eigenstates implies that the energy functional is not minimized and that there is excess potential energy in the system. The extra potential energy due to the difference between the initial electronic configuration and the true ground state is distributed equally between the kinetic and potential energies of the expansion coefficients [10]. If the motion of the coefficients is damped thus reducing their kinetic energy, potential energy must be drawn out of the system and converted to kinetic energy as required by equipartition of energy. As the process of drawing the excess potential energy from the system via added damping continues, the expansion coefficients relax to those values which minimize the Kohn-Sham functional. When the velocities of the coefficients become zero, the process is said to have converged and the resulting electronic states are solutions of the Kohn-Sham Hamiltonian, arrived at without repeated matrix diagonalizations.

There is an important but subtle instability which can arise with this method which is related to the time evolution of the Kohn-Sham Hamiltonian. In order to maintain self-consistency, the Hamiltonian must evolve as the wavefunctions approach their stationary values. The Hartree term in the Hamiltonian, in addition to being proportional to $\rho(\mathbf{r})$ also exhibits a quadratic divergence for small reciprocal lattice vectors. This means that for only small changes in charge density which are required to maintain self-consistency at each timestep, very large changes in potential can result. The situation is particularly severe for long or large supercells as corresponding reciprocal lattice vectors can be very small. The required timestep to suppress such instabilities may, in some circumstances, be impracticably small [11].

Direct methods of solution: steepest descents and more advanced algorithms

Direct methods, in the context of these calculations, are those which, rather than integrate equations of motion, cast the problem in its most natural form (that of a complex optimisation procedure) and directly locate the minimum of the Kohn-Sham energy functional in the space of all the relevant degrees of freedom. The most obvious such method is based on the standard steepest descents algorithm in which search directions at given points on a hyper-surface are determined by the local gradient at those points. Although it seems to be the most natural algorithm, certain problems do arise which prevent it from being the method of choice. The degree to which problems are important depends on the nature of the hypersurface being considered but are in general due to the fact that subsequent steepest descents search directions are orthogonal to preceding ones, but this leads to an inefficient series of search vectors for particular surfaces.

An optimally efficient algorithm would require independence of search directions on preceding ones. This requirement is the motivation for the conjugate gradients [12] method in which search directions are constructed from linear combinations of the local gradient and the previous search vector. One of the attractive features of the conjugate gradients approach for this type of complex minimisation problem is that it is guaranteed to converge to the minimum of the energy surface in a finite number of iterations [13]. The minimisation of the Kohn-Sham energy functional is well suited to this approach but there is an important difference which is that Kohn-Sham problem is a constrained minimisation problem with the constraint being that orthogonality of wavefunctions is maintained at all times. The relevance of this constraint to the original Kohn-Sham formulation is considered briefly in the next section.

§2.4 Connection with the Kohn-Sham equations

It has been stated that the Car-Parrinello algorithm is a method for solution of the Kohn-Sham equation (2.2.7) but the connection between the equations of motion (2.3.4a) and the Kohn-Sham equation (2.2.7) is not immediately obvious. In fact there is a striking dissimilarity between the two formulations which is that the Kohn-Sham equation is an eigenvalue equation for the occupied groundstate levels whereas the equations of motion for the ψ_i are valid whether or not they coincide with the Kohn-Sham eigenstates. The connection manifests itself when the equations of motion are considered in the special case of equilibrium, ie where the forces on the electronic configuration vanish. Then equation (2.3.4a) reduces to

$$\frac{\delta F^{C\text{-}P}[\{\psi_i(\mathbf{r},t)\};\{\mathbf{R}_I\}]}{\delta\psi^*_i(\mathbf{r},t)} = \sum_j \Lambda_{ij}\psi_i(\mathbf{r},t)) \qquad (2.4.1)$$

The LHS can be rewritten as

$$\frac{\delta F^{C\text{-}P}[\{\psi_i(\mathbf{r},t)\};\{\mathbf{R}_I\}]}{\delta\psi^*_i(\mathbf{r},t)} = \{-\nabla^2 + V(\mathbf{r}) + \int \frac{\rho(\mathbf{r}')}{|\mathbf{r}-\mathbf{r}'|}\,d\mathbf{r}' \qquad (2.4.2)$$

$$+ \mu^{LDA}{}_{xc}[\rho(\mathbf{r})]\}\psi_i(\mathbf{r},t)$$

which is identical to the LHS of the Kohn-Sham equation. The entire equation of motion formulation is thus equivalent to the Kohn-Sham eigenvalue problem if the eigenvalues of the Lagrange multiplier matrix Λ (for orthogonality and normalization constraints) are equal to the energies of the occupied Kohn-Sham orbitals.

§2.5 The Adiabatic Approximation: separation of quantum and classical mechanics

Two approximations will be made in the sections which follow. The first is the "frozen-core" approximation according to which it is assumed that in the formation of a solid, the character of inner-shell electron states differ negligibly from that of the corresponding free atom. The second is the adiabatic approximation which will be of central importance in simulation of ion dynamics and will be reviewed in this section in the context of total energy calculations. It is motivated by the observation that due to the great mass difference between electrons and nuclei, when a system of ions is moved, the accompanying electronic system can be assumed to relax to its ground state immediately. This allows for the possibility of separating the nuclear and electronic motions because the nucleus is static over the timescale of electronic motion. For all nuclear positions, there corresponds a unique many-body electronic ground state which defines a Born-Oppenheimer hyper-surface in $\{\psi_i\text{-}\mathbf{R}_I\}$ space. Due to the negligible overlap of nuclear wavefunctions, the dynamics of the ions can be treated by classical means because they constitute a system of distinguishable particles but the electronic wavefunction dynamics are inherently quantum-mechanical.

§2.6 Choice of basis set: plane waves

It is a feature of almost all *ab initio* band-structural or total energy calculations that the wavefunctions are represented as expansions in some convenient set of basis functions. Usually, the expansion is in terms of a plane wave basis set or in spherical harmonics with some techniques such as the Augmented Plane Wave (APW) method mixing both types depending on the assumed nature of the wavefunction in various regions in the unit cell. It should be stressed that in the discussions up to this point the basis set in which the variational wavefunctions are expressed has been completely general and, indeed no particular form is required in principle. For the pseudopotential calculations a plane wave basis set is chosen to represent the valence electron wavefunctions. An expansion of the wavefunctions in such a basis is independent of the crystal structure and it is expected that the valence charge density can be described to the same degree of accuracy for different crystal environments as is required for reliable total energy comparisons. In this expansion, the wavefunction is expressed simply as

$$\varphi(\mathbf{k},\mathbf{r}) = \Omega^{-1/2}\sum_{i} b_i(\mathbf{k} + \mathbf{G})\mathrm{Exp}[i(\mathbf{k}+\mathbf{G})\bullet\mathbf{r}] \qquad (2.6.1)$$

where Ω is the unit cell volume and $\mathbf{G}$ are the set of reciprocal lattice vectors. In addition to general simplicity, further advantages of a plane wave basis set are discussed in the context of ionic relaxation in subsequent sections. The number of plane waves included in the basis set must be sufficiently large so as to ensure accurate description of the valence states and a reasonably well converged total energy. Including more plane waves than are necessary for convergence simply treats the frozen core more accurately and increases the computational cost without benefit of an improved description of the valence states. The important point is that it is worth the effort of determining how small a basis set is necessary to achieve the desired convergence. In fact, it is even possible to use a basis set which is known to be slightly too small but to then apply a correction to the resulting total energy [14]. This straightforward correction will not be addressed further as it is not applied in any of the subsequent calculations.

§2.7 Pseudopotentials and their generation

2.7.1 Background

The motivation for the pseudopotential approach can be arrived at in a number of ways. The qualitative line of reasoning is based on the observation that, for several materials, the energy bands are not too dissimilar to free-electron bands. It is well known however, that electronic wavefunctions are, in fact, very different from plane wave eigenstates of a free electron Hamiltonian in the core regions of atoms even though the perturbation of the bands due to the ions is often quite small. The notion of a pseudopotential serves to provide an explanation for this apparently paradoxical situation by focusing attention on the effect of the lattice potential on the valence band structure. The pseudopotential, therefore is designed to represent the influence that a valence electron experiences assuming that the core electrons do not respond to any bonding effects. Within this approximation, there exists the possibility that many properties such as crystal structure, and optical spectra among others can be calculated without paying any detailed attention to the core electrons. The fact that the bonding electrons in a solid are nearly free suggests that the pseudopotential describing the valence electron-ion interaction is small compared to the Coulombic potential of a charged nucleus and that some type of cancellation of the strong electrostatic attraction exists. The cancellation is due to the effect of the Pauli principle which serves to exclude the valence electrons from the core region. This force nearly cancels the strongly attractive core potential.

The origin of a pseudopotential as a viable and possibly tractable approach to electronic structure calculations in solids can be perhaps best illustrated in the context of the orthogonalized plane wave (OPW) [15] method [16]. According to this approach the valence electron wavefunctions must be orthogonal to those of the core electrons. Expressed as vectors in Hilbert space this implies that the valence state vectors must have no projection on the core states. The situation can be expressed simply as follows:

$$| \psi >^{opw} = | \varphi > - \Sigma_c | c > < c | \varphi > \qquad (2.7.1)$$

where $|c>$ is a core state, $|\varphi>$ is a valence state (plane wave) and $|\psi>^{opw}$ is traditionally called an orthogonalized plane wave. The pseudopotential approximation is motivated by consideration of the form of the Hamiltonian operator in an OPW basis as shown in the following brief calculation.

$$H|\psi>^{opw} = H\{|\varphi> - \Sigma_c |c><c|\varphi> \} = E|\psi>^{opw}; \quad \text{where } H = \nabla^2 + V(r) \tag{2.7.2}$$

$$(\nabla^2 + V(\mathbf{r}))\{|\varphi> - \Sigma_c |c><c|\varphi> \} = E|\psi>^{opw} \tag{2.7.3}$$

$$\nabla^2|\varphi> + V(\mathbf{r})|\varphi> - \Sigma_c E_c|c><c|\varphi> = E\{|\varphi> - \Sigma_c |c><c|\varphi> \} \tag{2.7.4}$$

$$\nabla^2|\varphi> + V(\mathbf{r})|\varphi> + \Sigma_c(E - E_c)|c><c|\varphi> = E|\varphi> \tag{2.7.5}$$

$$\nabla^2|\varphi> + (V(\mathbf{r}) + \Sigma_c(E - E_c)|c><c|)|\varphi> = E|\varphi> \tag{2.7.6}$$

The form of expression (2.7.6) is equivalent to that of Equation (2.7.2) if the potential is redefined as $\Gamma = (V(\mathbf{r}) + \Sigma_c(E - E_c)|c><c|)$. The first term comprising Γ is attractive and the second corresponds to a repulsive operator. The "pseudo" wavefunction involved in equation (2.7.6) is that for a (pseudo)electron experiencing an influence only from the weak pseudopotential. Since the application of the resulting pseudopotential will be to solid state problems it is often expressed as a superposition of potentials centred at the crystalline lattice sites indexed by direct lattice vectors $\mathbf{R}_I$.

2.7.2 Generation: norm-conservation

It must be stressed that a pseudopotential is not something which is unique and as a result several different methods exist for calculating them. There are, however, simple and well-defined criteria any pseudopotential must satisfy [17,18,19,20]. These requirements are as follows:

For general pseudopotentials

1) A reasonable pseudopotential must produce correct structural (equilibrium lattice constants and elastic properties) and spectral properties of the valence electrons.

2) The pseudopotential must also remain valid over a range of crystalline environments i.e. exhibit transferability.

3) It must be calculationally efficient. (See next section on non-locality).

For *ab initio* pseudopotentials

1) pseudo-wavefunctions generate the same eigenvalues as atomic wavefunctions.

2) The first two derivatives of the pseudo-wavefunctions are continuous at the core radius.

3) The core charge from the pseudo-wavefunctions ($\int_{\text{core}} \Psi^*\Psi \mathrm{d}r$) is the same as that due to the atomic wavefunctions. This is the requirement of norm-conservation.

The notion of norm-conserving pseudopotentials arises both because of charge conservation and because there exists an important relation between the first energy derivative of the pseudowavefunction evaluated at a distance R from the nucleus and the integrated charge density within a sphere defined by radius R and centred on the nucleus [21]. This is expressed as

$$-2\pi \left[(r\psi)^2 \frac{d}{dE}\frac{d}{dr}\ln\psi\right]\Big|_{r=R} = 4\pi\int_0^R (\psi r)^2 dr \qquad (2.7.7)$$

The significance of this result is that if two potentials have the same eigenvalue spectrum and the same integrated charge density within a sphere of radius R, then not only will their scattering properties (phase shifts) be identical but the linear energy variation of these properties around E (at R) will also be equal. In the present context this means that if norm-conservation is included as a supplementary condition then the full potential and the pseudopotential will exhibit the same first order energy variation and transferability to different environments will be enhanced.

According to standard methods for pseudopotential generation, the all-electron eigenvalues and eigenfunctions are determined for an atom using $(\nabla^2 + V)\phi_l = \varepsilon_l \phi_l$. The resulting eigenfunctions are back-substituted in to the Schrödinger equation having a parameterised potential function of the form $V_l = \mathrm{Exp}[\{ar^4+br^3+cr^2 + d\}]$ (for $r < r_c$). The parameters (a,b,c,d) are determined by the above conditions. The pseudopotential then leads to new eigenstates ϕ_l^{ps} which are solutions of $(\nabla^2 + V_l)\phi_l^{ps} = \varepsilon_l \phi_l^{ps}$.

There are a vast number of different techniques and variants on the above method which also generate suitable pseudopotentials. One of the most recent attempts to systematise generation of optimized non-local *ab initio* pseudopotentials has been given by Lin *et al* [22].

2.7.3 Non-local pseudopotentials and Klienman-Bylander projectors

Generally, electrons having differing values of l , the orbital angular momentum quantum number, will experience different influences from the core and a proper description of these electrons requires a distinct pseudopotential for each value of l. Pseudopotentials which depend on l are called non-local and it will be these types which will be used in all pseudopotential calculations described in subsequent chapters. In the following section (and Appendix A) some of the computational difficulties associated with non-local pseudopotentials are discussed and one procedure (due to Klienman and Bylander, 1982) [23] for circumventing them is outlined.

The main complication associated with non-locality of a pseudopotential that its matrix elements in a plane wave basis are not simply functions of the difference of two reciprocal lattice vectors. This implies that the matrix elements require evaluation of a non-separable sum over different reciprocal lattice vectors. In order to illustrate how this comes about it is necessary first to understand how an angular momentum can be associated to an electron when its wavefunction is expanded in a plane wave basis which has no explicit dependence on l. Although the pseudopotential is diagonal in the angular momentum representation of the core states the same is not true for the valence state wavefunctions of the solid. The pseudopotential can be separated into a sum of terms with each term corresponding to s, p, d etc... symmetry. The most general nonlocal pseudopotential operator has the function of decomposing the pseudo-wavefunction into spherical harmonics and then acting with the appropriate nonlocal potential on each such decomposition. One general form of such an operator for a single atom is [24]

$$V(\mathbf{r}) = \sum_{lm} |Y_{lm}\rangle V_l(\mathbf{r}) \langle Y_{lm}| = \sum_{l} V_l(\mathbf{r})\, P_l \tag{2.7.8}$$

The pseudopotential can be decomposed into local and nonlocal terms:

$$V(\mathbf{r}) = V^{loc}(\mathbf{r}) + \sum_{l} (V_l(\mathbf{r}) - V^{loc}(\mathbf{r}))P_l = V^{loc}(\mathbf{r}) + \delta V(\mathbf{r}) \tag{2.7.9}$$

Where P_l is a projection operator which selects angular momentum l and $\delta V(\mathbf{r})$ is the nonlocal pseudopotential. The computational difficulties which arise from this description are briefly described next. The crystal potential, $V^{xtal}(\mathbf{r})$, that the electrons experience due to the presence of the ions is found by placing an ionic pseudopotential for each ion species at every lattice site occupied by that species of ion. The crystal symmetry enters the problem through the structure factor which has the function of determining the locations of ions in the unit cell. $V^{xtal}(\mathbf{G})$ is therefore given by

$$V^{xtal}(\mathbf{G}\text{-}\mathbf{G}') = \sum_{s} S_s(\mathbf{G}\text{-}\mathbf{G}')V(\mathbf{G}\text{-}\mathbf{G}') \tag{2.7.10a}$$

where the sum on s runs over all the species of ion in the unit cell [25] and $V(\mathbf{G})$ is the Fourier transform of the pseudopotential. $S_s(\mathbf{G})$ is the structure factor for species s and is given by

$$S_s(\mathbf{G}\text{-}\mathbf{G}') = \sum_{I} \mathrm{Exp}(i(\mathbf{G}\text{-}\mathbf{G}')\bullet\mathbf{R}_I) \tag{2.7.10b}$$

Where the sum is taken over the positions I of atoms of species, s, in the unit cell. In a total energy calculation terms of the form

$$E_{el\text{-}core} = \sum_{lm} \sum_{\mathbf{G}\mathbf{G}'} \langle\Psi|Y_{lm}\rangle V^{xtal}(\mathbf{G},\mathbf{G}')\langle Y_{lm}|\Psi\rangle \tag{2.7.11}$$

need to be evaluated. The wavefunctions $|\Psi\rangle$ are assumed to be expanded in a plane wave basis. If $V(\mathbf{r})$ were purely local then $V^{xtal}(\mathbf{G},\mathbf{G}')$ would have the simpler form $V(\mathbf{G}\text{-}\mathbf{G}')$ but this is not the case in general and substitution of Equations (2.7.10) into (2.7.11) gives a non-separable double summation over **k+G** and **k+G'** [Ref. 26 and the Appendix]. Evaluation of this term scales as the square of the number of plane waves in the basis set and makes implementation of nonlocal potentials impractical for certain systems. Klienman and Bylander (KB) have proposed a form for the non-local pseudopotential which is approximate but leads to a separable form for the summations. It is exact when applied to the pseudoatom but when applied to valence states in the solid which mix angular momentum components it is approximate as it does not project the wavefunctions onto a radially complete set of states. Although the computational cost reduction is significant, there is a possibility that the KB potential will introduce unphysical states, the wavefunctions of which have nodes in the core region [27]. There are now straightforward methods for locating and avoiding these "ghost states" [28,29] which have been applied to all the pseudopotentials used in subsequent calculations in Chapters 6 and 7.

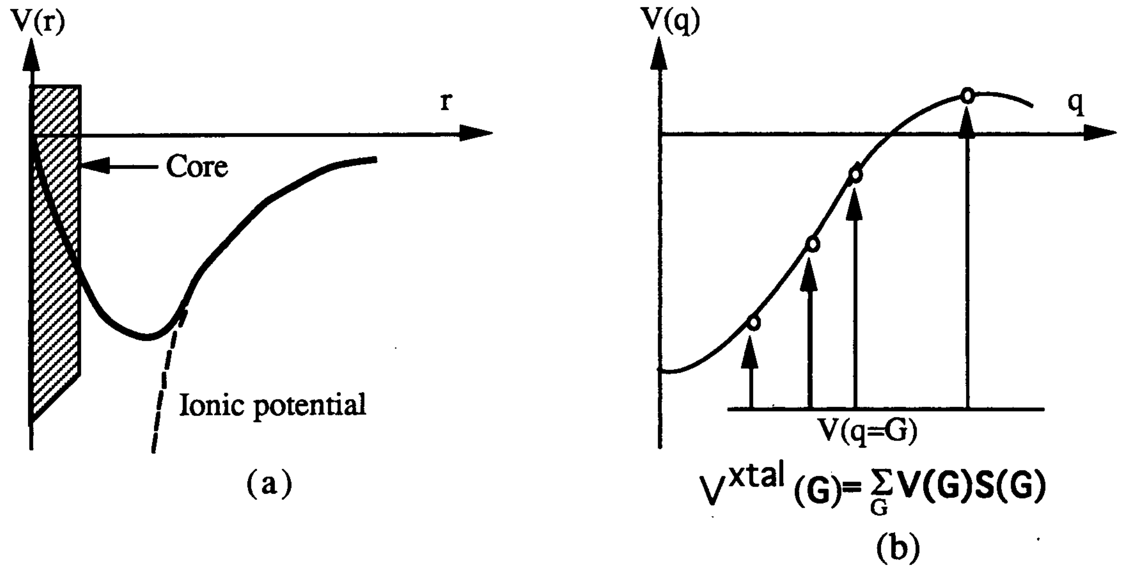

Figure 2.1 A typical pseudopotential in real space (a) and in reciprocal space (b). G is a general reciprocal lattice vector and S(G) is the structure factor which locates the positions of atoms in the unit cell. V(G) is often referred to as the pseudopotential form factor.

2.7.4 Difficulties with the pseudopotential approach

Perhaps the most obvious objection to the pseudopotential approach is that a pseudopotential is inherently non-unique. There is a mathematically well-founded reason for this which can be traced back to the origins of the pseudopotential in the OPW approach. The problem lies with the fact that the set of plane waves $\mathrm{Exp}[i(\mathbf{k}-\mathbf{G})\bullet\mathbf{r}]$ forms an orthonormal and complete set of basis functions and the additional "core states" to which they are orthogonal make the resulting basis set overcomplete. This overcompleteness imposes various linear relations between OPWs and leads to non-uniqueness of the OPW expansion coefficients [30]. The arbitrariness of the resulting pseudopotential is often not a problem in practice for a vast number of different solid state applications as the eigenvalue spectrum for the pseudo-valence states is equivalent to that given by the Schrödinger equation in the atomic case.

Despite the remarkable success of the pseudopotential approximation in describing electronic and structural properties of solids, there are cases where the technique has its limitations. The majority of such problems arise in the generation of good pseudopotentials. From the discussion given above, it may appear that since pseudopotential generation is so mechanistic, that it should be possible to produce equally good pseudopotentials for all atoms. In principle this is the case but in practice, not all atoms allow for generation of efficient pseudopotentials to be constructed and the reason for this can again be traced to the OPW scheme. The OPW method is limited to solids in which the valence band contains states having the same angular momentum symmetries as the core states to which they are required to be orthogonal [31]. Although this situation is satisfied in many materials, the first transition series contains elements which have 3d-valence states but no d-symmetry states in the core. The implication for the pseudopotential method is that such valence states experience a full screened coulomb potential with no repulsive component arising from the requirement of orthogonalization. The resulting pseudopotential is therefore very deep and requires a large number of basis states to be used. The computational advantages which make the pseudopotential method attractive are therefore lost.

§2.8 Hellmann-Feynman Theorem, force calculations and corrections

It is a natural feature of the Car-Parrinello algorithm that relaxation of the electronic charge density and ionic geometry can be achieved simultaneously. In order for this type of relaxation to occur the forces on the ions must be calculated and the ions moved in response to those forces. The Hellmann-Feynman force is related to the classical electrostatic potential due to the ions and the quantum-mechanical electronic charge density. According to the Hellmann-Feynman the force acting on a nucleus is given by the analytic gradient of the total energy expectation value:

$$\mathbf{F}_I = \nabla_I < \varphi | H_{tot} | \varphi > \qquad (2.8.1)$$

where $\nabla_I = \partial/\mathbf{R}_I$ is the derivative with respect to the position of the I^{th} ion. Htot is not the Kohn-Sham one electron Hamiltonian but is instead the total energy Hamiltonian which implies that there are contributions to the force of both electronic and nuclear origin. This is the Hellmann-Feynman Theorem which is stated without derivation. A proof is given in Chapter 6 as it is particularly relevant there as it is in Chapter 7. The shape of the total energy surface in this instance is more complicated than in the case of electronic relaxation for fixed ionic positions. The above prescription for force calculation is a general one but the forces are only meaningful within the adiabatic approximation, that is, if the electronic degrees of freedom coincide with the Born-Oppenheimer hyper-surface. Viewed as a minimisation problem this means that the gradients of the total energy hyper-surface are only required to point to the global minimum if the electronic configuration is in its ground state for the current nuclear configuration.

In what follows, a derivation of the Hellmann-Feynman force is given along with a discussion of other forces which depend on the basis set chosen and the degree of self-consistency achieved in the calculation of the charge density. A rather detailed discussion is given because proper Hellmann-Feynman force calculation will be of central importance in Chapter 6 where relaxation of ionic geometry is found to make a significant contribution to the formation energy of an inversion domain boundary in InSb. It will also be of importance in Chapter 7 where relaxation in complex Si structures is considered.

Below the Hellmann-Feynman Force is derived from an energy functional E_{tot} in which the charge density $\rho(\mathbf{r})$ and ionic pseudopotential $v(\mathbf{r})$ depend on the set of ionic positions $\{\mathbf{R}\}$.

$$E_{tot} = \int v(\mathbf{r},\{\mathbf{R}\})\rho(\mathbf{r},\{\mathbf{R}\})d\mathbf{r} + \frac{1}{2}\int \frac{\rho(\mathbf{r},\{\mathbf{R}\})\rho(\mathbf{r}',\{\mathbf{R}\})}{|\mathbf{r}-\mathbf{r}'|} d\mathbf{r}d\mathbf{r}' + \int t[\rho]\, \rho(\mathbf{r},\{\mathbf{R}\})d\mathbf{r} + \int \mu_{xc}[\rho]\rho(\mathbf{r},\{\mathbf{R}\})d\mathbf{r} + E_{ion} \qquad (2.8.2)$$

Where terms 3 and 5 of (2.8.2) are equivalent to terms 1 and 5 of (2.2.1). The force on ion I at position $\mathbf{R}_I$ is then

$$F_I = \nabla_I E_{tot} = \nabla_I E_{ion} + \int \rho(\mathbf{r},\{\mathbf{R}\})\nabla_I v(\mathbf{r},\{\mathbf{R}\})d\mathbf{r} + \int \left\{ v(\mathbf{r},\{\mathbf{R}\}) + \int \frac{\rho(\mathbf{r}',\{\mathbf{R}\})}{|\mathbf{r}-\mathbf{r}'|} d\mathbf{r}' + t[\rho] + \mu_{xc}[\rho] \right\} \nabla_I \rho(\mathbf{r},\{\mathbf{R}\})\, d\mathbf{r} \qquad (2.8.3)$$

where the product rule for differentiation has been applied. The integrand (in curly brackets) is exactly the functional derivative of the total energy functional with respect to charge density. As a result (2.8.3) can be re-expressed as

$$F_I = \nabla_I E_{tot} = \nabla_I E_{ion} + \int \rho(\mathbf{r},\{\mathbf{R}\})\nabla_I v(\mathbf{r},\{\mathbf{R}\})d\mathbf{r} + \int \left\{ \frac{\delta E_{tot}}{\delta \rho} \right\} \nabla_I \rho(\mathbf{r},\{\mathbf{R}\})\, d\mathbf{r} \qquad (2.8.4)$$

The first two terms of (2.8.4) are due to the classical Ewald force and the quantum mechanical charge density, respectively. Together they comprise the Hellmann-Feynman force, F_I^{HF}. If the stationarity condition on the total energy were strictly satisfied then $dE_{tot}/d\rho$ would be constant and the third term of (2.8.4) would be zero as particle number is independent of ion position. Scheffler *et al* [32] refer to the third term in (2.8.4) as the "variational force" and decompose it into contributions which arise from inaccuracies in the true Kohn-Sham potential and from artifacts of the basis-set itself. It might appear at first sight that the contribution to the variational force from non-self-consistency would be very small but this is not generally the case. The reason is that while the total energy is determined variationally and is therefore sensitive to deviations from self-consistency in charge density only to second order, the same is not true for the force which depends linearly on charge density. Successful application of the Hellmann-Feynman theorem thus requires a more accurate charge density than does a total energy calculation. In practice self-consistency is never achieved in a real calculation and the Hellmann-Feynman theorem should not normally be applied. Despite the fact that explicit calculation of the full variational force is completely tractable, it is not attributable to physical properties of the system under consideration and complicates the interpretation of the ionic relaxation. As a result is is preferable to identify those conditions under which the variational force may be considered negligible. One condition is simply that techniques are chosen such that the self-consistency in the calculation be maximised. In this respect it is found that pseudopotential methods are preferable to all-electron approaches. The problem with all-electron techniques is that small charge density changes in the highly localised core regions can have large effects on the potential but negligible effects on the bonding characteristics. This instability of the potential is suppressed within the frozen core approximation for which the pseudopotential method is the most suitable description and the non-self-consistent contribution to the variational force can be made negligibly small. The term associated directly with the basis-set has been described in detail in reference [32] and by Nakatsuji *et al* [33]. These workers considered the explicit expansion of wavefunctions in terms of general basis functions and investigated the decomposition of the remaining variational force into a number of contributions each of which is associated with one basis function in the finite set. It was shown that the variational force due to the basis set vanishes if the derivatives of the basis functions with respect to the parameters of distortion are themselves included in the basis set. In more quantum mechanical terms the basis set contribution to the variational force is strictly zero if the Hilbert space spanned by the basis is independent of atomic displacements. Gaussian orbitals form a basis set which satisfy this condition but the most simple choice is a plane wave basis. In addition to being well suited to the pseudopotential approximation they are delocalised and are not only independent of atomic distortions they are independent of atomic position as well.

§2.9 Details of the pseudopotential total energy calculation

For the pseudopotential calculations the CETEP [34] package was used.

2.9.1 Form of the exchange-correlation contribution

The difference between the Hartree and Hartree-Fock treatment of interacting electron systems is that the former neglects the fact that electrons having the same spin are mutually repelled because of the requirement of the Pauli principle that their wavefunctions be antisymmetric under the interchange operation of coordinates and spin. As was discussed in the section on pseudopotentials, an effective energy arises from this Pauli repulsion. The difference between the energies of an electron system as calculated with and without inclusion of the proper antisymmetry of the wavefunctions is called the exchange energy and is an inherently "manybody" effect. All electrons including those having the same spins are also correlated though not through the exchange interaction. This remaining "correlation" term must also be taken properly into account in total energy or band structural calculations.

The ground state properties of an electron gas are usually treated in the limit of either very high density (perfect gas) or the dilute limit (Wigner crystallisation). In an attempt to calculate the correlation energies for general fermi systems, Ceperly and Adler [6] have performed an exact stochastic simulation for the ground state at several densities. Since the calculation can only be performed at discrete densities an accurate interpolation scheme is required in order to make the results applicable to total energy calculations where the charge density appears as a continuous variable. There are a number of strategies for performing such a parameterization of the correlation energy of a homogeneous electron gas. The scheme proposed by Perdew and Zunger [35] is used in the pseudopotential calculations and the method of Vosko, Wilk and Nusair [1981] is employed in the full-potential linear augmented plane wave calculations which are described in a later section.

2.9.2 Dealing with divergent terms

Up to the present point in the discussion, a fairly straightforward picture of total energy calculation has been presented with no discussion of any inherent difficulties nor prescription for circumventing them. In this section, one of the more ostensibly troublesome features of these types of calculations, that of divergent contributions to the total energy, will be addressed as will means of overcoming the problems they generate.

The problem is to consider the electrostatic contributions to the functional in equation 2.4 which amount to all the terms apart from the kinetic- and exchange-correlation energies. The treatment will be in the **k**-space formulation of density functional theory in which the Kohn-Sham equation takes the form

$$\Sigma_{G'}\{((\mathbf{K} + \mathbf{G})^2 - \varepsilon_k)\delta(\mathbf{G}\text{-}\mathbf{G'}) + V^{xtal}(\mathbf{G}\text{-}\mathbf{G'}) + V_{coulomb}(\mathbf{G}\text{-}\mathbf{G'}) + V_{xc}(\mathbf{G}\text{-}\mathbf{G'})\}b_i(\mathbf{G'}) = 0 \qquad (2.9.1)$$

where

$$V^{xtal}(\mathbf{G}) = S(\mathbf{G})V_{ps}(\mathbf{G}) \qquad (2.9.2)$$

the $b_i(\vec{G})$ are defined in equation 2.6.1

and $V_{ps}(\mathbf{G})$ is the pseudopotential. The focus of this section will be on the behaviour of the second and third summands in the limit of small G. The contribution to the electronic total energy from the interaction of the electrons with their surroundings is

$$V_{interaction}(\mathbf{G}) = S(\mathbf{G})V_{ps}(\mathbf{G}) + \frac{4\pi e^2\rho(\mathbf{G})}{|\mathbf{G}|^2} + V_{xc}(\mathbf{G}) \qquad (2.9.3)$$

where the second term is the Fourier transform of the coulomb potential.

To examine the relevant divergences of these two terms the real-space pseudopotential can be decomposed into a short-ranged part $V_{sr}(\mathbf{r})$ (having finite Fourier transform at $\mathbf{G} = 0$) , and a long-range Coulombic part:

$$V_{ps}(\mathbf{r}) = V_{sr}(\mathbf{r}) - \frac{ze^2}{r} \qquad (2.9.4)$$

the Fourier transform of this quantity is

$$V_{ps}(\mathbf{G}) = V_{sr}(\mathbf{G}) - \frac{4\pi z e^2}{G^2\Omega} \qquad (2.9.5)$$

When this is substituted into equation (2.9.3) the first term exhibits a G^{-2} divergence from the $V_{ps}(\mathbf{G})$ factor and another divergence is observed in the second term representing the Fourier transform of the coulombic part of the potential. The details of how this issue is resolved is described in the rest of this section. The strategy is as follows: those quantities ($\rho(\mathbf{G})$ and $S(\mathbf{G})$) which multiply the individually divergent factors ($|\mathbf{G}|^{-2}$ and $V_{ps}(\mathbf{G})$) are expanded to second order in G in the hope of exposing any cancellation of divergent contributions. The expansions are

$$\rho(\mathbf{G}) = \rho(0) - i\alpha_1 \bullet \mathbf{G} - \frac{1}{2}\alpha_2 G^2 \qquad (2.9.6)$$

$$S(\mathbf{G}) = S(0) - i\beta_1 \bullet \mathbf{G} - \frac{1}{2}\beta_2 G^2 \qquad (2.9.7)$$

Substitution of these expressions into Equation (2.9.3) yields for the R.H.S.

$$(S(0) - i\beta_1 \bullet \mathbf{G} - \frac{1}{2}\beta_2 G^2)(V_{sr}(\mathbf{G}) - \frac{4\pi z e^2}{G^2\Omega}) +$$
$$\frac{4\pi e^2}{|\mathbf{G}|^2}\{\rho(0) - i\alpha_1 \bullet \mathbf{G} - \frac{1}{2}\alpha_2 G^2\}$$

Expanding these expressions and taking the limit as G -> 0 gives

$$S(0)V_{sr}(\mathbf{0}) + i\frac{4\pi e^2\rho(0)}{|\mathbf{G}|^2}(\frac{\beta_1}{S(O)} - \frac{\alpha_1}{\rho(0)}) \bullet \mathbf{G} +$$
$$2\pi\rho(0)(\frac{\beta_2}{S(O)} - \frac{\alpha_2}{\rho(0)}) + \text{terms of order } G$$

The first and third terms are constants but the second term still shows a residual divergence of order 1/G. It has been argued [36] that this term must be zero as it is related to a possible dipole moment which vanishes in the case of a monatomic basis as is considered here. In general it must be that the individually divergent G = 0 contributions to the total energy cancel exactly because there is no Coulomb potential at G = 0 in a neutral system so there cannot be a contribution to the total energy from the G = 0 component of the Coulomb potential. For pseudopotential calculations, a correction to this must be included because the form of a pseudopotential is not everywhere coulombic and a residual, non-coulombic contribution to the total energy exists at G=0. This correction to the potential is proportional to the integrated difference between the pseudopotential and the coulombic potential over the core region.

2.9.3 Orthogonalization schemes and calculations on metals

It may appear that of all the details involved in total energy pseudopotential calculations, the technique used to mutually orthogonalize the wavefunctions is one of the least important. This is, in fact, not the case and the reason has special implications for calculations on metallic systems.

Some orthogonalization algorithms used in the constrained minimisation of the total energy functional generate groundstate wavefunctions which are linear combinations of the true Kohn-Sham eigenstates which would have been determined had the Kohn-Sham equation been solved by traditional diagonalization procedures. In many cases all that one requires is the total energy difference between two structures and convergence to the exact Kohn-Sham eigenstates is not required. This is because the functional is minimized by a linear combination of eigenstates as well by the eigenstates themselves. For calculations on systems with partial occupancy of bands, however, states must be ordered according to energy so that proper filling of levels up to the Fermi energy is ensured. It is in this situation where the simple Gram-Schmidt process of orthogonalization of two linearly-independent vectors has an advantage over others. This simple method treats vectors in a well-defined order and the technique can be implemented so that the wavefunctions corresponding to higher bands are forced to be orthogonal to all lower bands. The implication of this is that the procedure will force convergence to the true eigenstates and will generate no mixing.

2.9.4 Brillouin zone sampling

The previous sections have described theories for calculating the Kohn-Sham eigenstates by various iterative minimisation techniques. These states exist at discrete points in the Brillouin zone and the density of these points increases with the real space volume of the crystal and is effectively infinite for real systems. There are however, only a finite number of occupied states per point. As calculation of ψ_i on an infinitely dense grid of points is obviously intractable, some method of approximation must be devised.

In the case of insulators and semiconductors, the functions to be integrated are continuous and infinitely differentiable as a result of occupied and empty bands. These integrals exhibit exponential convergence with respect to the spacing between divisions made in the Brillouin zone mesh. Metals present a more complex problem in that the relevant functions which must to be integrated over the zone are discontinuous due to partial filling of the bands but there have been attempts to simplify the problem for the metallic case [37]. If the assumption is made that the wavefunctions are not too rapidly varying, which implies that the wavefunctions at nearby k-points are similar, then it should be possible to represent the wavefunctions throughout k-space by a fairly coarse grid. This approximation is made in all the calculations which follow in subsequent chapters.

2.9.5 Summation of ion-ion interactions

Evaluation of the electrostatic energy of a collection of positive charges in a uniform compensating negative background as given by the pairwise summation of the Coulomb interaction in the total energy Hamiltonian is only conditionally convergent for infinite crystals. The results depend sensitively upon the geometry of the clusters taken for the summation. These difficulties can be circumvented by dividing the coulomb interaction into a short-ranged and a long-ranged component. Direct summation of the short-range part is naturally rapidly convergent. Fourier transformation of the residual long-range component results in a short ranged interaction in reciprocal space the sum of which is also rapidly convergent. The recipe for separation of the interaction is not unique but the one used in the following calculations is the following [38]. The electrostatic energy E_{es} is given by

$$E_{es} = \alpha_M(Z^2/Ra) \tag{2.9.10}$$

α_M is the Madelung coefficient and is given by

$$\alpha_M = R_a\{\frac{4\pi}{V_a}\sum_G \frac{\mathrm{Exp}(-G^2/4\eta)}{G2}|S(\mathbf{G})|^2 + \sum_R \frac{\mathrm{erfc}(\sqrt{\eta}R)}{R} + \frac{2\sqrt{\eta}}{\sqrt{\pi}} + \frac{\pi}{\eta V_a}\} \tag{2.9.11}$$

R and G are the real and reciprocal lattice vectors S(**G**) is the structure factor and erfc(x) is the complementary error function. The parameter η is usually chosen so as to obtain similar rates of convergence for the summed series in both real and reciprocal space.

§2.10 Full-potential techniques: the FLAPW method

2.10.1 Background

The starting point for this discussion will be the Kohn-Sham equation as expressed in section 2.2 within the LDA. Unlike the plane wave scheme previously described, the APW technique uses basis sets which are adapted to suit the crystalline environment. Historically, the APW method can be traced back to the work of Slater in 1937 [39] when it was proposed in order to circumvent some of the difficulties associated with satisfying the complex boundary conditions which arise in the cellular method.

In almost all applications of the APW method two such environments are considered. In one region, that in the vicinity of the ionic cores, the potential is taken as being spherically symmetric and in the interstitial regions the potential is taken as a volume-averaged constant. These two separate regions suggest different forms for the wavefunctions. Below, an outline of the basic theoretical concepts involved in the APW approach but far more detailed descriptions can be found in a number of sources [40,41,42].

2.10.2 The APW basis: an energy-dependent secular equation

In the ionic core region, the basis functions are defined as linear combinations products of radial equation solutions $U_l(r,E)$ and standard spherical harmonics $Y_{lm}(\theta,\phi)$ as shown below

$$\phi^{core}(\mathbf{k}_n,\mathbf{r}:E) = \sum_{lm} A^{n}_{lm}(k_n) U_l(r,E) Y_{lm}(\theta',\phi') \qquad (2.10.1)$$

The $U_l(r,E)$ represent regular solutions of the radial Schrödinger equation for energy E, inside the ionic core region.

In the interstitial region where the potential is volume averaged to a constant value, the basis function takes the form of a simple plane wave

$$\phi^{inter}(\mathbf{k}_n , \mathbf{r}) = \Omega^{-1/2} \exp(i\, \mathbf{k}\cdot\mathbf{r}) \qquad (2.10.2)$$

At the boundary between the ionic and interstitial regions these two forms for the wave functions must be matched in value. Typically the Bauer expansion of a plane wave in terms of spherical harmonics is used.

$$\exp(i\mathbf{k}\cdot\mathbf{r}) = e^{i\mathbf{k}\cdot\mathbf{r}_p} \sum_{l=0}^{\infty} \sum_{m=-l}^{m=l} 4\pi i^l j_l(k_n r') Y_{lm}(\Theta,\phi) Y^*_{lm}(\Theta',\phi') \tag{2.10.2a}$$

$$= \sum_{l\,m} (2l + 1)\, i^l\, j_l\, (k_n r')\, P_l \cos(\theta) \tag{2.10.2b}$$

With equation (2.10.2b) following from (2.10.2a) by use of the spherical harmonic addition theorem:

$$P_l \cos(Q) = \frac{4\pi}{2l + 1} \sum_{m=-l}^{m=l} Y_{lm}(\Theta,\phi) Y^*_{lm}(\Theta,\phi) \tag{2.10.3}$$

These expressions yield the coefficients involved in the spherical harmonic decompositions comprising the APW in the muffin-tin sphere . By equating the expressions for the wavefunctions in the core and interstitial regions at the boundary between the two, the expansion coefficients can be determined.

$$A^n_{lm}(k_n) = 4\pi\, i^l\, Y^*_{lm}(\Theta,\phi) \frac{j_l\,(k_n R_p)}{U_l(E,R_p)}\, e^{i\mathbf{k}\cdot\mathbf{r}_p} \tag{2.10.4}$$

Using this as the expansion coefficient the APW in the core region can be expressed as

$$\phi^{core}(\,\mathbf{k}_n,\mathbf{r}\mathbf{:}E) = e^{i\mathbf{k}\cdot\mathbf{r}_p} \sum_{l=0}^{l=\infty} \sum_{l=-m}^{l=+m} 4\pi\, i^l\, U_l(E,r) \frac{j_l\,(k_n R_p)}{U_l(E,R_p)} \times Y_{lm}(\theta',\phi') Y^*_{lm}(\Theta,\phi) \tag{2.10.5}$$

This expression is an exact eigenstate of the Schrödinger equation inside any individual spherically symmetric core region because it is a superposition of exact solutions. Also, the plane wave is an exact eigenstate for the Schrödinger equation in the interstitial region where the energy E is equal to k_i^2 throughout the region. It appears that the required matching condition is trivially satisfied for a <u>single</u> APW provided that the energy for the wavefunction <u>inside</u> the sphere is also equal to k_i^2. But, in the general case of a non-vanishing potential, a single APW will have a discontinuity in slope at the boundary between the core and interstitial regions and this property is not permitted for a solution to the Schrödinger equation. A superposition of APW functions is required in order to obtain wavefunctions possessing continuity of value and derivative at the boundary. The reason for this is that the effect of a spherically symmetric potential within the core regions is to scatter an incident plane wave. Any eigenfunction, therefore must include the scattered components as well. In the limit of vanishing ionic potential (the empty lattice) both the core and interstitial functions are continuous at R_p.

The crystal eigenfunction is therefore represented as a linear superposition of APWs, $\Phi_k(r)$, which are consistent with the translational symmetry of the lattice and satisfy the Bloch theorem. A putative solution of the Schrödinger equation is then

$$\Psi_k(r) = \sum_G \alpha_{k-G}\Phi_{k-G}(r)$$
$$\Phi_k(r) = \begin{cases} \phi^{\mathrm{inter}}(\mathbf{k}_n,\mathbf{r}) & r > R_p \\ \phi^{\mathrm{core}}(\mathbf{k}_n,\mathbf{r}:E) & r < R_p \end{cases} \qquad (2.10.6)$$

The most natural procedure for solution of this problem is to use the form for $\Psi_k(r)$ to determine the expectation value of the Hamiltonian and use the expansion coefficients as variational parameters. The variational procedure gives rise to a matrix equation which has a non-trivial solution when the resulting secular determinant vanishes. The secular equation itself has the standard form

$$\sum_j (H - E)_{ij}\, \alpha_{k-G_i} = 0$$
$$\text{with } (H - E)_{ij} = \langle APW:K+G_i | H - E | APW:K+G_j\rangle \qquad (2.10.7)$$

In principle this strategy for determining an acceptable set of α_{k-G} leads to the required relationship between energy and wavevector.

There are, however, serious difficulties associated with the present formulation. The cause of the problems stems from the implicit energy dependence of the basis functions. Firstly, the discontinuities in slope at the core radii for each APW make the evaluation of the matrix elements difficult. More troublesome than this however, is that the energy-dependence of the APW basis leads to a secular equation that is highly non-linear in energy. A computationally intensive root search must therefore take place at every sampled point in the Brillouin zone. The technique of linearization has been proposed to simplify these problems and is discussed next.

2.10.3 The (L)APW basis: energy-independent secular equation

The linearized modification of the basis [43] manifests itself only in the core region and replaces the previous form of $\varphi^{core}(\mathbf{k}_n,\mathbf{r})$ with the following expression:

$$\varphi^{core}(\mathbf{k}_n,\mathbf{r}) = \sum_{lm} \left[A_{lm}(\mathbf{k}_n)\, U_l(E_l,r) + B_{lm}(\mathbf{k}_n)\, (\partial U_l(El,r)/\partial E)\, E_l\right] Y_{lm}(\theta,\varphi) \qquad (2.10.8)$$

The coefficients are determined by the requirement that this interstitial function match in value and derivative the φ^{core} function at the limits of spherical potential symmetry. Unlike the original APW formulation, the value of E_l is not required to match the Kohn-Sham eigenvalue. Also, continuity of derivative is required in this case but not in the original APW form. The important difference between the APW and LAPW techniques is that the LAPW secular equation has no implicit energy dependence because the energy dependence has been removed from the LAPW basis set.

§2.11 Details of the FLAPW total energy calculation

Relativistic Effects and the APW method

In many solid-state problems relativistic effects are completely negligible but for certain solids and particular classes of problems they must be included at least approximately. For electronic structure and total energy calculations relativistic effects are appreciable for sufficiently heavy atoms, though the errors incurred in a non-relativistic treatment are partially self-cancelling. Within the atomic spheres electrons experience the very strong nuclear potential and move at relativistic speeds. On the other hand, electrons in the interstitial region experience substantially weaker influences and their kinetic energies become much smaller than their rest masses. This motivates a partitioning of space again into core and interstitial regions where the electron is treated fully relativistically in the former region and only semi-relativistically in the latter. This prescription is the one used in the calculations to be described in Chapter 5. The approach to fully-relativistic band structure calculations will be outlined below and subsequently, semi-relativistic corrections to the valence states will be described. More details of relativistic effects in electronic structure calculations can be found in a number of sources [44, 45, 46].

For the core states the full Dirac equation for a central field V(r) is solved. For the valence states only the effects of the mass-velocity and Darwin terms are included [47]. The spin-independent mass-velocity and Darwin terms manifest themselves as the next higher order corrections to the descriptions of an electron in the nuclear Coulomb field. The mass-velocity term, as its name implies, is a relativistic correction to the non-relativistic kinetic energy. The Darwin term is a relativistic correction to the potential energy which has no obvious classical analogue. Both these terms have the same symmetry as the crystal potential and have the effect of shifting eigenvalues without lifting degeneracies. In the fully relativistic Dirac formalism, the symmetry properties of the spin-orbit coupling are characterised by space and spin coordinates (double-group representation) and degenerate levels can be split by this interaction.

The relativistic APW method proceeds in an identical fashion to the nonrelativistic approach. In the field-free interstitial region, the relativistic form of a plane wave is chosen for the wavefunction

$$\phi^{\mathrm{inter}}(\mathbf{k}_n,\mathbf{r}) = -\frac{c\sigma\cdot\mathbf{p}\chi(m)e^{(i\mathbf{k}_n\cdot\mathbf{r})}}{E+2mc^2} \qquad (2.11.1)$$

Where $\chi(m)$ is a Pauli spinor and $m = \pm 1/2$. Inside the spherically symmetric potential core region, a linear combination of central field orbitals are chosen to match the interstitial wavefunction at the sphere's surface:

$$\phi^{\mathrm{core}}(\mathbf{k}_n,\mathbf{r}) = \sum A^{nm}_{\kappa\mu}\Psi^{\mu}_{\kappa} \qquad (2.11.2)$$

The Ψ^{μ}_{κ} are solutions of the Dirac equation and $A^{nm}_{\kappa\mu}$ are chosen to achieve the required matching. Determination of $A^{nm}_{\kappa\mu}$ specifies a single relativistic APW [48] and the strategy is then to expand a general wavefunction in terms of these and to proceed as in the nonrelativistic case.

Semi Core states

The problem associated with the "semi-core" states is an important one and also has direct relevance to the Chapter 5 calculations. There is usually a very straightforward and quantitative distinction made between core and valence states in electronic structure calculations. Core states are those for which the associated charge is confined entirely within the atomic sphere. Valence states are those with no associated charge in the sphere. The situation can arise, however, where a small percentage of charge exists outside of the core region. A third class of states called semi-core states must then be created. For computational purposes these semi-core states can be treated in a straightforward fashion by considering them as a distinct class of valence state.

§2.12 Comments: What is the State-of-the-Art?

Does there appear to be a particular technique which, in principle, is more powerful and versatile than others? One issue which has not been addressed in detail in the previous sections is the interrelationship between the various techniques. The connection between the pseudopotential approach and the OPW method has been explored but there are similar interrelations between almost all methods of electronic structure calculations including the cellular and LCAO methods. For example, the secular determinant resulting from the APW approach can be shown to have a standard pseudopotential form.

The question of whether there exists a "best" technique must at least partially focus on the practicality of actually applying the methods in a variety of realistic situations. For the computational aspects of this thesis, both the APW and pseudopotential approaches were employed in two disparate cases because neither one was appropriate, in practice, for both situations. The pseudopotential programs used in Chapter 6 are not well suited to the metallic calculations required for the work described in Chapter 5. Conversely, the APW method presently cannot be applied to the large cells used in Chapters 6 and 7 and also does not efficiently handle Hellmann-Feynman force calculations and subsequent ionic relaxation. The question of whether a given technique is optimal or even useful depends on the computational scheme developed to implement it and on the particular physical situation.

---

[1] W. Kohn and L.J. Sham *Phys. Rev.* **140** A1133 (1965).

[2] P. Hohenberg and W. Kohn *Phys. Rev.* **136** (1964) 864.

[3] L. Heiden and S. Lundqvist *J. Phys. C* **4** (1973) 2063.

[4] O. Gunnarsson and S. Lundqvist *Phys. Rev. B* **14** (1976) 4274.

[5] S.H. Vosko, L. Wilk and M. Nusair *J. Can. Phys.* **58** (1980) 1200.

[6] D.M. Ceperley and B. J. Adler *Phys. Rev. B* **45** (1980) 566.

[7] J.A. Alonso and N.H. Marsh Electrons in Metals and Alloys Academic Press Boston, 1989 pages 11,12.

[8] Methods in Computational Physics ed. B. Adler Volume **8**, (1968) Energy Bands of Solids. (This reference provides a very thorough description of the theory and practical implementation of traditional electronic structure computation by the Pseudopotential, APW, empirically adjusted OPW and KKR (Green's function) techniques).

[9] R. Car and M. Parrinello *Phys. Rev. Lett.* **55** (1985) 2741.

[10] M.C. Payne, M.P. Teter and D.C. Allan *J Chem Soc Faraday Transactions* **86** (1990) 1221.

[11] There may be other instabilities, particular to various integration methods which arise and are discused in detail for the Verlet Algorithm in Reference 10.

[12] M.P. Teter, M.C. Payne and D.C. Allan *Phys. Rev. B* **40** (1989) 12255.

[13] Details of the motivation for development of the conjugate gradients technique as applied to these calculations can be found in M.C. Payne, M.P. Teter, D.C. Allan , T.A. Arias and J.D. Joannopoulos *Rev. Mod. Phys.* **64** (1992) 1045. This review also considers other minimisation algorithms and covers techniques which treat the equations of motion directly.

[14] M.C. Payne and G.P. Francis*J. Phys. C* **2** (1990) 4395.

[15] N. Ashcroft and N.D. Mermin Solid State Physics (Holt-Saunders Pub.) New York (1976)

[16] W. Harrison, Pseudopotentials in the Theory of Metals (W.A. Benjamin. Inc., New York 1966).

[17] J.S. Lin (Cambridge University) private communication.

[18] D.R. Hausman *Phys. Rev. B* **40** (1989) 2940.

[19] N. Troullier and J.L. Martins *Solid State Commun.* **74** (1990) 613.

---

[20] G.P. Kerker *J. Phys. C* **13** (1980) L189.

[21] G.B. Bachelet, D.R. Hamann and M. Schlüter *Phys. Rev. B* **26** (1982) 4199.

[22] J.S. Lin, A. Qteish, M.C. Payne and V. Heine Submitted to *Phys. Rev.* ***B***.

[23] L. Klienman and D.M. Bylander *Phys. Rev. Lett.* **48** (1982) 1425.
Use of the Klienman-Bylander approximation to non-local pseudopotentials reduces the number of integrals required to evaluate $|Y_{lm}>V(r)<Y_{lm}|$ between plane waves from kn(n+1)/2 operations for each l to kn where k is the number of points in the brillouin zone at which the calculation is performed and n is the number of plane waves in the expansion.

[24] J. M. Ziman 1970, Solid State Physics ed. H. Ehrenreich, F. Seitz and D. Turnbull (New York) Academic Press. **26** 1.

[25] The reciprocal space implementation is described here because real-space methods are not straightforward in practice and are not used in subsequent calculations. In principle, however, the short-range of the nonlocality implies that system-size-scaling will be more favourable in real space.

[26] T. Oguchi and T. Sasaki *Prog. Theo. Phys. Suppliment* No. **103** (1991) 93.

[27] Strictly speaking, these unphysical states arise because the KB potential does not obey the Wronskian theorem (for wavefunctions of the same potential) which has the effect of ordering the eigenenergies according to increasing number of nodes of the wavefunction. This means that states with one or more nodes may have lower energy than that of the nodeless state.

[28] X. Gonze, P. Käkell and M. Scheffler *Phys. Rev. B* **41** (1990) 12264.

[29] I. Stich, R.Car, M. Parrinello and S. Baroni *Phys. Rev. B* **39** (1989) 4997.

[30] C. Herring *Phys. Rev.* **57** (1940) 1169.

[31] See [24]

[32] M. Scheffler, J.P. Vigneron, J.B. Bachelet *Phys. Rev. B* **31** (1985) 6544.

[33] H. Nakatsuji, K. Kanda, and T. Yonezawa *Chem Phys.Lett*. **75** (1980) 340 (This work was performed using a Hartree-Fock method).

[34] *CETEP* is *the Cambridge-Edinburgh Total Energy Package* [1992]. This program suite is used for the pseudopotential calculations which will be described in Chapters 6 and 7. It is based on the molecular dynamics method introduced by R. Car and M. Parrinello [1985] and is principally a result of the efforts of M.C. Payne, X. Weng, V. Milman, G. Francis, Uwe Bertram and Bjork Hammer.

[35] P. Perdew and A. Zunger *Phys. Rev. B* **23** (1981) 5048.

[36] P. Bagno, L.F.D. Rose and F. Toigo *Adv. Mod. Phys.* **40** (1991) 686.

[37] M. Methfessel and A. T. Paxton *Phys. Rev. B* **40** (1989) 3616.

[38] K. Fuchs. *Proc. Roy. Soc.* London **A151** (1935) 515.

[39] J.C. Slater *Phys. Rev.* **51** (1937) 846.

[40] C.M. Quinn An Introduction to the Quantum Chemistry of Solids (Clarendon Press) Oxford 1973.

[41] J.C. Slater *Phys. Rev* . **92** (1953) 603.

[42] J.C. Slater and M. Saffren *Phys. Rev.* **92** (1953) 1126.

[43] P. Blaha , K Schwarz , P Sorantin and S.B. Trickey *Computer Phys. Commun.* **59** (1990) 399.

[44] U. Rössler and J. Treuch *Rep. Prog. Phys.* **35** (1972) 883.

[45] G.W. Pratt and L.G. Ferreira *Proc. 7th International Conf. : Physics of Semiconductors* , ed M. Hulin. (For a detailed account of how individual relativistic terms affect electronic levels).

[46] T.L Louks *Phys Rev* **139** (1964) A1333; also
— The Augmented Plane Wave Method: A guide for performing electronic structure calculations: 1967 (New York: Benjamin)

[47] B.H. Bransden and C.J. Joachain Physics of Atoms and Molecules Longman London and New York. 1983 Appendix 7.

[48] In general Ψ_k^m is a two-component wavefunction comprised of components ψ and ϕ.

The ϕ component is appreciable only near the nucleus. Both components cannont be made simultaneously continuous at the sphere boundary but this causes no complication as only ψ is relevant there.

CHAPTER 3

DEVELOPMENT AND IMPLEMENTATION OF THE IMAGE PLATE AREA DETECTOR

§3.1 Background and motivation

Chapter 1 was intended, in part, to represent an introduction to conventional powder diffraction techniques and practices. Despite the success of powder diffraction as a structural tool, its utility as a high pressure technique is plagued by experimental obstacles. These obstacles exist both for neutron and x-ray powder methods but apart from introductory remarks the following discussion will focus only on aspects of x-ray studies.

High-pressure structural studies have, for many years, been undertaken using single-crystal samples and have yielded a great deal of information regarding high-pressure properties and behaviour including pressure-induced structural phase transitions. Although an undeniably valuable technique, the single crystal method is inappropriate for several important applications. For instance, it is well known that a great number of materials, including the III-V and group IV semiconductors, undergo pressure-induced first-order structural phase transitions which shatter samples and render single crystal methods inadequate for the study of high-pressure phases by diffraction techniques. In principle, powder diffraction techniques are ideally suited to these types of applications but, in practice, conventional detection systems severely limit the reliability of the method and almost entirely preclude *ab initio* structural solution of unknown phases.

In a traditional high-pressure powder diffraction experiment, most of the diffracted radiation is undetected in the experiment as the detector subtends only a small portion of the Debye-Scherrer cone of diffracted radiation. There are several implications of this which severely reduce the practical utility of angle-dispersive powder diffraction at high-pressure. For example, in order to determine the positions of atoms in a unit cell the relative peak intensities of an x-ray diffraction pattern must be known accurately. However, the nature of traditional powder diffraction at high-pressure does not allow for routine determination of relative intensities. The reason for this is that since only a small fraction of diffracted radiation is collected the resulting diffraction pattern can be substantially affected by preferred orientation and inaccuracies due to poor powder averaging. In addition to these problems, the small proportion of diffracted intensity which is detected in an experiment leads to poor signal to noise ratios.

In summary, power diffraction does indeed circumvent several of the obstacles incurred in single crystal techniques but traditional powder methods create additional difficulties of their own. One of the most straightforward means of obviating these difficulties without losing the advantages of powder diffraction is to directly exploit the intrinsic 2-dimensional (2D) nature of the experiment. In other words a detector designed to intercept and record a significant fraction of the diffracted beam would surely be preferable to standard scanning detection of only a minute fraction thereof. The image plate represents such a 2D x-ray detection system which stores the diffracted image in the form of colour centres as described in section 3.6. The application of the image plate detector as a general purpose x-ray photon sensor was reported first in Japan [1,2] but its subsequent adaption for high-pressure structural investigations followed shortly thereafter [3,4,5]. The present study is not the only example of the use of an image plate detector in high-pressure instrumentation. There are a few other references [6,7] in which an image plate is used in this context but none apply the method with a view towards full crystal structure determination at high pressure as will be done in this work. A brief description of the basic experimental arrangement is given below. As the focus of the present work is on results of image plate experiments the reader is referred to the literature for a more detailed description of technique development.

§3.2 Experimental arrangement

The apparatus used for image plate data collection of high-pressure powder diffraction patterns is shown in Figure 3.1 and has been designed specifically for use on the powder diffraction station (9.1) of the Daresbury Laboratory Synchrotron Radiation Source (SRS) but is portable to other stations. Conical-aperture diamond anvil pressure cells (DACs) are used in all image plate experiments so as to take maximum advantage of the 2-dimensional nature of the detector. The preliminary design of the image plate system described here as well as very early results have been reported in several recent articles [3,4,8]. Due to the extreme sensitivity of the image plate, great care must be taken to ensure that all forms of background radiation are sufficiently well shielded from the plate's surface. This can be easily accomplished with the use of thin Pb sheets placed over the beam's primary entrance port and collimation devices. Some of the first image plate exposures showed a vast array of contaminants from sources such as scatter from harmonics of the main beam off the gasket and collimation devices as well as a high background due to the high levels of radiation in the experimental hutch.

The beamline arrangement used in these studies consists of a primary Pb shield with a large aperture designed to block the low angle scatter from 'hard' (small wavelength) radiation passing through the monochromator. No reduction of beam size occurs at this stage. The main beam then enters a tungsten-carbide collimator terminated with a Pt pinhole which defines the required beamsize to be of order 100 μm.

Once the beam size has been reduced to a sufficiently small value, the DAC is aligned to ensure that the small beam passes through the sample and has minimal contact with the surrounding gasket material. The following technique is used. Once the beam has been collimated an image of the beam is made on x-ray sensitive paper. A telescope is then focused on the image and the cross-hairs of the telescope are moved until they are in the image centre. The paper is then removed and a DAC is placed on the mount and moved until the sample is in focus at the centre of the cross-hairs.

On Station 9.1 at Daresbury, the monochromated beam contains a small $\lambda/3$ component [9]. Despite the fact that the flux of the $\lambda/3$ component is small compared to that of the main λ component, the high energy harmonic of the main beam is only partially attenuated by the Pt pinhole whereas the main component is totally attenuated. Upon exiting the pinhole, the beam thus contains an increased fraction of the $\lambda/3$ harmonic which may lead to contaminant peaks in the final diffraction pattern. The value and sensitivity of the image plate detection method can only reach its full potential if all known sources of contamination are removed. In some cases contamination from harmonics of the beam can be reduced provided a wavelength is chosen so that its $\lambda/3$ harmonic is near the absorption edge of the pinhole material. The K-shell absorption edge of Pt occurs at a wavelength of 0.158 Å which would correspond to the $\lambda/3$ harmonic of a 0.474 Å main beam. The situation is shown schematically in Figure 3.3.

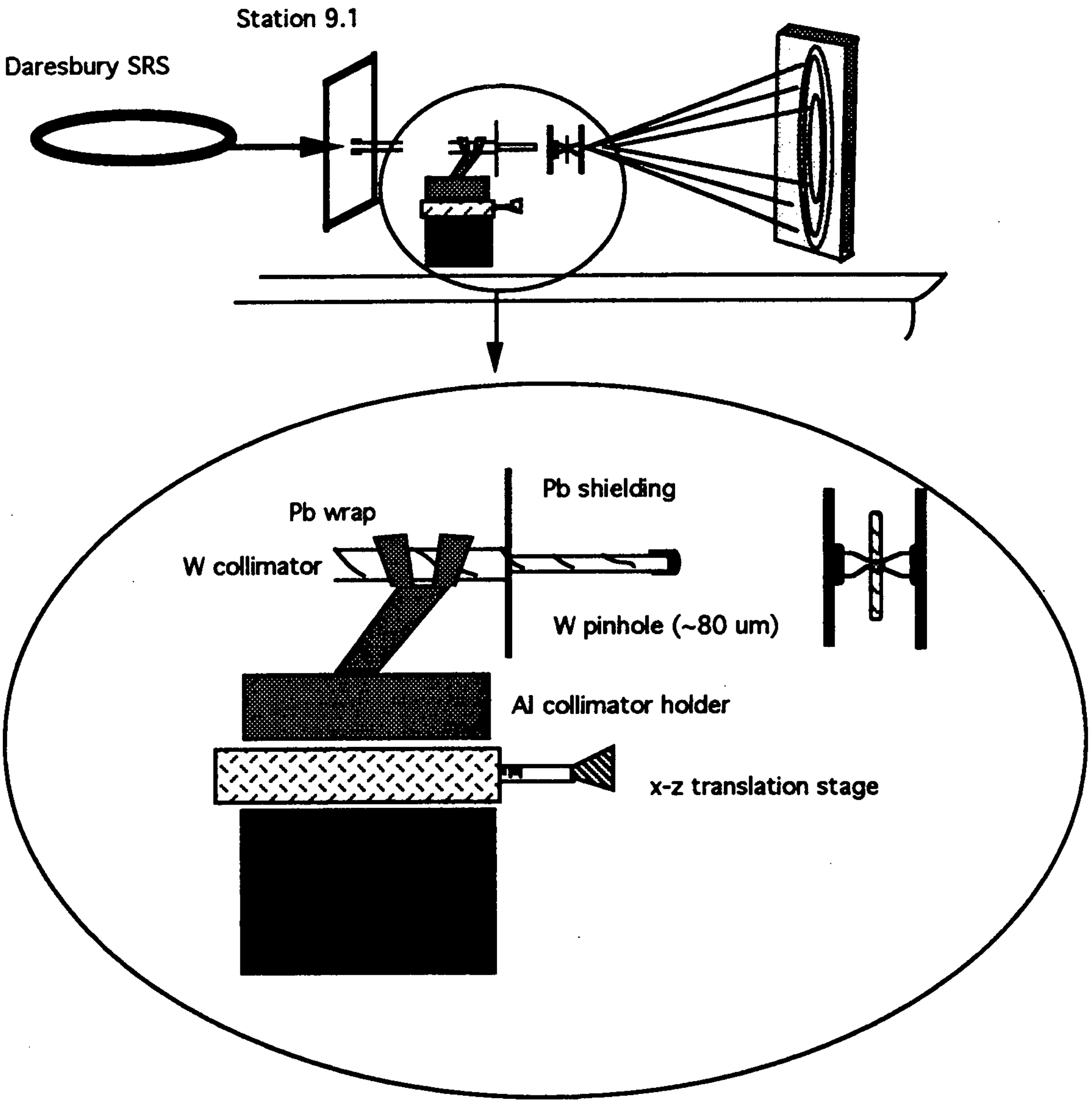

Figure 3.1 Experimental arrangement and beamline configuration for a standard high-pressure powder diffraction experiment using the image plate area detection system. The above apparatus was designed specifically for use on powder diffraction station 9.1 of the Daresbury Laboratory Synchrotron Radiation Source (SRS) but is easily adaptable to several other stations and the principle is general. The inset shows a detailed view of the secondary collimation mount and DAC. Primary collimation and initial beamsize definition occurs via slits in the monochromator housing. Tungsten or Platinum is typically used as the pinhole material.

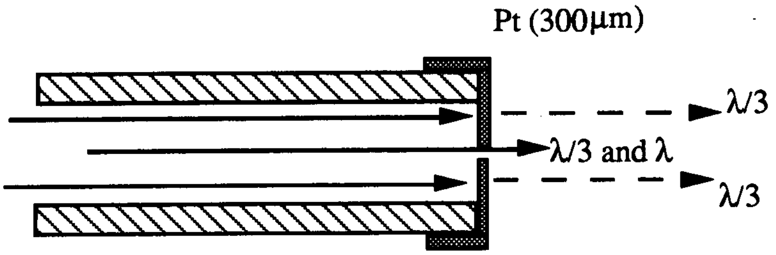

Figure 3.2 Detail of the tungsten carbide collimator and Pt pinhole. The initial beamsize is approximately 0.5 x 0.5 mm^2 and is reduced by the Pt pinhole to a final size of between 50 μm and 80 μm. In general the λ/3 harmonic of the main beam is of sufficiently high energy so as to pass through the 300 μm thick pinhole material.

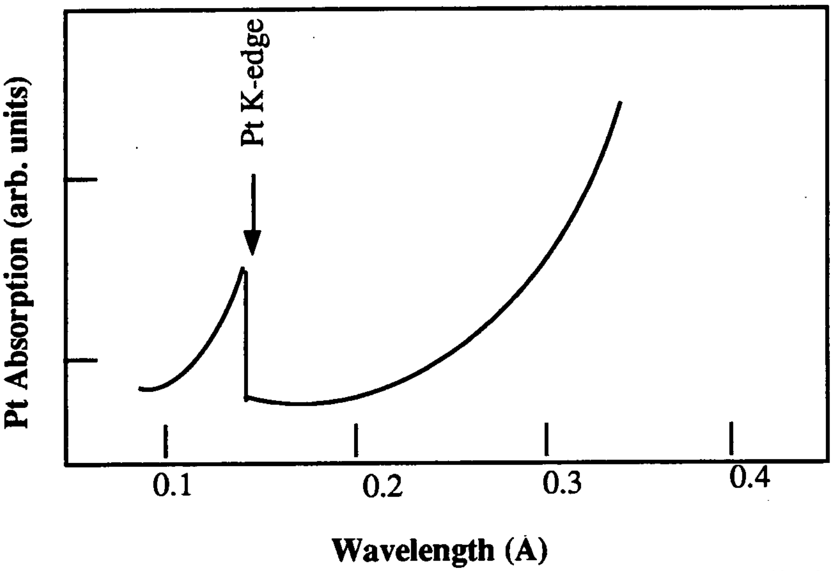

Figure 3.3 Illustration of the technique used to eliminate contaminant diffraction peaks arising from scatter from harmonics of the main beam. The main beam wavelength is chosen so as to have its λ/3 harmonic near the absorption edge of the pinhole material thus substantially attenuating this component from the exiting beam.

§3.3 The image plate: data acquisition and processing

The principle of image plate operation is based on information storage (and retrieval) in the form of quasi-stable, x-ray-induced colour centres. The image plate area detector is a photostimulable phosphor screen constructed from a thin coating of BaFBr:Eu^{2+} crystals in an organic binder and mounted on a flat aluminium plate. An x-ray image is temporarily "recorded" when high energy radiation (eg, x-rays, ultraviolet light, or gamma rays) produces localized electronic states (F-colour centres) [10] via excitation of an electron from the Eu^{2+} into the conduction band. This process results in an excited $BaFBr^-$ complex which has a characteristic absorption band centred at approximately 600 nm. It is found that these colour centres can exist without substantial degradation (recombination) for several days at room temperature.

After formation of these colour centres, the image plate is scanned by slowly drawing it over a scanning He-Ne laser (wavelength = 633 nm, 10 mW power) which induces photostimulated luminescence from the colour centres. The laser beam is focused to an 88 μm spot size. A diagram of the scanning process is shown in Figure 3.4. The intensity of the luminescence is collected by fibre-optic coupler and is subsequently converted into digital signals which are then stored as a digitised image by a computer. The result is a quantitative representation of the original image on the plate. Reading of a standard image plate (20 x 25 cm) requires approximately 10 minutes and 11 Mbytes of disk space is required to store the resulting file. The advantages of these types of storage phosphors over film include a linear dynamic range covering five orders of magnitude and a sensitivity enhancement which can approach a factor of 300 depending on wavelength [11]. Storage phosphors are indefinitely erasable and reusable. Image plates used in these studies have now been exposed and erased nearly 1000 times. Kodak Phosphor plates are used for all of these studies and a Molecular Dynamics 400A Phosphor Imager is used to read the image plates.

§3.4 Integration of the diffraction pattern

Although the 2-dimensional representation of the diffraction pattern generated by the image plate has proved very useful in interpreting the collected data as will be discussed later, it is necessary to convert the image into a standard 1 dimensional diffraction pattern suitable for input into powder diffraction analysis packages such as those which perform unit cell indexing and Rietveld refinements. This is achieved by integrating the image azimuthally around the Debye-Scherrer rings. In principle this is a straightforward procedure but some care is required in practice due to the presence of several geometric non-idealities such as slight improper alignment of the image plate with respect to the incident beam as well as inaccurate determination of the beam centre.

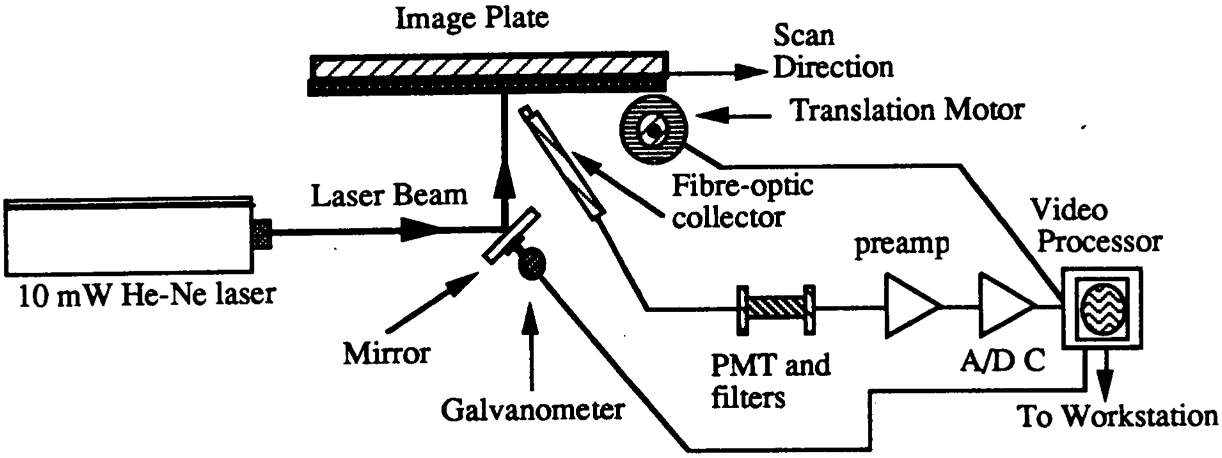

Figure 3.4 The image plate scanning process. 20x25 cm image plates are scanned with a 10 mW He-Ne laser by means of a galvanometer-controlled mirror assembly. The Gaussian beam is focused to a spot size of 88 µm at the plane of the phosphor plate which defines the "pixel size" of the image. It takes approximately 50 µsec for the laser to traverse one pixel. A DEC-5200 workstation is used for image manipulation and data analysis.

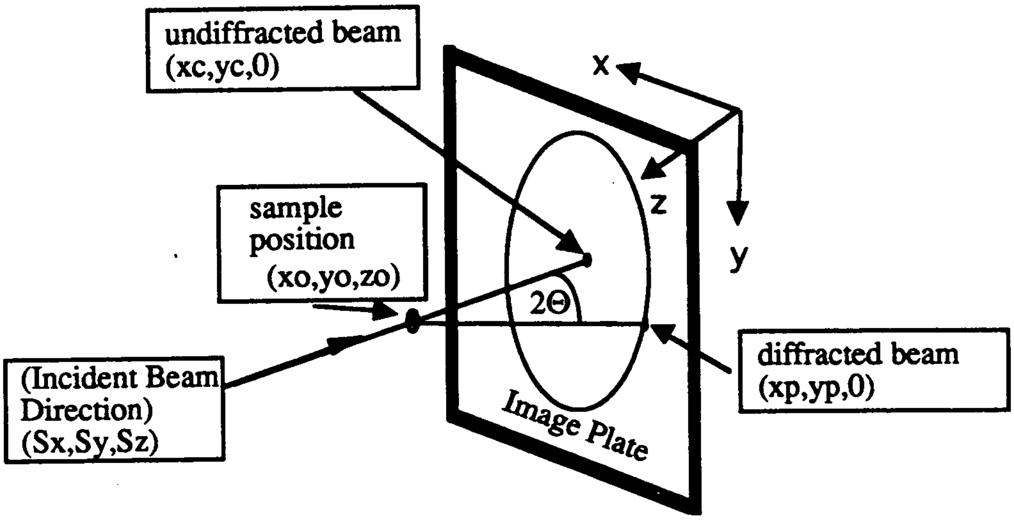

Figure 3.5 Illustration of the relative sample, plate and incident beam geometries showing the definition of the coordinate system orientation used in the subsequent analysis and azimuthal integration of the recorded image.

The relative geometry of the image plate and incident beam are shown in Figure 3.5. Assuming a perfectly flat plate surface, the relationship between pixel position $(x_p,y_p,\ )$ and the diffraction angle (Θ) is simply

$$\mathrm{Cos}(2\Theta) = \frac{(x_c - x_o, y_c - y_o, z_c - z_o)(x_p - x_o, y_p - y_o, - z_o)}{|(x_c - x_o, y_c - y_o, z_c - z_o)||(x_p - x_o, y_p - y_o, - z_o)|} \tag{3.1}$$

The sample location in space is denoted by the position vector having components (x_o,y_o,z_o) and the position on the image plate where the incident beam strikes is given by the position vector having components $(x_c,y_c,0)$. These parameters are not independent and are related by $(x_o,y_o,z_o) = (x_c,y_c,0) + R(S_x,S_y,S_z)/S_z$ which, upon substitution into (3.1), leads to

$$\mathrm{Cos}(2\Theta) = \frac{(y_p - y_c)S_y + (x_{pixel} - x_c)S_x - R/S_z}{\sqrt{(\{(R/S_z)^2 - 2(R/S_z)\}\gamma + (x_p - x_c)^2 + (y_p - y_c)^2)}} \tag{3.2}$$

$$\gamma = (x_p - x_c)S_x + (y_p - y_c)S_y \tag{3.3}$$

Of the parameters: R, the vector components of S, x_c and y_c only R (the sample to plate distance) can be determined experimentally with sufficient accuracy by a calibration method. The other parameters must be determined by a sufficiently robust algorithm which will calculate the beam centre and accommodate tilted plate geometries. The algorithm chosen proceeds as follows: The digitised image is sectored into 160 partitions as shown in Figure 3.6 and a 1D diffraction pattern for each partition is calculated. The sectors are recombined according to Equation 3.2 and initial values of S, x_c and y_c are used to form a trial 1D diffraction profile. The quantities S, x_c and y_c are then iteratively varied in an attempt to maximize the sharpness of the final 1D image [12]. The sharpness is defined as the overlap between diffraction patterns constructed from the different sectors. An illustration of the improvement in pattern quality obtainable when full azimuthal integration of the image is performed relative to various types of partial integration is shown in Figure 3.7.

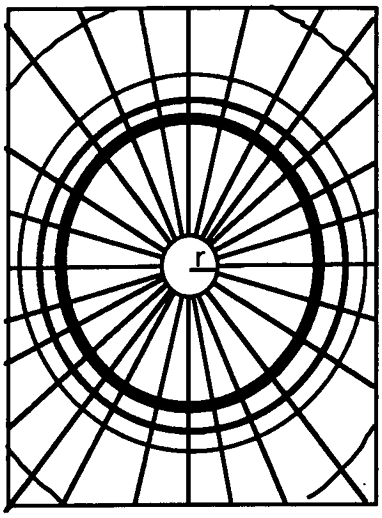

Figure 3.6. Schematic of an image plate pattern sectored over pixels a distance r from the beam centre. Sectoring the raw data represents a reduction of data points from 2800x2000 to 160 x 2500.

§3.5 Initial results: tests on standards and pattern quality

Figure 3.8 shows an azimuthally integrated 2D diffraction pattern of an La_2CuO_4 sample in a Mao-Bell DAC as collected with the image plate as well as a Rietveld least-squares fit to the data. The splitting of the diffraction peaks at 16 and 21° arises from the slight orthorhombic distortion of the unit cell at room temperature. Most Rietveld refinement packages require the the input data to be in a format in which the observed intensity is recorded as a function of discrete, equiangular steps in 2Θ. Though this is the most natural state of affairs for conventional scanning detectors for which scan limits are specified by a start and finish angle and a stepsize it is not natural for a flat plate which intercepts a cone of diffracted radiation. Instead, the data is recorded and the resulting pattern is expressed in units of pixel size. Even if the sample to plate distance is known accurately the conversion from pixels to degrees of 2Θ will not result in an equiangular spacing of the data points. One method of getting around this problem would be to modify the refinement source code so as to allow for arbitrarily spaced data points. However, by far the easiest

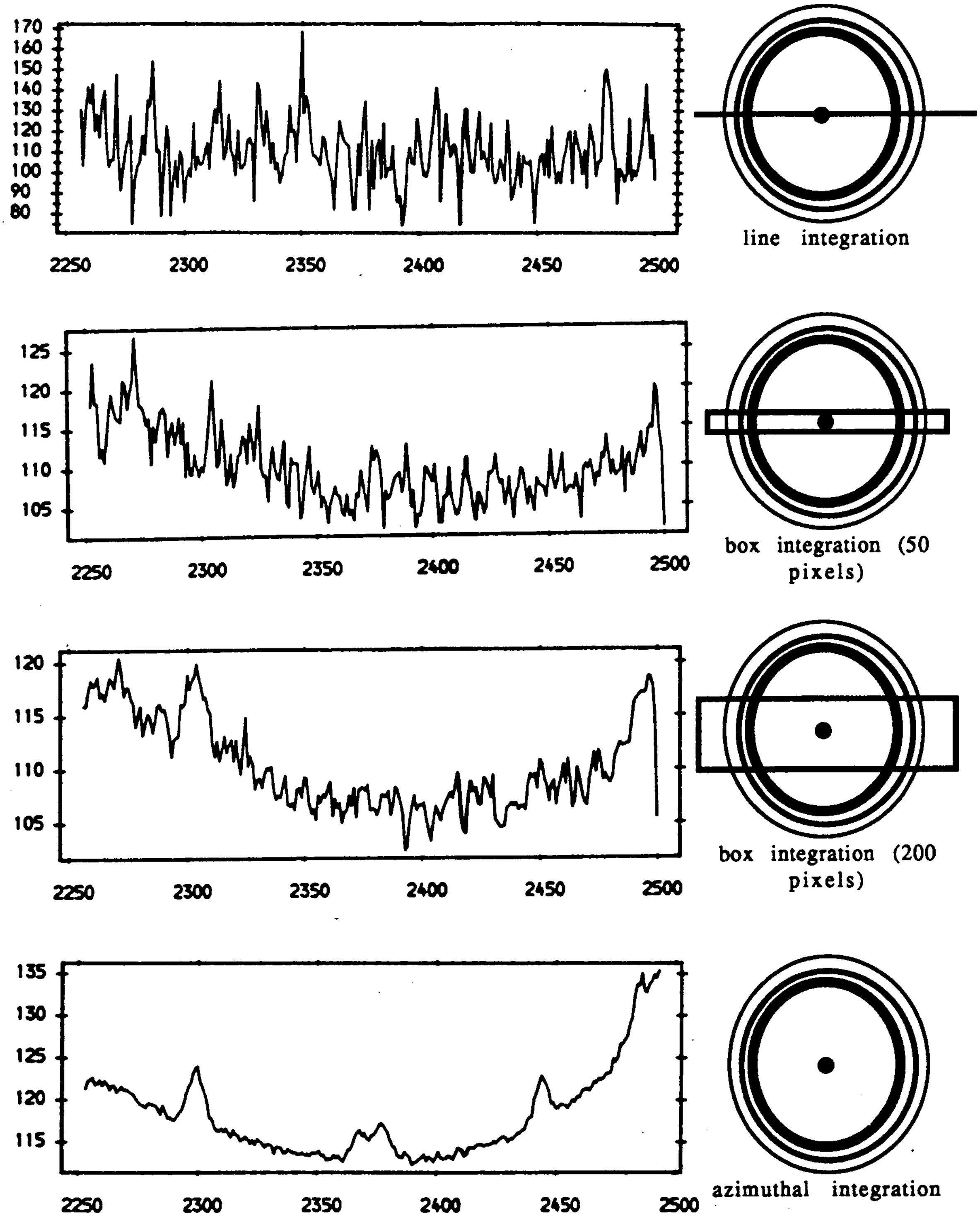

Figure 3.7 Illustration of the advantages of full azimuthal integration of the Debye-Scherrer powder diffraction rings over simpler partial integration techniques.

option, is to simply interpolate between the data points and evaluate the interpolation at equally spaced intervals. This is the practice followed for all Rietveld refinements of image plate data.

It appears that there exists a certain degree of arbitrariness in what is actually referred to as the "data" in an integrated image plate exposure. The problem does not arise in the case of a 2D image where the data is simply the intensity at a given (x,y) point on the digitised image. But the appearance of the integrated image can differ significantly depending on coarseness of the interpolation.

One of the earliest tests of the data quality obtainable on the image plate from a sample in a high pressure phase was performed on InSb as this material was to be of central importance in future studies. The sample to image plate distance was reduced so as to intercept a large amount of the diffracted beam. A one hour exposure resulted in the pattern shown in Figure 3.9.

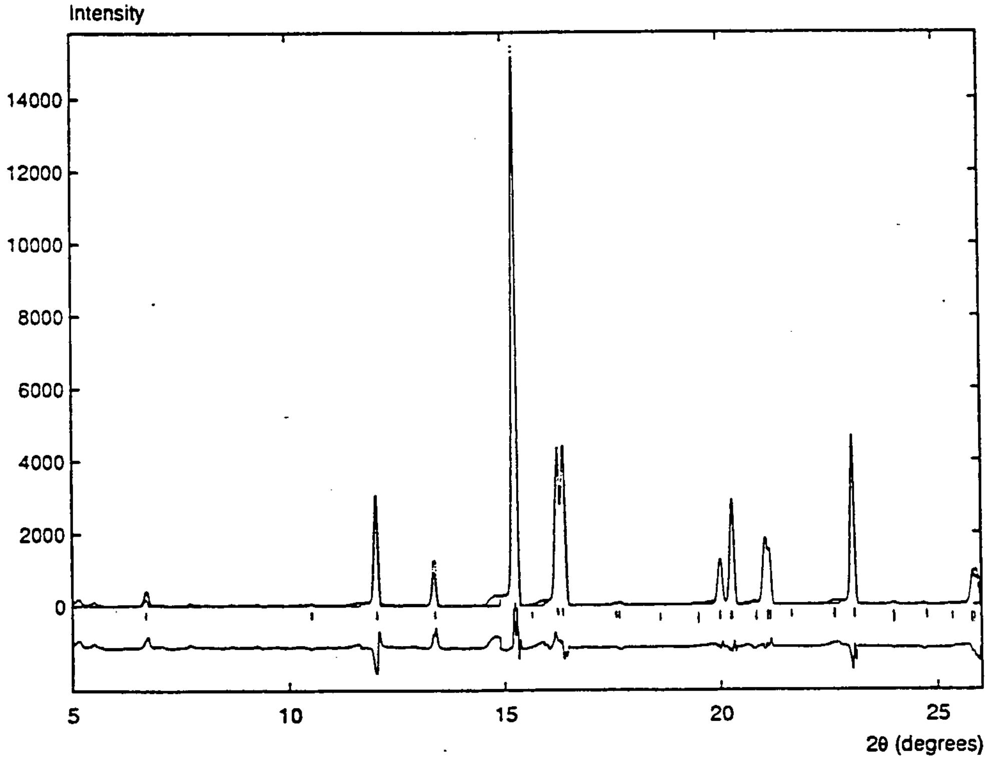

Figure 3.8 Rietveld refinement of a powder diffraction pattern of La_2CuO_4 in a Mao-Bell pressure cell at ambient pressure collected using the image plate area detector. The splitting of peaks at 16 and 21° is due to the slight orthorhombic distortion at room temperature. The features at the base of strong peaks is due to "over-reading" of the plate by the laser. This has been corrected and the effect is absent in later patterns.

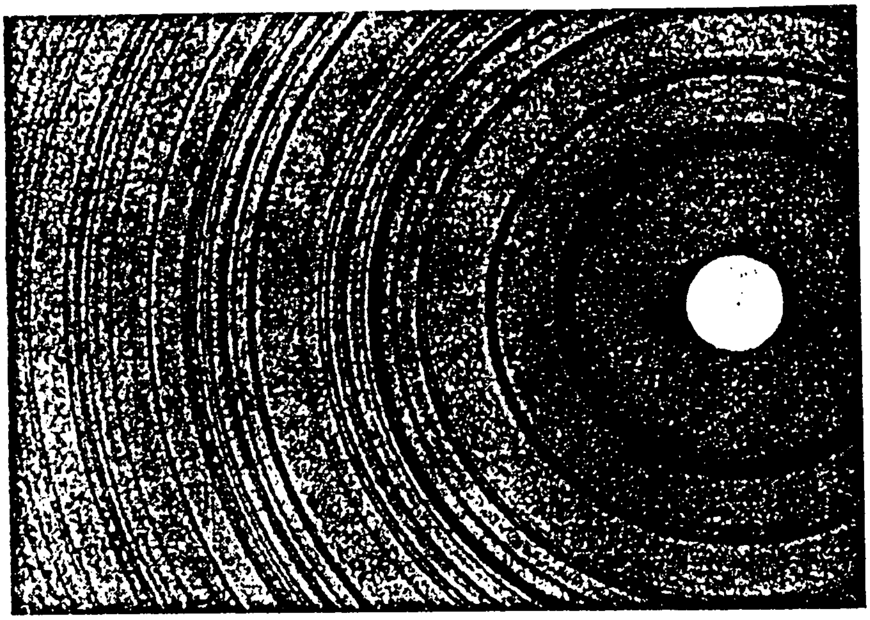

Figure 3.9a Image plate exposure of InSb in one of its high-pressure phases. The amount of information contained in the resulting integration is shown in the following figures.

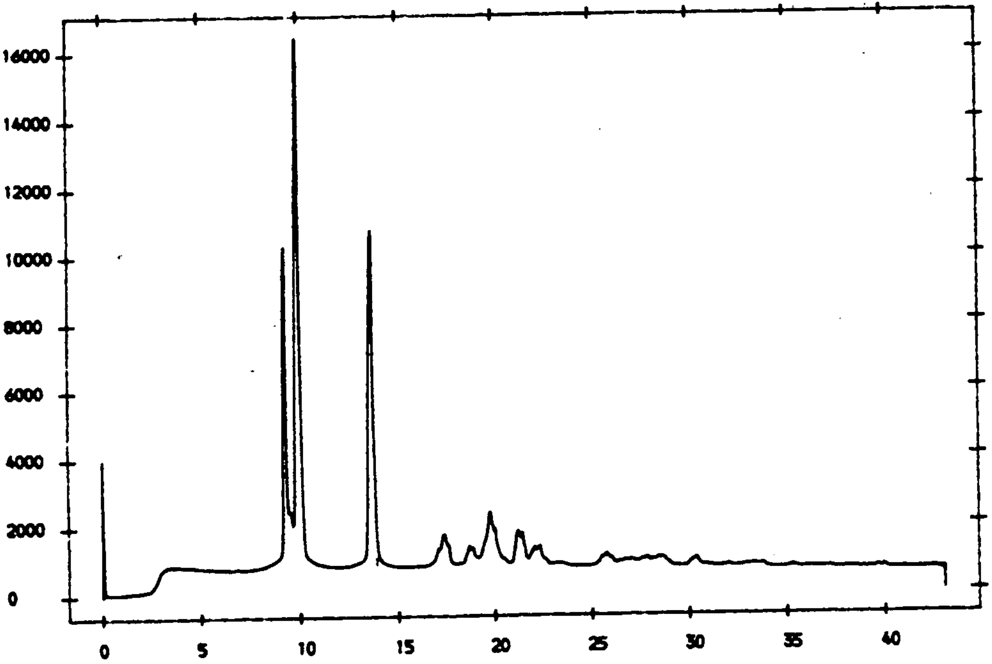

Figure 3.9b One-dimensional diffraction profile obtained by full azimuthal integration of the image shown in Figure 3.9a according to the algorithm described in the preceding sections. The exposure time required to collect this pattern was approximately 14 minutes.

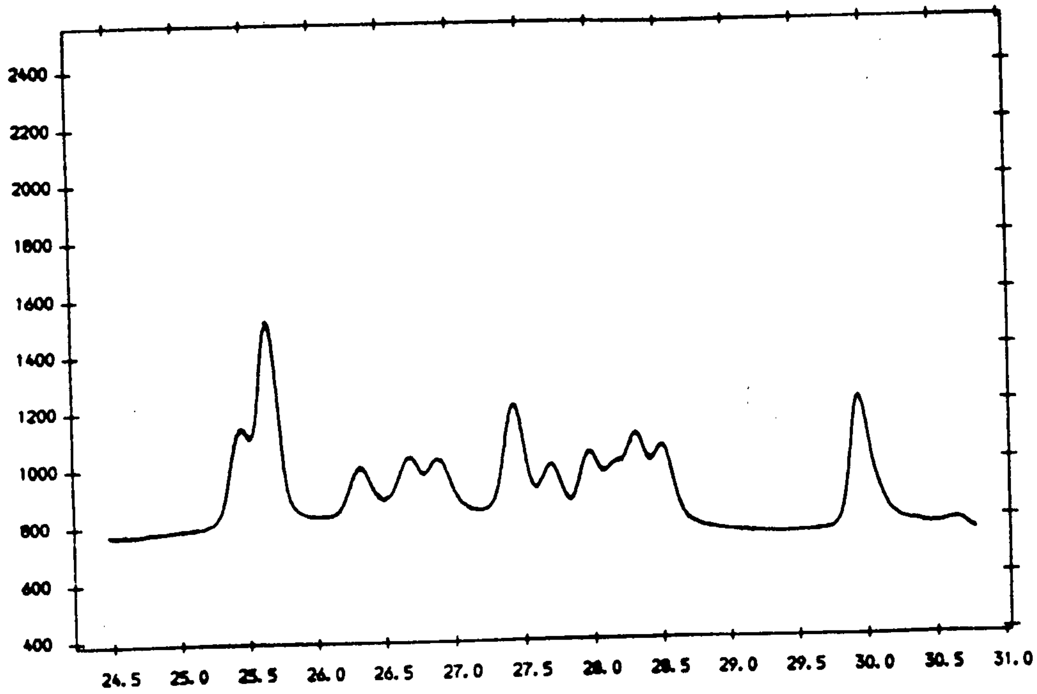

Figure 3.9c Expanded view of the profile shown in Figure 3.9a detailing the high-angle region.

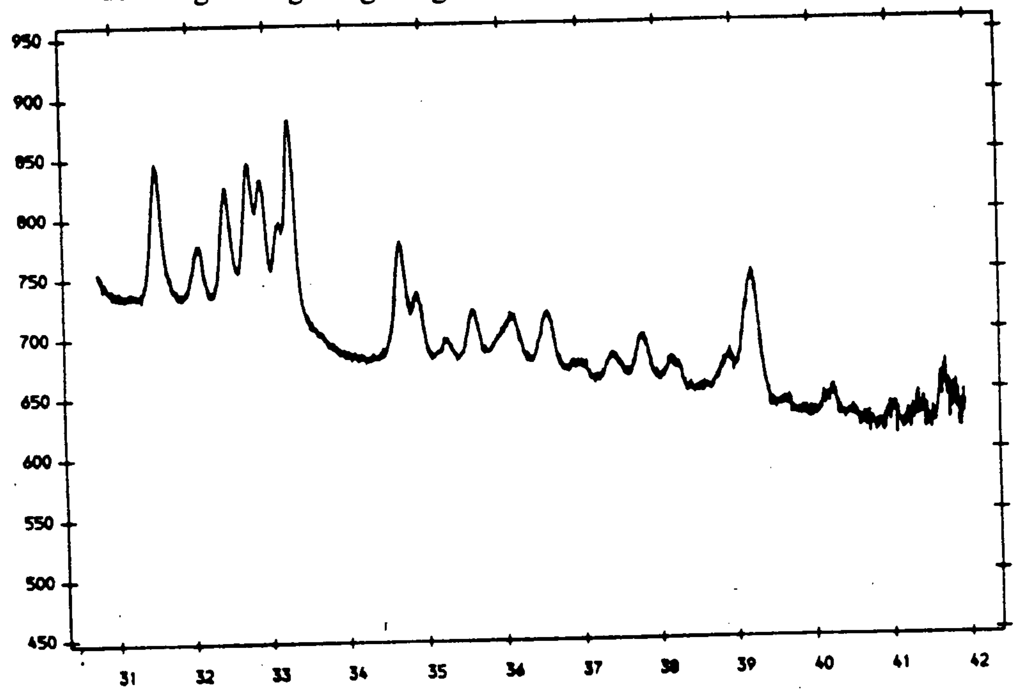

Figure 3.9d Further expanded view detailing the highest angle portions of the profile.

§3.6 Future goals and limits on the technology

There are, at present, two distinct goals in high-pressure angle-dispersive powder diffraction. The first is technique-driven, conceptually simple but non-trivial in practice. It is to extend the realm of study to increasingly higher pressures with a view towards performing angle-dispersive powder diffraction in the megabar (> 100 GPa) regime. The second goal is to exploit the potential sensitivity of detectors such as the image plate to observe subtle pressure-induced effects. This would include the study of valence fluctuations, incommensurate modulations or ordering of nearly isoelectronic species in high-pressure phases. The latter goal has , to some extent, been realized with the recent confirmation of ordering in InSb at high pressure. Potential benefits of smaller-scale image plate systems are discussed next.

In principle, a synchrotron-based image plate system for high pressure powder diffraction would be preferred over any conventional laboratory source such as a rotating anode for reasons of beam intensity and wavelength tunability. In practice, however, the advantages of a synchrotron source lead to competition for experimental time at central facilities and to restricted running schedules. In addition, the complexity of synchrotron maintenance may result in beamline shutdowns for unspecified durations. In light of these considerations it would be of interest to determine exactly what can be achieved on a conventional laboratory-based rotating anode source and whether, for at least some applications, it would be a viable alternative to a synchrotron source. The utility of such a system is briefly assessed in the present section and is based on a series of initial experiments on rotating anode sources. In addition, an outline of a preliminary rotating anode system design is given.

Results of recent preliminary test experiments using a conventional laboratory source suggest that, with proper beamline optics design, the image plate detector used in conjunction with a rotating anode x-ray source does represent a viable alternative to the synchrotron for many standard applications of high pressure structural studies. In light of the high quality of data obtainable from such a system, several experiments on InSb were performed which served to resolve outstanding issues which remained from previous image plate studies on InSb. These will be addressed in

Chapter 5. A preliminary design for a two-port rotating anode image plate system is shown in Figure 3.10.

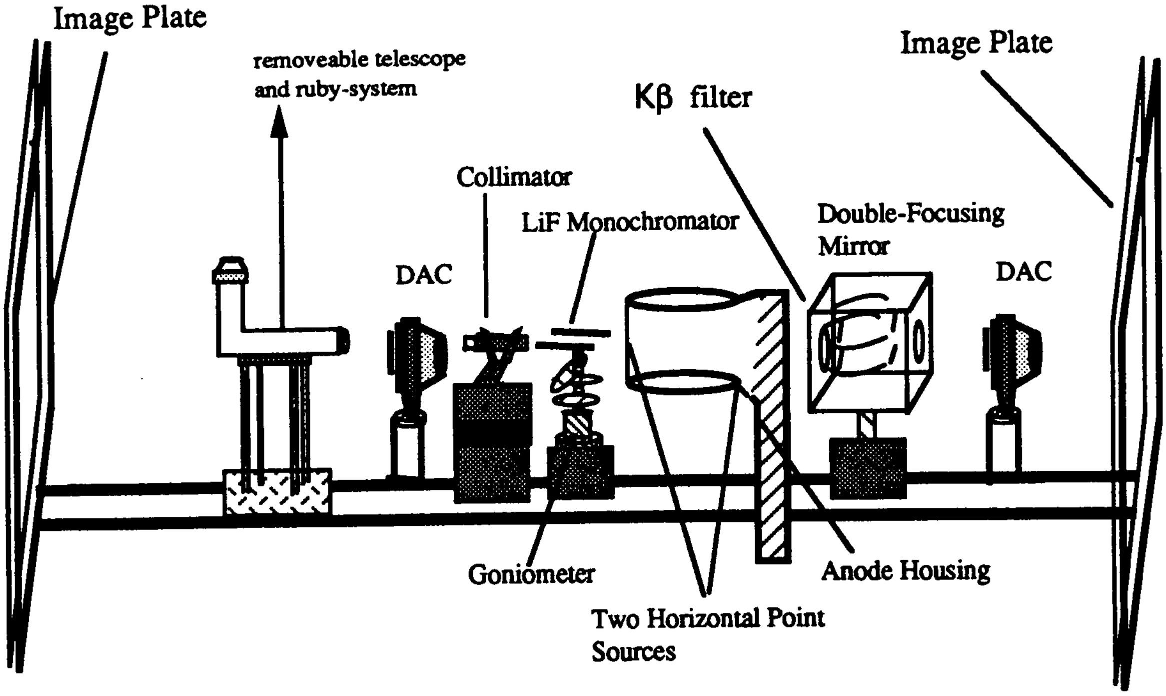

High Resolution Side High-Intensity Side

Figure 3.10 Preliminary design for a two-port rotating anode source to be based in the University of Edinburgh and used in conjunction with an image plate area detector.

---

[1] I. Tanaka, M. Yao, M. Suzuki, K. Hikichi, T Matsumoto, M. Kosasa and C. Katamiya *J. Appl Cryst.* **23** (1989) 334.

[2] Y. Amemiya, Y. Matsushita, T. Nakagawa, Y. Satow, J. Miyahara and J. Chikawa *Nucl. Instrum. Methods* **A226** (1988) 645.

[3] R.J. Nelmes, M.I. McMahon, P.D. Hatton, R.O. Piltz, J. Crain, R.J. Cernik and G. Bushnell-Wye, *High-Pressure Research* **8** (1992) 677.

[4] R.J. Nelmes, M.I. McMahon, P.D. Hatton, R.O. Piltz, J. Crain, R.J. Cernik and G. Bushnell-Wye, *Rev. Sci. Instrum*. **63** (1992) 1039.

[5] P.D. Hatton, M.I. McMahon, R.O. Piltz, J. Crain and R.J. Nelmes, *High-Pressure Research* **9** (1992) 194.

---

[6] M. Ueno, A. Onodera, O. Shimomura and K. Takamura *Phys. Rev. B* **45** (1992) 10123.

[7] M. Ueno, K. Hasegawa, R. Oshima, A. Onodera, O. Shimomura, K. Takamura,H. Nakae, T. Matsuda and T Hirai *Phys. Rev. B* **45** (1992) 10226.

[8] R.J. Nelmes, M.I. McMahon, P.D. Hatton, J. Crain, R.O. Piltz, To appear in *Jap. J. Appl. Phys.* Proceedings V-HPSP (Conference on the Physics of Semiconductors at High Pressure - 1993).

[9] A Si (111) monochromator is used on this station. The intensity of the (222) Bragg reflection at $\lambda/2$ is negligible but this is not the case for the (333) reflection at $\lambda/3$.

[10] R.F. Johnston, S.C. Pickett and D.L. Baker, *Electrophoresis* **11** (1990) 355.

[11] M. Ito and Y. Amemiya *Nuc. Instrum. and Methods* **A310** (1991) 369. This reference gives a detailed analysis of the energy dependence of performance of an image plate detector.

[12] R.O. Piltz, M.I. McMahon, J. Crain, P.D. Hatton, R.J. Nelmes, R.J. Cernik and G. Bushnell-Wye, *Rev. Sci. Instrum.* **63** (1992) 700.

CHAPTER 4

PRESSURE-INDUCED STRUCTURAL TRANSITIONS IN TETRAHEDRAL SEMICONDUCTORS

§ 4.1 Introduction

4.1.1 Historical perspective

The high pressure properties of semiconductors have been the subject of continued study for well over fifty years with both experiment and theory experiencing several revolutions of various magnitudes which served to provide continued and renewed motivation for study [1,2,3]. Before embarking on a review of these studies, the original motivation for them should be addressed.

The experimental efforts made to exploit pressure as an experimental variable, despite the complications, is due to the great richness, variety and importance of pressure-induced structural and electronic effects in solids. Controlled pressure application can alter interatomic distances to a far greater degree than can temperature variation. This reduction of interatomic separation occurs at constant thermal energy and affords a very pure and unique probe of condensed matter. These considerations are perhaps most important in the context of semiconductors at high pressure.

As will be discussed in detail in the following sections, pressure induces polymorphic metallisation transitions in semiconductors and fortunately, some of these transitions occur at experimentally accessible pressures. It therefore comes as no surprise that the III-V semiconductor InSb, with the lowest transition pressure, is perhaps the most well studied under pressure.

From the point of view of high pressure experimentation, the most influential revolution was undoubtedly the introduction of the diamond-anvil pressure cell which allows for extended hydrostatic pressure regimes to be accessed. There are numerous reviews of DAC techniques and technology and only a brief outline of basic principles will be presented in the following sections. It will be one aim of this chapter to illustrate how the image plate area detector, despite its simplicity, also represents a revolutionary advance in high-pressure structural studies.

4.1.2 Experimental

A comprehensive review of pressure-induced structural studies on tetrahedral semiconductors will not be attempted here but a detailed overview of the experimental results on several III-V and group IV semiconductors is necessary in order to put the results of the image plate project into perspective. There do exist a number of references [4,5] in the literature which treat the topic well and serve to outline the situation regarding phase transitions in these systems prior to the adaption of the image plate for high-pressure studies in 1991.

The vast majority of experimental efforts on pressure-induced structural phase transitions in III-V and elemental (group IV) semiconductors have been performed with energy-dispersive x-ray diffraction techniques. As a general rule, it is found that these materials transform from their ambient pressure, semiconducting zincblende structure to the tetragonal metallic β-Sn configuration under high pressure conditions.

Some of the earliest experimental high-pressure studies on tetrahedral semiconductors using DAC technology were designed to investigate the P-T diagram of InSb since InSb exhibits one of the lowest transition pressures of any III-V semiconductor. The first recorded high-pressure study on InSb was reported by Gebbe *et al* [6] in 1960 but the pressure-induced transition from zincblende was incorrectly attributed to a melting transition. The transition was later reinvestigated and it was confirmed [7] that the transition observed by Gebbe was indeed a solid-solid transition and that it was accompanied by a volume collapse of nearly 20%. The crystal structure of this high-pressure form of InSb was assigned to the diatomic analogue of the β-Sn structure and was subsequently referred to in the literature as InSb-II.

Although there is often agreement regarding the identification of pressure-induced phase transitions in this material there is far less accord reached about the interpretation of the diffraction patterns obtained in each of the observed phases. In all studies prior to those described here the distinction between In and Sb could not be made and it will be shown in this and subsequent chapters, how the distinction can have far-reaching implications on the understanding of pressure induced phenomena in III-V semiconductors.

Other x-ray diffraction experiments revealed pressure-induced behaviour quite different from that reported in these early studies. Kasper and Brandhorst [8] obtained no transition in InSb until a pressure of 30 kbar at which point the ambient pressure zincblende phase transformed to a simple orthorhombic structure InSb-IV having lattice constants a=2.92 Å, b=5.56 Å and c=3.06 Å. The atomic positions were reported to be at (0,0,0) and $(0,\frac{1}{2},\alpha=\frac{1}{2})$. These results prompted a long series of experiments designed to determine which of the two high-pressure forms was to be interpreted as the equilibrium form [9]. McWhan and Marezio [9] reported that passing rapidly through the transition produced InSb-II whereas slower pressure increase resulted in InSb-IV. On the basis of these results it was concluded that InSb-II was the stable high-temperature form as heating would occur during rapid increase of pressure and reconversion to the stable room-temperature phase (InSb-IV) would be very slow. These investigations also led to the discovery of another form InSb-III by Banus and Lavine which was apparently stable at elevated temperatures [10] and high-pressure (T>575K and P ~30 kbar). These workers also presented a phase diagram of InSb based on their own investigations and on the vast amount of prior work [11,12,13,14]. This phase diagram is reproduced in Figure 4.1.

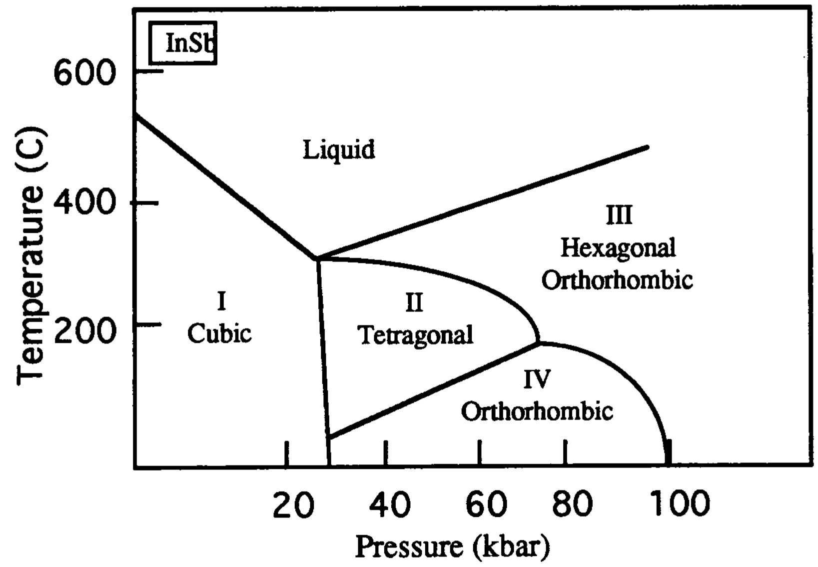

Figure 4.1 The Phase diagram of InSb as reported by Banus and Lavine [10] showing the stability fields of InSb I, II, III and IV.

Even in these early stages of structural studies on InSb there was uncertainty regarding the interpretation of the diffraction patterns. Specifically, Kasper and Brandhorst [8] suggested that the InSb-II phase may not, in fact, assume the β-Sn structure. This and any other remaining structural issues were, however, left uninvestigated for nearly ten years until InSb was reinvestigated by Yu, Spain and Skelton [15]. This was intended to be the definitive structural study of InSb under pressure. These workers obtained the same orthorhombic phase reported by Kasper and Brandhorst but suggested that the positional parameter a was equal to 0.25 rather than 0.5. The spacegroup for this phase was reported to be Pmm2. The phase diagram of Banus and Lavine suggested that heating will induce a transition to InSb-II but this was not observed. Upon heating the sample Yu, Spain and Skelton reported a transition to a new phase the structure of which they were unable to determine from their data. Further room-temperature structural studies on InSb using the energy dispersive powder method and a synchrotron radiation source [16] focussed on the cubic to InSb-IV transition which these workers reported to occur at 28 kbar but required further pressure increase for completion. A fit to their powder pattern was in general agreement with that of Yu *et al* [15] but the positional parameter was reported as 0.38 as opposed to 0.5. Consideration of the energetics associated with this structure suggest that it may, in fact, not be favourable as each atom in this six-fold coordinated structure has four identical atoms as near neighbours. This argument only holds if site-ordering of the atoms on the lattice is assumed but the features in the diffraction pattern required to determine site-ordering are too weak to be detected by conventional diffraction methods. It is generally assumed that these structures are site-ordered for the purposes of making connections with total energy calculations but there is no *a priori* justification for this in the diffraction evidence. This issue will be of central importance in the chapters which follow. Vanderbourgh *et al* [16], in an attempt to avoid the problems of having four near neighbours of the same species proposed that the true unit cell was was doubled along the a and c axes of the Pmm2 unit cell; an atom in the resulting cell then has 6 near neighbours of unlike species. Upon pressure increase from above 60 kbar new peaks arose in the diffraction pattern of Vanderbourgh *et al* [16] which could not be interpreted or indexed. This was attributed to a transition to a new phase

(InSb-V) which tends towards a hexagonal structure with increasing pressure.

Despite all these efforts a clear and consistent picture of pressure-induced structure adoption in InSb failed to materialise. Specifically, the appearance of InSb-V in the stability field of InSb-IV , the failure of Yu, Spain and Skelton to obtain InSb-II upon heating and the doubts expressed by Kasper and Brandhorst regarding the structure of InSb-II motivated the present study using an image plate area detector in its first application as a high-pressure tool for full structural determination.

The degree to which high-pressure studies have been performed on other tetrahedral semiconductors is far less extensive. This is due to the fact that other semiconductors have transition pressures far higher than that of InSb thus complicating the experimental process and subsequent analysis. Nevertheless, some results do exist and will be outlined. Energy dispersive x-ray diffraction on GaAs at high pressure suggested a transformation to the orthorhombic structure with spacegroup Pmm2. Subsequent pressure increase resulted in a further transition to a body centred orthorhombic structure with spacegroup Imm2 but the atomic ordering could not be determined [17]. Anomalous diffraction was used in an attempt to better distinguish between the constituent atoms in the Pmm2 high pressure phase but weak peaks due to antiphase scatter between Ga and As were not observed [18]. This was attributed to Ga and As atoms randomly occupying lattice sites at high pressure. This interpretation will be of central importance in subsequent sections.

4.1.3 Theoretical

As III-V semiconductors form a class of simple, isostructural compounds with topologically equivalent band structures it seems natural to attempt to construct some type of general model for pressure-induced phase transitions in these materials. Essentially the theoretical problem is to consider the system $A^{N}B^{8-N}$ where A and B represent simple metal or metalloid elements (not rare earths or transition elements) and N indicates the number of valence electrons on species A. This general family of compounds includes the tetravalent semiconductors. The hope is that with either empirical, *ab initio* techniques or methods developed from a combination of the two can lead to a global picture of the high-pressure phase transitions. The focus of the discussion will be on those members which crystallize in the zincblende structure at ambient pressure. It should be mentioned that a detailed quantitative model of first-order phase transitions is a very formidable problem due to the discontinuous changes in interaction energy associated with the large volume collapses.

One of the earliest attempts to consider pressure-induced transitions in these materials was made by Phillips [19] and Van Vechtin [20] who assumed a power-law scaling of covalent contribution to the bonding and made a connection between the dielectric constant for a semiconductor and its average optical energy gap. In compound semiconductors, the contribution to the average gap $<\Delta>$, is due to both a covalent and ionic contribution. In a nearly free electron picture, these two contributions can be viewed as producing two perturbing potentials which give rise to the energy gap. These two contributions are related to the the average gap by $<\Delta>^2 = E_h^2 + C^2$ with E_h and C being the covalent (homopolar) and ionic (charge transfer) parts, respectively. For group IV semiconductors, C = 0. Phillips and Van Vechtin define the following relationship for the ionicity f_i:

$$f_i = \frac{C^2}{<\Delta>^2}$$

For highly ionic compounds, having f_i above about 0.6, charge transfer destabilizes the tetrahedral coordination of the bond in favour of a sixfold structure. The critical value of ionicity which determines the preferred coordination is often quoted as $f_i = 0.78$. The reason this is called a dielectric theory is that the dielectric constant determines the bond polarizability which is helpful in determining the bond character and electron density. This approach allows certain insights to be gained into the relationship which exists between structure and electronic properties without the need for full-scale electronic structure calculations.

Within this model the ambient pressure zincblende structure is stabilized by the semiconducting energy gap. Upon compression of this structure, the energy difference between the bonding valence states and the antibonding conduction levels is reduced. Prior to metalisation by band closure (which would occur at nearly 30% compression in GaAs) other metallic phases intervene. The bond charge transfer to the conduction band which is required for the transition is prevented from occuring at ambient pressure by the energy gap. At high-pressure, a critical ionicity can be defined which determines whether the material will transform to the NaCl or β-Sn configuration. Despite the appeal this approach has in its general validity and simplicity, the experimental results to be presented in this chapter suggest that the actual processes involved in phase transitions in tetrahedral semiconductors are governed by processes far too subtle to be included in so general a model.

With the advent of large-scale computational facilities, reliable *ab initio* total energy calculations designed to solve the one-electron Kohn-Sham equations were developed and used to successfully describe relative structural stability and certain pressure-induced phenomena within the margin of error associated with existing experimental methods [21,22]. Generally, these methods employ the pseudopotential and frozen core approximations which are described in Chapter 2 but it must be stressed that a salient feature of all these calculations is that they are entirely comparative in nature and only a few candidate structures can be considered. It is in this respect that experimental input is most crucial in tests of these total energy calculations. Unfortunately, as has been alluded to in Chapter 3 there are serious difficulties associated with conventional high-pressure powder diffraction which often render data interpretation unreliable. As a result of this experimental limitation, the high-pressure structures of the III-V semiconductors remain largely undetermined and in no theoretical calculation can the possibility be discounted that there exist other structures with lower total energies than any of those being considered. Nevertheless the results of *ab initio* total energy methods are remarkable achievements. For the specific case of pressure-induced phase transitions in tetrahedral semiconductors a general picture has emerged but as will be argued shortly, there exist important exceptions to the attractive, simple models. The theoretical situation prior to the results of the image plate project is summarized in Figure 4.2. A brief summary of the agreement between experimental and theoretical results regarding the stable high-pressure phases of III-V semiconductors is shown in Table 5.2.

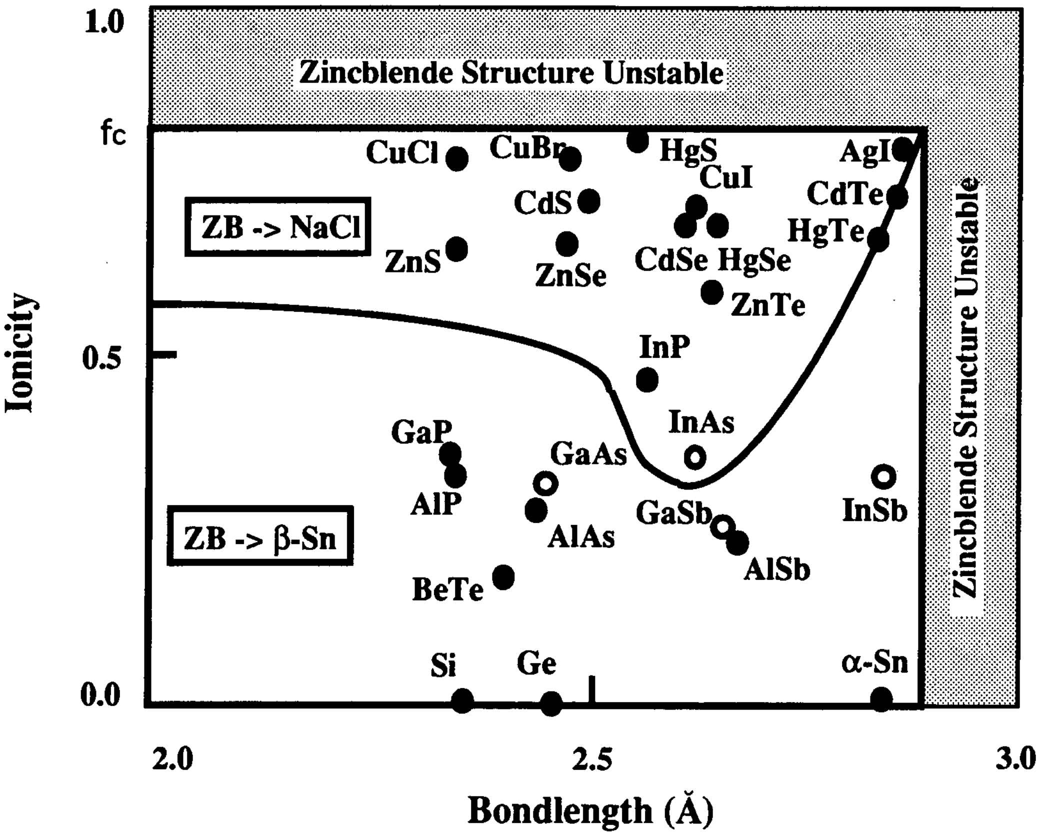

Figure 4.2 High-pressure structural trends in tetrahedral semiconductors as functions of ionicity and bondlength. Redrawn after Chelikowsky [23] showing f_c, (critical ionicity for zincblende stability). The open circles indicate the materials which will be investigated in the present work.

It should be mentioned that the calculated energy differences between candidate structures of prototypical III-V, II-VI and I-VII semiconductors show a distinct trend. as illustrated in Figure 4.3. For the more ionic compounds the energy differences are found to be quite large whereas for the mixed covalent/ionic materials such as III-V's the calculated differences are quite small. As a result, they require great care in computation because convergence with respect to Brillouin-zone sampling , basis functions, and self-consistent iteration cycles become increasingly important as the energy differences decrease. The issues regarding sampling density of the Brillouin zone are greatly compounded by the fact the high-pressure phases of these materials are metallic. This and other questions regarding convergence of total energy calculations in metals will be deferred until the following chapters.

The situation as presented above is, however, slightly

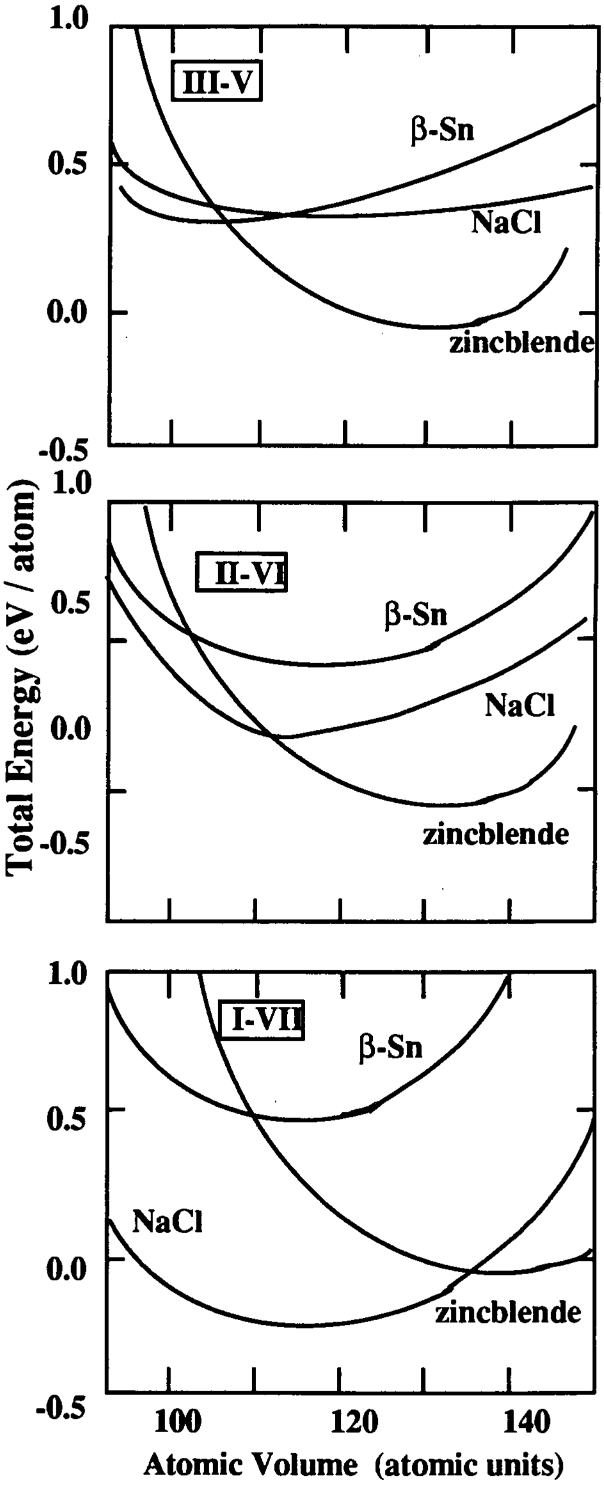

Figure 4.3 Calculated equation of state curves for ambient and high-pressure forms of prototypical semiconductors. After Chelikowsky [23].

misleading in that, in addition to there being a trend in total energy differences between structures depending on a material's ionicity, there is also a trend in the degree to which LDA techniques are in accord with experiment. It is generally found that LDA treatments of highly ionic materials tend to result in poorer agreement with experiment than do more covalent materials. As the focus of this and following chapters is on III-V materials where good agreement is obtained, detailed discussion of these discrepancies will be omitted.

§ 4.2 Image plate studies on InSb

4.2.1 Experimental details

Source

All the x-ray diffraction data presented in this section were collected on the powder diffraction station (9.1) of the Synchrotron Radiation Source (SRS) at Daresbury Laboratory. The wavelength on this station was tunable between 0.40 Å and 2.90 Å and was selected using a Si(111) double crystal monochromator. Although the (222) Bragg reflection of Si is extremely weak the (333) is often not negligible and the signal due to this harmonic may have to be attenuated depending on the choice of operating wavelength. The details of shielding and beamline optics including collimation have been given in the preceding chapter and can also be found in several recent references [24].

Diamond Anvil Cells and Samples

Diamond Anvil Cells (DACs) of the Merrill-Bassett and "Diacell" design type were used in these studies. Both have conical apertures with a maximum scattering angle in excess of $2\theta = 40°$. Samples of InSb having purities of 99.99% and 99.9999% were used and were finely ground and then floated in alcohol to obtain the finest possible powder. The samples were loaded into DACs along with a 4:1 mixture of methanol and ethanol. Pressures approaching 50 kbar were intended to be reached in this study which limited the sample chamber diameter to between 150 and 250 µm. The hydrostatic pressure was measured using the wavelength shift of the R_1 ruby fluorescence line [25] The synchrotron beam was collimated to a diameter of less than half that of the sample chamber in order to avoid scatter from sides of the gasket.

Wavelength Calibration

It was anticipated that, due to the nearly isoelectronic nature of the constituent atoms (In and Sb) anomalous scattering near the absorption edge of In would be required to confirm long-range crystalline order in the high-pressure phases. As a result the operating wavelength must be calibrated accurately. Such care would normally not be required since the accurate determination of cell dimensions and compressibilities are of secondary importance.

In general a 2-Θ scan of the Bragg peaks of a standard Si capillary sample was performed and the measured peaks fitted to a pseudo-voight function. The wavelength could then be determined to a few parts in 10^4 by varying it until the measured and calculated peak positions were coincident with those corresponding to the Si. To determine position of the In-K absorption edge, the absorption of a sample of InSb in a capillary was measured as a function of wavelength. As will be discussed in more detail in what follows the application of absorption edge effects will be of extreme importance to the success of these experiments.

4.2.2 Results for the zincblende to β-Sn transition in InSb

A structural phase transition in InSb is observed to occur at approximately 20 kbar and is found to be nearly complete by 23 kbar. The very earliest observable stages of the transition as evidenced in the diffraction pattern are shown in Figure 4.4. The observed peak positions in the pattern obtained after the transition had proceeded to near-completion (Figure 4.5(a)) suggest a tetragonal body-centred lattice and the relative peak intensities are consistent with an atomic arrangement consistent with that of the β-Sn structure. All atomic positional parameters in this structure are fixed by the spacegroup symmetry. This tetragonal phase is not identified with that of the orthorhombic InSb-II which is the implied stable structure at this pressure according to the Banus and Lavine phase diagram [13]. Figure 4.5a shows the integrated diffraction pattern of the tetragonal phase as recorded on the image plate. A least-squares fit to this profile is shown in Figure 4.5(b). The fit was made using the β-Sn configuration as the assumed structure and the refined lattice parameters were determined to be a = 5.697(1) Å, c = 3.104(1) Å. Unit cell indexing and observed and calculated d-spacings are shown in Table 4.1.

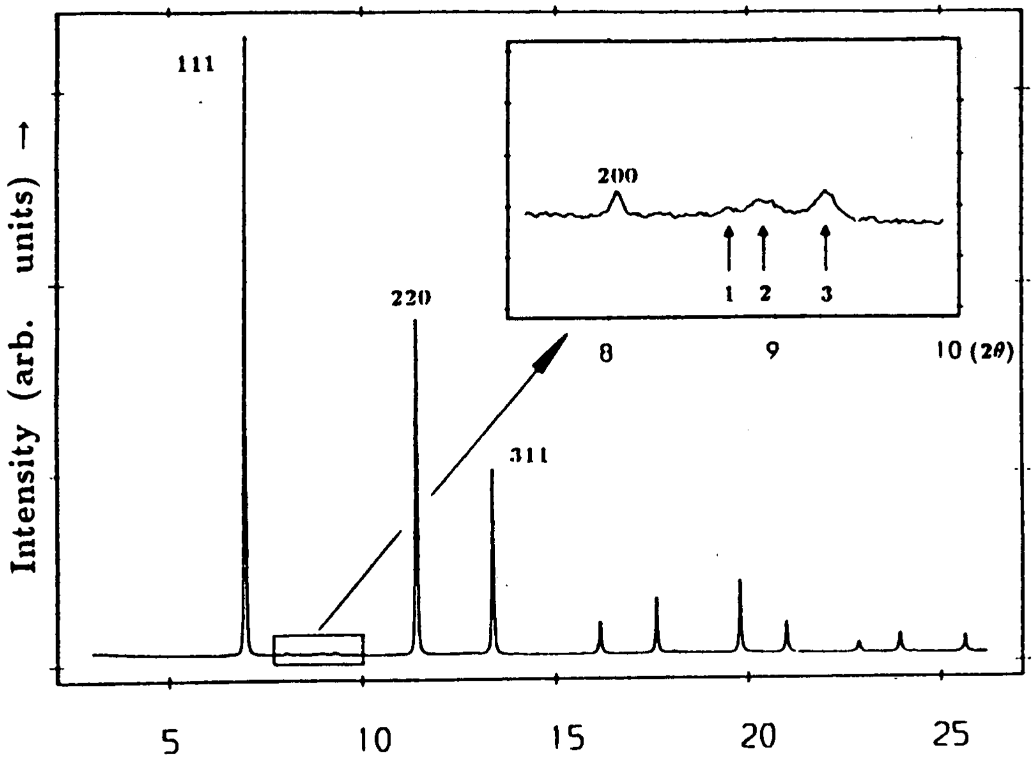

Figure 4.4 Image plate diffraction pattern of InSb collected in the primarily cubic phase but illustrating weak features (inset) associated with the incipient transition to the β-Sn and orthorhombic phases. The pattern was collected at approximately 21 kbar. The (111), (220), (200) and (311) lines of the cubic phase are indexed. The weak (200) "difference" reflection of the cubic phase arises from the nearly exact cancellation of In and Sb antiphase scattering.

Table 4.1 Observed and calculated d-spacings and reflection indices for the β-Sn high-pressure phase of InSb.

hkl	d_{obs}	d_{calc}	δd
200	2.850	2.848	0.002
101	2.728	2.725	0.003
220	2.010	2.014	-0.004
211	1.974	1.969	0.005
301	1.618	1.620	-0.002
112	1.448	1.448	0.000
400	not resolved	1.424	n/a
231	1.406	1.408	-0.002
240	1.272	1.274	-0.002
141	not resolved	1.262	n/a
312	1.176	1.176	0.000

431/051	1.068	1.070	-0.002
103/332	1.016	1.018/1.016	+/- 0.002
440/531	1.001	1.007/1.001	+/- 0.006

The quality of the resulting fit suggests that the model is appropriate, however there are features which are evident in the diffraction pattern which require further discussion. There are peaks from a minority component of another high pressure phase in this pattern which will be discussed in detail later. The weak but allowed 110 reflection of the β-Sn phase is apparently absent from the diffraction pattern. This reflection is due to the difference in scattering strength between the constituent In and Sb atoms and therefore would be strictly absent if the scattering strengths were equal. The x-ray scattering strengths of In and Sb are very similar but not identical suggesting that such difference scattering in InSb will be weak but it was easily observable in the zincblende phase even without resorting to anomalous diffraction. Also, simulations suggests that under anomalous diffraction conditions coupled with full integration around the Debye-Scherrer rings, this weak feature of the diffraction pattern should be clearly visible in this high-pressure phase.

There are however, two conditions which must be satisfied (and are in a perfect crystal) in order for this reflection to be visible. Firstly, the crystal must exhibit well-ordered occupation of the lattice sites by the atomic species. In other words, "difference" reflections such as the (110) in the diatomic β-Sn structure are observable only if the structure is site-ordered over a lengthscale comparable to the coherence length of the radiation. A sketch of the ordered unit cell is shown in Figure 4.9. The other condition is that reflections in the <110> direction (in this case) must not be significantly broader than other reflections. Such a situation might arise if stacking faults of a particular orientation were formed at the transition. In the present case of the (110) reflection in the β-Sn phase of InSb, the (220) in-phase refection is not observed to be significantly broader than others and simulations suggest that the 110 difference peak, though weak, should be clearly observed if it were of the same width as the (220) reflection (Figure 4.5(b), inset (x1 curve)). Furthermore, simulations also indicate that a preferential broadening of the difference peak (relative to the 220 reflection) by a factor of roughly 8 would be required to render the difference scattering indistinguishable from a smoothly varying background (Figure 4.5(b), inset (x3 and x8 curves)). It should be mentioned that there is some degree of anisotropic peak broadening, suggestive of crystalline imperfections, evident in the diffraction pattern with reflections of index (h00) being broader than all others. A simple tentative explanation for these observations is that the lattice sites of the β–Sn structure of InSb are randomly occupied by the constituent atoms. In addition, crystalline imperfections such as twin boundaries or stacking faults also appear to be present. Certain aspects of this interpretation will be reassessed later in section 4.2.6 in light of further experimental observations.

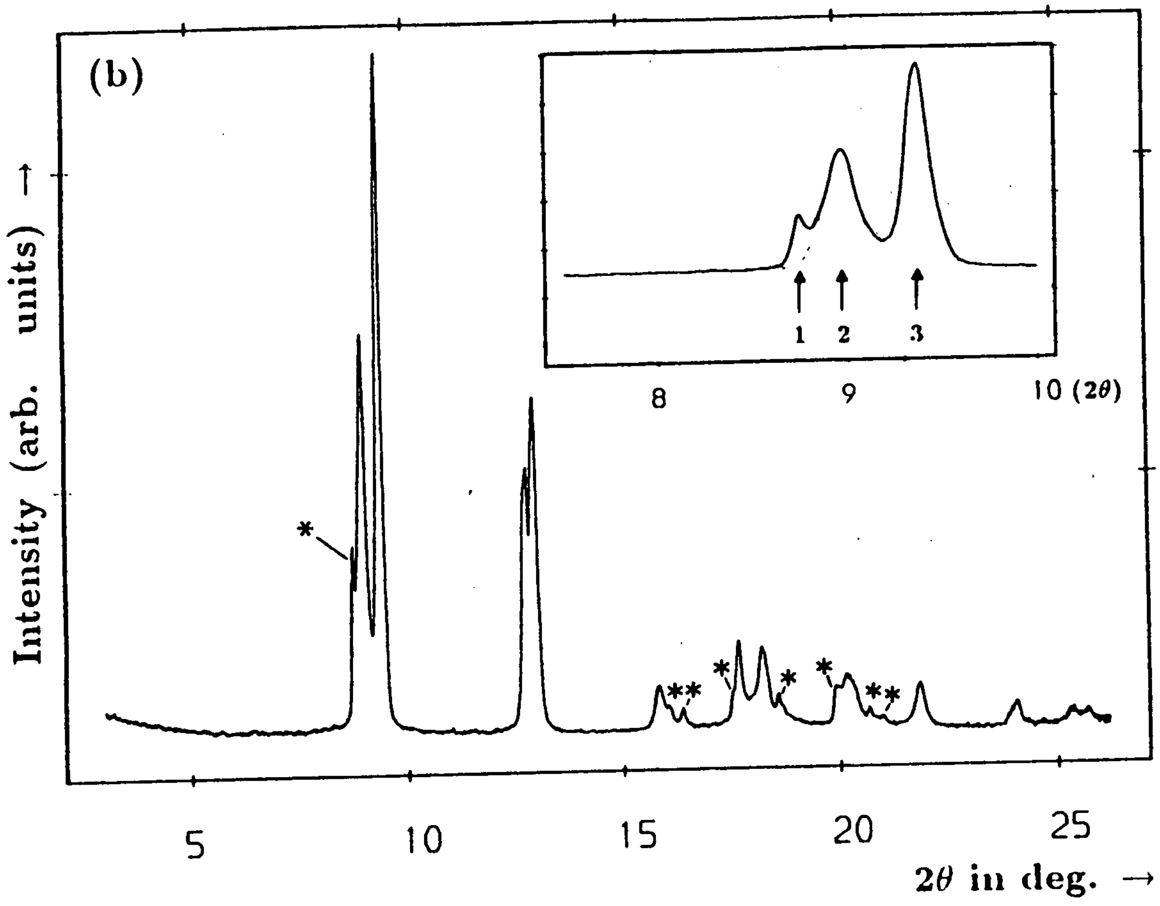

Figure 4.5(a) Diffraction pattern of the β-Sn primary phase. The secondary phase will be discussed in more detail in the following section but the features in the diffraction profile due to this phase are indicated by *-symbols.

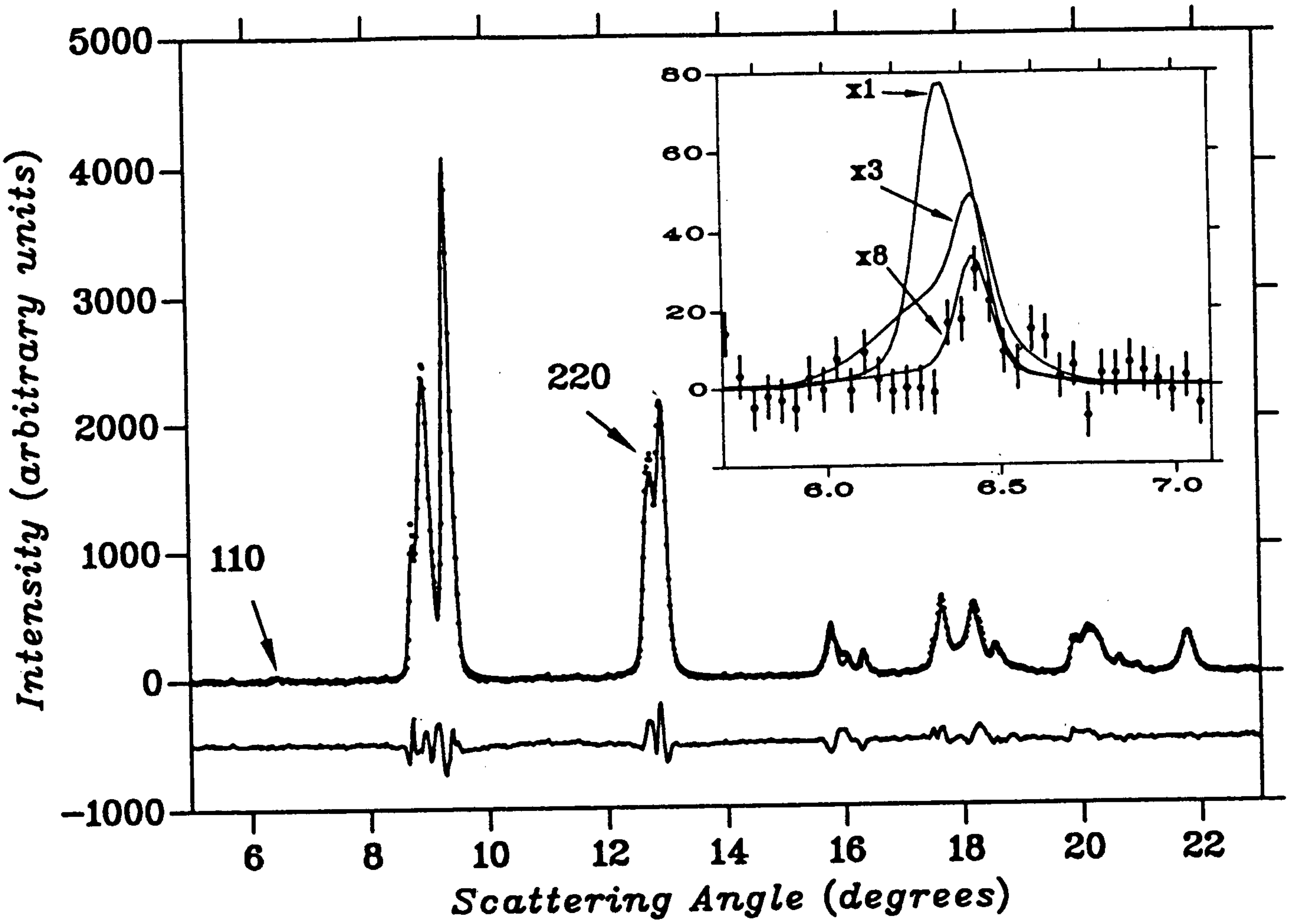

Figure 4.5(b) Two-component Rietveld least squares fit to the diffraction pattern of InSb collected in the β-Sn primary phase. The secondary phase will be discussed in more detail in the following section. The inset shows the degree of preferential broadening which would be required to render the (unobserved) difference scattering indistinguishable from a smoothly varying background. The weak peak at 6.45° is due to difference scattering from a minority component which is also present.

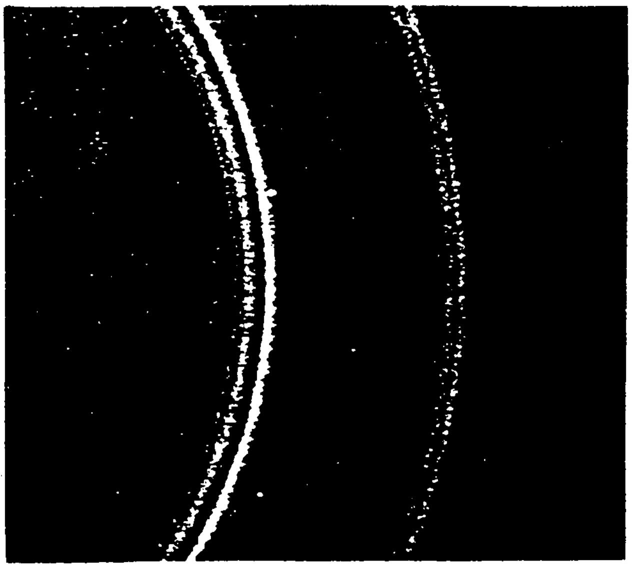

Figure 4.5(c) Two-dimensional diffraction pattern collected in the β-Sn primary phase. Subsequent azimuthal integration of this pattern results in the one-dimensional profiles shown in Figures 4.5 a and b.

4.2.3 β-Sn to BCO structural transition in InSb

The zincblende to β-Sn transition is observed to take place only over a very narrow pressure range. The β-Sn high-pressure phase of InSb is observed to transform over time or under slight pressure increase to yet another high-pressure structural form. This new structure of InSb is similar to but distinct from that of β-Sn. Indexing of the diffraction profile (Shown in Figure 4.6 (a)) indicates an orthorhombic unit cell. Reflections found to be absent from the profile were given by the condition h+k+l = odd suggesting body-centering of the unit cell. The best fit to the diffraction pattern was obtained by assuming the Imm2 spacegroup. The proposed crystal structure for this phase is shown in Figure 4.10 and is characterised by a single atomic positional parameter, denoted by u, which is not fixed by the spacegroup symmetry. In all patterns collected in this high-pressure phase a small minority component of the β-Sn phase remains. A least squares fit (Figure 4.6(b)) to the diffraction pattern of this orthorhombic phase suggests that the positional parameter u is approximately equal to 0.47 in fractional units.

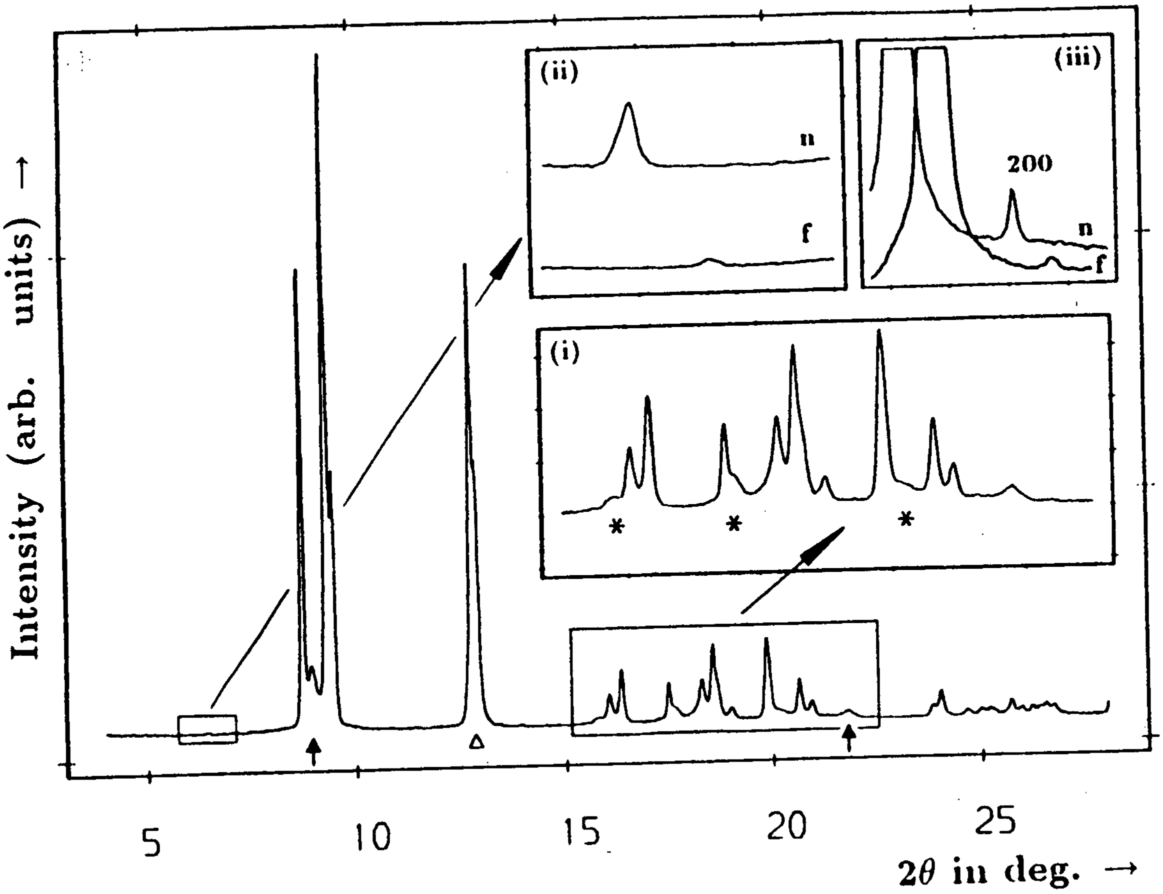

Figure 4.6(a) The diffraction pattern of InSb collected in the BCO primary phase. The minority β-Sn phase also contributes weak features to the profile which are marked by arrows for the non-overlapped minority phase lines. The pattern was collected at a pressure slightly above 21 kbar. Insets ii and iii show the behaviour of the (110) and (200) difference reflections near (n) and far (f) from the In-absorption edge. Other contributions to the profile from the β-Sn phase (inset i) are manifested by the broadened base of peaks from the β-Sn phase (Δ) and as shoulders from overlapped lines (*).

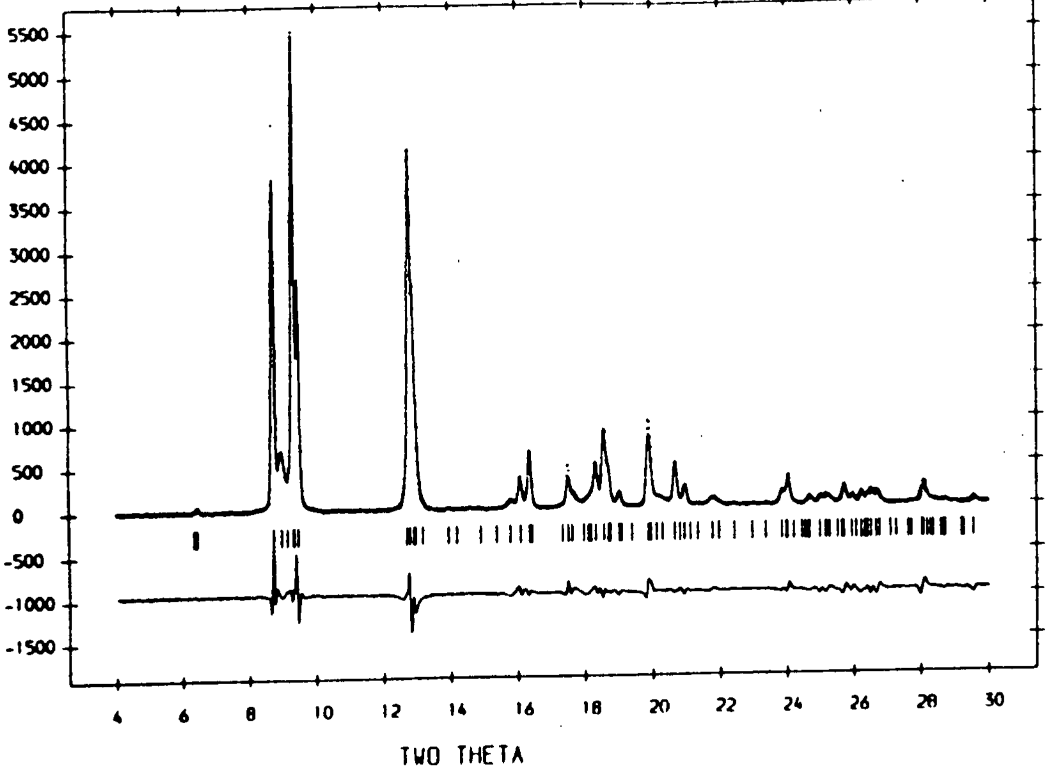

Figure 4.6(b) The Rietveld least-squares fit to the diffraction pattern shown in 4.3 (a) assuming the Imm2 spacegroup. The minority β-Sn component was also included in the refinement.

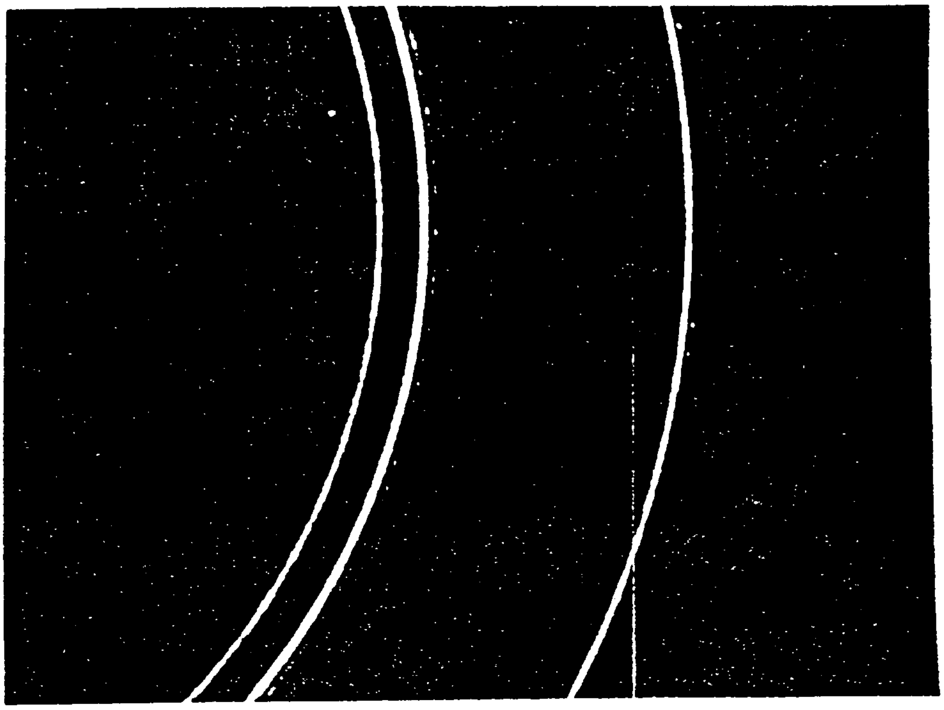

Figure 4.6(c) Two-dimensional diffraction pattern as collected on the image plate. Subsequent azimuthal integration of this pattern results in the standard one-dimensional representations shown in 4.6(a) and 4.6(b).The exposure time was approximately 15 minutes.

Perhaps the most significant feature evident in the diffraction pattern of this phase is the clear observation of difference scattering which is most obvious in the (110) reflection at 6.5°. Confirmation that this reflection does indeed represent scattering due to alternate planes of ordered In and Sb atoms can be made by examining the intensity of this reflection near the absorption edge of InSb. This is illustrated in Inset (ii and iii) of Figure 4.6a. No prior application of absorption edge effects under high pressure has been found in the literature though it has proven to be an indispensable technique for the present study.

The BCO structure has not previously been a candidate structure in total energy calculations of structural stability in III-V semiconductors, many of which suggested that the β-Sn form would be the stable one at high pressures. It is useful to view the present results within the framework of previous reports on the high-pressure phenomenology of InSb obtained with more conventional techniques. Specifically, the β-Sn structure (InSb-II) might easily manifest itself in a diffraction profile as a lower resolution form of the pattern collected in the Imm2 phase. The situation is depicted in Table 4.2.

The definitive experimental results from the image plate implies that the body-centred orthorhombic high-pressure form of InSb should be included as a candidate structure in comparative total energy calculations and Chapter 5 describes a preliminary attempt to do this. In chapter 5 the results of a full-potential linear augmented plane wave (FLAPW) study of the tetragonal β-Sn and body-centred orthorhombic (BCO) structures are presented.

4.2.4 The stable high-pressure form of InSb up to 50 kbar: modulation of the BCO structure

After the β-Sn to BCO transition is complete even the BCO high-pressure phase appears to be unstable, under certain conditions, with respect to a further deformation to a much lower symmetry structure. Over time and without any intentional change of conditions the continuous Debye-Scherrer rings characteristic of the BCO phase slowly become discontinuous. This behaviour is attributed to increasing crystallite size and has been observed previously in high-temperature x-ray studies using photographic techniques of recrystalization and grain growth.

Table 4.2 Illustration of the possible reason for the prior misidentification of the Imm2 structure as β-Sn. The groups of reflections shown in brackets may not be resolved by lower resolution techniques. Structural parameters are also given in these phases. V stands for unit cell volume.

hkl for Imm2	2Θ at λ= 0.4446 Å	Average Peak Position †	McWhan and Marezio observed position*	β-Sn calculated peak positions*	hkl for β-Sn
200	8.72	8.72	8.79	8.80	200
011	9.31				101
020	9.47	9.36	9.39	9.33	
211	12.75			12.46	220
220	12.88	12.79	12.87	12.84	
002	16.05				211
031	16.35	16.25	17.53		
400	17.49	17.49	17.53	17.64	112
202	18.30			17.66	400
231	18.55	18.56	18.62	17.92	231
022	18.66				
040	19.03				
411	19.86			19.77	240
420	19.92	19.88	19.99	20.00	141
222	20.65				
240	20.96	20.75	20.79	21.66	312
402	23.85				
431	24.05	23.98	24.00	23.65	501

Imm2 structural parameters		β-Sn structural parameters	
a(Å)	5.847(1)	a(Å)	5.79
b(Å)	5.388(1)	b(Å)	5.79
c(Å)	3.181(1)	c(Å)	3.10
V(Å^3)	100.21(4)	V(Å^3)	103.9

†Average position is weighted peak intensities

*peak positions are re-expressed in terms of the incident wavelength used in the image plate experiments

As this process continues to completion it becomes evident that while almost all discontinuous rings are coincident with those of the BCO pattern some new discontinuous rings appear which are not. The implication of this is that the phase which gives rise to these discontinuous rings is of lower symmetry than that of the BCO phase. It should be mentioned that the β-Sn phase is still present at this stage

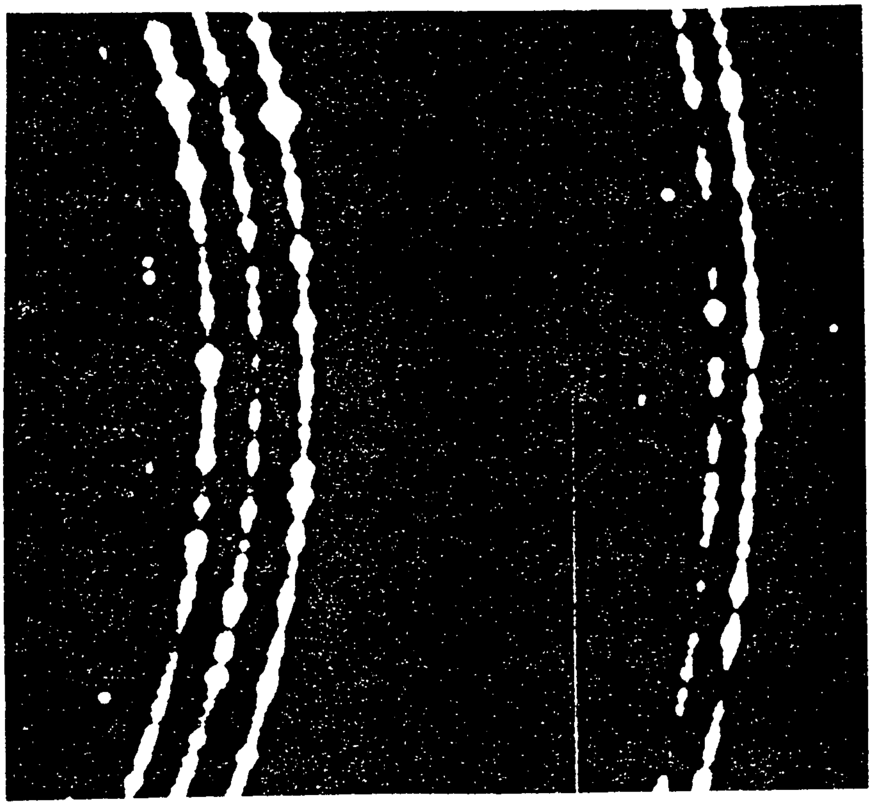

Figure 4.7(a) 2-Dimensional diffraction pattern of InSb recorded using an image plate at 25 kbar and 100°C illustrating the speckled nature of the diffraction pattern which is one of the obvious signatures of the transition to the modulated structure.

and does not decrease in volume fraction over time or under pressure increase.

The crystallographic nature of the superstructure to which the BCO phase transforms will be discussed next. The strong reflections of the supercell pattern are indexable on a simple orthorhombic unit cell with dimensions a = 2.925 Å b = 5.617 Å and c = 3.0647 Å and having spacegroup symmetry Pmm2. Further crystallographic information can be found in reference [26]. This structure is consistent with that proposed for InSb by Yu, Spain and Skelton [16]. In addition to these reflections there are many weaker reflections present which suggest that the true unit cell is much larger and may in fact be directly related to the BCO phase by a simple modulation. A 2a x 3b x 2c unit cell is found to successfully account for all of the observed superstructure reflections and the absence conditions suggested by this indexing imply A-face-centering. If this model is correct and the supercell can be considered as a modulation of the BCO structure then absorption edge effects should be observable in the diffraction pattern of this phase to a similar degree as they were in the BCO phase. This is found to be the case as illustrated in Figure 4.7(b) which is the azimuthal integration of the 2D image shown in Figure 4.7(a).

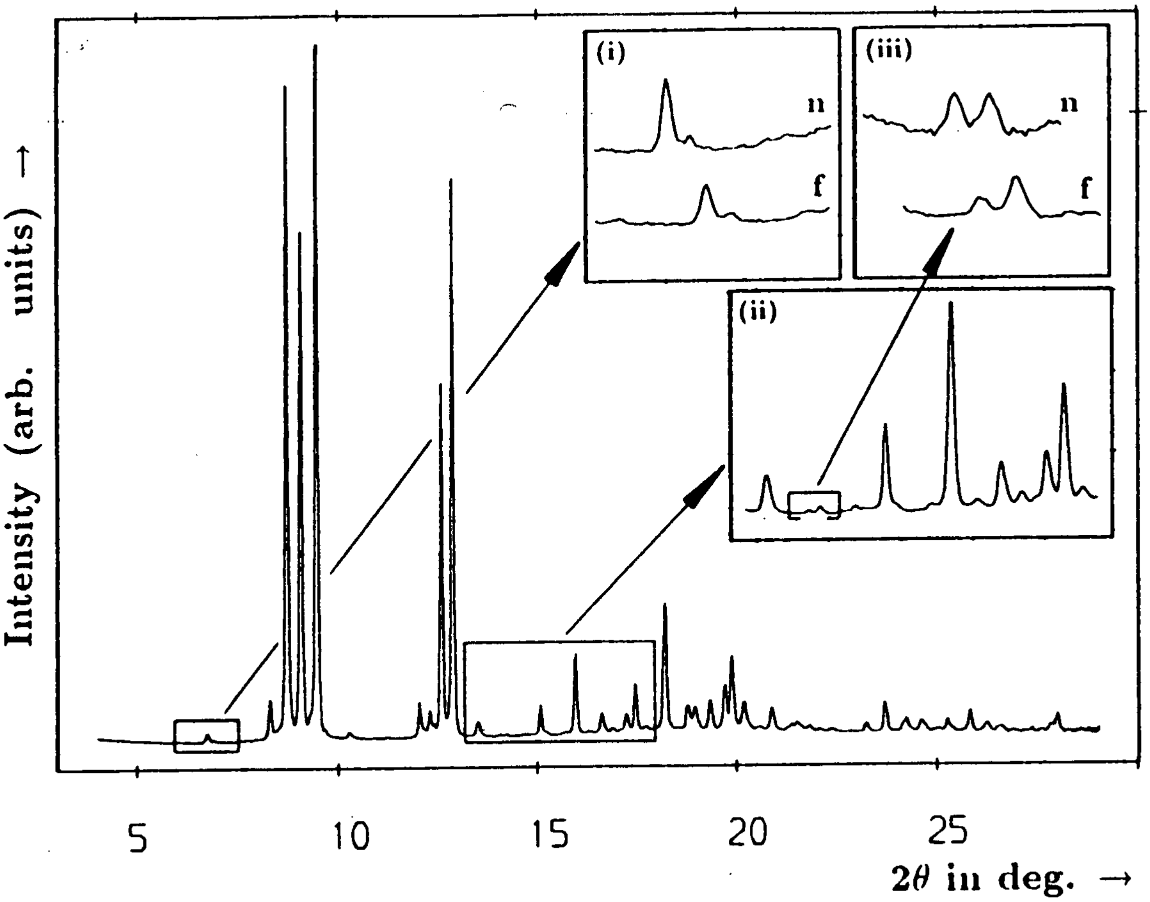

Figure 4.7(b) Azimuthal integration of the diffraction pattern shown in Figure 4.7(a) Inset (i) illustrates the response of a weak low-angle reflection to changes in incident wavelength as the K-absorption edge of In is approached. The labels 'n' and 'f' refer to exposures at incident wavelengths near (n) and far (f) from this edge. Inset (ii) shows a similar behaviour for other reflections and inset (iii) shows this region enlarged still further and is a testament to the wealth of structural information available using the image plate method in conjunction with more conventional powder diffraction technology. The exposure time taken for this pattern was less than 2.5 hours.

4.2.5 Comments on the diffraction pattern of the modulated structure

The structure corresponding to what appears to be the stable high-pressure form of InSb gives rise to a very distinctive diffraction pattern which can only be successfully interpreted using an area detector system such as the image plate. The speckled rings associated with this pattern would presumably cause unreliable relative intensities to be recorded by a conventional scanning diffractometer. Although the image plate seems ideally suited to the observation of such a pattern, the interpretations of the observations are not entirely obvious. One very general line of reasoning does seem to account for the results: the β-Sn to BCO to modulated BCO sequence of phase transitions is consistent with successive increases in domain size with the modulated structure having the largest domains which give rise to the speckled diffraction image.

Several questions arise, however, if this interpretation is made:

1) If the modulated structure is the stable high-pressure form, are the intermediate phases required kinetically?

2) Is there a connection between structure and domain size as is implied by the present results?

3) How does the domain size actually change in each of these phases?

Question 1 has already been partially addressed experimentally. For conditions intended to be identical to those under which the cubic to β-Sn transition at 21 kbar was observed cases were found in which no transition occurred until 30 kbar when an apparently direct cubic to modulated BCO transition was observed with apparently no intermediate structures being formed. When this type of direct transition takes place the discrete powder rings characteristic of this phase are not observed. Instead, continuous rings are found at angles corresponding to the modulated BCO structure (the integration of which is shown in Figure 4.8). It should also be noted that the relative intensities of the powder profiles collected in the modulated phase appear to depend on whether the transition route proceeds directly from the zincblende phase or by transiting the BCO phase. This situation can be explained without invoking yet another structure by attributing the differences to severe preferred orientation effects present after the direct transition. The modulated pattern collected after transiting the BCO phase would, according this interpretation, be the most faithful representation of the actual structure. Of course, other types of modulations within the supercell could also be present, thus affecting the relative intensities.

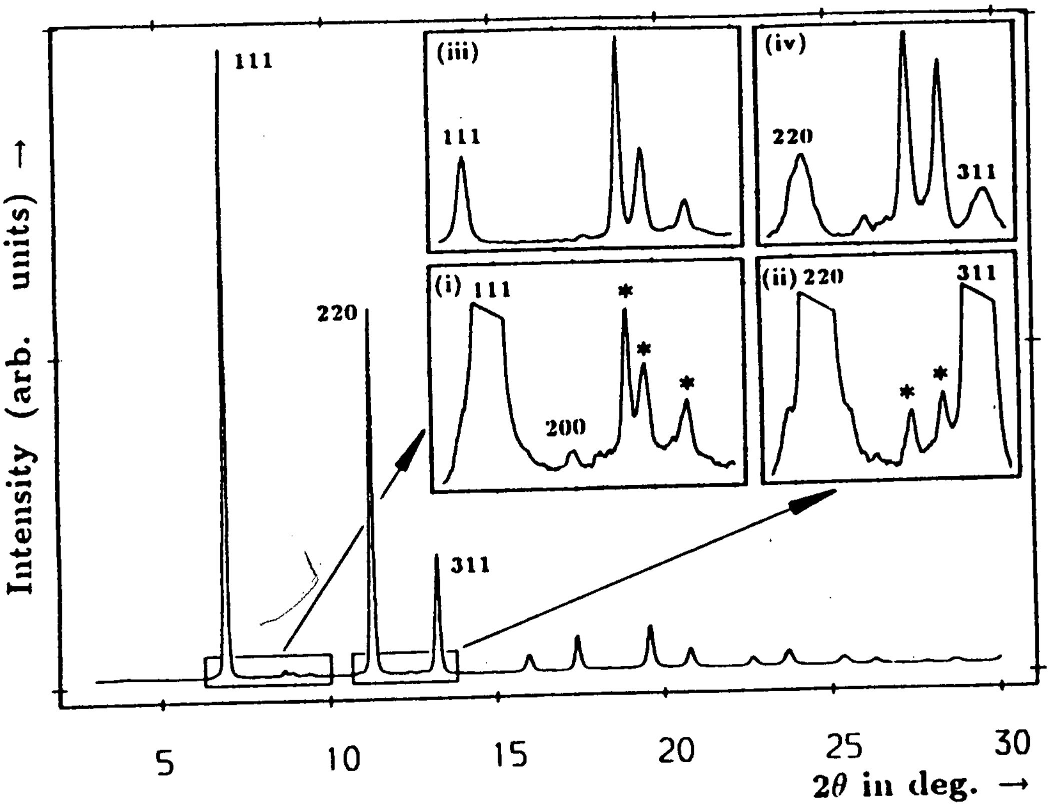

Figure 4.8 A diffraction profile illustrating that a direct transition route from zincblende to the modulated Imm2 structure exists. Its formation therefore does not require transiting any intermediate phases. The main plot and insets (i) and (ii) show the initial indications of the transition The *-symbols indicate diffraction peaks from the high pressure phase. Insets (iii) and (iv) show the same regions as (i) and (ii) after the transition has proceeded further.

The obvious interpretation is that the direct zincblende to modulated BCO transition need not proceed by transiting the other two phases but this conclusion is not without serious consequences. Firstly it raises the issue of what governs the transition route and it also partially raises Question 2. Prior to the observation of the direct transition it appeared that there was a relationship between domain size and the modulation of the BCO phase although the nature of the relationship was not clear. The confirmation of the direct route seems to contradict that conclusion. The third question is motivated by the hope to gain some insight into the actual nature of the transition and will be addressed in more detail in the next section.

As simulations using *ab initio* methods for the modulated structure are impractical , at present, the only available information upon which a model of the transition can be based is that which is obtainable from the diffraction evidence alone. In the section which follows, an attempt is made to develop a consistent picture of the observed sequence of phase transitions in InSb. Although InSb has been the focus of the experimental and theoretical work a limited amount of information is available for other III-V semiconductors including GaAs and GaSb. Where similarities or striking dissimilarities between the nature of the pressure-induced phase transitions among these compounds are known they will be mentioned and commented upon.

4.2.6 Models of the high-pressure behaviour of InSb

In this section an attempt will be made not to repeat the phenomenological aspects of the transitions as determined experimentally but to emphasize the interpretation of the results and some of the conclusions are necessarily speculative. A discussion of the zincblende to β–Sn transition in InSb and subsequent conversion to the BCO phase will be given first with particular attention focused on the characteristic features of the diffraction patterns of these phases. As had been stated previously, a transition to a β–Sn structure is observed to occur at 21 kbar on the upstroke. In this phase, the lattice sites were assumed to be randomly occupied by the constituent atoms. This structure of InSb was then observed to gradually or under slight pressure increase transform to a closely related but site-ordered structure. The diffraction pattern of the β–Sn phase differs in character to that of the BCO phase in that all the diffraction peaks in the β–Sn profile are significantly broader than those of the BCO pattern and difference scattering which was so clearly observed in the BCO pattern is not observed in the pattern collected in the β–Sn phase. Recovered (depressurized) samples of InSb and GaSb were also investigated in order to determine the nature and completeness of the retransformation to the zincblende phase. It was found that the zincblende phase was recovered in all cases albeit with broadened peaks. Difference scattering was also not observed in either of these two compounds in the recovered forms. The most simple interpretation of the lack of difference scattering in both the high-pressure and recovered forms of these materials is that the two phases are site-disordered implying a 50% probability of finding any atom of a given species on any lattice site. This simple interpretation however has two important shortcomings. First, it is unlikely that a totally random occupation of the lattice sites will occur during the transition. A more appropriate description would therefore involve a certain degree of short-range site-occupation order characterised by lengthscale over which this order is lost. The resulting picture would then be one of a network of small, separate, ordered domains partitioned by disordered boundaries. This model is also arrived at by consideration of the observed β–Sn to BCO structural transition which occurs with negligible volume change. As stated earlier these two structures are closely related to each other and a simple kinetic pathway exists between them. A study of the energetics of traversing this pathway is one of the subjects treated by density functional methods in Chapter 5. For the present discussion it will be assumed that the transition takes place by this most direct route in which an orthorhombic distortion of the β–Sn structure accompanies a rigid shift of the atom positions from (1/2,0,1/4) and (0,1/2,3/4) to (1/2,0,u) and (0,1/2,u) where u = ~1/2. This distortion results in the BCO structure. If the site-disordered interpretation of the β–Sn pattern were correct, then the β–Sn to ordered BCO transition would require a large degree of diffusion which seems unlikely in view of the apparent ease of the transition. If the assumption is made that ordered domains are separated by defect boundaries then the transition to the BCO structure would involve migration or annealing out of these boundaries which give rise to increasing coherent domain sizes. The observation of speckled Debye-Scherrer rings is consistent with development of even larger domains through crystal growth. In what follows a model for such defect boundaries is constructed in an attempt to account for the observed peak broadening and the apparent absence of difference scattering in the β-Sn phase. The objective is to explain both the general peak broadening characteristic of the β-Sn diffraction profile as well as the lack of difference scattering. Peak broadening in powder diffraction is generally indicative of extended crystal imperfections such as small crystallite size, inhomogeneous strains or planar defects separating the crystal into small coherent domains. The observed peak broadening of the β-Sn and

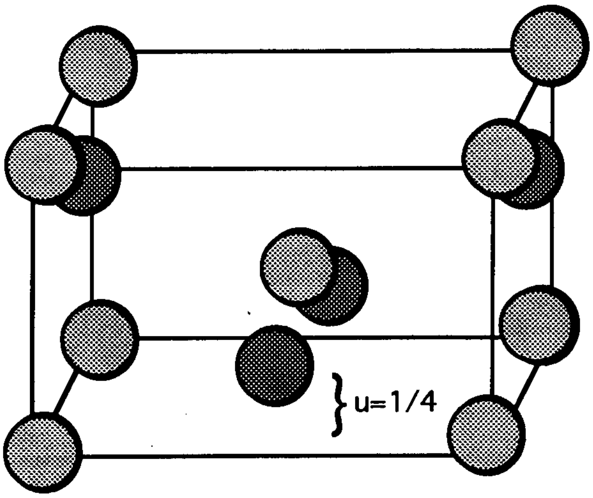

Figure 4.9 The high-pressure β-Sn form of InSb. It is this atomic arrangement which was considered to be preferred as the high pressure structure of most III-V and group IV semiconductors prior to the results of the image platestudies. The figure shows atomic ordering on the lattice sites but no In/Sb antiphase scattering was observable. Two simple deformations of this structure give rise to the body-centred-orthorhombic structure having spacegroup Imm2.

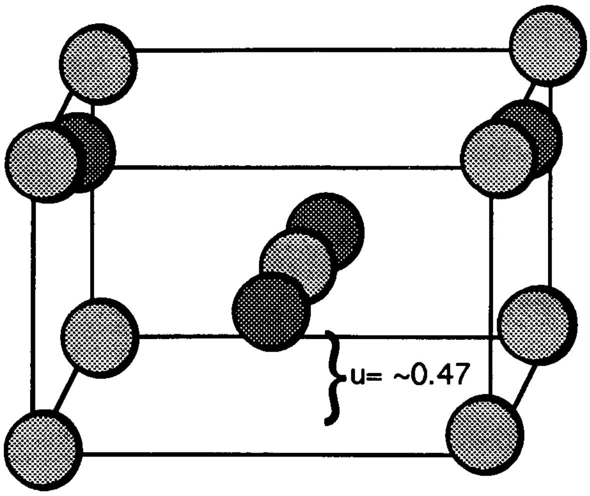

Figure 4.10 The high-pressure body-centred orthorhombic structure structure of InSb having spacegroup Imm2. The ordering of In and Sb atoms on the lattice has been confirmed using anomalous diffraction at the K-shell absorption edge of In. For a = b, c ≈ a/2 and u = 0.25 this structure is equivalent to β-Sn.

recovered zincblende forms of InSb can be explained by a high concentration of planar defects induced at the phase transition. The broad in-phase peaks are consistent with a network of twins or other similar defects occurring approximately every 200 - 400 Å [27]. Normally, a domain boundary disrupts the arrangement of scattering sites and will have no preferential effect on difference scattering peaks such as the (110) reflection in the β-Sn phase in InSb. Such defect boundaries will broaden difference peaks to the same extent as other corresponding in-phase reflections. A model involving general planar defects therefore, will explain the overall broadness of the β-Sn profile but will not be sufficient to account for the apparent absence of the difference scattering. Since the site-disordered interpretation has been argued against, another mechanism must be invoked to render the difference peak of β-Sn or recovered InSb unobservable. There is one particular type of extended imperfection - an inversion domain boundary (IDB) for which the arrangement of scattering sites is preserved across the boundary but the atomic species are interchanged from their perfect configuration. A sketch is shown in Chapter 6. The presence of IDBs therefore will not affect those reflections which arise from constructive interference from all scattering sites However, IDBs will preferentially affect difference reflections and their effect is to preferentially broaden them relative to in-phase peaks. As discussed earlier, analysis of the observed powder line widths obtained in the β-Sn phase indicates that the (110) difference peak must be at least 8 times broader than the (220) in-phase peak in order to render it indistinguishable from a smoothly varying background [27].

It must be emphasised that there has been no suggestion that IDBs in high-pressure or recovered forms of III-V semiconductors have been observed by powder diffraction in these experiments. Rather, the IDB model is intended as a useful picture for visualizing the very complex microstructures which are created at these strongly first-order structural transitions. The important point is that image plate technology now affords the capability to observe (or be confident about not observing) the subtle evidence in powder diffraction profiles which determines such basic issues as site-ordering. This is, in a sense, a revolutionary advance as it has now led not only to more detailed phase diagrams of semiconductors under pressure but to the identification of entirely new factors associated with the transitions such as defect formation. The exact role these factors play in or as a result of the structural transitions can at present, only be speculated upon. To do more requires tractable models of the transitions involved. The IDB model is a particularly attractive one in that it is simple, amenable to theoretical treatment, consistent with experiment, and appears to be a reasonable approximation to certain aspects of the real situation.

The semiconductors GaAs and GaSb have also been investigated using the image plate technique albeit in less detail than that for InSb. Tentative conclusions regarding the behaviour of GaSb at high pressure are that it also transforms to the same BCO structure as does InSb though the degree of distortion from the β-Sn structure is less pronounced than it is in InSb. The diffraction peaks in this phase are very broad and difference scattering is also not observed at high pressure nor in the recovered form. In Chapter 6 it will be shown that the IDB formation energy of GaSb in the zincblende phase is lowest among the III-Vs which is consistent with it having lowest ionicity. A full structural determination of the high pressure phase of GaAs has been hampered by extreme broadening of the powder lines.

§4.3 Summary, conclusions and understanding the results

Upon pressure increase from ambient, zincblende InSb is observed to transform to a metastable phase having the β-Sn crystal structure which subsequently converts to the BCO structure Over time a modulation of the BCO phase develops and appears to be accompanied by growth of large crystallites. Occasionally, a direct transition to the modulated structure is observed. The BCO phase is identified with InSb II in the previous phase diagram but the structure of InSb II had been erroneously assigned to that of β-Sn in the literature. The first successful application of anomalous diffraction under pressure confirmed site ordering in this phase but not in the β-Sn phase.

Despite the large increase in formation and sensitivity afforded by the image plate technique the question of whether it has led to a deeper understanding of the phase transitions in this material or has merely demonstrated that the situation is more complicated than was previously believed, may be asked. The structural determinations themselves have only limited relevance outside the field of crystallography though they are a testament to the remarkable sensitivity of the image plate system. The structural solutions presented in this chapter, taken by themselves, contribute little to the the understanding of the nature of the phase transitions involved. In this chapter an attempt has been made to develop a consistent, qualitative and pictorial model which answers and raises certain questions regarding the nature of the phase transitions in this and related materials. In the following two chapters, certain aspects of these models will be treated quantitatively using *ab initio* density functional approaches.

---

[1] P.W. Bridgeman The Physics of High Pressure (Bell, London, 1952).

[2] A. Jayaraman, *Rev. Sci. Instrum.* 57 (1986) 1013.

[3] G. Martinez, "Optical properties of Semiconductors Under Pressure" in Handbook on Semiconductors Ed. T.S. Moss p181 (1980).

[4] T. Soma, *J. Phys. C* **11** (1978) 2669.

[5] A.L. Ruoff and M. Baublitz in Physics of Solids Under High Pressure (North Holland Publishing, J.S. Shilling and R.N. Shelton editors - 1981).

[6] H.A. Gebbie, P.L. Smith, I.G. Austin and J.H. King *Nature* **191** (1960) 1096.

[7] A. Jayaraman, R.C. Newton, and G.C. Kennedy *Nature* **191** (1961) 1288.

[8] J.S. Kasper and H. Brandhorst *J. Chem. Phys*. **41** (1964) 3768.

[9] D.B. McWhan and M. Marezio *J. Chem. Phys.* **45** (1966) 2508.

[10] M.D. Banus and M.C. Lavine *J. Appl. Phys.* **40** (1968) 409 and references cited therein.

[11] J.C. Jamieson *Science* **139** (1963) 845.

[12] M.D. Banus, R.E. Hanneman, A.N. Mariano, E.P. Warekois, H.C. Gatos, and J.A. Kafalas, *Appl. Phys. Lett.* **2** (1963) 35.

[13] R.E. Hanneman, M.D. Banus, H.C. Gatos, *J. Phys. Chem. Solids* **25** (1964) 293.

[14] Y. Kato and T. Ikezu, *Phys. Lett.* **23** (1966) 644.

[15] S.C. Yu, I. Spain and E. F. Skelton *J. Appl. Phys.* **49** (1978) 4741.

[16] C.A. Vanderbourgh, Y.K. Vorha and A.L. Ruoff *Phys. Rev. B* **40** (1989) 12450.

[17] S.T. Weir, Y.K. Vohra, C.A. Vanderbourgh and A.L. Ruoff *Phys. Rev. B* **39** (1989) 1280.

[18] O. Shimomura, T. Kawamura, T. Fukamachi, J.B. Kortright and W.K. Warburton Photon Factory Proposal Number 640M - and O. Shimomura (Private Communication).

[19] J.C. Phillips *Rev. Mod. Phys.* **42** (1970) 317.

[20] J.A. Van Vechtin *Phys. Rev. B* **7** (1973) 1479.

[21] S. Froyen and M.L. Cohen *Phys. Rev. B* **28** (1983) 3258.

[22] S.B. Zhang and M.L. Cohen *Phys. Rev. B* **39** (1989) 1450.

[23] J.R. Chelikowsky *Phys. Rev. B* **35** (1987) 1174.

[24] R.J. Nelmes, M.I McMahon, P.D. Hatton, R.O. Piltz, J. Crain, R.J. Cernik and G. Bushnell-Wye *High Pressure Research,* **8** (1992) 667.

[25] G.J. Piermarini, S. Block, J.D. Barnett, and R.A. Forman *J. Appl. Phys.* **46** (1975) 2774.

26 R.J. Nelmes, M.I McMahon, P.D. Hatton, J. Crain and R.O. Piltz *Phys. Rev. B* **47** (1993) 35.

27 J.Crain, G.J. Ackland, R.O. Piltz and P.D. Hatton *Phys. Rev. Lett.* **70** (1993) 814.

CHAPTER 5

STRUCTURAL STABILITY OF METALLIC InSb AT HIGH-PRESSURE

§5.1 Introduction

5.1.1 Background and motivation

The detailed structural information on III-V semiconductors at high pressure which has recently been made routinely available through the development and implementation of the image plate detector system has implications which extend far beyond the realm of physical crystallography. In the following two chapters a series of computational/theoretical studies motivated by the results of the image plate experiments are presented.

In this chapter the central theme is to explore the degree to which detailed *ab initio* calculations using largescale computational facilities can be of value in understanding and interpreting the diffraction data. One of the conclusions of the previous chapter was that despite the fact that the crystal structures involved in the sequence of pressure-induced phase transitions in InSb have now essentially all been determined using the image plate technique, a complete picture is still lacking. This is particularly true in regard to the nature of the β-Sn phase and its relationship to the ordered body-centred orthorhombic structure. It is hoped that, as these two phases are relatively simple, they will therefore be amenable to theoretical treatment through total energy calculations and that such calculations can, if performed with sufficient accuracy, lend insight into the relative stabilities of these two phases and address the issue of whether there exists a favourable transition route between them. This type of calculation therefore represents an extension of the more traditional total energy calculations which only attempt to determine the most stable structure out of a set of candidates.

The work discussed herein is also somewhat different to that of previous total energy calculations in that the experimental results for the high-pressure behaviour of InSb appear to be conclusive even in the observation of very subtle effects. This implies that the reliability of various state-of-the-art *ab initio* methods can be extensively tested and compared. A discussion on the merits of two such techniques will be discussed in §5.3.

§5.2 Aims of the calculation

The calculations which form the subject of this chapter are designed to investigate the relative structural stability of the body-centred orthorhombic (BCO) and the β-Sn high-pressure metallic phases of InSb. Specifically the issue is to determine which structure is predicted to be energetically more favourable and to examine the factors governing structural stability. Predicted charge densities and electronic band structures which are by-products of these calculations will also be used in comparing the structures considered.

In addition, a detailed computational treatment of the observed β-Sn to BCO transition will be described. This amounts to defining simple structural parameters which describe the transition out of the β-Sn phase and investigating the individual energy costs incurred in performing the deformations associated with each of the parameters.

Before one can have any faith in the calculated properties or relative stabilities of the high-pressure phases of InSb a test must first be made to determine how well a given technique performs when applied to the ambient-pressure phase. Therefore, after a particular technique is chosen, the first objective must be to calculate the equilibrium structural properties of the compound in question. Once total energies as a function of unit cell volume are obtained, the thermodynamic transition pressure between the phases can be simply calculated by equating the derivatives of total energy with respect to volume in the phases of interest. The main purpose of this chapter is to determine the degree to which *ab initio* techniques can account for and contribute to the understanding of some of the subtle pressure-induced structural effects which are observed in InSb.

§5.3 Choice of Computational Technique

In principle the objectives of the calculation would be amenable to treatment by several methods including a pseudopotential calculation of the type discussed in Chapter 2 in which the relevant deformations of the β-Sn lattice could be performed by allowing atoms to move in certain directions under the influence of Hellmann-Feynman forces. The pseudopotential approach has perhaps been the most often used technique for structural stability studies of the present kind [1,2]. There are, however, computational problems which make the application of the pseudopotential method impractical. One of these problems is of a computational nature and could be avoided by making appropriate amendments to the code. It is that the two high-pressure phases of InSb which are of interest here are both metallic which implies that a very dense Brillouin zone sampling is required to accurately describe the Fermi surfaces associated with these structures. In the semiconducting zincblende phase, wavefunctions are calculated at 4 special (unrelated) k-points, but for metals this number may be as large as several hundred. The current parallel version of the pseudopotential code (CETEP) treats the k-points serially and the compute time therefore scales linearly with the number of sampling points. It would, however, be possible to modify the code to allow for treatment of the k-points in parallel thus substantially speeding the process. Perhaps this route would have been chosen were it not for another complication which arises from the nature of the electronic structure of InSb and cannot be avoided in a pseudopotential treatment. For a successful application of the pseudopotential approach a clear separation of core and valence states must be made. However, the energy levels of the In 4d states are only about 5 eV below the valence band minimum. As the differences between total energies for these similar crystal structures are small, care must be taken to treat all possible contributions to the bonding which means that in the case of InSb it may not be justified *a priori* to treat the d-levels as being part of the frozen core.

It is for these reasons that the pseudopotential approach was not applied to the present case. In the following chapter, the situation will be different in that the aims of the calculation will not be achievable unless the pseudopotential approach is used. The technique chosen instead is a full-potential linear augmented plane wave FLAPW method the principles and theory of which has been described in some detail in the closing sections of Chapter 2. The APW method has been applied successfully to the study of structural stability in several materials having very different bonding characters [3,4].

§5.4 Computational details and LDA band structures

5.4.1 Details of the calculation

The calculations which are described in this chapter were performed exclusively at Daresbury Laboratory on the Meiko i860 hypercube. The Vosko-Wilk-Nusair [5] form of the LDA potential was used in the calculations. A distinction between core and valence electrons was then made. Core electrons were defined as those whose charge densities are confined within the muffin-tin radius. These electrons are treated fully relativistically by solving the Dirac equation for the spherical component of the potential. The valence electrons were treated semi-relativistically which means that the mass-velocity and Darwin terms were included but spin-orbit effects were not. In contrast to previous pseudopotential calculations on III-V semiconductors, the shallow 4d levels of In and Sb were considered as occupied by valence band as opposed to core electrons. In regard to Brillouin zone sampling the special k-point sets were generated using the Monkhorst-Pack algorithm [6]. For the core electrons 4,4 and 6 special k-points were used for the zincblende, tetragonal β-Sn and BCO structures, respectively. This small number is sufficient for these bands because they are all fully occupied. With these sets of k-points the total energy was found to converge to within 0.5 mRyd or 6.8 meV. For the valence bands 10 special points were used for the zincblende structure which is relatively few compared to that required for a metal (see next section). The two high-pressure phases considered here are metallic and require a very dense k-point sampling. For the valence bands of the β-Sn and BCO phases, 160 and 288 k-points were used, respectively. Further increase in sampling density affected the calculated total energies by less than 0.3 mRyd/cell. Further details of the calculation and convergence tests are reported elsewhere [7].

Since this is a full-potential treatment the final results are not dependent on the chosen dimensions for the cutoff of the muffin-tin spheres. Nevertheless a value of 2.4 atomic units (1.27 Å) was used for the calculations. As discussed in chapter 2, within the muffin-tin spheres the wavefunctions are expanded in terms of spherical harmonics. For these calculations the cutoff angular momentum quantum number was 12.

5.4.2 A note on band structure calculation in the LDA

One of the by-products of a total energy calculation is the electronic band structure. The sum of the electronic eigenvalues gives the electronic contribution to the calculated total crystal energy (cohesive energy) of the solid. Before describing the results and conclusions of the calculations several general points should be raised regarding total energy and band structure determination using density functional methods and the local density approximation.

Density functional theory and the local approximation have been shown to be extremely useful approaches to describing the electronic and structural properties of solids under a wide variety of conditions. They are, however, ground state theories and have certain intrinsic limitations. One such limitation which arises naturally is that the calculated excited state levels may not be accurate because the occupation of excited states is not a ground state condition. In fact, it is not simply a question of making an inaccurate calculation: it is not even strictly correct to associate the Kohn-Sham eigenvalues with excitation energies. In the case of the Hartree-Fock theory Koopman's theorem states that a single-particle eigenvalue ε_i corresponding to the single-particle wavefunction u_i is associated with the energy required to remove an electron occupying that state [8]. In the present context the only relevant point is that there is no Koopman's Theorem for density functional methods and the interpretation of one-electron exited state eigenvalues becomes more complex.

In the present work, the emphasis is on ground state properties which are not believed to be strongly affected by the first or higher conduction bands. As a result, possible cures for the problems of LDA band structures will not be dealt with here.

§5.5 Results and discussion

5.5.1 Structural properties of zincblende InSb

The first part of this study is concerned with the calculation of the equilibrium structural properties of InSb in its ambient pressure zincblende crystal structure. As this fourfold coordinated structure is semiconducting, relatively few points in the Brillouin zone are required to be sampled in the calculation and still achieve k-point convergence. This type of calculation constitutes a very standard procedure. The zincblende structure is cubic and all positional parameters are fixed by spacegroup symmetry which implies that all that is required is a calculation at several different unit cell volumes. The result of this calculation is shown in Figure 5.1. The points show the calculated total energies and the curve is a fit to the Murnaghan equation of state [9] from which can be calculated the equilibrium structural properties such as the equilibrium lattice constant bulk modulus and its volume derivative. The form of the Murnaghan equation of state used for the fit is

$$E(V) = E_o + \frac{B_o V\{B_o'(1-\frac{V_o}{V}) + (\frac{V_o}{V})^{B_o'} - 1\}}{B_o'(B_o'-1)} \tag{5.1}$$

where E_o is a constant and B_o and B_o' are the bulk modulus and its first volume derivative, respectively. These three quantities and V_o (the equilibrium volume) are used as fitting parameters.

It was found that the calculated equilibrium lattice constant determined from the minimum of the total energy curve underestimates the experimental (room-temperature) lattice constant by approximately 1%. The calculation was, of course, performed at zero temperature so some of the error is due to the small thermal contraction which would occur but it is not sufficient to account fully for the disagreement. Nevertheless, the results represent an improvement over the most successful pseudopotential calculations on zincblende InSb for which the agreement with experiment can be between 2 and 3 %. The bulk modulus is related to the curvature (second derivative) of the energy vs volume relation and is a measure of the compressibility of the material. The agreement between calculated and experimental bulk moduli is usually far worse than that for equilibrium lattice constant. For this calculation, the agreement was within 7.5% of the experimental value which is quite good for a fully *ab initio* treatment.

5.5.2 Relative phase stability: electronic contributions and band structures

The diatomic β-Sn structure is body-centred tetragonal and has spacegroup *I4m2*. The diatomic basis is specified by an atom of one species at the origin (0,0,0) and an atom of another species at (0, 1/2, u) with u = 1/4.* The positional parameter u will be of importance in investigating the transition route from β-Sn to the BCO structure. As the β-Sn phase has a tetragonal structure there is freedom in the c/a ratio and a series of total energy calculations were performed in order to determine its minimum theoretical value. The c/a ratio which minimized the total energy was found to be 0.561 which is approximately 4% larger than the reported experimental value. This value of the c/a ratio was then used in subsequent total energy calculations of this phase.

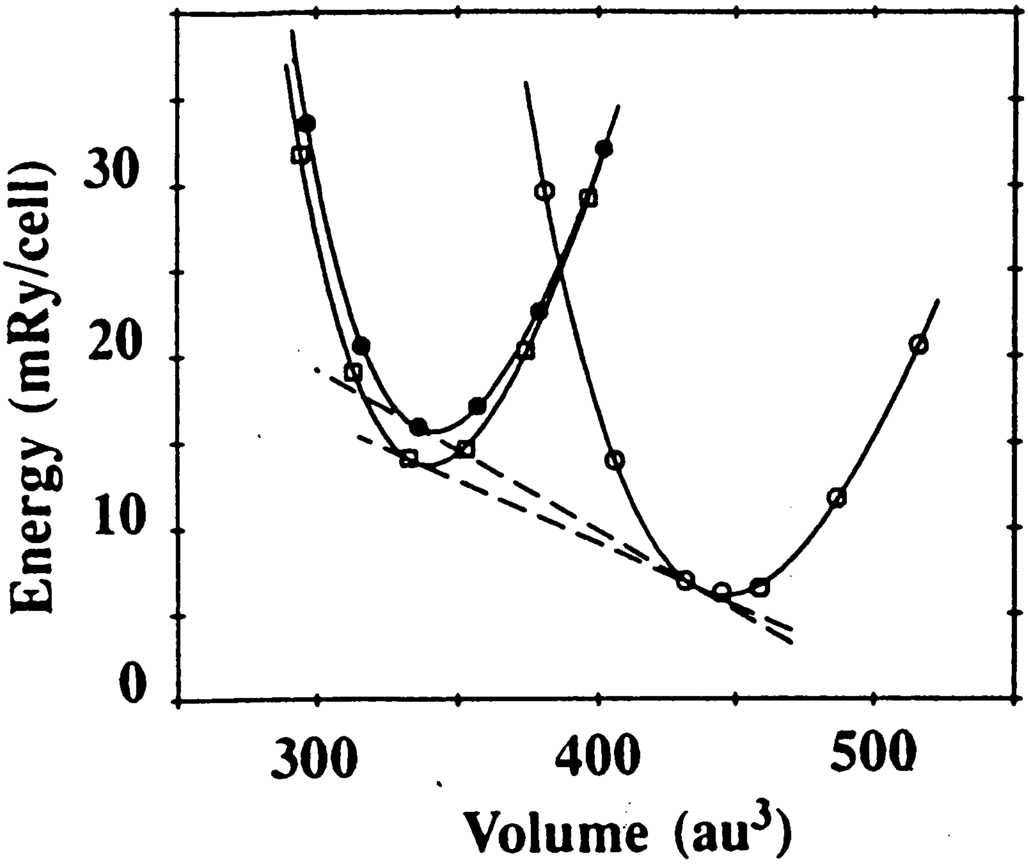

Figure 5.1 Calculated total energies as a function of unit cell volume for InSb in the zincblende (open circles), β-Sn (solid circles) and Imm2 (open squares) crystal structures.The curves are fits to the Murnaghan equation of state and the slopes (shown by dashed lines) give the calculated pressures at which the zincblende to β-Sn and zincblende to Imm2 transitions occur. Atomic units are used.

The calculation of total energy in the BCO phase (spacegroup *Imm2*) is slightly more involved because the structure is orthorhombic but is still straightforward. The structure is also determined by a diatomic basis with the positions of each species given by (0,0,0) and (0,1/2,u) where u is not fixed by spacegroup symmetry as it was in the β-Sn structure. The initial lattice constants were chosen to be equal to those determined experimentally: a = 5.816 Å, b = 5.362 Å, c = 3.161 Å and the positional parameter u = 0.47. These parameters were determined in some of the early image plate experiments. First the volume which yielded the minimum energy was determined from the calculation and then the positional parameter, u, was varied at fixed volume. The third stage of the calculation was performed at fixed volume and u-value and the a/b ratio was calculated at a fixed value of c and then the a/c ratio was varied at a fixed value of the a/b ratio. The resulting structural parameters which correspond to the calculated minimum energy configuration were found to be a/b = 1.095 and c/a = 0.546 with u = 0.47 ± 2.0%. Using these refined structural parameters the total energy as a function of unit cell volume was calculated and compared to that of the β-Sn phase. The results are shown in Figure 5.1.

As is evident in the figure, the BCO structure of InSb was calculated to be more stable than that of the β-Sn phase by approximately 27 meV/unit cell (2 mRyd/cell). This value of the energy difference is very small but still considerably larger than the numerical uncertainties present in the calculations.

The electronic band structures for the three phases of InSb considered were calculated from the self-consistent potentials using the structural parameters corresponding to the theoretical minimum energy configuration and are shown in Figure 5.2 a-c. Only the valence and conduction bands are shown. The band structure at ambient pressure has been presented by other workers [10] and will not be discussed in detail here. However certain points are deserving of comment. Firstly, the calculated band structure shows the zincblende phase to be semimetallic with a vanishing energy gap at the Γ-point of the Brillouin zone in contrast to the experimental results indicating a narrow direct gap of 0.23 eV. To investigate whether this disagreement may be due to spin-orbit effects not accounted for in this calculation (for the valence electrons) a fully relativistic calculation using the Green's Function method of Korringa-Kohn-Rostoker (KKR) was performed [11]. The result was however in agreement with that of the FLAPW calculation and suggested that the problem was likely to be related to the LDA itself as discussed in Section 5.4. The band structure calculation in the ambient pressure phase was performed as a test in order to compare the result with previous work before proceeding to the calculations on metallic phases. The results for the zincblende phase were found to be almost identical to those of Svane and Antoncik [10] who also reported an exactly vanishing direct gap from a semi-relativistic Linear Muffin Tin Orbital (LMTO) calculation. LDA band gaps are occasionally corrected empirically [12], however, without any empirical input the FLAPW calculation reproduced the InSb valence band structure accurately. The calculated valence band energies for X3, X1 and L3 states (see Figure 5.2) are close to their experimental values [13] for the FLAPW, KKR and LMTO calculations.

5.5.4 Calculated electronic charge densities

The calculated valence charge densities in the zincblende, β-Sn and BCO phases are shown in figures 5.3a through 5.5a. The bonding character in the solid can be most directly examined by subtracting the free atom charge densities from the calculated densities. The resulting plots (after subtraction) are shown in Figures 5.3b through 5.5b. Some degree of covalency in the bonding is evident from these plots in all three cases but it is strongest in the ambient pressure phase. The similarity of the band structures in the high-pressure phases is reflected in the valence charge densities as well and there is no obvious piece of evidence from the electronic configuration which suggests that the BCO structure should be more stable than that of β-Sn.

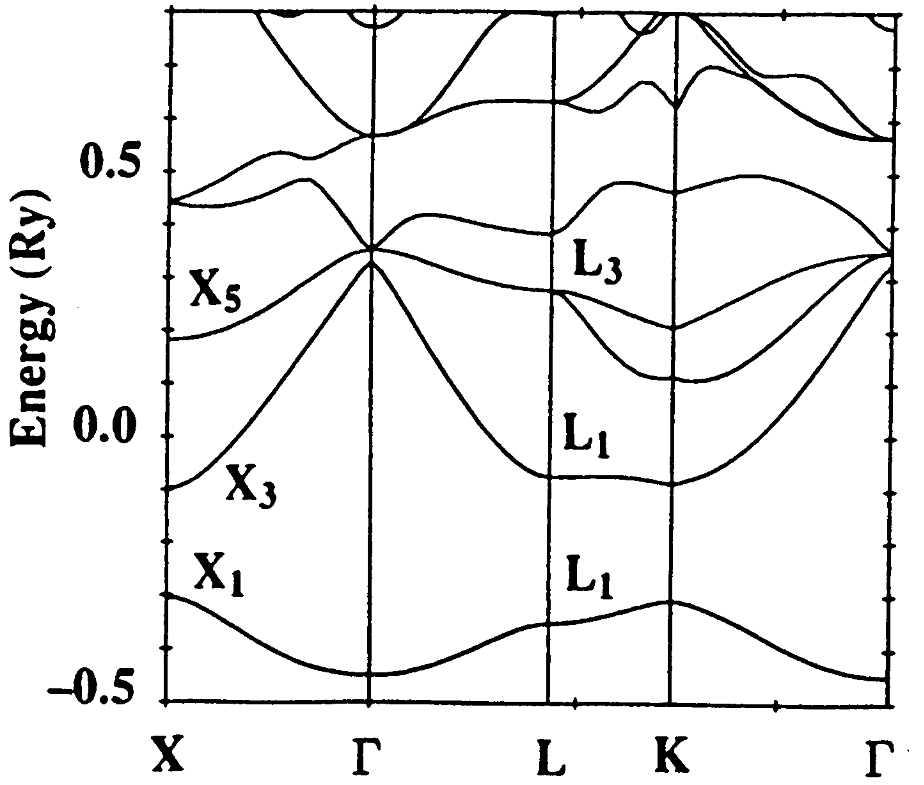

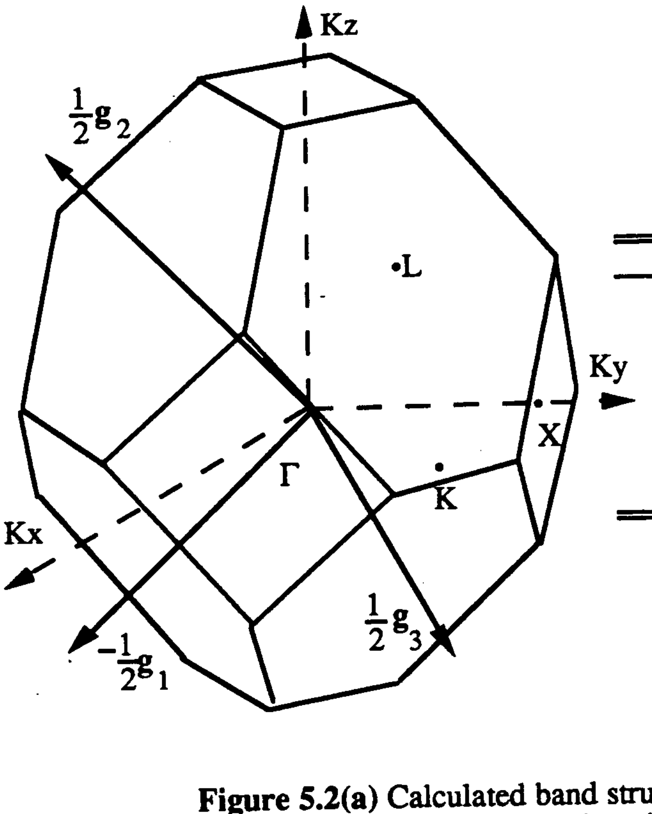

Point	Coordinates
Γ	(000)
X	$(\frac{1}{2},0,\frac{1}{2})$
L	$(\frac{1}{2},\frac{1}{2},\frac{1}{2})$
K	$(\frac{1}{2},\frac{1}{2},0)$

Figure 5.2(a) Calculated band structures of InSb in the zincblende structure. The relevant directions in the Brillouin Zone are shown below the band structure.

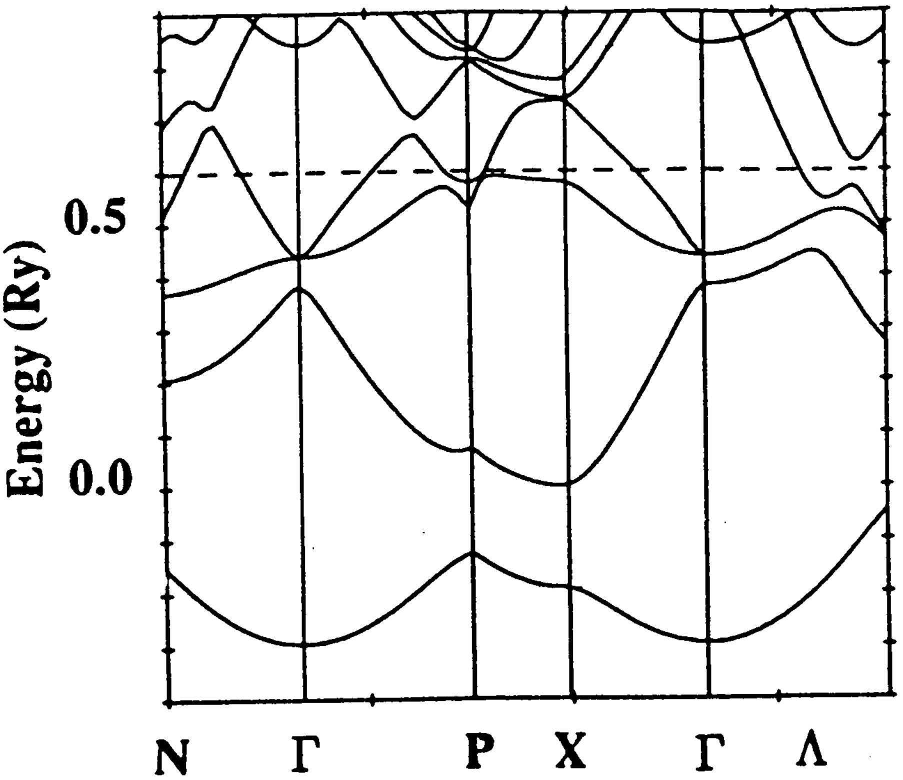

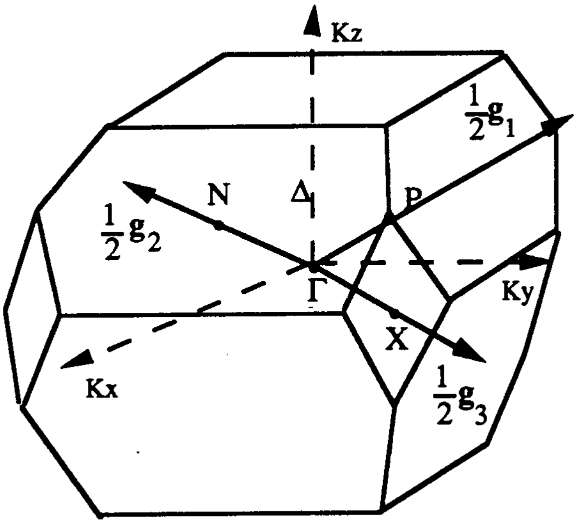

Point	Coordinates
Γ	(000)
N	$(0,\frac{1}{2},0)$
P	$(\frac{1}{4},\frac{1}{4},\frac{1}{4})$
X	$(0,0,\frac{1}{2})$

Figure 5.2(b) Calculated band structures of InSb in the β-Sn structure. The Fermi energy is indicated by dashed line. The relevant directions in the Brillouin Zone are shown below the band structure.

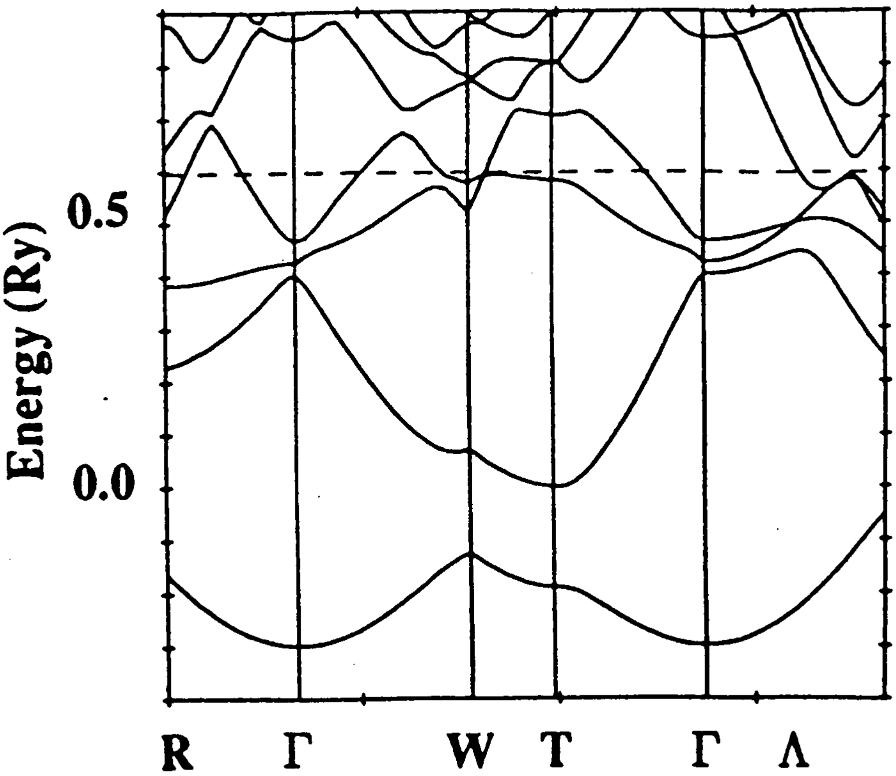

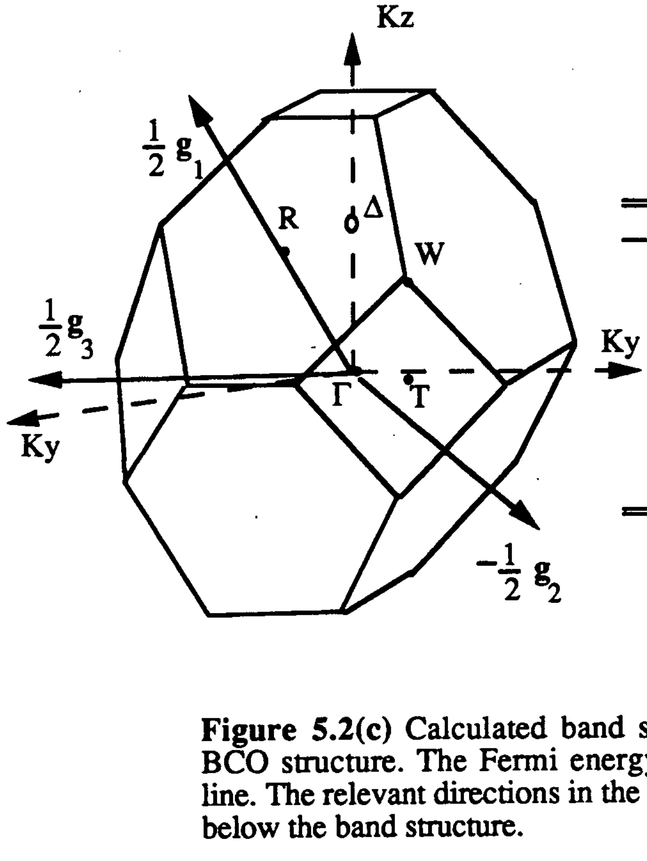

Point	Coordinates
Γ	(000)
R	$(\frac{1}{2},0,0)$
W	$(\frac{3}{4},-\frac{1}{4},-\frac{1}{4})$
T	$(\frac{1}{2},-\frac{1}{2},0)$
Δ (ΓΔ)	(α,α,-α)

Figure 5.2(c) Calculated band structures of InSb in the BCO structure. The Fermi energy is indicated by dashed line. The relevant directions in the Brillouin Zone are shown below the band structure.

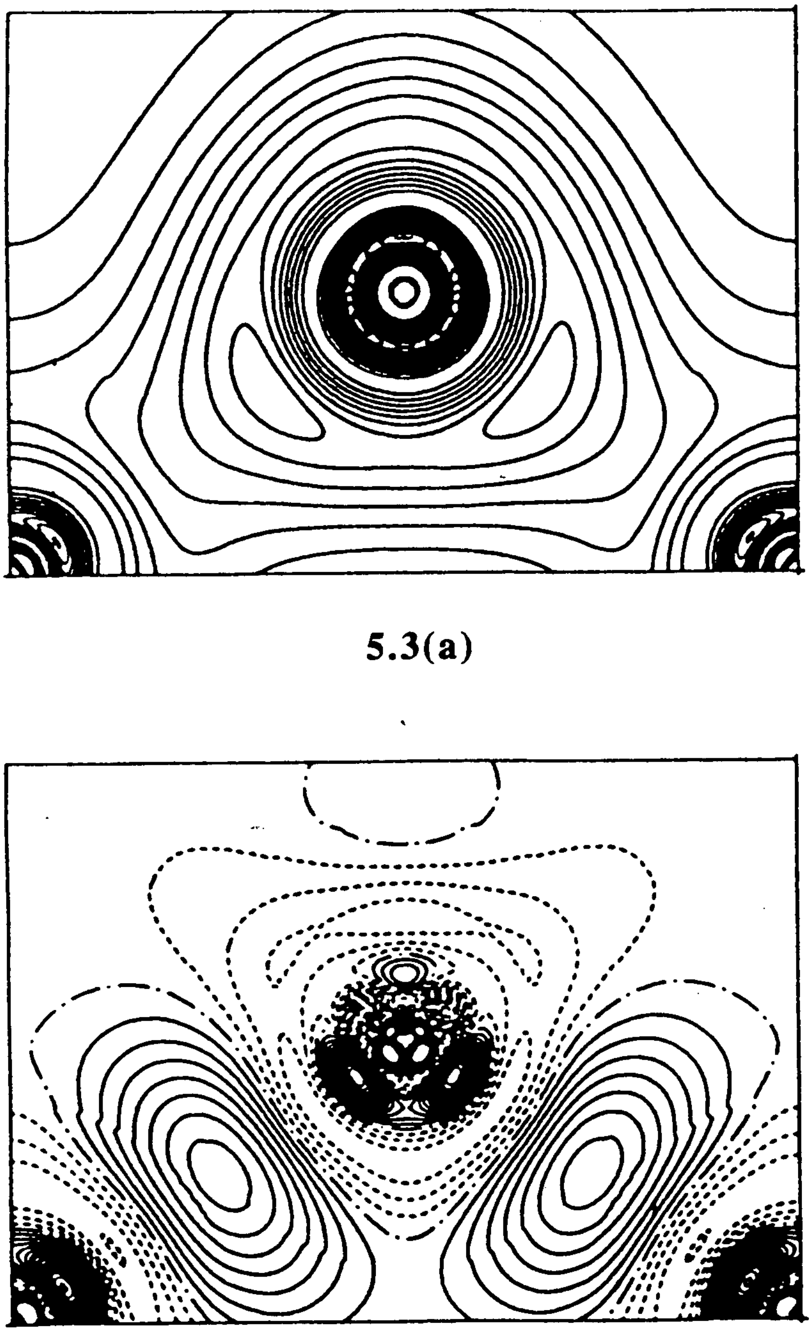

5.3(a)

5.3(b)

Figure 5.3 Calculated charge densities for InSb in the zincblende phase (a) and the resulting charge density after subtraction of the contribution from the free atom (b) illustrating the relatively large degree of covalent character in the bond compared to that for the two high-pressure metallic phases shown in the following figures.

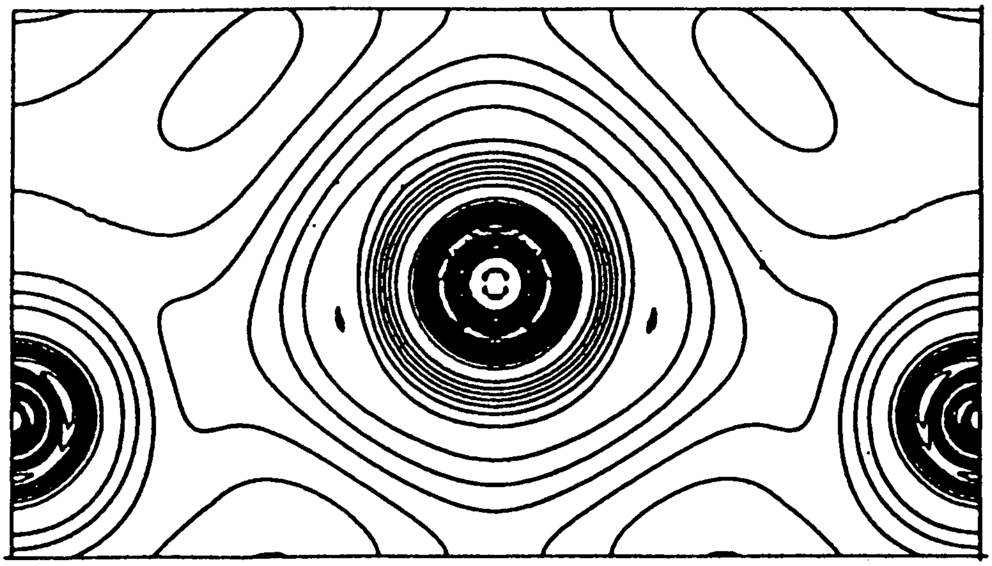

5.4(a)

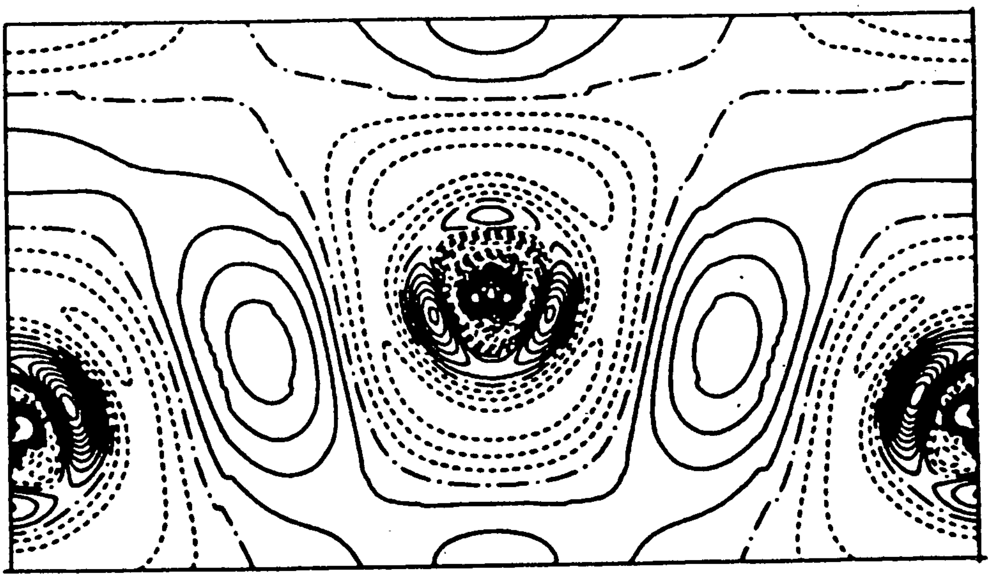

5.4(b)

Figure 5.4 Calculated charge densities for InSb in the β-Sn phase (a) and the resulting charge density after subtraction of the contribution from the free atom (b).

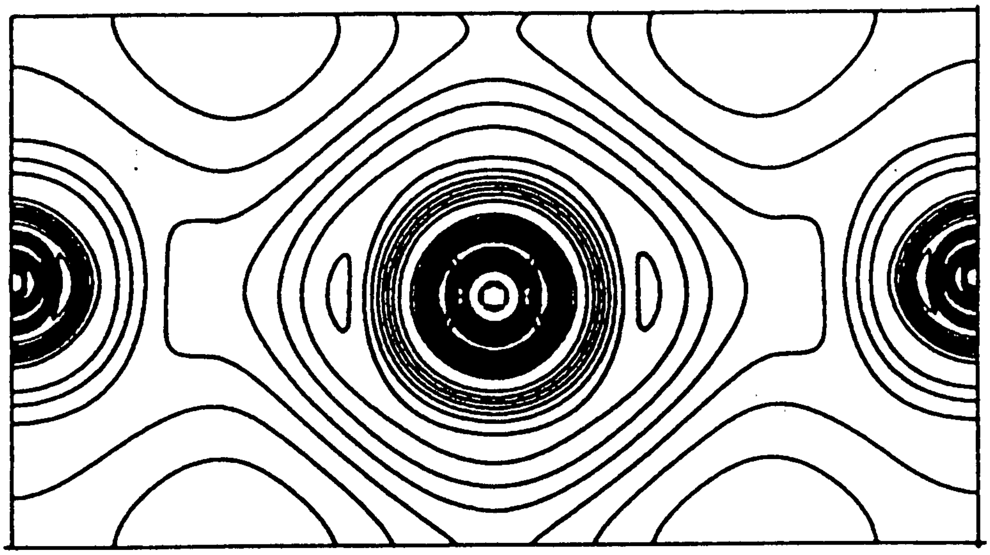

5.5(a)

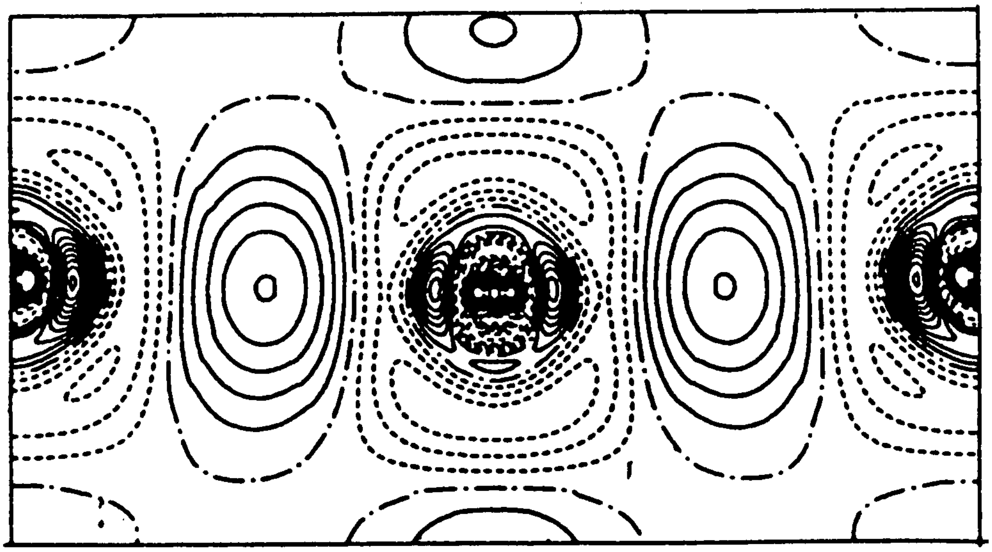

5.5(b)

Figure 5.5 Calculated charge densities for InSb in the BCO phase (a) and the resulting charge density after subtraction of the contribution from the free atom (b).

5.5.5 Electrostatic contributions and conclusions regarding stability

In order to pursue the origin of the stability further, the Madelung energy (the energy of a system of positive and negative point charges) was investigated. It is found that the BCO configuration corresponded to a lower Madelung energy than did the β-Sn structure. The results for the Madelung energies in the β-Sn and BCO structures are -11.71 and -11.88 Ryds/unit cell, respectively. The contributions to the total energy are summarized below in Table 5.1.

Table 5.1 Calculated InSb total energy decompositions for the three structural forms considered. Shown in the table are the total energy, and its contributions from the kinetic, Coulomb and exchange-correlation terms as well as the valence band energies and electrostatic contributions. The units of energy are in mRyd/(unit cell).

Structure	Total	Kinetic	Coulomb	Ex-corr	Band	Madelung
zincblende	-24712.733	26017.009	-50089.596	640.171	0.243	-49.070
β-Sn	-24712.724	26016.883	-50089.443	640.164	1.883	-55.748
BCO	-24712.726	26016.916	-50089.471	640.171	1.868	-55.965

5.5.6 Calculated transition pressures: Motivating an experiment

Transition pressures of structural phase transitions can be determined in a total energy density functional calculation of this kind by finding the slope of the line tangent to the energy-volume curves of both phases. The situation is shown generally in Figure 5.6 and for the pressure-induced transition in InSb in Figure 5.1. The theoretically predicted zincblende to BCO transition pressure was found to be 10.7 kbar. This corresponds to a calculated volume change of 23.5%. This is substantially lower than the experimental value of 22.5 kbar which was obtained on the upstroke and corresponds to a 52% discrepancy. The calculated zincblende to β-Sn transition pressure was found to be approximately 14 kbar. It is noted that the temperature dependence of transition pressure is not expected to account for such a large difference. One unappealing conclusion is that the LDA somehow severely underestimates the total structural energy differences in InSb.

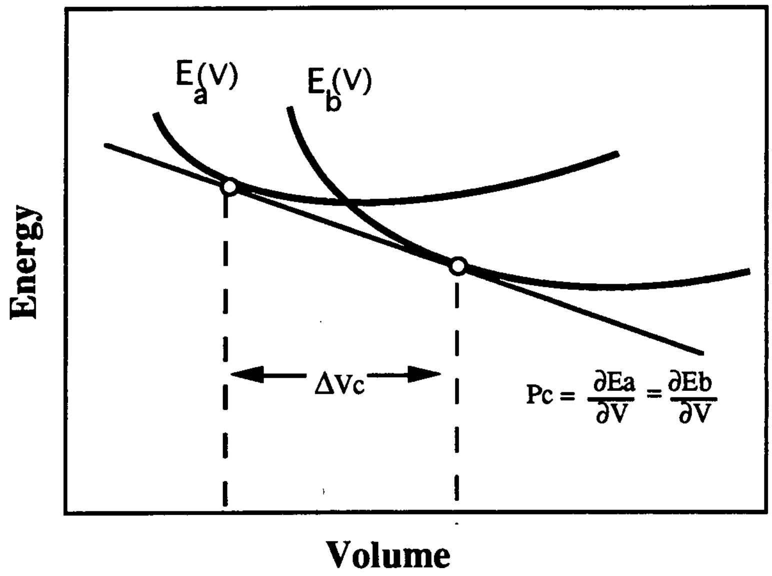

Figure 5.6 The 'common-tangent' construction for a pressure-induced structural phase transition at T=0. The transformation occurs at the pressure for which the tangents of the energy-volume curves coincide. A volume collapse of magnitude ΔV_c accompanies this strongly first-order transition.

It is noted however, that the excellent agreement between experimental and calculated structural properties afforded by these calculations suggests that the LDA itself is not the main cause of the discrepancy and another explanation must be sought.

Previous pseudopotential calculations predicted a transition to the β-Sn structure at 33 kbar (See Table 5.2) which is in better agreement with the experimental results on the upstroke. These strong disagreements in transition pressure between the two calculations can perhaps be attributed to the way in which the two calculations treat the In/Sb 4d electrons. In the present FLAPW approach these were treated as valence band electrons which respond to the nature of the bonding and to volume changes. It is believed that the influence of the In/Sb 4d electrons on the structural properties may be particularly important because there is significant charge density associated with these states outside of the muffin-tin sphere. In contrast, the pseudopotential approach treats these states as part of the assumed frozen core and neglects any structurally-dependent effects. According to this line of reasoning, the FLAPW should perform better than the pseudopotential approach for this type of calculation. In reality, it appears that both techniques accurately describe the equilibrium structural properties with the FLAPW results being in slightly better agreement with experiment in regard to the equilibrium lattice constant and bulk modulus than is the pseudopotential predictions as would be expected.

Why then should the FLAPW approach do so poorly in calculating the transition pressure? Since no evidence suggested that the calculation was in substantial error, perhaps the experimental results require further attention. As has been illustrated in the previous chapter, the transition pressure was assigned to that pressure at which the first indication of a transition could be detected. Since observations were made on mixtures having less than 1% of the high-pressure phase present is seems unlikely that this method of determining the transition pressure overestimates the true value so as to account for the discrepancy between experiment and theory. One issue which has yet to be discussed is that of hysteresis in the transition pressure measurement. In other words how similar are the transition pressures if measured on the upstroke and downstroke and on what do the differences depend? Although the answers may be complicated and depend on transition kinetics one thing is certain: a total energy calculation does not address such concerns. A total energy calculation of the type discussed in this and the following chapter deals with energies of structures in equilibrium and therefore transition pressures can be calculated using the simple relationships between energies, volumes and pressures afforded by equilibrium thermodynamics. If the transition pressure observed in an experiment depends sensitively on whether it is measured on the upstroke or downstroke then the exact meaning of 'experimental transition pressure' becomes ambiguous and difficult to reconcile with the 'equilibrium thermodynamic transition pressure'.

With these considerations and the possible origin of the discrepancy between the experimental and calculated transition pressures in mind, it would appear that another experiment on InSb is required in which once in the high-pressure BCO phase, pressure is gradually released until the zincblende phase is nearly recovered. Unfortunately, the DACs with which the experiments at the SRS, Daresbury were performed are of a type which makes gradual and controlled pressure release impractical. Had more suitable DACs been available it is likely that these "reverse transition" experiments would have been done during the normal course of experimentation on InSb at Daresbury even before the theory suggested that they would be necessary in order to resolve the issue concerning the transition pressure.

In Chapter 3 several experiments were described which were designed to explore the possibility that a rotating anode x-ray source could be successfully used as a viable alternative to a synchrotron radiation source for high-pressure powder diffraction in some circumstances. That work was performed at the Himeji Institute of Science and Technology in the Hyogo Prefecture in Japan and at that institution DACs of the slot aperture type were available. Generally speaking, conical aperture DACs are preferred to slot cells in order to make maximum advantage of the 2-dimensional nature of the image plate. However, the design of the slot cell is such that pressure is controlled by a gear-box mechanism which allows for calibrated pressure increase or, more importantly for this case, pressure decrease.

Encouraged by the results of the feasibility tests on the rotating anode, a high pressure experiment to investigate the behaviour of InSb upon pressure decrease in the BCO phase was performed using the slot-aperture DAC. The sample was loaded along with the standard methanol ethanol 4:1 mixture and Cr-enriched ruby for pressure calibration. Pressure was increased until a nearly complete conversion to the BCO phase was observed [14]. Pressure was then slowly decreased and diffraction patterns were recorded at all stages. No evidence of the reverse transition was observed at a pressure of 15 kbar. Even at a pressure of 12.5 kbar only partial conversion to the cubic zincblende phase was observed and finally, by 9.5 kbar, the zincblende phase has become dominant. Using the same criterion for the transition pressure as was used in the determination on the upstroke, transition pressure on the downstroke is therefore placed between 9.5 and 12.5 kbar. The zincblende-BCO transition thus shows considerable hysteresis which is consistent with its first-order nature.

The FLAPW calculation suggested that the BCO stability field extended down to pressures of approximately 11 kbar which appears to be in excellent agreement with the subsequent experimental result obtained by depressurization of the BCO phase. Although this result is encouraging and suggests that the FLAPW calculations have been very successful in describing the structural properties, relative phase stabilities and transition pressures of InSb, two other questions can now be raised. One question is how can one actually define what is meant by the experimentally observed transition pressure. A related question is that in light of these findings, why is it that such excellent agreement is found in the literature between calculated and experimantal transition pressures measured on the upstroke?

Some of these issues have already been raised elsewhere . Besson *et al* [15] investigated GaAs at high pressure and it was concluded that the pressure-induced structural transition was characteristic of a polymorphic structural transition which proceeds via the propagation of instabilities along well-defined crystalline directions. It was also alluded to in the conclusions of this paper that the experimental values for transition pressures in other compound semiconductors may have also been greatly overestimated if only upstroke measurements are made. For example, in GaP for which the transition pressure was placed at 240 kbar [16], incipient opacity at 200 kbar has been observed and large variations in optical properties were observed at 180 kbar [16].

Despite the possible ambiguities in experimentally determining the transition pressures in the highly first-order transitions in semiconductors, there has been much emphasis placed on comparisons of this quantity with theoretical predictions for which an unambiguous recipe exists. In Table 5.2 is shown a comparison of calculated structural properties and transition pressures for several zincblende semiconductors. The results shown in Table 5.2 motivate certain comments. In view of the overall success of *ab initio* methods in describing structural trends in these materials, the large hysteresis effects, makes it difficult to unambiguously interpret the discrepencies between experimental and calculated results for the AlP and AlAs transition pressures. As with all these calculations, there exists the possibility that there exists a structure having a lower total energy than any of those considered. For the case of AlP and AlAs, for which no structure determination at high pressure has been reported, the rocksalt (RS) structure predicted by calculations may not be the correct one.

Table 5.2 Comparison of calculated and experimental structural behaviour at high pressure. The stable high pressure structure, and transition pressure is considered. Observed and calculated equilibrium lattice constants are also shown . Unless otherwise indicated, the calculated results are from Zhang and Cohen [2]. The designation RS stands for the Rocksalt (NaCl-type) structure. The designation "orth." refers to an orthorhombic unit cell having undetermined atomic positions.

Ambient Pressure Structure compound	lattice constant a_o(Å)		High Pressure Structure*		Transition Pressure (kbar)	
	Expt[17].	Calc.	Expt.	Calc.	Expt.	Calc.
AlP	5.451	5.471	Not Reported	RS/β-Sn[n]	140[a],170[b]	93,269[m],238[n]
AlAs	5.662	5.678	Not Reported	RS/β-Sn[n]	120[c]	76,220[m],220[n]
AlSb	6.135	6.153	RS[b]/β-Sn[d]	RS/β-Sn[f,n]	83[b],125[d],115[e]	56,76[n] 122[m],100-133[f,]
GaP	5.451	5.386	β-Sn[c]	RS/β-Sn[f,n]	200-240[b,c]	217,230 - 430[f],216[m], 245[n]
GaAs	5.653	5.601	orth[b,g,†]	RS/β-Sn[f,n]	(136,90)[i],162[h]	160,>200[f], 180[m],167[n]
GaSb	6.118	6.032	β-Sn[e]/BCO[†]	β-Sn	80[d],90[e,†],60-74[j]	63,>80[f],80[n]
InP	5.869	5.688	RS[d,e]	RS	105-110[c]	133[f],128,117[n]
InAs	6.036	5.906	RS[d,e,k,†]	RS	70[k],102[d],100[e]	84,92[m],72[n]
InSb	6.490	6.359 6.426[†]	β-Sn[d]/orth[b]/BCO[†]	β-Sn/BCO[†]	22[d], 25[l] (23,9.5-12.5)[††]	33,11[†],19[n]

[a] Reference 18 [e] Reference 19 [i] Reference 16: up- and downstroke, respectively

[b] Reference 20 [f] Reference 21 [j] Reference 22

[c] Reference 23 [g] Reference 24 [k] Reference 25

[d] Reference 26 [h] Reference 27 [l] Reference 28

[m] Reference 29 - Only transformation to β-Sn was considered

[n] Reference 30

[†] Present Work [††] Present Work: up- and downstroke, respectively

* All calculations have been performed assuming site-ordered high-pressure structures but such ordering has only been investigated in references marked by (†) and of those, it has been confirmed unambiguously only in the BCO phase of InSb. See Chapter 4 for details.

Nevertheless if another structure were found to have even lower calculated total energy than RS, its calculated transition pressure would be reduced further thus making the disagreement even larger. It therefore seems likely that proper consideration of hysteresis effects and the role of defects will be of importance in modeling phase transitions in both these compounds. For AlSb there is a large variation in the reported experimental value for the transition pressure to the metallic phase though the pseudopotential calculations of Zhang and Cohen [2] again underestimate even the lowest reported transition pressure. The calculation, of Soma [23] based on a perturbation treatment, appears to do better in this respect but the final result is very sensitive to certain features in the model potential and the functional form chosen to model the electronic screening. Despite the apparent improvement in pseudopotential predictions of the transition pressures in the case of Ga(Sb,As and P), in GaP, the rocksalt structure is predicted to be stable in comparison to a β-Sn structure, contrary to experimental results. According to the dielectric theory of Phillips, GaP (ionicity 0.33) would transform to the RS structure. The model potential calculations of Soma correctly predict stability of β-Sn but report an uncertainty in the transition pressure of nearly 200 kbar . For GaAs, atomic positions in the orthorhombic unit cell are not known and for GaSb, although calculations and previous experiment appear to agree on transition pressure and predict stability of β-Sn over RS, results of the image plate studies indicate that GaSb does not transform to the β-Sn structure. The In-compounds appear to be reasonably well-described but it is interesting that transition pressures for InP are slightly overestimated in calculations in view of the importance of hysteresis effects in InSb.

5.5.7 Stability of the β-Sn phase under distortions

Having established that the body-centred orthorhombic structure of InSb is energetically more favourable than the tetragonal β-Sn structure in agreement with experiment, the question of the kinetic route through the transition remains. An attempt to treat this transition using total energy considerations will now be presented. The BCO structure can be obtained from the β-Sn structure by an orthorhombic distortion and an accompanied shift of the positional parameter from the value of 0.25 to nearly 0.50. The issue is to investigate the stability of the β-Sn phase with respect to these distortions which effectively parameterize the structural transition.

Two sets of calculations were performed: firstly for several values of the positional parameter u for a fixed value of the a/b ratio and secondly for u fixed and variable a/b ratio. As stated previously, an a/b ratio of 1.0 corresponds to the β-Sn structure when u = 0.25. Changing the a/b ratio corresponds to an orthorhombic distortion of the β-Sn structure. The results of these investigations are summarized in Figure 5.5. It is found that the β-Sn structure is stable with respect to the individual distortions. Increasing the positional parameter from 0.25 in the β-Sn phase increases the total energy as does performing a pure orthorhombic distortion with u fixed at 0.25. However, the β-Sn structure is found to be unstable with respect to a simultaneous orthorhombic distortion and increase of positional parameter. The minimum energy is found to occur at an orthorhombic distortion of approximately 8% with the positional parameter at roughly 0.45. The results are shown in Figure 5.5.
The calculated orthorhombic distortion and positional parameter corresponding to the minimum energy are found to be in excellent agreement with the experimental structural information obtained from the image plate.This type of calculation would also be of value when considering the stability of semiconductors for which the β-Sn structure is most stable at high pressure. Such an undertaking would possibly lead to further insight into the electronic origins or consequences of the observed transitions in InSb.

§5.6 Conclusions: The question of generality

A first principles local density functional calculation based on the FLAPW method has been applied to the study of structural stability and total energies of InSb in the zincblende, β-Sn and body-centred orthorhombic crystal structures. The investigation was motivated by the experimental results obtained through a series of extensive high-pressure investigations of this compound which employed the image plate area detector. It was found that the equilibrium structural properties and transition pressures were in excellent agreement with experiment and that the high-pressure β-Sn structure is unstable with respect to a related orthorhombically distorted structure. The electrostatic interaction is found

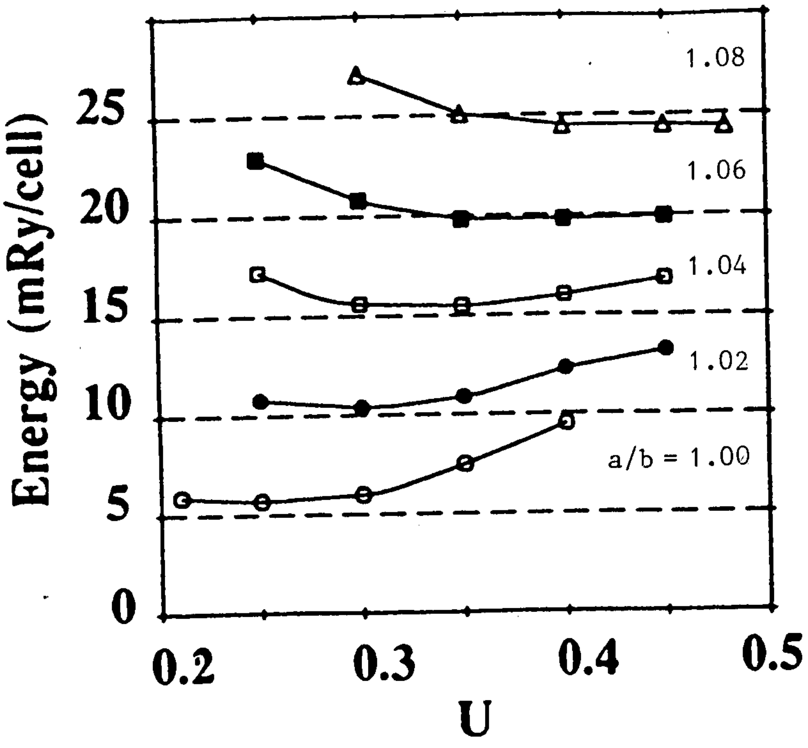

Figure 5.5. The total energy of InSb in the β-Sn structure as a function of two independent distortions. The figure shows the total energy as a function of the positional parameter, u, for several values of the a/b ratio. The undistorted β-Sn structure corresponds to a/b = 1 and u=0.25. The plot suggests that the β-Sn structure is stable against either of these distortions performed individually but is unstable with respect to simultaneous orthorhombic deformation and increase of the positional parameter.

to be the most important factor in determining the relative stability although the energy differences involved are very small. This result is in contrast to several studies which suggested that the β-Sn configuration would be the most stable. However, the BCO structure treated here had not previously been considered as a candidate structure.

These studies have, hopefully, contributed to the understanding of the phase transitions of this most complicated but well-studied material. However, the question of how general these conclusions are remains to be seen. Despite the obvious similarities between III-V compounds, their high-pressure behaviour is not guaranteed to be similar and the distortions which stabilize the BCO phase over the β-Sn phase in InSb may not be favourable in other compounds. It should be mentioned at this point that a certain amount of image plate data does exist for the compound GaSb.

Extreme broadening of the GaSb peaks at high pressure makes it difficult to determine the structure at present but preliminary studies indicate that the high pressure form of GaSb definitely does not correspond to the β-Sn structure and is, instead, very likely the same Imm2 structure as observed in InSb though a slight distortion cannot be ruled out. InAs, however has now been confirmed to transform to NaCl structure as previous calculations had predicted [31]. Nevertheless there exists at least some evidence which suggests that aspects the complex pressure-induced behaviour observed so clearly in InSb can also be found in other related materials.

One of the obvious general conclusions from this work is that it has suggested a very detailed long term program of study which would involve a coordinated experimental and theoretical/computational effort. The goal of such a program would be to investigate the degree to which the results from the investigations on InSb represent general behavioural trends in III-V materials at high pressure which simply previously eluded observation because of limitations imposed by the data quality. At present it appears that previous investigations using relatively insensitive high-pressure detection systems led to a far oversimplified picture with which theoretical results were found to be consistent. It may be that a substantial revision of both experimental and theoretical understanding of phase transitions in these systems is required. In the next chapter, further new features observed in the diffraction patterns of InSb at high pressure are treated using *ab initio* total energy methods which support such a case for renewed interest in these phenomena.

---

[1] M.T. Yin and M.L. Cohen *Phys. Rev. Lett.* **50** (1983) 1172.

[2] S.B. Zhang and M.L. Cohen *Phys. Rev. B* **35** (1987) 7604.

[3] S. Massida, B.I. Min and A.J. Freeman *Phys. Rev.* B (1988) **38** 1991.

[4] M. Weinhert, E. Wimmer and A.J. Freeman *Phys. Rev. B* **26** (1982) 4571 .

[5] S.H. Vosko, L. Wilk and M. Nusair *Can. J. Phys.* **58** (1980) 1200.

[6] H.J. Monkhorst and J.D. Pack, *Phys. Rev. B* **13** (1976) 5188.

[7] G.Y. Guo, J. Crain, P. Blaha and W.M. Temmerman, to appear in *Phys. Rev. B* **47** (1993).

[8] J. Calloway and N.H. March in *Solid State Physics* **34** (1984).

[9] F. D. Murnaghan *Proc. Natnl. Acad. Sci.* USA **30** (1944) 244.

[10] A. Svane and E Antoncik *J. Phys. C* **20** (1987) 2683.

[11] G.Y. Guo, J. Crain and W.M. Temmerman-Unpublished results of KKR calculations on InSb performed at Daresbury Laboratory.

[12] M. Cardona N.E. Cristiensen and G. Fasol *Phys. Rev. B* **38** (1948) 1806.

[13] X-ray and ultraviolet photoemission spectroscopy experiments performed by L. Ley, R.A. Pollak, F.R. McFeely, S.P. Kowalczyk and D.A. Shirley *Phys. Rev. B* **9** (1974) 600.

[14] H. Kawamura, Y. Akehama, P.D. Hatton and J. Crain - To be published.

[15] J.M. Besson, J.P. Itié, A. Polian, G. Weill, J.L. Mansot and G. Gonzolez *Phys. Rev. B* **44** (1991) 4214.

[16] J.P Pinceaux, J.M. Besson, A. Rimsky and G. Weill, *High Pressure Science and Technology. Proceedings 8th AIRAPT.* Pergamon Press. (1980).

[17] From R.W.G. Wyckoff, Crystal Structures (Interscience, New York, 1963).

[18] J. Wanagel, V. Arnold and A.L Ruoff *J. Appl. Phys.* **47** (1976) 2821.

[19] S. Minomura and H.G. Drickamer *J. Phys. Chem. Solids* **23** (1962) 451.

[20] S.C. Yu, I.L. Spain and E.F. Skelton *Solid State Commun.* **25** (1978) 49.

[21] T. Soma, *J. Phys. C* **11** (1978) 2669, The range of calculated transition pressures is due to different forms for the electronic screening functions.

[22] S.T. Weir, Y.K. Vohra, and A.L. Ruoff *Phys. Rev .B* **36** (1987) 4543.

[23] M. Baublitz and A.L. Ruoff *J. Appl. Phys.* **53** (1982) 6178.

[24] S.T. Weir, Y.K. Vohra,C.A. Vanderborgh and A.L. Ruoff *Phys. Rev. B* **39** (1989) 1280.

[25] Y.K. Vohra, S.T. Weir and A.L. Ruoff *Phys. Rev. B* **31** (1985) 7344.

[26] J.C. Jamieson *Science* **139** (1963) 845.

[27] T. Goto, Y. Syono, J. Hakai and Y. Nakagawa *Solid State Commun.* **17** (1976) 831.

[28] N.B. Owen, P.L. Smith, J.E. Martin and A. Wright, *J. Phys. Chem. Solids* **24** (1963) 1519.

[29] J.A. Van Vechtin *Phys. Rev. B* **7** (1973) 1479.

[30] J.R. Chelikowsky *Phys. Rev. B* **35** (1987) 1174.

[31] J. Crain, R.O. Piltz and P.D. Hatton, unpublished.

* u is fixed by spacegroup symmetry,

CHAPTER 6
PHASE-TRANSITION-INDUCED DEFECTS IN TETRAHEDRAL SEMICONDUCTORS: PSEUDOPOTENTIAL CALCULATIONS

§6.1 Introduction

6.1.1 Motivation and background

All perfect crystals by their definition exhibit spatial regularity in the sense that if a crystal site is chosen at random, all other sites can be generated by translations through linear combinations of primitive vectors of the appropriate Bravais lattice. In two dimensions, 5 distinct Bravais lattices exist and 14 are found in 3-dimensions. Just as massless springs and frictionless pulleys are useful idealizations which ignore unnecessary complications, so is the concept of a perfect crystal. No crystal is absolutely perfect and a certain number of defects of various types are always present. If, however, most atoms of a solid are perfectly ordered in the sense described above, the *effects* of the imperfections which are present can be safely ignored and the solid considered crystalline.

There is a vast range of imperfection types associated with crystalline matter. For example, there can be localized or point defects which involve a single lattice site and have the effect of displacing neighbouring atoms from their equilibrium positions. There can also be compositional disorder as in the case of β-brass and other binary alloys as well as ordered domains separated by defects. In phase I of cyclohexane (See Chapter 1) and several other molecular crystals there is disorder in the molecular orientation on a well-defined lattice. Solids also contain non-localized or extended defects which are either linear or planar. One of the most common line defects is a dislocation.

There has been a great deal of interest in the electronic consequences of defects in semiconductors. All defects have the effect of reducing symmetry and mixing otherwise independent electron eigenstates but in the case of semiconductors the situation is particularly interesting as defects can have the effect of introducing states in to the forbidden energy gap.

The motivation for the work described in this chapter has its origins in structural studies at high pressure, specifically in subtleties of the diffraction patterns of InSb as obtained in the β-Sn and BCO phases the analysis of which led to the development of the IDB model. Although previously mentioned, it must be stressed that the IDB picture has been invoked in the present context as a useful and relevant model of certain consequences of the pressure-induced polymorphic transitions in InSb and other compound semiconductors.

6.1.2 Diffraction from defected crystals: analytical treatment of the effect of Inversion Domain Boundaries (IDBs)

Each of the different varieties of crystalline defects has a signature in the way it modifies the diffraction pattern of a perfect specimen. The effects which will be considered are crystal size, strain and various types of faulting with emphasis on a particular type of imperfection - an inversion domain boundary for which the effects will be discussed in some detail analytically in what follows.

During formation or growth of a binary crystal, AB, with a structure having two distinct crystallographic sites 'a' and 'b', nucleation can take place at many different places. At this stage, the distinction between which species occupies a given site is arbitrary and at the different nucleation sites, different choices for this occupation can be made. In the simplest example, half a crystal 'chooses' A for the 'a' site and the other half makes the opposite choice. These two regions constitute antiphase domains and are energetically equivalent because each A-atom is surrounded by unlike B-atom near neighbours. The division between these regions is called an antiphase (or inversion) domain boundary and must necessarily contain 'wrong' bonds which are either A-A type bonds or B-B type bonds. Inversion domain boundaries are known to be common internal interfaces in several materials with the prototypical example being Cu_3Au [1].

In dealing with diffraction experiments on crystals possibly containing IDBs it is important to appreciate that the effect of IDBs on diffraction patterns is not intuitively obvious. In order to illustrate the analytical treatment of diffraction from crystals containing IDBs the simple case of Cu_3Au will be considered but the major results and conclusions are general. The problem is to determine the effect of IDBs on integrated intensity of Bragg reflections.

The unit cell considered in this example has dimensions $2N_1a_1$, N_2a_2 and N_3a_3. The inversion domain boundary is normal to the $\mathbf{a}_1$. Each atom in the left half of the crystal is displaced by $(\mathbf{a}_2+\mathbf{a}_3)/2$ relative to the corresponding positions in the other half. The resulting crystal is therefore characterised by two perfectly ordered regions separated by an inversion boundary.

Following Warren [1] the expression for the diffracted intensity is given by

$$I = I_e FF^* \prod_{m=1}^{3} \frac{\sin^2(\pi h_m N_m)}{\sin^2(\pi h_m)} (1+e^{\pi i(h_2+h_3+2N_1h_1)})(1+e^{-\pi i(h_2+h_3+2N_1h_1)}) \qquad (6.1.1)$$

$$(m=1,2,3)$$

where I_e is a constant and F is the structure factor. If the change of variables $h_1 = h + h_1'$, $h_2 = k + h_2'$ and $h_3 = l + h_3'$ is made [2], the intensity is then given by

$$I = I_e FF^* \prod_{m=1}^{3} \frac{\sin^2(\pi h'_m N_m)}{(\pi h'_m)^2} \, 2(1+(-1)^{k+l}\cos(2\pi h'_1 N_1)) \qquad (6.1.2)$$

In general the integrated intensity of a reflection having indices (hkl) is given by

$$P = C\int I(h'_1,h'_2,h'_3)\, dv \qquad (6.1.3)$$

$$(C = \text{constant and } dv=dh'_1dh'_2dh'_3)$$

For the case of in-phase scattering, for which k+l = even, (6.1.2) becomes

$$I = I_e FF^* \prod_{m=1}^{3} \frac{\sin^2(\pi h'_m N_m)}{(\pi h'_m)^2} \qquad (6.1.4)$$

integration of Eq. (6.1.4) gives the integrated diffracted intensity as $P=2CI_eFF^*N_1N_2N_3$ [1] which is identical to the situation in which there are no inversion domain boundaries. Antiphase scattering occurs in this structure for k+l= odd for which (6.1.2) is

$$I = I_e FF^* \prod_{m=1}^{3} \frac{\sin^2(\pi h'_m N_m)}{(\pi h'_m)^2} \, 4\sin^2(\pi N_1 h'_1) \qquad (6.1.5)$$

which is zero exactly at the point $h'_1=0$. The intensity of the antiphase or "difference scattering" is therefore strictly vanishing exactly at the point hkl in reciprocal space for k+l = odd. The integrated intensity as given by (6.1.3) is, however, non-vanishing and is the same as that given by integration of (6.1.4).

The result is that the presence of inversion domain boundaries has the effect of broadening difference reflections without reducing the integrated intensity. If present in sufficient concentration, however, the intensity of broadened difference reflections may be partially or totally lost in the long tails of reflections or in a smoothly varying background.

6.1.3 Inversion domain boundaries in zincblende crystals

In the specific case of zincblende semiconductors inversion domains are often discussed within the context of epitaxial growth. For example inversion domain boundaries have been observed in GaAs when grown on {001} Ge substrates [3].

In general there is no lattice mismatch between two inversion domains but there is expected to be some displacement of the atoms at the boundary itself. The magnitude of the displacement depends on the particular compound and orientation of boundary as well as on other factors which will be considered later in the chapter.

There are three distinct classes of IDB. The simplest, called a *type 1 IDB* occurs when the boundary is stoichiometric and requires that the IDB plane lie parallel to at least one a/4<111> vector. Examples of this type of boundary in the zincblende structure include the {110} and the {112}. It is possible that the boundary is comprised of only one species of atom in which case the interface is referred to as a *type 2 IDB*. A type *3 IDB* is formed when there is an unequal mix of wrong bonds but the behaviour of such a system depends sensitively on their relative number. It has been reported that inversion domain boundaries show a strong preference for formation along the {110} planes [2].

§ 6.2 Ab-initio treatment of defects

6.2.1 Aperiodic systems, Bloch's theorem and the 'supercell method'

The discussion given in Chapter 2 was an attempt to review the theory behind total energy calculations in systems for which Bloch's theorem is strictly satisfied. The treatment of a single symmetry breaking feature such as an isolated defect in an otherwise perfect crystal appears not to be possible with such techniques although the perturbation relative to the perfect case may be small. The study of such defects could, however, be made tractable by surrounding a defect with a region of perfect material and then applying periodic boundary conditions to the "supercell". In order to avoid interaction between the supercells it is necessary to choose relatively large supercells having a sufficient amount of perfect material. In principle, convergence of the calculated defect energy may be monitored by systematic increases in supercell size though this may be prohibitively time consuming when dealing with compute-times which scale as some power of the system size. Such convergence tests will not be performed in the present work.

6.2.2 Aims of the calculation

The power of modern computer technology makes very ambitious and largescale calculations possible but clear goals are required in order that the limited available computational resources are used efficiently with a minimum of wasted running time. The goal of the calculations to be described here is to determine the energy cost of forming a candidate defect in zincblende InSb using an appropriate supercell. The formation energy is calculated relative to the perfect structure. This type of problem is very well suited to the capabilities of the total energy pseudopotential technique because bonding in solids is principally governed by the response of valence electrons as opposed to those in the core. For calculations, the implication of this is that although convergence of total energy for a given structure and pseudopotential may require a very high value of cutoff energy (hence many plane waves), convergence of energy difference between two structures may be achieved with a lower cutoff and reduced computational effort. This is because at a low cutoff, relative to that required for total energy convergence, further increase in cutoff will have the effect of treating core states more accurately thus lowering the total energy of each structure by a constant amount, keeping the energy difference unchanged.

It would also be of great interest to consider the problem of IDB energetics in the high-pressure metallic forms of InSb in addition to the ambient pressure phase. Unfortunately, as has been discussed in Chapters 2 and 5, pseudopotential calculations on metals are complicated by the need to make very careful sampling of the Brillouin zone near the Fermi surface. The relatively large numbers of atoms required to describe defect conditions by the supercell method make implementation of the current pseudopotential approach impractical. This difficulty can be overcome by suitable changes to the architecture of the parallel algorithms in the code and such calculations will be attempted using the pseudopotential strategy in the future. In Chapter 5, the relativistic APW approach was applied to investigate structural stability in metallic polymorphs of InSb and it may seem surprising that it is not also applied in this context. It will be shown in this chapter that structural relaxation in the vicinity of the the defect boundary plays an important role in determining the energetics of defect formation. An accurate description of such ionic positional relaxation under the influence of Hellmann-Feynman forces is therefore an important ingredient for an accurate calculation. As this is not normally possible with the standard APW approach [4] the present chapter will be restricted to discussion of IDBs in the zincblende phase of several III-V semiconductors.

§ 6.3 *Ab initio* pseudopotential study of IDBs in the tetrahedral semiconductor InSb

6.3.1 Calculation procedure, implementation of structural relaxation and proof of the Hellmann-Feynman theorem

The procedure of determining defect energies by subtracting the energy of the defect supercell from that of the perfect supercell would provide, in principle, the value of the energy difference between the perfect structure and that corresponding to the (110) boundary *provided* the relative positions of the ion sites were identical in the two structures. In the real solid, however, the relative positions of the ions will be locally distorted from those of the perfect zincblende lattice in the region of the defect thus altering the total energy. If this distortion is neglected in the calculation the resulting defect formation energy will be overestimated. As discussed in Chapter 2, total energy pseudopotential methods using plane waves as basis states allow for straightforward evaluation of the Hellmann-Feynman forces on the ions which give rise to the local distortion. The structural relaxation can then be simulated by moving the ions by an appropriate amount in the direction of the calculated force, but care must be taken to ensure the applicability of the Hellmann-Feynman theorem and the accuracy of the calculated Hellmann-Feynman forces. In the present section a discussion of the Hellmann-Feynman theorem is given with particular emphasis on aspects of practical computation.

In general, the force on ion I at position $\mathbf{R}_I$ is given by d/d$\mathbf{R}_I$ Etot which is the <u>total</u> derivative of the expectation value of the total energy Hamiltonian with respect to the ionic position. This is <u>not</u> the Hellmann-Feynman theorem which states that the force is given by the <u>partial</u> ionic position derivative of the expectation value. Expansion of the total derivative, using the implicit function theorem gives

$$\mathbf{F}_I = \frac{\partial}{\partial \mathbf{R}_I} E_{tot} + \Sigma_i \frac{\partial E_{tot}}{\partial \psi_i(\mathbf{r})} \frac{\partial \psi_i(\mathbf{r})}{\partial \mathbf{R}_I} + \Sigma_i \frac{\partial E_{tot}}{\partial \psi^*_i(\mathbf{r})} \frac{\partial \psi^*_i(\mathbf{r})}{\partial \mathbf{R}_I} \tag{6.3.1}$$

$$\frac{\partial E_{tot}}{\partial \psi_i(\mathbf{r})} = H\psi_i(\mathbf{r}) \tag{6.3.2}$$

$$\mathbf{F}_I = \frac{\partial}{\partial \mathbf{R}_I} E_{tot} + \Sigma_i \langle \frac{\partial}{\partial \mathbf{R}_I} \psi_i(\mathbf{r}) \mid H\psi_i(\mathbf{r}) \rangle + \Sigma_i \langle \psi_i(\mathbf{r}) H \mid \frac{\partial}{\partial \mathbf{R}_I} \psi_i(\mathbf{r}) \rangle \tag{6.3.3}$$

This is then the most general form for the analytic expression of the force but a substantial simplification results if the wavefunctions are eigenstates of the Hamiltonian. If the electronic variables are coincident with the Born-Oppenheimer surface, which means that the $\psi_i(\mathbf{r})$ are instantaneous eigenstates of H, then $H\psi_i(\mathbf{r}) = \varepsilon_i \psi_i(\mathbf{r})$ and the force can be expressed as

$$\begin{aligned} \mathbf{F}_I = \frac{\partial}{\partial \mathbf{R}_I} E_{tot} + \{ \Sigma_i \langle \frac{\partial}{\partial \mathbf{R}_I} \psi_i(\mathbf{r}) \mid \varepsilon_i \psi_i(\mathbf{r}) \rangle + \\ \Sigma_i \langle \psi_i(\mathbf{r}) \varepsilon_i \mid \frac{\partial}{\partial \mathbf{R}_I} \psi_i(\mathbf{r}) \rangle \} \end{aligned} \tag{6.3.4}$$

Upon factoring out the energy eigenvalue ε_i the term in curly brackets is simply expressed by the product rule for differentiation as

$$\sum_i \varepsilon_i \frac{\partial}{\partial \mathbf{R}_I} \langle \psi_i(\mathbf{r}) \mid \psi_i(\mathbf{r}) \rangle \tag{6.3.5}$$

But this term is strictly zero because the wavefunctions are normalized to a constant so only the explicit dependence of the total energy on position is relevant for force calculation. In other words only the partial derivative need be calculated if the electronic configuration is an eigenstate of the total energy operator:

$$\mathbf{F}_I = \frac{\partial}{\partial \mathbf{R}_I} E_{tot} \tag{6.3.6}$$

which is the Hellmann-Feynman theorem.

Since, in the real solid, the adiabatic approximation which states that the electronic system is in its ground state with respect to any instantaneous ionic configuration is assumed to hold the Hellmann-Feynman criterion is satisfied. The same conditions which are assumed to hold 'naturally' in real systems in order for the Hellmann-Feynman theorem to be applicable must be 'achieved' in a simulation. In this case all that is required in the calculation is that the electronic relaxation must be nearly converged before the calculated forces are accurate and point to the direction of minimum energy for the ionic system.

6.3.3 Choice of candidate boundary

Due to the fact that the aim of the calculation is not to perform an exhaustive study of many possible boundaries there is some freedom in the choice which allows for the selection of a physically plausible and computationally convenient one. There exist both polar and non-polar boundaries in the zincblende structure. Calculation of the non-polar (110) boundary in the zincblende structure is straightforward but the supercells required to model the (001) and (111) boundaries contain inequivalent non-stoichiometric interfaces and the proper definition of the interface energy for a non-stoichiometric boundary is not trivial. Since the (110) boundary has been observed to be a common one experimentally and it is computationally simple it will be chosen as the subject of the following study. A projection of the (110) boundary is shown in Figure 6.1. The atomic positions in the supercell representation of the IDB are shown in Tables 6.1 (a) and (b).

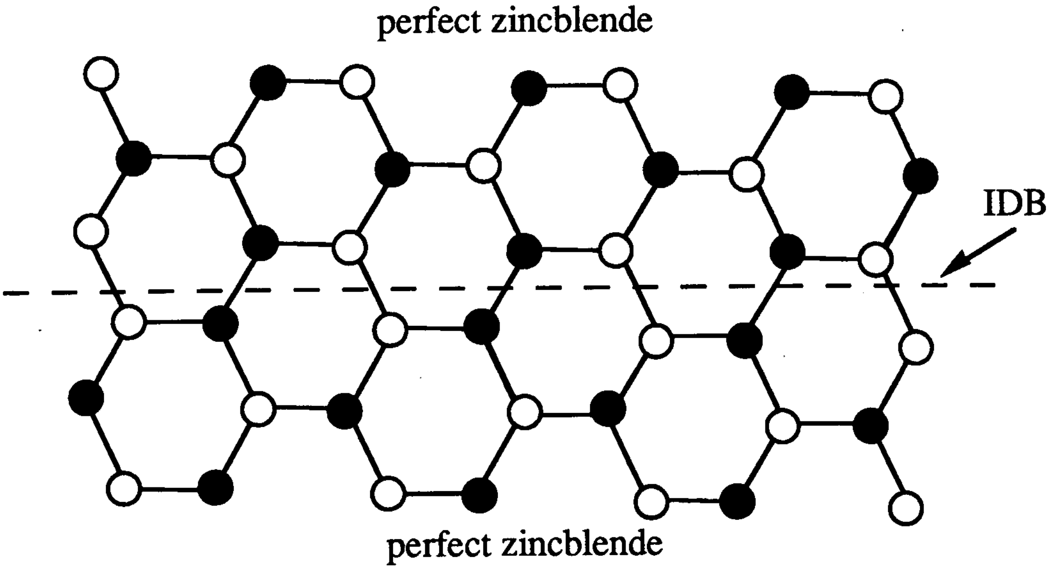

Figure 6.1 Projection of the (110) Inversion Domain Boundary in a zincblende crystal.

Table 6.1 (a) Atom positions in fractional coordinates of the supercell axes representing a (110) inversion domain boundary for a zincblende semiconductor. The positions for the 'perfect' analogue are shown in Table 6.1 (b).

Ion	Type	x	y	z
1	1	0.00	0.00	0.00
2	1	0.25	0.00	0.1667
3	1	0.75	0.50	0.3333
4	1	0.25	0.00	0.5000
5	1	0.00	0.00	0.6667
6	1	0.50	0.50	0.8333
1	2	0.75	0.50	0.0000
2	2	0.50	0.50	0.1667
3	2	0.00	0.00	0.3333
4	2	0.50	0.50	0.5000
5	2	0.75	0.50	0.6667
6	2	0.25	0.00	0.8333

Table 6.1 (b) Atom positions in fractional coordinates of the supercell axes representing the 'perfect' zincblende supercell.

Ion	Type	x	y	z
1	1	0.00	0.00	0.00
2	1	0.50	0.50	0.1667
3	1	0.75	0.50	0.3333
4	1	0.25	0.00	0.5000
5	1	0.00	0.00	0.6667
6	1	0.50	0.50	0.8333
1	2	0.75	0.50	0.0000
2	2	0.25	0.00	0.1667
3	2	0.00	0.00	0.3333
4	2	0.50	0.50	0.5000
5	2	0.75	0.50	0.6667
6	2	0.25	0.00	0.8333

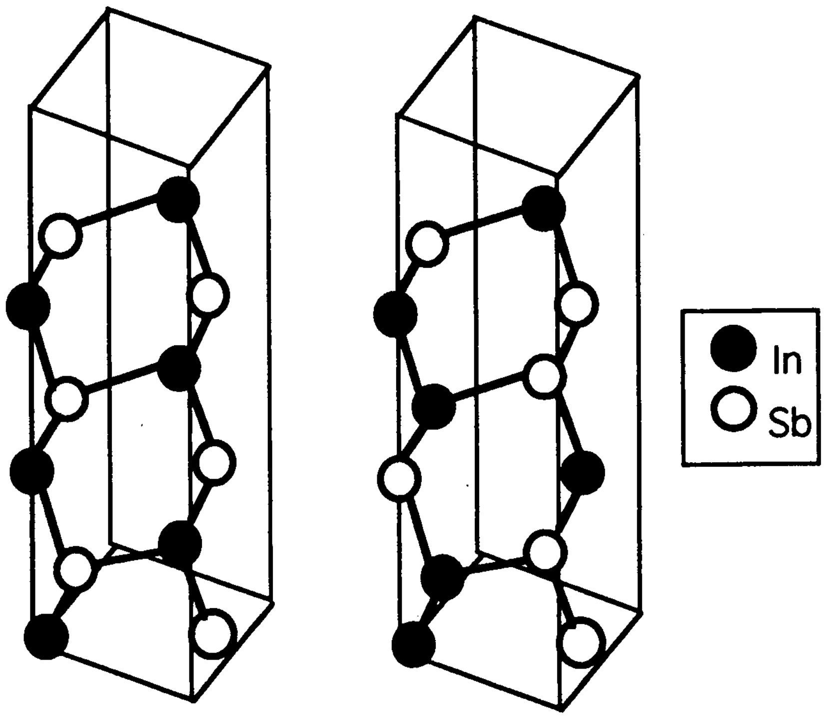

(a) - perfect (b) - defected

Figure 6.2 The IDB supercells for the defected (b) and perfect (a) cases used for all calculations on zincblende semiconductors.

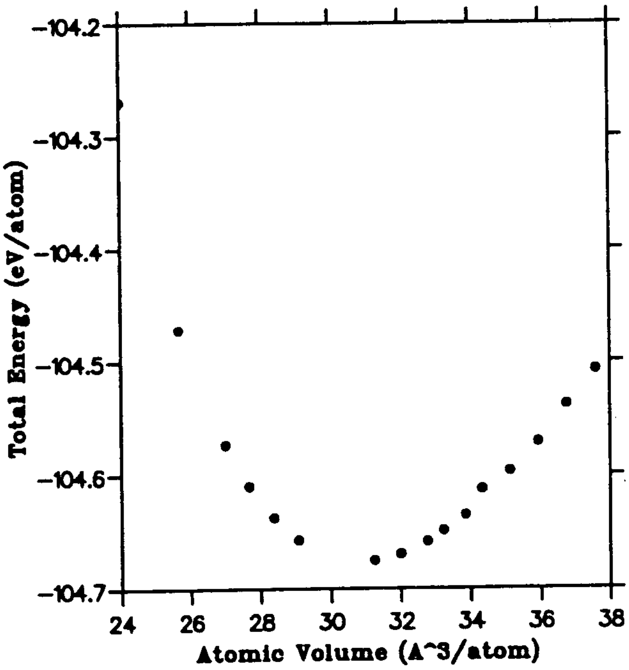

Figure 6.3 Total energy as a function of unit cell volume for zincblende InSb as calculated from *ab initio* pseudopotentials.

6.3.4 Results and discussion

a) Tests of the InSb pseudopotential, zone-sampling convergence

Before applying the InSb pseudopotential to the problem of calculating the formation energy of a planar defect, it must first be tested in order to determine whether it reproduces the correct structural properties of the perfect crystal. Tests using 1, 4, and 16 k-points were performed in the 8-atom cubic cell. Negligible differences in energy were obtained between the 4 and 16 k-point runs. As the computational cost of these calculations scales linearly with number of k-points all future calculations were performed with a 4 k-point set. Although system geometry may affect k-point convergence, as systems become larger it becomes increasingly impractical to test the convergence of energy with respect to Brillouin zone sampling and this was, in fact, not tested for the calculations on the supercells. The total energy as a function of volume for InSb using a 400 eV cutoff energy for the plane waves is shown in Figure 6.3.

b) Unrelaxed geometry

Calculations were performed on the 12-atom InSb supercell representing two (110) IDBs in the zincblende structure. The supercell dimensions were taken as a = 6.273 Å b = 4.435 Å and c = 13.307 Å and were obtained by minimising total energy with respect to unit cell volume for the perfect lattice. The lattice constant was found to be approximately 3% smaller than the room temperature lattice constant of InSb. The a and b cell dimensions are constrained to be commensurate with the perfect cubic structure but the supercell dimension along the c-axis can expand perpendicular to the plane of the defect boundary. An energy cutoff of 400 eV for the plane wave basis set was used. Electronic relaxation proceeded until energy convergence was better than 10^{-4} eV/atom. Identical cutoff and k-point sampling was used for both the perfect and defected supercells. A value of 0.35 eV/(wrong-bond) was calculated as the difference in energy between the perfect and unrelaxed IDB supercells which corresponds to 0.18 eV/atom . This value is similar to that calculated using the Linear Muffin-Tin Orbital (LMTO) method for the {110} IDB energy in unrelaxed GaAs as reported by Lambrecht *et al* [5]. As the LMTO method represents a fixed basis-set technique, the contribution to the formation energy which arises from ionic position relaxation at the boundary cannot be estimated from the calculation. The plane-wave pseudopotential approach, however, as discussed in Chapter 2 does not use a fixed basis-set for expansion of the wavefunctions which implies that the positions of the ions can be relaxed under the influence of Hellmann-Feynman forces and that the effect of such relaxation on the energetics can be calculated. This is discussed for the case of InSb in the next section.

c) Relaxed geometry

Strictly speaking two different types of relaxation are required before the calculated 'relaxed geometry' can be achieved in the simulation. First, and most importantly, is the relaxation of the relative ionic positions in the vicinity of the defect. The second is the unit cell relaxation perpendicular to the plane of the defect boundary. It is found that relaxation of the ionic degrees of freedom contributes a nearly 20% additional reduction of the energy cost of forming a (110) IDB. Figure 6.4 illustrates the effect of expansion of the unit cell in a direction perpendicular to the plane of the defect boundary. The energy difference between the fully relaxed defect structure and that calculated for the perfect supercell was found to be 0.285 eV/(wrong-bond) or 0.145 eV/atom. Using these results for the calculated wrong bond energies it is possible to make some comparisons between the energies of site disordered configurations and an IDB-type microstructure based on simple counting of wrong bonds. Site disorder up to the percolation threshold (where long-range order is lost) requires an order of magnitude more wrong bonds than does a 50 Å IDB microstructure. Based on the present calculation, site-disorder requires an energy of roughly 0.5 eV/atom. The pressure-induced phase transition occurs with a volume change of 20% which supplies an energy of 0.08 eV/atom from the PΔV contribution. This is insufficient to cause largescale site-disorder throughout the crystal. However, the energy required to form a 50 Å IDB microstructure (one boundary per 10 layers) is, on average, 0.05 eV/atom which is comparable to the PΔV energy [6] and could be supplied by the phase transitions.

§ 6.4 Studies of inversion domain boundaries in other tetrahedral semiconductors

6.4.1 Motivation

The above discussion on InSb motivates the question of what determines the energies of these defects in general. It is likely that ionicity of the compound as well as the atomic size ratios and bondlengths play the dominant roles. To explore the sensitivity of IDB formation energies to these parameters, similar *ab initio* pseudopotential studies have been carried out for other selected III-V semiconductors. Of principle interest are the compounds having dissimilar ionicites or bondlengths. In the present section the energetics of the 110 IDB will be considered for GaSb

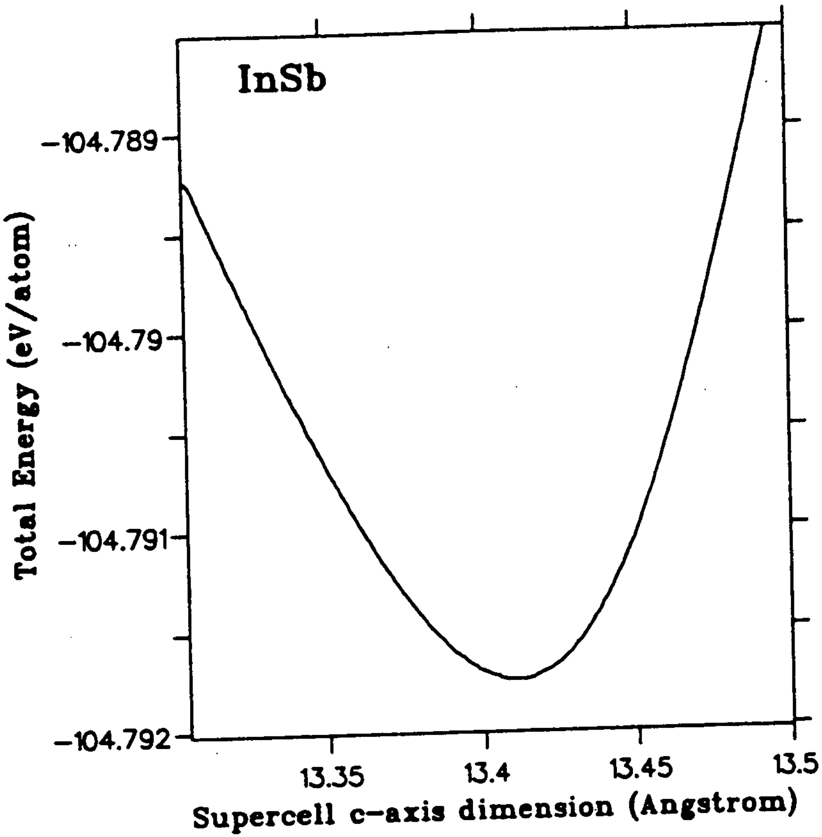

Figure 6.4 Illustration of the effect of supercell relaxation perpendicular to the plane of the defect boundary. It is found that unit cell relaxation contributes an approximately 5% reduction to the total formation energy of the boundary.

as this material has a relatively low ionicity and InAs which, by contrast has a rather high ionicity.

6.4.2 Comments on the calculation

As was done with the InSb calculation, the lattice constant corresponding to the calculated minimum total energy was determined for an 8 atom cubic zincblende unit cell for each of the semiconductors considered. The energy as a function of volume is shown for GaSb and InAs in Figures 6.5 and 6.6 which represent the compounds having the greatest relative ionicity difference of the materials considered. All calculations were performed with identical k-point sampling and energy cutoff for the plane waves. Using the predicted minimum lattice constant, supercells representing a (110) inversion domain boundary were constructed

in an analogous fashion to those for InSb. The calculations to determine the minimum energy lattice constant were performed on the University of Edinburgh's serial computer 'Festival' and the calculations on the IDB supercells were performed both on the parallel supercomputer 'Maxwell', the Daresbury Laboratory CONVEX C2000 mini-supercomputer and on the AlphaVax. An initial test was performed on an 8 atom unit cell of silicon on the three computers which confirmed that they produce identical results within rounding errors.

It was generally found that the calculated equilibrium lattice constants for the III-Vs consistently were between 2 and 3% too small as compared to their experimentally determined values. For calculations on the defected supercells Hellmann-Feynman forces were evaluated and the ions were moved under their influences until the forces were less than 0.1 eV/Å.

6.4.3 Results of the calculations

For InAs, the agreement between experiment and calculated equilibrium lattice parameter was approximately 2.8%. The supercell dimensions were 5.844 Å x 4.129 Å x 12.38 Å prior to unit cell relaxation. An energy difference of 2.46 eV/cell (0.205 eV/atom) was calculated for the perfect and defected supercells without structural relaxation. Upon relaxation of the ionic positions only a very modest

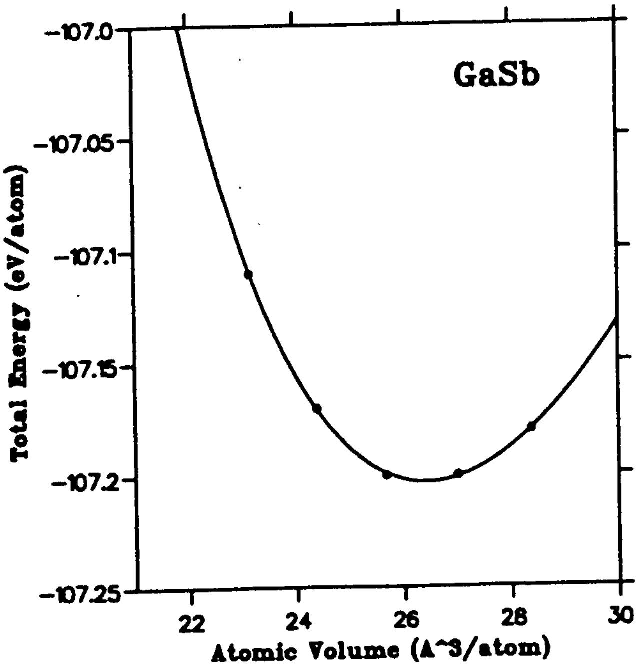

Figure 6.5. Energy vs lattice constant for the tetrahedral semiconductor GaSb. The calculated equilibrium lattice constant was found to underestimate the experimental value by approximately 3%. Curves are fits to the Murnaghan equation-of-state.

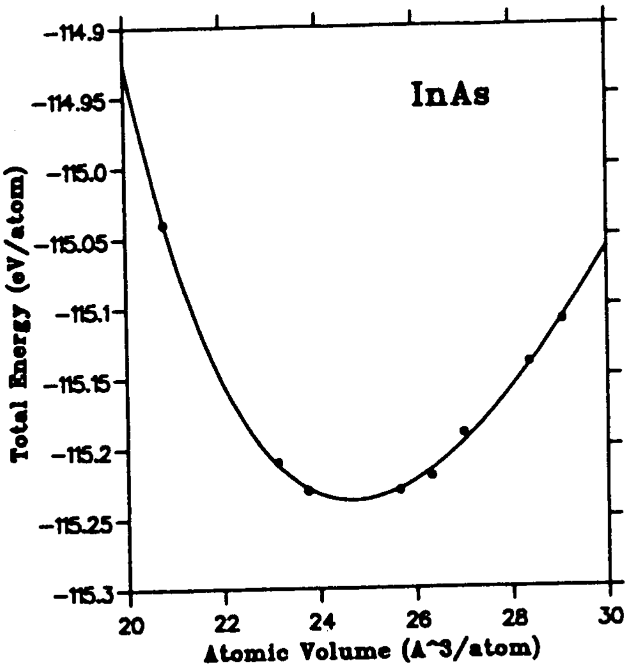

Figure 6.6. Energy vs lattice constant for the tetrahedral semiconductor InAs. The calculated equilibrium lattice constant was found to underestimate the experimental value by less than 2 %. Curves are fits to the Murnaghan equation-of-state.

reduction to a value of 0.199 eV/atom was observed. This is in marked contrast to the behaviour found for InSb where structural relaxation led to a 20% energy decrease.

For GaSb, a supercell having dimensions of 5.94 Å x 4.200 Å x 12.60 Å was used. The calculated equilibrium lattice constant agreed with experiment to 2.9% of the experimental value. The calculated energy difference between the perfect supercell and the unrelaxed defected supercell was found to be 1.136 eV/(unit cell) or 0.094 eV/atom. Relaxation of the ionic positions lowered the energy cost of 110 IDB formation to 0.06 eV/atom. The effect of subsequent unit cell relaxation perpendicular to the defected boundary is shown in Figure 6.7. It is found to have a very small effect on the formation energy compared to that

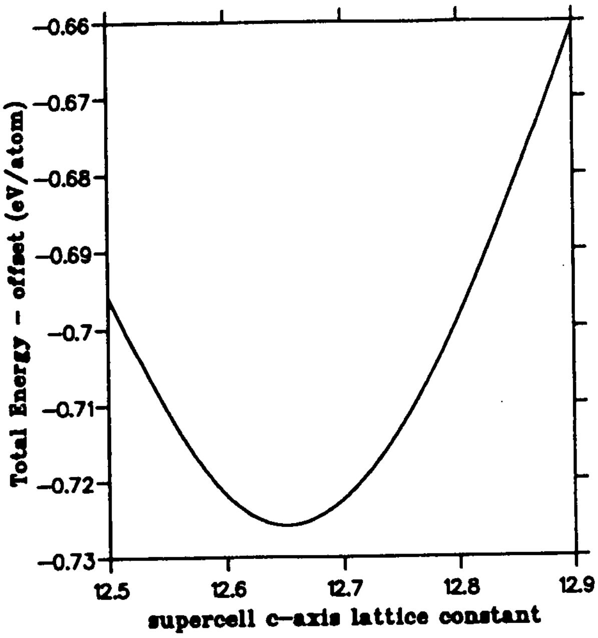

Figure 6.7 Calculated total energy for a 12-atom GaSb supercell representing a (110) IDB as a function of expansion perpendicular to the plane of the boundary.

achieved for ionic positional relaxation. This value of the IDB energy was the lowest of any of the semiconductors considered in this investigation.

6.4.4 Discussion

The results of this preliminary survey of IDB energetics suggest that ionicity plays a significant role in determining the energetics of tetrahedral semiconductors. It was found that the IDB formation energy increased with increasing ionicity as was expected. Certain points, however, are worthy of further comments. Namely, the relaxation at the defect boundary observed for InAs was substantially lower than that found for InSb or GaSb. The reason for this apparent insensitivity of total energy to positional relaxation is not obvious at present and further investigations on even more highly ionic materials will be necessary to more fully explore this issue. The results for GaSb indicate that IDBs should be most common in this material assuming that the phase-transition kinetics are similar. There is some evidence in the image plate results to support this conjecture. As mentioned briefly in Chapter 4, it was found that both the high-pressure and recovered zincblende structures of GaSb showed no visible signs of difference scattering though it should be a factor of 10 larger than in InSb. However, the failure to observe it cannot be entirely attributed to IDBs as the peak widths obtained in the GaSb powder pattern were generally broader than those of InSb, indicative of a smaller particle size.

§6.5 Summary and conclusions

Results from a novel application of anomalous high-pressure x-ray diffraction using an image plate detector have motivated the present *ab initio* study of inversion domain boundary energetics in tetrahedral semiconductors [5]. Consideration of the experimental evidence and results of total energy calculations leads to a persuasive argument against largescale site-disorder in the high-pressure or recovered phases of InSb. Preliminary computational and experimental investigations on other tetrahedral semiconductors suggest that the conclusions arrived at for InSb are likely to be relevant for other materials as well. More generally, this chapter has attempted to illustrate an example of how modern diffraction techniques, coupled with 'simple' energy considerations can give new insights into the nature of highly first order structural transitions and can even allow for meaningful speculation on the microstructures which result from the large volume collapses.

---

[1] B.E. Warren X-ray diffraction Dover Publications, London (1991).

[2] Explicitly, $h_1 = h + h'_1$, $h_2 = k + h'_2$, $h_3 = l + h'_3$. From Reference [1], assuming N_1, N_2 and N_3 are not small the intensity is closely confined to integer values of $h_1h_2h_3$. The change of variables implies $h'_1h'_2h'_3$ will be small and that $h_1h_2h_3$ can be replaced by integral values of hkl.

[3] N.H. Cho, B.C. DeCooman, C.B. Carter, R. Fletcher and C.B. Wagner *Appl. Phys. Lett.* **47** (1985) 879.

[4] Recently, promising steps have been taken in the development of accurate force calculations using the APW approach For example, J.M. Soler and A.R. Williams *Phys.*

Rev. B **40** (1989) 1560 and *Phys. Rev. B* **42** (1990) and T. Oguchi (private communication). According to this method the force on an atom is determined only by integrals over the muffin-tin spheres though additional steps are required to 're-orthonormalise' the wavefunctions after ionic displacement. These authors have expressed an interest in the IDB problem and have agreed to pursue FLAPW calculations on the high-pressure phases of semiconductors including relaxation at the boundary.

5 W.R. Lambrecht, C. Amador and B. Segall *Phys. Rev. Lett.* **58** (1992) 1363.

6 J.Crain, G.J. Ackland, R.O. Piltz and P.D. Hatton *Phys. Rev. Lett.* **70** (1993) 814.

Chapter 7
STRUCTURAL METASTABILITY IN HIGHLY CONDENSED SEMICONDUCTORS

§7.1 Introduction: computer experiments and the present limits of *ab initio* methods

In this final chapter, an attempt is made to illustrate an example of how *ab initio* computational methods can go beyond serving to confirm (or be at odds with) experimental results. This is because several of the calculations have been performed on materials which have not yet been synthesized. Specifically, the present chapter is concerned with structural and electronic properties of topologically complex silicon structures which are metastable with respect to diamond. These materials are of particular importance in modeling the electronic and optical properties of amorphous materials. The sequence of crystal structures: diamond, wurtzite, BC8 and ST12 (in order of increasing complexity) has been used in order to study the development of the properties of amorphous materials as a limiting form of stepwise increase of short-range disorder in crystalline phases.

The topological differences between BC8 and diamond structure Si underlie the observed metastability. For BC8 to diamond reconversion to occur, 25% of the tetrahedral bonds must be broken and reformed. A slightly lesser degree of bond-breaking is required to transform BC8 into the wurtzite structure. It has been suggested that the defect structure of microcrystalline Si in the β-Sn phase may act as nucleation centres for the BC8 phase upon depressurisation.

In addition to all that can and has been addressed by standard *ab initio* density functional methods, there remains a host of unresolved questions regarding more general issues about metastable phase formation in tetrahedrally coordinated semiconductors. For example, other materials such as the partially ionic III-V compounds which adopt similar high-pressure structures to purely covalent Si appear not to transform to the BC8 structure upon depressurisation. Instead, a defected zincblende structure striated by twins and inversion domain boundaries is recovered in InSb, GaAs, InAs, GaSb and perhaps many if not all others. In this chapter, density functional total energy pseudopotential methods will be applied to several III-V semiconductors in the diatomic equivalent to the BC8-Si structure in an attempt to determine whether the failure of the BC8 structure analogue to form in compound semiconductors is likely to be a result simply of total energy differences between the BC8 and zincblende structures or of unfavourable conditions encountered during depressurisation.

In order to develop a fuller understanding of relative structural stability in Si, it is necessary to determine free energies of the phases in question over a range of temperatures. Despite the promise of present-day density-functional methods, the determination of free energies from first-principles techniques is not yet possible. Such information is only accessible through classical interatomic potentials. Despite the topological dissimilarities between diamond and BC8 the character of the bonding may be sufficiently similar so that straightforward application of Si pair potentials and bond-bending forces can be applied to investigate the issue of structural stability of BC8 with respect to diamond. If pair potentials are found to be accurate representations of the relevant physics then a sufficiently thorough lattice-dynamical calculation can be performed so as to allow for free energies to be determined. This will be addressed and preliminary results given in the closing section.

§7.2 Pressure-induced tetrahedral forms of highly condensed silicon

7.2.1 Background to the BC-8 form of silicon

Silicon exists naturally in the diamond structure (Si-I) and upon pressurization is reported to transform to the metallic β-Sn structure (Si-II). Rapid depressurization, however, does not result in a conversion back to the original ambient pressure diamond structure. Rather, a superdense, semimetallic form of silicon (Si-III) is produced. The pressure ranges over which these and other phases are found are summarised in Table 7.1 The first evidence of such behaviour was revealed through experiments on silicon in which the electrical resistivity was monitored as a function of pressure [1]. Upon compression above 200 kbars, the resistivity of Si was observed to drop by 5 orders of magnitude, relative to its ambient pressure value. Subsequent pressure release from the metallic phase resulted in an increase in resistivity by a factor of less than 100 thus suggesting that a more metallic form of silicon had been formed. The structure of this semimetallic phase was determined by early x-ray diffraction studies [2,3] which have now been confirmed by more recent and more sensitive experiments [4,5,6,7] in which further pressure-induced phases of Si have been identified. It should be stressed that when pressurised into any of its metallic forms, Si will apparently not reconvert to the diamond structure and that either BC8 or more complex metastable structures are created.

Diffraction evidence suggests silicon-III is body-centred cubic having a lattice parameter of 6.64 Å and 8 atoms per unit cell. Systematic absences indicate that the likely spacegroup is Ia3-T_h^7 and the structure requires specification of only a single positional parameter x which has been experimentally determined to be approximately 0.1003 +/- 0.001. The structure (Figures 7.1 a-c) is characterised by a more efficient packing of Si tetrahedra than exist in the usual diamond structure. These tetrahedra are, however, distorted from their ideal configuration and the distortion gives rise to two bondlengths (A and B) and angles (α and β). Each atom is connected to nearest neighbours by one (shorter) type-A bond and three longer type-B bondsat ambient pressure. Despite the 10% higher density in BC8-silicon relative to diamond structure silicon, the average near neighbour distances are larger which is indicative of weaker covalent bonding. The bondlengths in the BC8 structure are completely determined by the positional parameter x and the lattice constant a [8] as follows: $R_A = 2a(3^{1/2})x$ and $R_B = a(0.25 - 2x + 8x^2)^{1/2}$.

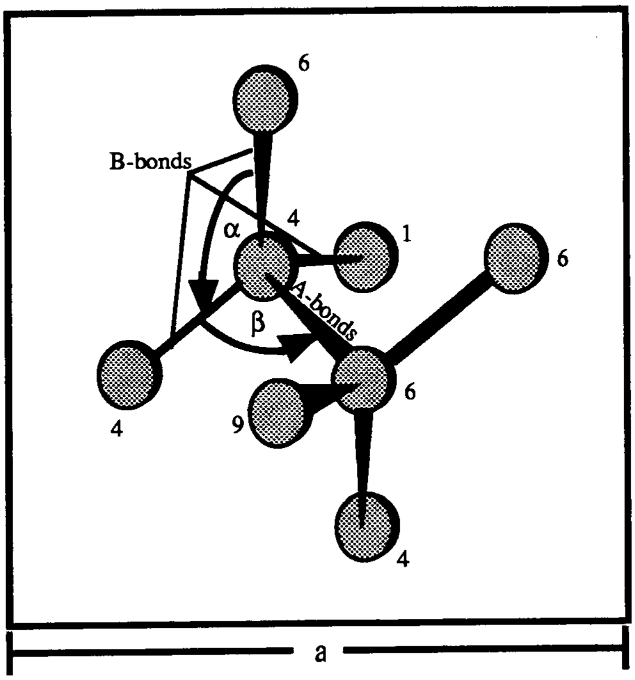

Figure 7.1a [001] projection of the distorted tetrahedral bonding arrangement in the superdense form of silicon in the BC8 structure based on the structure reported by Wentorf and Kasper in 1964. The numbers beside the atoms indicate their elevation in units of (a/10). At ambient pressure the cubic lattice constant, a is 6.64 Å. The A and B bondlengths are 2.37 Å and 2.38 Å respectively at ambient pressure. These give rise to tetrahedral bonding angles of $\alpha = 108.2°$ and $\beta = 98.2°$.

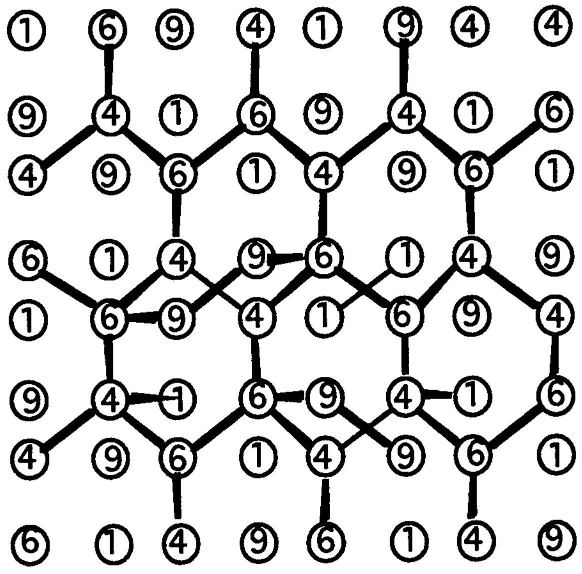

Figure 7.1b [001] projection of the BC8 structure. The numbers indicate atom position elevations in units of a/10.

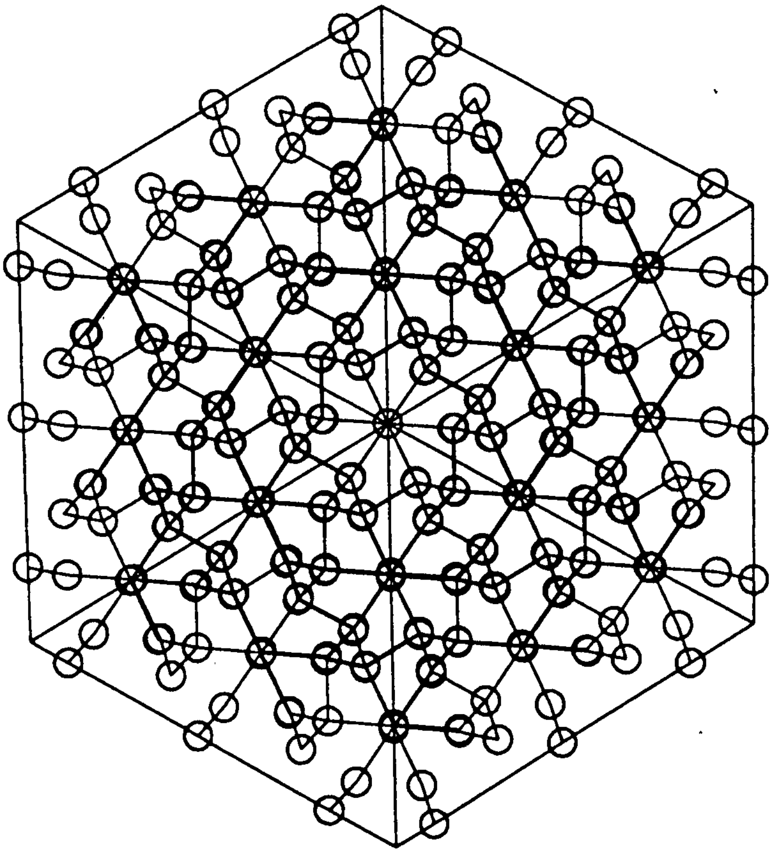

Figure 7.1c [111] projection of the BC8 structure illustrating the complexity of the bonding.

Table 7.1 The Pressure-induced phases of silicon and the pressure ranges in which they are found experimentally.

Designation	Structure	Stability Field (kbar)
I	diamond (cubic)	0 -> ~110
II	β-Sn (tetragonal)	~110 -> ~150
III	BC8	~110 -> 0
V	primitive hexagonal	~140 -> ~400
VII	hexagonal close packed	>400

7.2.2 Prior studies on BC8-silicon

In an attempt to understand its metastablity with respect to the diamond structure, Si-III (BC8) has been the subject of several *ab initio* density functional pseudopotential calculations of total energy [8,9,10]. Similar calculations have been performed for carbon in the BC8 structure. For carbon, the BC8 structure was found to be stable relative to diamond and all metallic phases whereas it was determined to be metastable relative to diamond in the case of Si over all pressure ranges. Also, the energy of BC8-Si was found to be comparable to that of amorphous Si.

The work in references [8] and [9] was performed by including plane waves up to energies of 12 Ry. Relaxation of the BC8 structure in this work involved calculation of the force on the ions for two different values of the positional parameter x "from which the bond stretching force constant for the A bonds was extracted" [8]. These calculations predicted the equilibrium BC8 structure at V/Vo = 0.903 (where Vo = 20.204 Å: the experimental equilibrium atomic volume for diamond). The energy difference between BC8 and diamond structure Si at their respective minimum energy configurations was found to be 0.13 eV/atom.

One issue which has yet to be addressed is that of the semimetallic nature of the BC8 phase in Si. An estimate of the error incurred in a total energy calculation by neglecting band overlap has been discussed by Janak [11] and Biswas *et al* [8]. The estimate is based on the result that the variation in the density functional total energy E_{tot} with respect to state occupation f_i is equal to the variational energy eigenvalue of that state ε_i. This consideration then provides a means of interpreting density functional eigenvalues. Estimation of the small total energy differences relative to the ground state can be made within the context of one electron energies.

The total energy difference incurred by slight changes of population of levels is given by

$$\delta Etot = \sum_i \delta f_i \, \varepsilon_i .$$

For BC8-Si it was found [8] that the small Fermi surface contains an upper bound of 0.2 electrons (out of 32 per unit cell) gives rise to a change in total energy of less than 5 meV/atom which suggests that corrections to total energies as a result of semimetallic character are negligible compared to the energy differences between phases.

§7.3 III-V Semiconductors in complex tetrahedral structures: Computer experiments on fictitious compounds

7.3.1 Tests on BC8-Si

In an attempt to determine why the formation of dense tetrahedrally bonded structures such as BC8 and ST12 (See section 7.3.3) appear to form exclusively in purely covalent systems such as silicon and germanium, whilst the zincblende structure is recovered from high-pressure in compound semiconductors, a series of *ab initio* calculations have been performed on Si, AlSb and InAs in the diamond and BC8 phases. These were chosen so as to investigate a range of bondlengths and ionicities. Si was investigated first as a test in order to determine how well the results agree with the existing prior calculations and to explore any differences in structural relaxation under the influence of Hellmann-Feynman forces relative to that reported previously. Results of these *ab initio* calculations on Si will then be compared with those of subsequent empirical calculations [12].

Calculations were performed using *ab initio* non-local ionic pseudopotentials for Si. Exchange and correlation was incorporated according to the parameterized Ceperley and Adler scheme as discussed in Chapter 2 [13]. Plane waves up to 250 eV (~18.4 Ry) were used [14]. Brillouin zone integration was approximated by 4 special k-points for both the diamond and BC8 structures. The BC8 structure was relaxed under the influence of Hellmann-Feynman forces until the calculated forces were less than 0.001 eV/Å. These double-precision calculations were performed exclusively on the AlphaVax supercomputer at the University of Edinburgh.

The calculated results regarding equilibrium structural properties are in good agreement with those of prior studies for both the stable and metastable forms. The equilibrium lattice constant and bulk modulus were found to be 6.54 Å and 0.89 GPa, respectively for the BC8 structure. The BC8 lattice constant agrees to within 1.2% of that reported from experiment [15]. The present calculations predict the Si-BC8 structure to be slightly higher in energy than the diamond structure at the respective energy minima of both configurations. The calculated value of the energy difference (~0.12 eV/atom) between the two structures compares very well with the value of 0.13 eV/atom reported by Biswas

[8]. The calculated pressure dependence of the internal structure of BC8 (including the two Si-Si bondlengths and angles) is represented in Figures 7.2a and 7.2b and will also be addressed in greater detail in a later section when comparison to an empirical calculation using Si interatomic pair-potentials is made.

The calculated atomic positions of the fully relaxed BC8-Si structure evaluated at the minimum energy lattice constant are shown in Table 7.2 along with the calculated residual forces. Valence charge densities are shown in Figure 7.3 in a plane containing Si-Si bonds of both A and B types.

The value of x which fully relaxed the BC8 structure at the minimum energy lattice constant was found to be 0.10016 which is equal to the experimental value within the reported measurement error [3]. It is clear from present and prior work that structural properties of BC8 Si can be well described by the LDA using *ab initio* pseudopotentials. In what follows the present techniques are applied with the objective of gaining insight into the formation and stability of more complex tetrahedral structures in Si and other materials and to attempt to draw some conclusions regarding the effect of temperature. In order to accomplish certain aspects of these goals the application of empirical Si potentials must also be investigated and will form the subject of a future section.

7.3.2 Metastability of the BC8 structure in compound semiconductors

In the present section structural stability of the BC8 diatomic analogue is considered for the tetrahedral semiconductors InAs and AlSb. in order to expose and explore the reasons why complex tetrahedral forms appear not to be created upon depressurisation of the III-Vs from metallic phases which are similar to if not isostructural with those of Si. First, however, a certain amount of experimental input is required to confirm that the BC8 structure is definitely not found in these compounds. Data taken on the image plate has shown that for all tetrahedral semiconductors (apart from Si) investigated up to the time of writing (InSb, GaAs, GaSb,

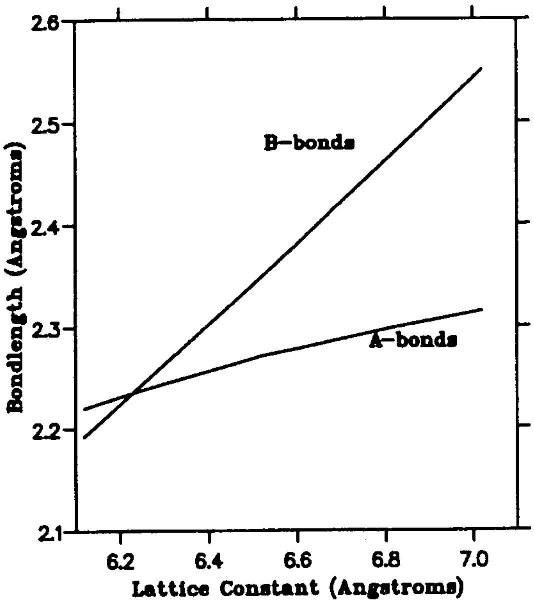

Figure 7.2a Calculated pressure dependence of the BC8 structure of Si. At a crossover point corresponding to a lattice constant of approximately 6.2 Å the 3 B bonds are predicted to become shorter than the A bond.

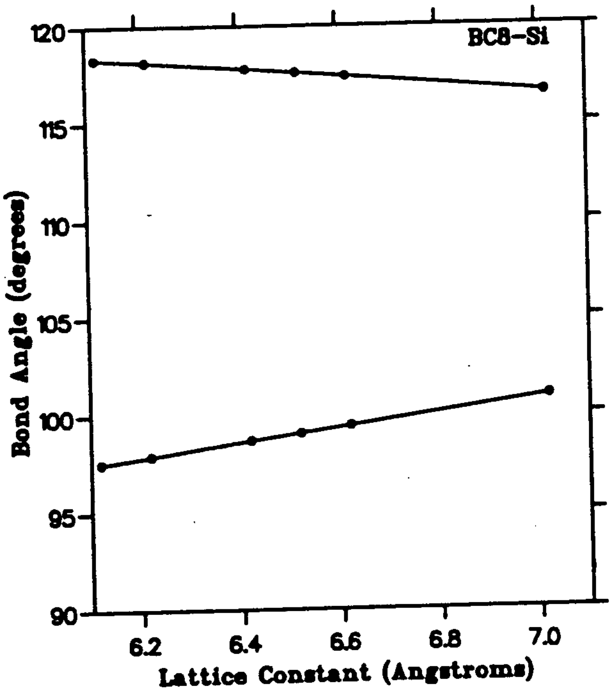

Figure 7.2b Calculated pressure dependence of the two BC8-Si bond angles as a function of compression.

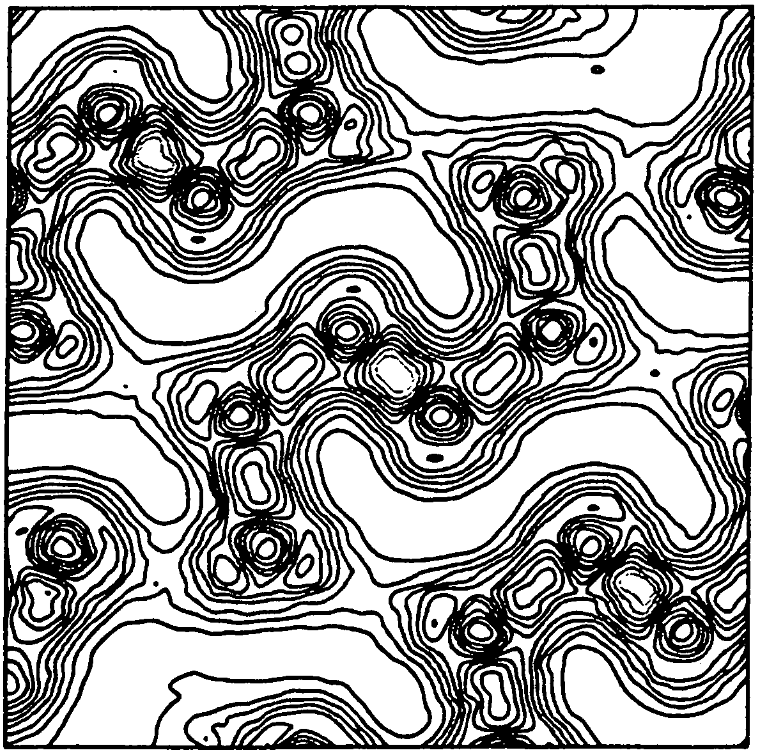

Figure 7.3 Valence charge density for BC8-Si illustrating the covalent bonding and charge distribution in a plane containing both A and B bonds.

Table 7.2 Calculated atomic positions for fully relaxed BC8 Si at the minimum energy lattice constant. A simple cubic representation (SC16) of the body-centred BC8 structures is used which requires 16 atoms in the primitive unit cell. The small residual forces on the atoms after structural relaxation are also shown.

	Atom Positions (Fractional coords.)			Forces (eV/Å)		
Atom	x	y	z	Fx	Fy	Fz
1	0.100177	0.100190	0.100168	-0.000514	0.000028	0.000031
2	0.899814	0.899813	0.899804	-0.000117	0.000847	0.000587
3	0.399763	0.899804	0.600195	0.000809	0.001235	-0.000779
4	0.600137	0.100152	0.399829	0.000106	0.001050	-0.000300
5	0.899816	0.600204	0.399804	-0.000685	-0.000907	0.000093
6	0.100813	0.399827	0.600146	-0.000780	0.000292	0.000819
7	0.600143	0.399858	0.899816	0.000473	-0.000782	0.000171
8	0.399789	0.600221	0.100186	0.000139	-0.001426	-0.000813

9	0.699171	0.399813	0.600157	-0.000763	-0.000443	0.000202
10	0.399825	0.399810	0.399786	-0.000520	0.000295	0.001075
11	0.899782	0.399810	0.100185	0.000646	0.000729	-0.000639
12	0.100160	0.600155	0.899820	-0.000352	-0.000624	-0.000141
13	0.399811	0.100204	0.899820	-0.000352	-0.000459	-0.000165
14	0.600177	0.899834	0.100169	-0.000195	0.000414	0.000102
15	0.100128	0.899866	0.399821	0.001003	-0.000517	0.000342
16	0.899770	0.100223	0.600192	0.000915	-0.001040	-0.000591

InAs) only reconversion to the zincblende structure has been observed upon depressurisation. No references to transformation to more complex tetrahedral materials such as BC8 in other III-Vs could be found in the literature and it appears that the BC8 structure only exists in Si.

The *ab initio* density functional calculations on AlSb and InAs have been performed using identical methods to those described for the Si calculations. The trial lattice constants for these materials were determined by assuming that the ratio of the BC8 to diamond structure lattice constants would be approximately preserved in BC8 versions of compound semiconductors. In the present section, only the details for the AlSb calculations will be given. Figure 7.4a shows the calculated energy as a function of atomic volume for AlSb in the zincblende and fully relaxed BC8 structures. It is found that the calculated total energy difference between the BC8 and zincblende structures for this material is approximately 0.07eV/atom as compared to 0.12 for the difference in Si.

The fully relaxed atomic positions for a slightly compressed BC8-AlSb structure are given in Table 7.3 and the two bondlengths are shown as a function of compression in Figure 7.4b. As was found for the case of BC8-Si, BC8-AlSb also displays a bondlength crossover. For the AlSb case, however, the crossover point occurs much closer to the equilibrium lattice constant than it does in Si. Perhaps the most important conclusion which can be drawn from these detailed quantitative calculations is neither detailed nor quantitative. This conclusion is that despite the success that *ab initio* total energy methods have had in describing the metastable BC8 phase found experimentally in Si, the same considerations do not appear to be sufficient to explain why this structure is not observed in other systems.

7.3.3 Empirical and *ab initio* treatments of BC8 and ST12 silicon

Although Si appears to be unique in its adoption of the metastable BC8 [16] phase upon depressurisation Ge exhibits distinct but analogous behaviour. It also adopts the β-Sn structure at high pressure but does not revert to the BC8 structure when pressure is released nor does it transform back to the diamond structure [17]. Instead, pressure release results in yet another arrangement of densely packed tetrahedra which nearly preserve the ideal diamond structure Ge bondlengths. Structural identification of this phase was reported in 1964 by Kasper and Richards [3]. This superdense form of Ge is simple tetragonal (ST) (a = 5.93 Å, c = 6.98 Å) having 12 atoms in the unit cell and has come to be referred to as the ST12 form. The spacegroup was determined to be $P4_32_12$ (D_8^4) or its enantiomorph.

The structure is completely determined by the specification of two lattice constants and 4 free atomic positional parameters. The density is approximately 10% greater than that of diamond and the bondlengths are roughly 1% larger than in the ambient pressure form. All atoms are not unique in ST12 as there are two distinct atomic environments. This leads to very intriguing topological considerations and a wide variety of substructures. There are 4 atoms of type a and 8 of type b. The type b atoms form spiral chains along the unique axis and the type a atoms bridge atoms in different spirals. All of the spirals in the ST12 structure rotate in the same direction and give the structure a well-defined helicity. The fivefold and sevenfold ring configurations of ST12, which serve to preserve local tetrahedral bonding without inducing large strains, are common features in models of (2x1)-Si(111) surface reconstructions and amorphous semiconductors. The angular distortions which were relatively small in the BC8 structure are much more appreciable in ST12. A projection of the ST12 structure is shown in Figure 7.5. The observation that upon depressurization Ge adopts the ST12 structure and Si the BC8 structure despite their otherwise isostructural character at ambient and high pressure motivates a study with a view to determining the origins of the different behaviour. In the present section the combined results of empirical and *ab initio* calculations are considered in attempt to investigate whether the semimetallic nature of these dense metastable phases precludes successful application of pair potentials. The results from these calculations

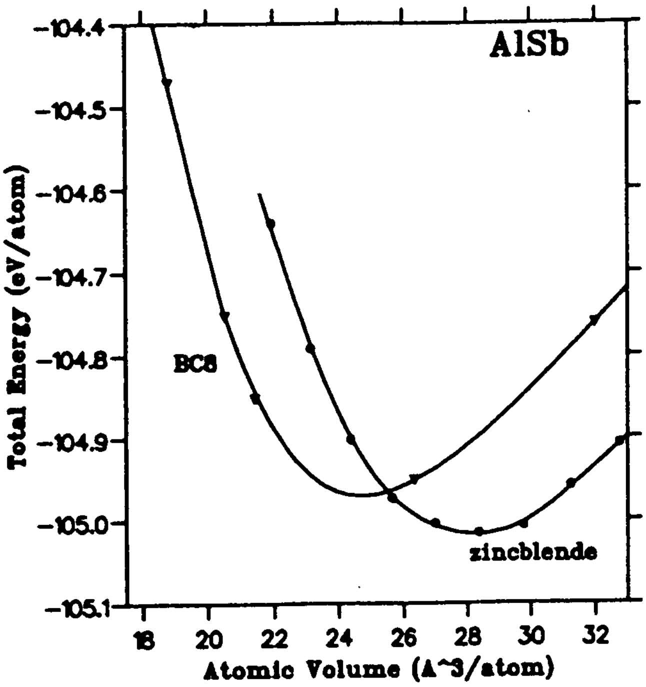

Figure 7.4a Total energy as a function of atomic volume for the III-V semiconductor AlSb in the zincblende and BC8 structures. The curves represent polynomial fits to the data and are not equations-of-state.

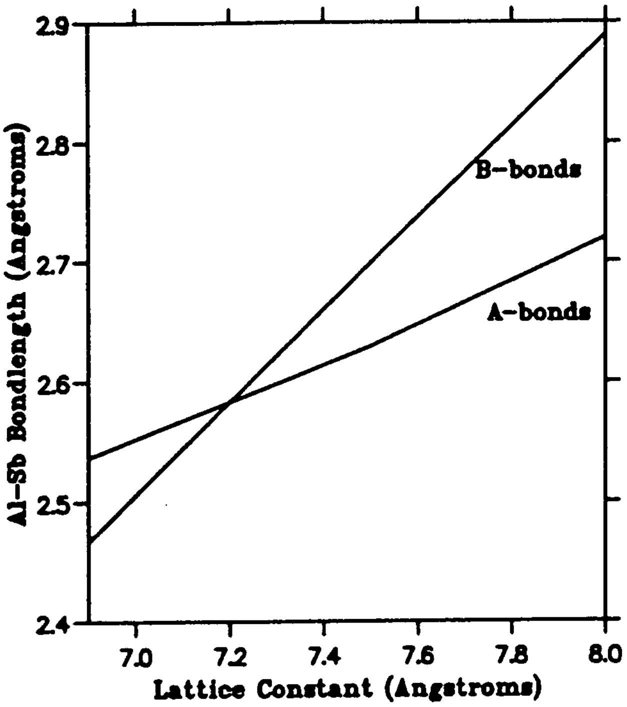

Figure 7.4b Calculated Al-Sb bondlengths as a function of compression for AlSb in the BC8 structure. As was predicted for BC8-Si, a crossover to a condition where there are three short bonds and one long bond is found in this material as well.

are then applied in order to address the question of relative phase stability of BC8 and ST12 Si.

Table 7.2 Calculated atomic positions for fully relaxed BC8 AlSb at a compressed lattice constant of 6.9 Å. A simple cubic representation (SC16) of the body-centred BC8 structure is again used. Residual forces on the atoms after structural relaxation are also shown.

		Atom Positions (Fractional coords.)			Forces (eV/Å)		
Type	Atom	x	y	z	Fx	Fy	Fz
1	1	0.105567	0.105591	0.105566	-0.005621	-0.004436	-0.004827
1	2	0.394391	0.894426	0.605598	0.004674	0.004676	-0.005152
1	3	0.894412	0.605595	0.394409	0.005538	-0.006269	0.005651
1	4	0.605553	0.394432	0.894417	-0.004664	0.005004	0.004938
1	5	0.394449	0.394443	0.394436	0.005177	0.005165	0.006197
1	6	0.105601	0.605597	0.894416	-0.005477	-0.005731	0.004074
1	7	0.605590	0.894410	0.105573	-0.004369	0.005629	-0.004623
1	8	0.894427	0.105561	0.893257	0.006002	-0.004675	-0.005764
2	1	0.894427	0.893261	0.605554	0.012566	-0.011947	-0.014151
2	2	0.60617	0.106718	0.393262	0.014222	0.014515	-0.012014
2	3	0.106743	0.393264	0.606739	0.012027	0.013244	0.012014
2	4	0.393256	0.606756	0.106752	-0.013158	0.012127	0.013218
2	5	0.606753	0.606786	0.606760	0.013158	0.011797	0.012461
2	6	0.893253	0.393275	0.106718	-0.013516	-0.013240	0.013629
2	7	0.393265	0.106731	0.893276	-0.013127	0.013878	-0.013162
2	8	0.106766	0.893249	0.393224	0.011546	-0.012863	-0.012321

Empirical potential treatment of superdense Si

Strategies for the development of empirical interatomic potentials for Si have been the subject of a vast amount of effort [18,19,20]. A three-body force-potential approach has also been developed recently for III-V compound semiconductors [21,22]. Apart from essential comments, no review of the subject will be attempted here. Despite the enormous variety of approaches to the problem the common theme underlying all such empirical models is the idea that the energy of a system of atoms is a sum of single-atom energies associated with each site. The energy at each site is expressed as continuous function of the relative positions of all other atoms. The relevant interactions giving rise to the energy of the assembly of atoms can be decomposed into one-, two- and three-body etc. terms. The model used in the present study [23] attributes cohesion to the electrons and assumes a pairwise repulsion between ions. Each pair of valence electrons exists in a two-centre orbital the energy of which is a function only of the separation between ions. The functional forms for the interactions are chosen as follows. The repulsive part of the interaction is modeled by a simple exponential and the strength of the covalent bonding is represented by the radial part of the p-wavefunction of a hydrogenic atom. The energy E, within this model is then expressed by a sum over the pairwise repulsion and a second sum of the electrons in the covalent bonds:

$$E = \sum_{ij=1}^{N} A e^{-\alpha r_{ij}} + \frac{1}{2}\sum_{i=1}^{N} \sum_{n=1}^{4} B r_{ik_n} e^{-\beta r_i k_n} + \sum_{i} \sum_{n=1}^{3} \sum_{m=n=1}^{4} C(\mathrm{Cos}(\omega R_{k_m k_n}) + \frac{1}{3}) \tag{7.3.1}$$

The sum over n runs through the four electron pairs in the bond having atom i as one of their foci and k_n as the other. The separation between the ions on which the orbital is centred is r_{ik} and C is a free parameter which determines the strength of the bond-bending forces [18] which are bond-bond repulsive interactions. The minimum of the third term falls at the tetrahedral angle, $\omega R_{k_m k_n}$, in diamond structure Si. The inclusion of this term will be particularly important when low frequency vibrations of various Si structures are considered. The fitting parameters in this model are the four quantities A,B, α and β and can be fitted to experimental data such as cohesive energy, lattice parameter and bulk modulus. The present formulation describes cohesion in terms of electron bonding as opposed to effective pairwise interactions. Energy is minimised with respect to atomic position. It is found, rather surprisingly that the pressure-induced diamond to β-Sn structural transition is well described with the present model. However, as with all other empirical formulations, the experimentally observed transition to the simple hexagonal structure [24,25] however is not predicted. Nevertheless the method appears to provide sensible results even in 6-fold coordinated metallic structures. For these structures the

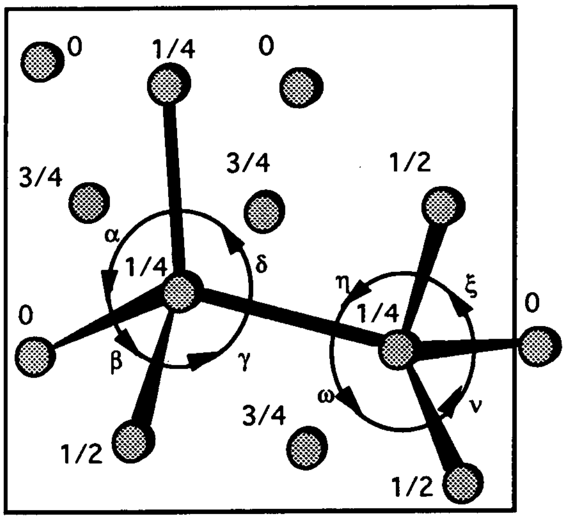

Figure 7.5 The [001] projection of the ST12 structure found only metastably in Ge depressurised from its metallic form. The numbers beside the atoms represent elevations of the positions in units of the cell dimension of the unique c-axis. The values of the angles (represented as Greek letters) are shown in table 7.3. This structure has analogues in keatite and in a high pressure form of ice (Ice-III)

Table 7.3 Structural Details for ST12 Ge as reported by Kasper and Richards [3].

parameter	value
$\alpha(^\circ)$	98.2
$\beta(^\circ)$	102.8
$\gamma(^\circ)$	94.2
$\delta(^\circ)$	98.3
$\eta(^\circ)$	94.3
$\omega(^\circ)$	104.4
$\upsilon(^\circ)$	105.6
$\xi(^\circ)$	119.5
a(Å)	5.93
c(Å)	6.94
density g-cm^3	5.90

model assumes that only four neighbours of a given atom are bonded to it and configurations of higher than effective tetrahedral coordination imply a resonance between bonding arrangements. In view of the fact that the BC8 and hypothetical ST12 structures of Si are a semimetal and a semiconductor, respectively which maintain tetrahedral Si coordination it is possible that the present empirical approach may provide an accurate description of these phases and expose certain trends which would be otherwise inaccessible through *ab initio* methods [26]. For example, an accurate empirical treatment of these phases would then allow an exhaustive lattice dynamical study to be performed. While this would be a useful endeavour in itself it would also provide the crucial ingredient for determination of free energies of these phases which cannot be extracted from present-day first-principles approaches.

The total energies of Si in the diamond, β-Sn, BC8 and ST12 structures as calculated with the empirical approach described above are shown in Figure 7.6. The response of the internal structure to isotropic compression for BC8 Si [27] is shown in Figure 7.7. This figure also shows a detailed comparison between the predictions of the density functional and empirical calculations.

Biswas *et al* [8] attempted an approximate relaxation of the ST12 structure by constructing a "force matrix" C_{ij} which was defined by

$$E\text{-}Eo = \frac{1}{2}\sum_{ij} Xi\, C_{ij}\, Xj \qquad 7.2$$

$$F_i = \frac{\partial E}{\partial Xi} = \sum_j C_{ij}\, Xj \qquad 7.3$$

where Xj were taken as the set of structural parameters and F_i were the stresses. Six pairs of calculations led to the construction of the full C_{ij} matrix but "numerical noise" in the calculation precluded successful structural relaxation by this method. In the present work the empirical structural results for the fully relaxed ST12-Si were used as the starting point for the subsequent pseudopotential calculation. In the *ab initio* treatment, the internal degrees of freedom are fully relaxed under the influence of Hellmann-Feynman forces at each volume considered. The results of the density functional calculation for the energy vs volume of ST12 are shown in Figure 7.8.

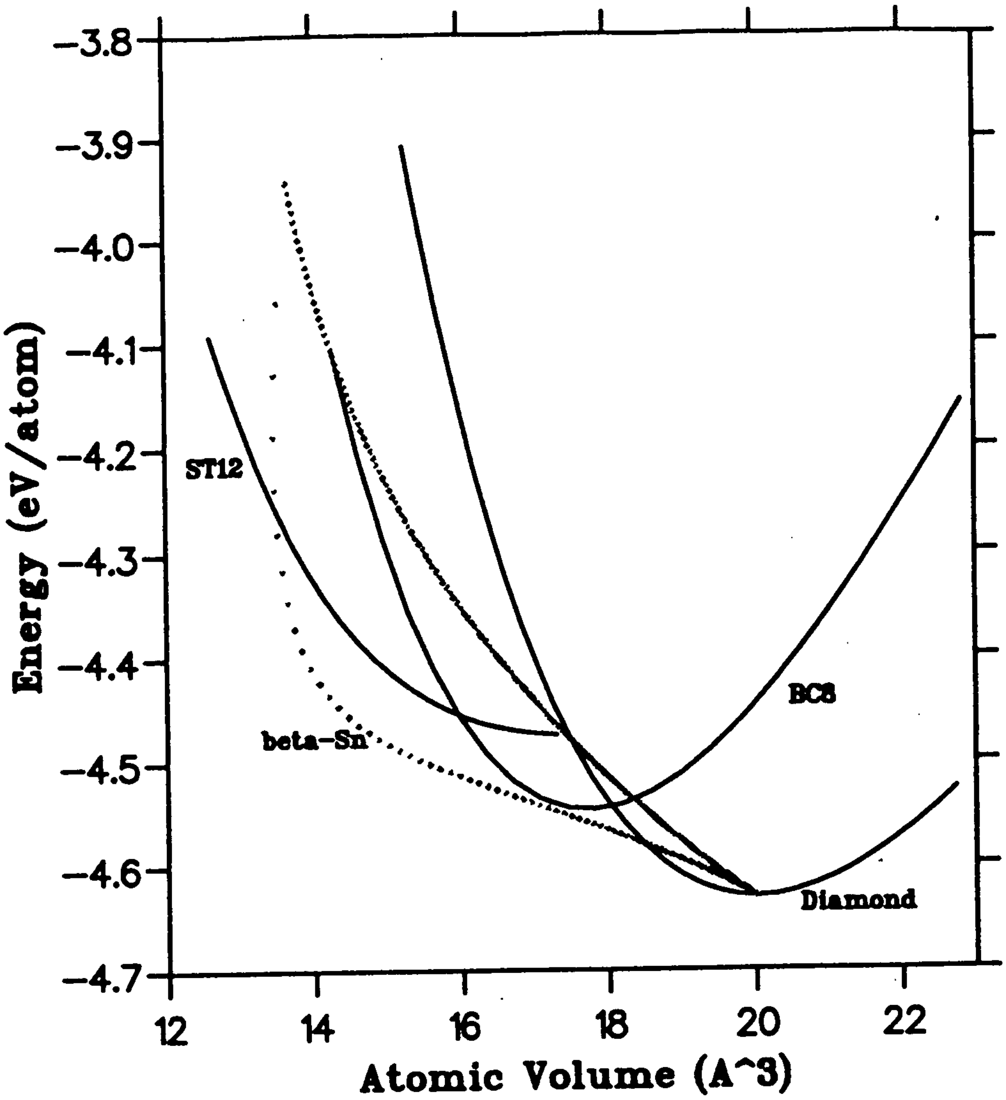

Figure 7.6 Total energy of Si in the diamond, BC8, and ST12 structures as calculated using the empirical approach of Reference [18].The dotted curve represents the minimum point on the energy volume curve for the β-Sn structure at a range of c/a ratios.

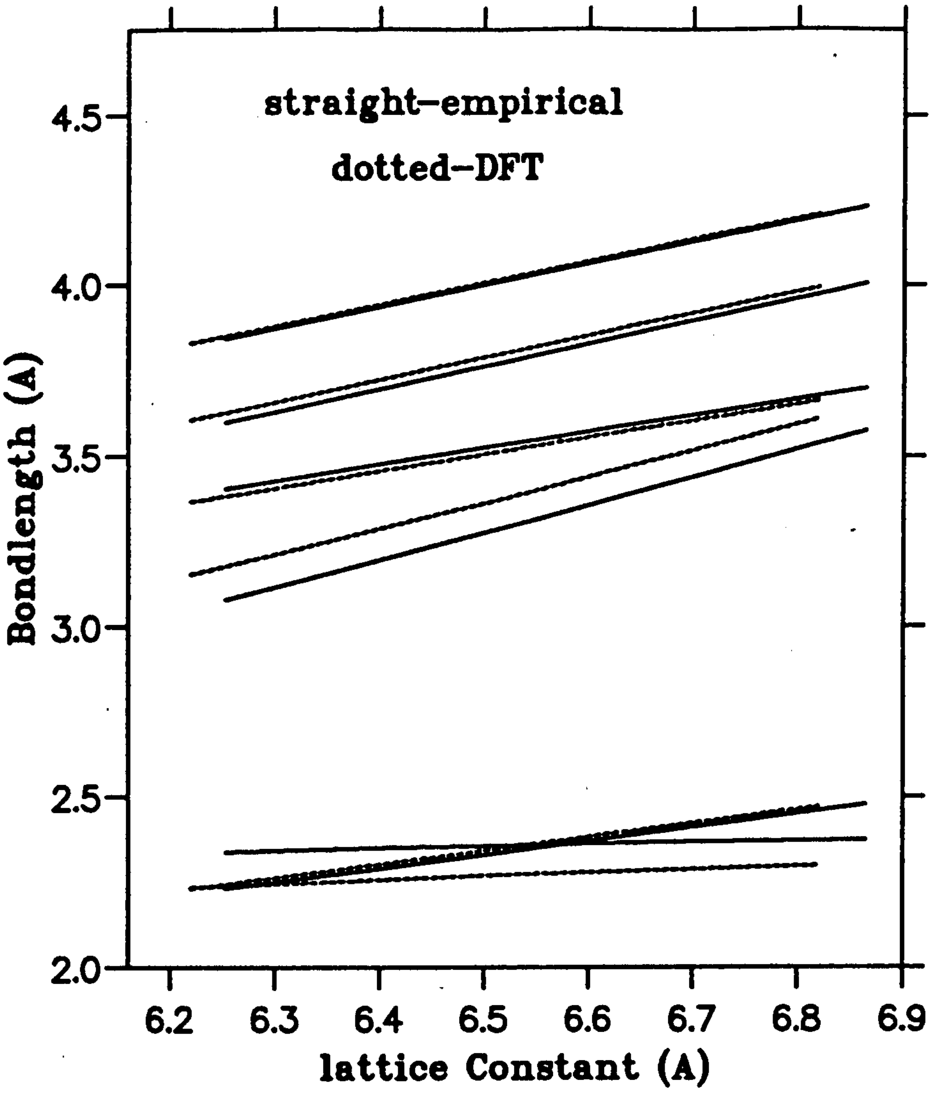

Figure 7.7 Comparison of the structural relaxation of BC8-Si as predicted by *ab initio* pseudopotential and empirical calculations. Shown in the figure are the calculated bondlengths for the inequivalent A and B bonds in the structure. The next-near-neighbor distances are also shown.

The starting configuration used for empirical calculation of the ST12-Si unit cell and structural relaxation was taken to be the same as that found experimentally for ST12 Ge as reported by Kasper and Richards [3]. The ambient pressure unit cell dimensions and the 12 atom positions corresponding to minimum energy according to the empirical calculation for Si in the ST12 structure are shown in Table 7.4. These parameters were then taken as the initial configuration for a subsequent density functional treatment. Figure 7.10 illustrates the evolution of the Hellmann-Feynman force components on the atoms at several stages of the calculation towards convergence.

Table 7.4 Calculated minimum energy structural parameters and unit cell dimensions for Si in the ST12 structure as determined by empirical interatomic potentials at a c/a ratio of 1.08. The fractional coordinates compare well to those determined experimentally by Kasper and Richards [3] for ST12-Ge. This calculated c/a ratio differs approximately by 7% from that observed in Ge and is found to be sensitive to bond-bending forces. These parameters were used as the starting configuration in a subsequent density functional pseudopotential calculation using the approach of Car and Parrinello the results of which are shown in Table 7.5 and Figure 7.8.

Atom	x	y	z
1	0.183778	0.385066	0.252124
2	0.816224	0.614934	0.752124
3	0.114934	0.683778	0.002124
4	0.885066	0.316224	0.502124
5	0.385066	0.183778	0.747876
6	0.614934	0.816224	0.247876
7	0.316224	0.885066	0.497876
8	0.683778	0.114934	0.997876
9	0.090888	0.090888	0.000000
10	0.909112	0.909112	0.500000
11	0.409112	0.590890	0.750000
12	0.590890	0.409112	0.250000

lattice constants

a =b=5.7617Å

c=6.2545Å c/a=1.085

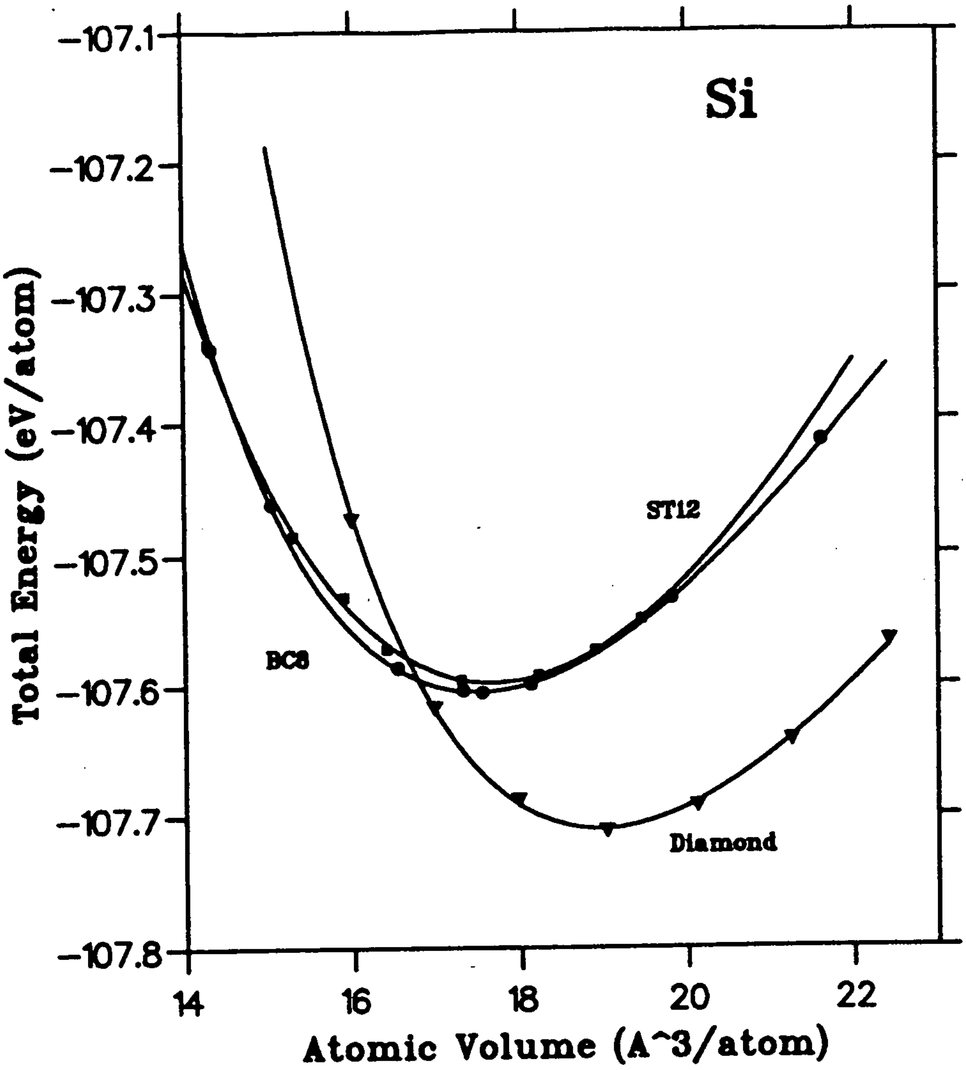

Figure 7.8 Total energy of Si in the diamond, BC8 and ST12 structures as calculated using *ab initio* pseudopotentials with a plane wave basis set and an energy cutoff of 250 eV. Both the BC8 and ST12 structures were fully relaxed under the influence of Hellmann-Feynman forces. The energy difference between diamond and BC8 was found to be 0.13 eV/atom. The curves represent fits to the Murnaghan equation of state [Eq 5.1] in each of the three phases considered. The ST12 c/a ratio is 1.23 and its determination is discussed in the text and in Figures 7.9 a and b.

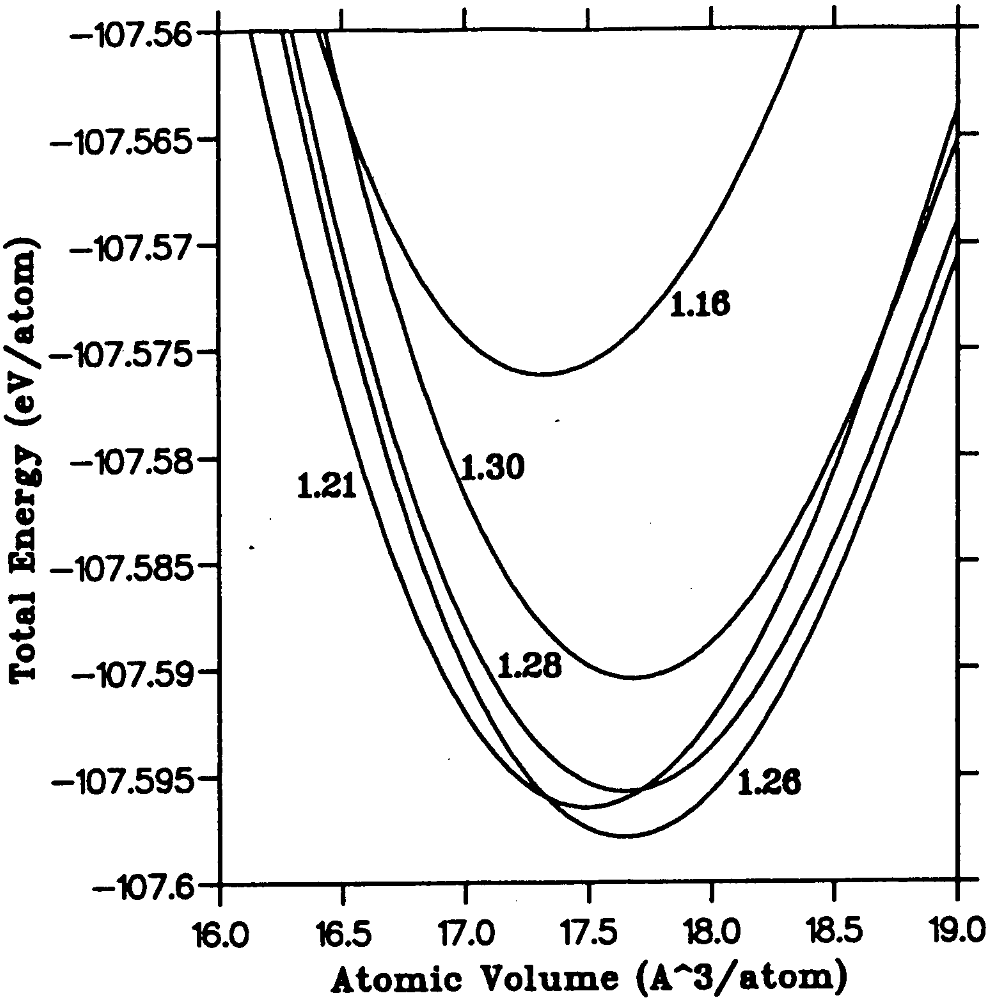

Figure 7.9a The sensitivity of total energy to c/a ratio in ST12-Si as determined by density functional pseudopotential calculations. The figure shows Murnaghan equation-of-state fits to calculated points at c/a ratios of 1.08,1.16,1.21,1.26 and 1.30. At each c/a ratio, total energy was calculated at (at least) 7 volumes reasonably equally spaced over the range of atomic volumes shown. The approximate minimum c/a ratio of 1.23 is approximately 5% larger than that reported for ST12-Ge.

As ST12-Si is tetragonal the fully relaxed total energy as a function of unit cell volume has been calculated at a range of c/a ratios and the results are shown in Figures 7.9a and b. It is found that both the equilibrium unit cell

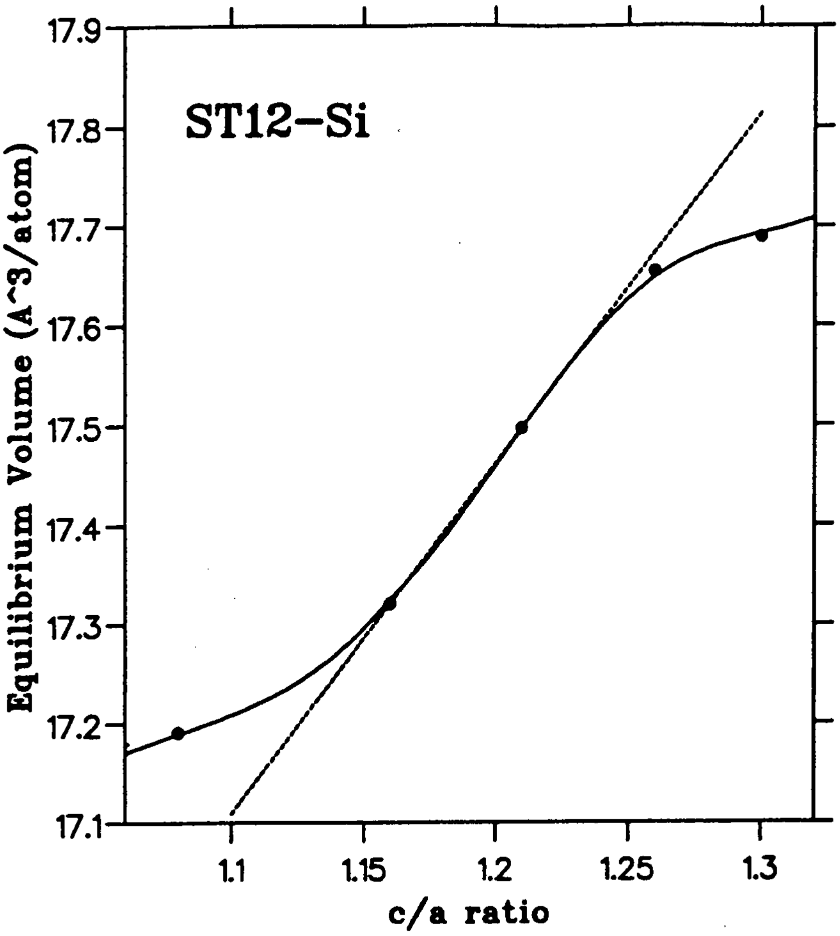

Figure 7.9b The equilibrium volume of ST12-Si as a function of c/a ratio. Two regimes of c/a values are identified in which the equilibrium volume appears to be relatively insensitive to changes in c/a ratio. However, over most of the c/a range investigated a strong dependence is observed. The dashed line is a guide to the eye illustrating the degree to which equilibrium volume variation with c/a appears to be linear.

volume and total energy are sensitive functions of the c/a ratio. The total energy differs by nearly 70 meV/atom between c/a = 1. 08 and c/a= 1.23 and the equilibrium atomic volume varies by nearly 0.5 Å^3/atom over the same range of c/a ratio. This sensitivity to c/a ratio is not as pronounced in

Table 7.5 Calculated minimum energy structural parameters and residual forces (in eV/Å) for Si in the fully relaxed ST12 structure as determined by density functional pseudopotential calculations using the approach of Car and Parrinello. The unit cell parameters and starting configuration of the atoms were the same as those predicted to be of lowest energy by the above empirical calculation.

atom	Positions(fractional coordinates)			Forces after relaxation (eV/Å)		
	x	y	z	F_x	F_y	F_z
1	0.175294	0.379277	0.247283	-0.00354	-0.00701	-0.03282
2	0.824754	0.620769	0.747282	0.014094	0.08079	0.027840
3	0.120824	0.675202	0.997343	0.024593	-0.03089	-0.01580
4	0.879208	0.324819	0.497353	-0.01825	0.028231	-0.00614
5	0.379244	0.175250	0.752822	-0.00775	-0.01346	0.035242
6	0.620733	0.824779	0.252762	0.001790	0.013928	0.026026
7	0.324825	0.879192	0.502733	0.029893	-0.01811	0.013430
8	0.675171	0.120810	0.002711	-0.03933	0.019918	0.010251
9	0.084943	0.084927	0.000058	-0.01274	-0.02083	-0.00400
10	0.915102	0.915110	0.500019	0.023631	0.022499	0.004695
11	0.415136	0.584857	0.740064	0.030041	-0.03300	0.004412
12	0.584855	0.415155	0.249996	-0.41948	0.031875	-0.00433

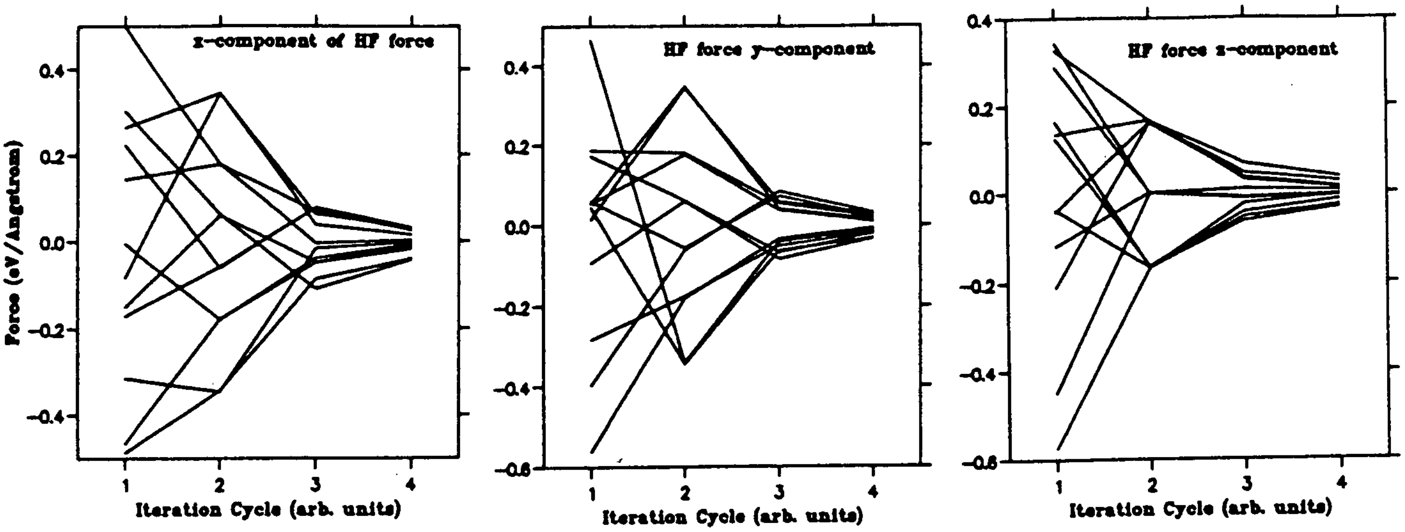

Figure 7.10 (a) **Figure 7.10 (b)** **Figure 7.10 (c)**

Figure 7.10 Evolution of Hellmann-Feynman forces on atoms in the ST12 structure of Si. Figures (a) (b) and (c) are the x, y and z components respectively. Cycle 1corresponds to the forces on atoms in the configuration calculated empirically to be most stable for the given unit cell dimensions.

the empirical calculations as it is in the density functional treatment.

§7.4 Future work: free energies and predictive calculations

Ideally one wishes to investigate structural stability of crystalline phases not only at zero temperature but over a range of temperatures. Unfortunately the extension of *ab initio* density functional calculations to finite temperatures is not simple although extensions of the Hohenberg-Kohn theorem to finite temperatures have been discussed [28]. According to this generalisation the grand potential of a system is a unique functional of the density at that temperature and is a minimum when evaluated at the true groundstate density. A method of implementing these generalized versions of the Hohenberg-Kohn theorem has not yet been developed and they will not be considered further.

The observed and hypothetical metastable phases of Si provide a unique opportunity to investigate free energy considerations as empirical and *ab initio* results appear to lead to similar conclusions regarding relative structural stability and its pressure dependence. In view of these conclusions it might be possible to make reliable estimates of phase stability in Si at finite temperatures. This is the topic of the present section and the strategy is as follows.

The prerequisite for a free energy calculation is knowledge of the lattice dynamical density of states for each of the structures to be considered. The analysis will be based on the classical theory of the harmonic crystal [29,30] in which the allowed phonon frequencies and displacements are determined by a dynamical matrix. The potential energy of a crystal in the harmonic approximation is

$$U_{\text{harmonic}} = \frac{1}{2} \sum_{\mathbf{R}\mathbf{R}'} u^{\mu}(\mathbf{R}) D_{\mu\nu}(\mathbf{R}-\mathbf{R}') u^{\nu}(\mathbf{R}') \qquad (7.4.1a)$$

$D_{\mu\nu}(\mathbf{R}-\mathbf{R}')$ is the second derivative of the interaction potential with respect to position:

$$D_{\mu\nu}(\mathbf{R}-\mathbf{R}') = \nabla^{\mu}_{\mathbf{R}} \nabla^{\nu}_{\mathbf{R}'} V(\mathbf{R}-\mathbf{R}') \qquad (7.4.1b)$$

Where V(**R**-**R**') is a pairwise interaction potential. The resulting equations of motion (in matrix notation) are

$$M\ddot{u}^{\mu}(\mathbf{R}) = -\sum_{\mathbf{R}'} D(\mathbf{R}-\mathbf{R}')u^{\nu}(\mathbf{R}') \qquad (7.4.2)$$

Substitution of plane wave trial solutions of the form $u^{\mu}(\mathbf{R},t) = \varepsilon \exp\{i\mathbf{k}\bullet\mathbf{R} - i\omega t\}$ into the equations of motion gives rise to the following eigenvalue equations for the displacement vectors and corresponding vibration frequencies.

$$M\omega^2\varepsilon = D(\mathbf{k})\varepsilon \qquad (7.4.3a)$$

$$D(\mathbf{k}) = \sum_{\mathbf{R}} D(\mathbf{R})\exp\{-i\mathbf{k}\bullet\mathbf{R}\} \qquad (7.4.3b)$$

where D(**k**) is the dynamical matrix. From these considerations it is, in principle, possible to construct the phonon dispersion curves and density of states appropriate for general three-dimensional crystals. In the present context the technique will be applied in conjunction with the analytic interatomic potential used for Si in its diamond, BC8 and ST12 structures in the previous sections. The purpose will be to investigate the lattice dynamical consequences suggested by the slight alterations in the bonding configurations and to use the resulting information as the basis for estimates of relative phase stability at finite temperature.

The density of phonon modes for Si in the diamond, BC8 and ST12 structures as calculated with the above method are shown in Figure 7.11. Clusters of approximately 500 atoms were used for each structure. The temperature dependence of the vibrational free energy can then be obtained from the Bose-Einstein distribution. In this preliminary study it was found that the free energies of BC8 and ST12-Si exhibit a crossover at a temperature of very roughly 1000 K suggesting that ST12-Si may be the form obtained by depressurising the metallic β-Sn phase at elevated temperatures. The error associated with this crossover temperature is very large (~500K) but the point is that at least initial steps have been taken to consider the effects of temperature on relative structural stability. By analogy with Ge, it is likely that this phase would be long-lived and metastable. Due to the topological dissimilarities, it seems unlikely that there exists a simple kinetic route between the BC8 and ST12 structures. Consequently, it does not seem possible to transform BC8 to ST12 directly by heating [31,32].

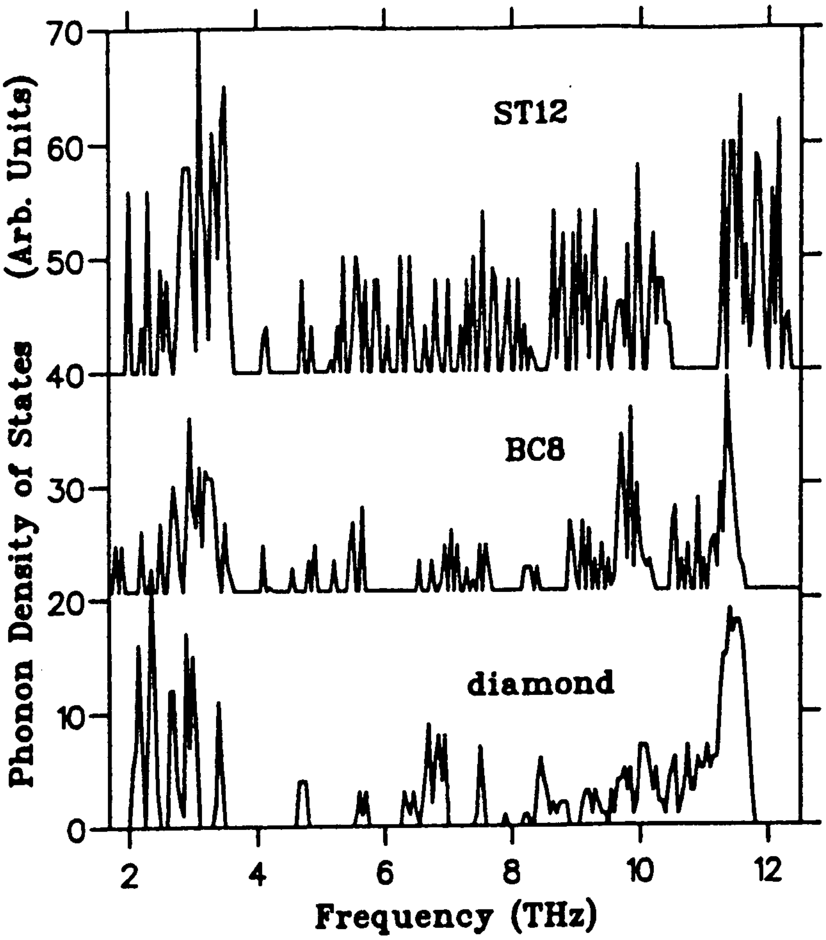

Figure 7.11 Calculated phonon density of states for Si in the diamond, BC8 and ST12 structures as determined using the empirical interatomic potential of reference [18].

§7.5 Summary and conclusions

This chapter has presented a detailed investigation of structural trends in complex tetrahedral silicon structures using first principles methods. Good agreement between density functional predictions and those of emprical calculations and experiment is found. This agreement has allowed conclusions regarding relative phase stability to be drawn from the combined results with a level of confidence which would not be possible using any of the methods individually. These phase stability predictions are easily testable and motivate simple high-pressure/high-temperature experiments.

---

[1] S. Minomura and H.G. Drickamer *Phys. Chem. Solids* 23 (1962) 451.

[2] R.H. Wentorf and J.S. Kasper *Science*, 139 (1964) 338.

[3] J.S. Kasper and S.M. Richards, *Acta Cryst.* **77** (1964) 752.

[4] J.Z. Hu and I.L. Spain *Solid State Commun.* **51** (1984) 263.

[5] J.Z. Hu, L.D. Merkle, C.S. Menoni and I.L. Spain *Phys. Rev.* *B* **34** (1986) 4679.

[6] J. Crain, R.O. Piltz, S. Johnson and P.D. Hatton Unpublished.

[7] G. Weill, J.L. Mansot, G. Sagon, C. Carlone and J.M. Besson *Semicond. Sci. Technol.* **4** (1989) 280.

[8] R. Biswas, R.M. Martin, R.J. Needs and O.H. Nielson, *Phys. Rev. B* **35** (1987), 9559.

[9] M.T. Yin *Phys. Rev. B* **30** (1984) 1773.

[10] R. Biswas, R.M. Martin, R.J. Needs and O.H. Nielson, *Phys. Rev. B* **30** (1984), 3210.

[11] J.F. Janak, *Phys. Rev. B* **18** (1978) 7165.

[12] J. Crain, G.J. Ackland, B.Reid, S.J. Clarke, R.O. Piltz and P.D. Hatton, *Sixth International Workshop on Computational Condensed Matter Physics* (1993) (*International Centre for Theoretical Physics* - Miramare, Trieste, Italy)

[13] The Wigner interpolation form for exchange and correlation was used in the work of Biswas *et al* Ref [8,10].

[14] Biswas *et al* used a cutoff of 12 Ry. Plane waves from 6 to 12 Ry were treated in the second-order Löwdin scheme. This is a tehnique for reducing the computational cost of dealing with very large Hamiltonian matrices required to treat the BC8 structure.

[15] See Reference [5]

[16] Kasper and Richards (Ref [3] pages 754-5) point out that while BC8 appears to be a novel structure for an element it has distinct resemblences to antimonides of zinc and cadmium which exist in distorted tetrahedral arrangements in orthorhombic unit cells.

[17] M. Imai, K. Yaoita, Y. Katayama, J.Q. Chen and K. Tsuji Proc. 5th International Conference on "*The Structure of Non-Crystalline Solids*" (Sendai, Japan, 1991): In this work it was found that a BC8 version of Ge could be synthesised from the β-Sn phase at low temperature and high pressure but ST12-Si could not be formed under any conditions they investigated.

[18] P.N. Keating *Phys. Rev.* **145** (1966) 637.

[19] F.A. Stillinger and T.A. Weber *Phys. Rev.* B **31** (1985) 5262.

[20] R. Biswas and D.R. Hamann *Phys. Rev. Lett.* **55** (1985) 2001.

[21] R.K. Singh and S. Singh *Phys. Rev. B* **39** (1989) 671.

[22] R.K. Singh and S. Singh *Phys. Rev. B* **45** (1991) 1019.

[23] G.J. Ackland *Phys. Rev. B* **40** (1989) 10351.

[24] J.Z. Hu and I.L. Spain *Solid State Commun.* **51** (1984) 263.

[25] R.J. Needs and R.M. Martin, *Phys. Rev. B* **30** (1984) 5390.

[26] J.D. Joannopolous and M.L. Cohen in Solid State Physics vol 31 p 71 and *Phys Rev. B* 7, (1973) 2644: In these references it is argued that odd-fold rings such as those which characterise ST12 generally tend to widen the energy gap and that even-fold rings as found in BC8 introduce states in the gap. Band structural calculations reported in this reference suggest that ST12-Si will have a gap in excess of that found for diamond structure Si. Amorphous Si is also characterised by a well-defined energy gap.

[27] A structural phase transition from BC8 to β-Sn will occur after compression to roughly 85 kbar. This implies that these calculations can only be experimentally investigated over a small spread of lattice constants which correspond to this pressure range.

[28] N.D. Mermin *Phys. Rev.* **137** (1965) A1441.

[29] N.W. Ashcroft and N.D. Mermin Solid State Physics, (Holt, Reinhart and Winston, 1976, USA pages 437-440).

[30] A.A. Maradudin, E.W. Montroll and G.H. "Weiss Theory of Lattice Dynamics in the Harmonic Approximation" in Solid State Physics Supplement 3, 1963.

[31] J. Crain, G.J. Ackland, B. Reid, S.J. Clarke, M.C. Payne, V. Milman, R.O. Piltz and P.D. Hatton *Phys. Rev. B* (Submitted).

[32] G.J. Ackland, S.J. Clarke and J. Crain *Phys. Rev. B* (Submitted).

Appendix A

Separable non-local forms for pseudopotentials

The concern of this discussion is to illustrate how the difficulties in implementation of non-local pseudopotentials using a plane wave basis set and the methods of Klienman and Bylânder. The general form for the ionic potential is given by

$$V_{ion} = \sum_{lm} |Y_{lm}> V_l(\mathbf{r} - \mathbf{R}_I) < Y_{lm}| \tag{A.1}$$

and the resulting energy is defined as

$$E_{ion} = \sum_{lm} <\psi|Y_{lm}> V_l(\mathbf{r} - \mathbf{R}_I) < Y_{lm}|\psi> \tag{A.2}$$

using the plane wave expansion

$$\psi(\mathbf{r}) = \sum_{\mathbf{G}} b_{\mathbf{G}} \exp[i(\mathbf{k}+\mathbf{G})\bullet\mathbf{r}] \tag{A.3}$$

equation A.3 becomes

$$E_{ion} = \sum_{lm} < \sum_{\mathbf{G}} b^*_{\mathbf{G}'} \exp[i(\mathbf{k}+\mathbf{G}')\bullet\mathbf{r}] | Y_{lm}> V_l(\mathbf{r}-\mathbf{R}_I) \text{ x } < Y_{lm} | \sum_{\mathbf{G}} b_{\mathbf{G}} \exp[i(\mathbf{k}+\mathbf{G})\bullet\mathbf{r}]> \tag{A.4}$$

$$E_{ion} = \sum_{lm\mathbf{G}\mathbf{G}'} b^*_{\mathbf{G}'} V_{l\mathbf{G}\mathbf{G}'} b_{\mathbf{G}} \underline{P}_l \exp [i(\mathbf{G}-\mathbf{G}')\bullet\mathbf{R}_I] \tag{A.5}$$

which is a non-separable double sum over reciprocal lattice vectors and the number of operations required for its evaluation scales as the square of the number of plane waves in the basis set. $\underline{P}_l$ is a projection operator for angular momentum l and the exponential factor arises from the structure factor as discussed in the main text. The KB form of the nonlocal pseudopotential is introduced as follows.

$$V^{KB}_{ion} = V_{local} + \sum_{lm} \frac{|\delta V_l \phi_{lm}><\phi_{lm}\delta V_l|}{<\delta V_l \phi_{lm}|\delta V_l|\delta V_l \phi_{lm}>} \tag{A.6}$$

where V_{local} = an arbitrary local pseudopotential and $\delta V_l = V_l - V_{local}$. The projectors are only appreciable in the core region. When applied to the pseudoatomic wavefunctions $|\phi_{lm}\rangle$ the KB potential is exact as shown below.

$$V_{ion}^{KB}|\phi_{lm}\rangle = V_{local}|\phi_{lm}\rangle + \sum_{l'm'} \frac{|\delta V_{l'}\phi_{l'm'}\rangle\langle\phi_{l'm'}\,\delta V_{l'}|\phi_{lm}\rangle}{\langle\delta V_l\phi_{l'm'}|\delta V_{l'}|\delta V_{l'}\phi_{l'm'}\rangle} \qquad (A.7)$$

$$V_{ion}^{KB}|\phi_{lm}\rangle = V_{local}|\phi_{lm}\rangle + |\delta V_{l'}\phi_{l'm'}\rangle = V_l|\phi_{lm}\rangle \qquad (A.8)$$

The cost of applying the KB pseudopotential is investigated next. In a plane wave basis the non-local pseudopotential projectors are of the form

$$\langle\psi|V_{ion}^{KB}|\psi\rangle = \sum_{lmGG'} \frac{b^*_{G'}\exp[-i(\mathbf{k}+\mathbf{G}')\bullet\mathbf{r}]|\delta V_l\phi_{lm}\rangle\langle\phi_{lm}\delta V_l|b_G\exp[i(\mathbf{k}+\mathbf{G})\bullet\mathbf{r}]}{\langle\delta V_l\phi_{lm}|\delta V_l|\delta V_l\phi_{lm}\rangle} \qquad (A.9)$$

$$= \sum_{lm} \frac{\sum_{G'} b^*_{G'}\exp[i(\mathbf{k}+\mathbf{G}')\bullet\mathbf{r}]|\delta V_l\phi_{lm}\rangle \sum_{G}\langle\phi_{lm}\delta V_l|b_G\exp[i(\mathbf{k}+\mathbf{G})\bullet\mathbf{r}]}{\langle\delta V_l\phi_{lm}|\delta V_l|\delta V_l\phi_{lm}\rangle} \qquad (A.10)$$

Expression (A10) is a product of separable sums over G and G' which replaces the double summation encountered previously in (A9). The resulting operation count now scales linearly with basis set size.

Figure B.1

BC8-Si valence charge density isosurfaces as calculated using *ab initio* pseudopotentials. Several contour levels are shown. A relatively low value for the contour threshold recovers the ball-and-stick picture shown in Figure B.2.

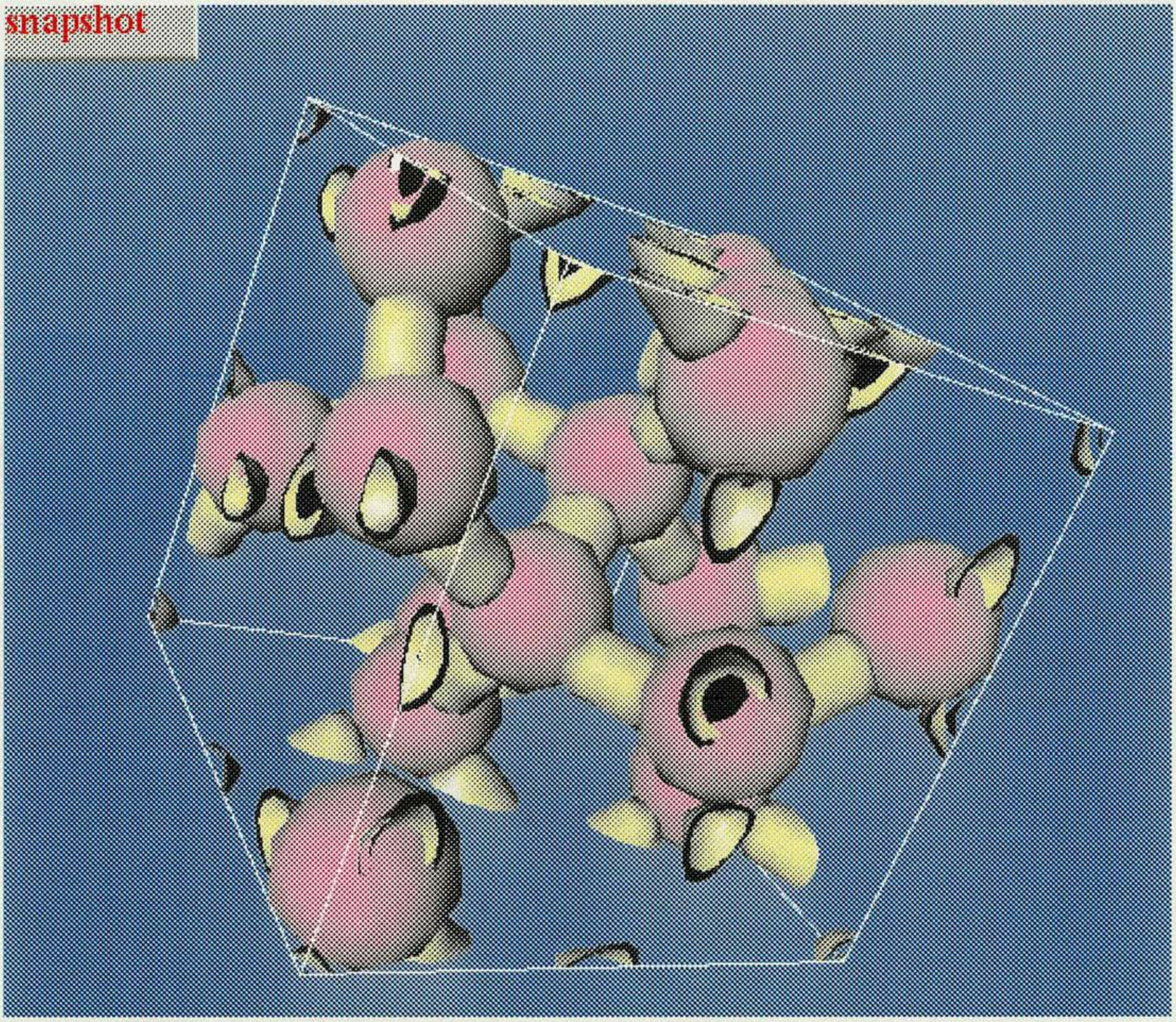

Figure B.2

See Caption of Figure B.1

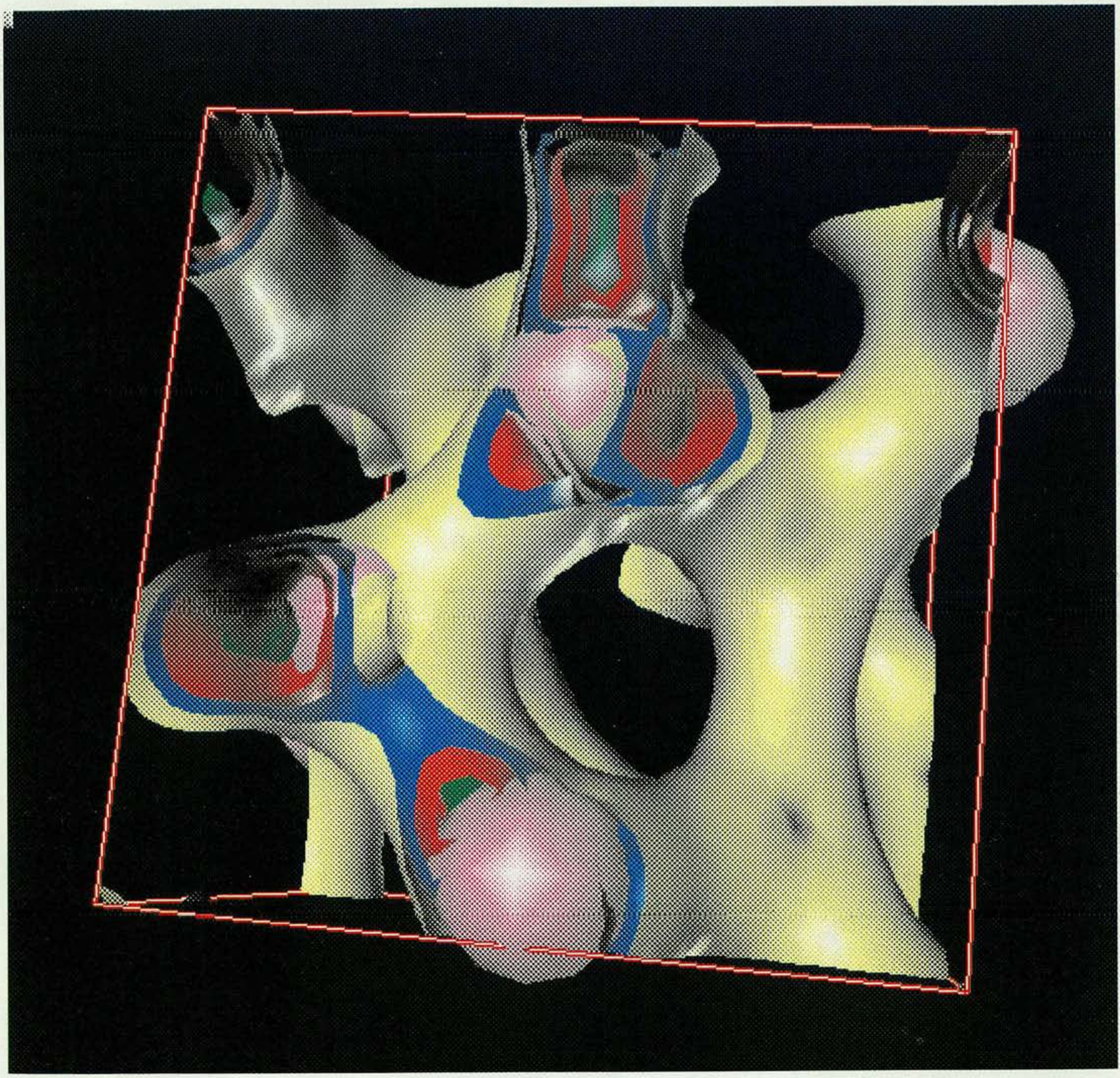

Figure B.3

ST-12 Si valence charge density iso surface showing a five-fold ring and the distortions of the tetrahedral bonding arrangement.